universität wien

DISSERTATION / DOCTORAL THESIS

Titel der Dissertation /Title of the Doctoral Thesis

„Polarons on transition-metal oxide surfaces“

verfasst von / submitted by

Michele Reticcioli

angestrebter akademischer Grad / in partial fulfilment of the requirements for the degree of

Doktor der Naturwissenschaften (Dr. rer. nat.)

Wien, 2018 / Vienna 2018

Studienkennzahl lt. Studienblatt / degree programme code as it appears on the student record sheet:	A 796 605 411
Dissertationsgebiet lt. Studienblatt / field of study as it appears on the student record sheet:	Physik
Betreut von / Supervisor:	Univ.-Prof. Cesare Franchini

Abstract

The formation of polarons, i.e., charge carriers (electrons or holes) coupled with the lattice vibrations, is a pervasive phenomenon on transition-metal oxide surfaces, with a strong impact on the physical properties and functionalities of the hosting materials. This doctoral project focuses on rutile TiO_2(110), a prototypical oxide surface, prone to form strongly localized (so called small) electron polarons. By performing a systematic analysis in the density-functional theory framework, supported by surface sensitive experiments, the fundamental polaronic properties are described in detail, clarifying the role of polarons in interesting applications. The polaron formation turns out to be more favorable on specific titanium sites on the subsurface layer, due to the local electrostatic potential and lattice flexibility. Positively charged intrinsic impurities, such as oxygen vacancies and titanium interstitials, exert an attractive interaction on the (negatively charged) polarons. As a consequence, polarons tend to populate sites in the proximity of these defects, maintaining, however, their intrinsic mobility, even at low temperature. The polaron-polaron repulsion appears to be very strong, especially at short distances. This repulsive interaction undermines the stability of the surface, ultimately driving structural reconstructions. In addition, polarons influence significantly the chemical reactivity of the hosting material, as investigated for the CO adsorption. In fact, molecules adsorbing on a polaronic site are strongly bound to the surface, due to a partial transfer of the polaron charge towards the adsorbate. These findings clarify long standing issues concerning oxide surfaces, which are key in established and emerging technologies; moreover, the adopted techniques and physical interpretations set the route for further investigations on other interesting phenomena and applications connected to polarons, such as electron transport, optical absorption, thermoelectricity, magnetoresistance, and high temperature superconductivity.

Zusammenfassung

Die Entstehung von Polaronen, also von Ladungsträgern (Elektronen oder Löcher) die an Gitterschwingungen gekoppelt sind, stellt ein weit verbreitetes Phänomen an Oberflächen von Übergangsmetalloxiden mit starken Auswirkungen auf die Eigenschaften und Funktionalitäten dieser Materialien dar. Diese Doktorarbeit befasst sich mit Rutil TiO_2(110), einer beispielhaften Oxidoberfläche, welche dazu neigt stark lokalisierte (kleine) Elektron-Polarone zu bilden. Um fundamentale Eigenschaften von Polaronen und deren Rolle in wertvollen Anwendungen beschreiben zu können wurde eine systematische Analyse basierend auf der Dichtefunktionaltheorie und unterstützt von Oberflächen-sensitiven Experimenten durchgeführt. Es wird gezeigt, dass sich Polarone vermehrt an speziellen Gitterplätzen von Titan Atomen in einer Schicht unterhalb der Oberfläche bilden. Verantwortlich dafür ist ein lokales, elektrostatisches Potential und eine gewisse Gitterflexibilität. Positiv geladene Punktdefekte, wie zum Beispiel Sauerstoffleerstellen oder interstitielle Titan Atome, üben eine anziehende Kraft auf (negativ geladene) Polarone aus. Dies hat zur Folge, dass sich Polarone bevorzugt in der Nähe der Defekte aufhalten, aber dabei ihre intrinsische Mobilität beibehalten und das sogar bei niedrigen Temperaturen. Die Polaron-Polaron Abstoßung scheint sehr stark zu sein, vor allem bei geringen Distanzen. Diese abstoßende Wechselwirkung hat Auswirkungen auf die Stabilität der Oberfläche und führt letztlich zu strukturellen Rekonstruktionen des Kristallgitters. Des weiteren beeinflussen Polarone maßgeblich die chemische Reaktivität des Wirtsmaterials, wie am Beispiel von CO Adsorption untersucht wurde. Als Adsorbat dienende Moleküle werden durch partiellen Transfer der Polaronladung stark an Stellen gebunden, die durch Polarone besetzt sind. Die Erkenntnisse dieser Arbeit ermöglichen es, seit langem bestehende Fragen bezüglich Oxidoberflächen zu beantworten, welche für viele Anwendung von großer Bedeutung sind. Außerdem können die eingeführten Techniken und physikalischen Interpretationen für weitere interessante Untersuchungen, wie zum Beispiel für den Elektronentransport, die optische Absorption, die Thermoelektrizität, magnetoresistive Effekte und den Hochtemperatursupraleiter verwendet werden.

Doctoral Thesis Dissertation

Polarons

on transition-metal oxide surfaces

Universität Wien - University of Vienna (Austria)
Faculty of Physics
Center for Computational Materials Science

Doctor canditate:
Michele Reticcioli

Doctorate Supervisor:
Univ.-Prof. Cesare Franchini

2015 – 2018

Contents

List of Figures

List of Tables

Publications

List of scientific documents related to the doctorate project. The complete list of personal publications is attached at the end of the dissertation.

[1] M. Reticcioli, U. Diebold, G. Kresse and C. Franchini, *Small polarons in transition metal oxides*, **Springer Handbook of Materials Modeling 2nd edition** (accepted in 2018).

[2] M. Reticcioli, I. Sokolović, M. Schmid, U. Diebold, M. Setvin and C. Franchini, *Interplay between adsorbates and polarons: CO on rutile TiO_2(110)*, **Phys. Rev. Lett.** (accepted in 2018).
arXiv:1807.05859

[3] M. Reticcioli, M. Setvin, M. Schmid, U. Diebold and C. Franchini, *Formation and dynamics of small polarons on the rutile TiO_2(110) surface*, **Phys. Rev. B** 98, 045306 (2018).
DOI:10.1103/PhysRevB.98.045306,
arXiv:1805.01849

[4] M. Reticcioli, M. Setvin, X. Hao, P. Flauger, G. Kresse, M. Schmid, U. Diebold and C. Franchini, *Polaron-Driven Surface Reconstructions*, **Phys. Rev. X** 7, 031053 (2017).
DOI:10.1103/PhysRevX.7.031053

[5] M. Setvin, M. Reticcioli, F. Poelzleitner, J. Hulva, M. Schmid, L. A. Boatner, C. Franchini and U. Diebold, *Polarity compensation mechanisms on the perovskite surface $KTaO_3$(001)*, **Science** 359, 6375, 572-575 (2018).
DOI:10.1126/science.aar2287

Attended conferences

List of conferences and public events where the main results of the project where presented and discussed.

2018 Faculty open presentation, University of Vienna (Austria), invited talk.

2018 ViCoM Conference: From Electrons to Phase Transitions, Vienna (Austria).

2018 School on Electron-Phonon Physics from First Principles, ICTP Trieste (Italy), contributed poster.

2018 IWOX Workshop, Pradollano (Spain), contributed talk.

2018 IWOX Workshop, Pradollano (Spain), substituting invited speaker.

2018 TU Seminars, Vienna University of Technology (Austria), invited talk.

2017 ViCoM Fall Workshop, Stadtschlaining (Austria).

2017 ViCoM Workshop, Graz (Austria), contributed talk.

2017 Workshop on Charge Trapping Defects in Semiconductors and Insulators, York (United Kingdom), contributed talk.

2017 APS March Meeting, New Orleans (United States), contributed talk.

2017 Electron Phonon Interactions APS Tutorial, New Orleans (United States).

2017 Computational Magnetism Winter School, Vienna University of Technology (Austria), contributed poster.

2016 ViCoM Fall Workshop, Vienna (Austria).

2016 ViCoM Young Researches Meeting, Vienna (Austria), contributed poster.

2016 32nd European Conference on Surface Science ECOSS, Grenoble (France), contributed talk.

2016 ViCoM Workshop, Stadtschlaining (Austria), contributed poster.

2016 80th Annual Conference of the DPG, Regensburg (Germany), contributed talk.

2016 10th International Workshop on Oxide Surfaces, Dalian and Liaoyang (China), contributed talk.

Preface

I am glad to present here my doctoral dissertation, finalizing the project "Polarons on transition-metal oxide surfaces" (March 2015 – December 2018), carried out under the careful supervision of Prof. Cesare Franchini at the Faculty of Physics and Center for Computational Materials Science of the University of Vienna (Universität Wien). The project was enriched by the precious and inspiring collaboration with the experimental surface-science group led by Prof. Ulrike Diebold from the Vienna University of Technology (Technische Universität Wien).

Aim of the project

This project investigated via computational techniques supported by experiments the chemical and physical phenomena taking place in transition metal oxides, aiming to describe the interplay of dimensional confinement and electron-lattice interactions.

Outline of the topic

Oxides are the heart of a wide range of well established and emerging technologies, and their surfaces are key to device functioning. Moreover, besides their technological importance, these systems represent a fertile playground for the investigation of fundamental physical properties. In fact, these compounds are usually well suited for many experimental techniques, and can generate a great variety of interesting phenomena.

Typically, oxides exhibit relatively flexible and ionic crystals, which turn out to be suitable for excess-charge trapping and polaron formation, in particular on the surface. A polaron is a quasiparticle originating from the interactions between charge carriers (electrons or holes) and lattice ion vibrations, owning peculiar properties (typical manifestations include charge localization on specific lattice sites, local alteration of the lattice bond lengths, and a characteristic energy peak well localized in the band gap region). Polarons are classified as small or large depending on some specific properties, including the extension of the spatial localization of the electronic charge. The question whether excess charge in transition metal oxides forms free or trapped carriers is a crucial aspect, since it drastically affects the material functionalities.

From the computational point of view, describing the many, often com-

peting, collective phenomena in reduced dimensions requires methods at the frontier of the material science research.

Our study

We approached the study of this intriguing and intricate subject by analyzing the (110) surface of rutile TiO_2, an archetypal system which is prone to form electron small polarons.

We performed a vast set of calculations in the density-functional theory framework; the ability to control the formation of polarons allowed us to obtain a systematic analysis of the polaronic TiO_2(110) surface, in excellent agreement with the scanning-tunneling and atomic-force microscopy measurements performed by the experimentalists, guided by Ulrike Diebold, Martin Setvin and Michael Schmid. An overview of the computational and experimental techniques useful to tackle the study of polarons in oxides was gathered into a book chapter, describing in particular the methods refined for TiO_2 and suggesting possible applications [1].

The tight collaboration with the experimental group led us to achieve a solid interpretation of interesting phenomena driven by polarons on TiO_2(110). The most relevant results of our research are collected and presented in scientific articles, discussing the effects of polarons on molecular adsorption [2], the intrinsic properties of polarons [3], and the thermodynamic stability of polaronic surfaces [4].

Additional data on the reactivity of TiO_2(110) have been collected by Igor Sokolović, from the experimental group, who performed experiments and calculations (the results are not included in this dissertation).

Besides the study carried through with TiO_2, this project set the basis for the investigation of polarons in perovskite-type oxides. We analyzed the stability of the $KTaO_3$(001) perovskite surface, an ionic crystal which undergoes structural reconstructions in order to compensate the surface polarity [5]. The comprehension of the surface stabilization mechanisms is a preliminary step towards the study of the polaronic properties of this class of compounds.

Additionally, the properties of small polarons were analyzed for the $SrTiO_3$ perovskite via density functional theory. In this case, Muhammad Shafiq, a visiting Ph. D. student from the Abbottabad University of Science and Technology (Pakistan), performed the calculations under our supervision. The analysis is in a preliminary stage, thus, these results have not been published yet, nor they are included in this dissertation.

The most relevant outcomes of this project have been also presented in numerous conferences, and highlighted by third-party reviews [6, 7].

This dissertation

This dissertation focuses on the most interesting results obtained by our study on small polarons on TiO_2(110). It presents the results collected in our publications together with unpublished data.

The core of the dissertation is structured in six main chapters followed by the appendix: an abstract opens each chapter, presenting briefly the ongoing topic and the connection with our published works.

Chapter 1 ("Introduction") introduces the concept of polarons and the significant aspects of transition metal oxides, TiO_2 in particular. The methods adopted to pursue our investigations are described in Chapter 2 ("Methods"). Chapter 3 ("Properties of polarons on the rutile TiO_2(110) surface") discusses the results at the core of our study, with a detailed description of the properties of small polarons on TiO_2(110). The effects of polarons on the material properties and surface phenomena are reported in Chapter 4 ("Surface stability and structural reconstruction") and Chapter 5 ("Adsorbates and polarons: CO on TiO_2(110)"), respectively. Chapter 6 ("Conclusions") concludes the main text, with a general outline on the major findings, discussing possible future routes.

The appendix presents complementary insights on the main outcomes of this doctorate project. Technical details on simulations of small polarons are reported in Appendix A ("Polarons in TiO_2: Crucial aspects of the computational setup"). Appendix B ("Polarity driven reconstructions in $KTaO_3$") collects the results obtained for the $KTaO_3$(001) surface thermodynamic stability. Appendix C ("Additional figures") lists additional figures, which show supplementary details regarding the topics discussed in the main text; these figures are referenced directly from the main text.

Acknowledgements, the Bibliography and the complete list of my publications, conclude the dissertation.

Vienna, December 2018

Chapter 1

Introduction

The formation of polarons is a pervasive phenomenon in transition metal oxide compounds, with a strong impact on the physical properties and functionalities of the hosting materials. In its original formulation the polaron problem considers a single charge carrier in a polar crystal interacting with the surrounding lattice. Depending on the spatial extension of the polaron quasiparticle, originating from the coupling between the excess charge and the phonon field, one speaks of small or large polarons.

This chapter introduces the main physical concepts concerning polarons in oxides, with a special focus on small polarons on rutile TiO_2(110) [1], the central aspect of this doctorate project.

Contents

1.1 Transition metal oxides

Transition metal oxides (TMO), *i.e.*, compounds including oxygen and transition metal atoms, have raised a vast interest in many scientific fields [8]. The popularity of these systems is due to several reasons. First of all, TMO's show a great variety of interesting magnetic, optical and electronic properties, brought about by the outer d electrons of the transition metals and the polarizability of oxygen atoms [9]. The wide range of TMO's comprises insulators at one end, and metals at the other, including also high-temperature superconductors. The surface of oxides can be inert and suitable as corrosion protection layer, or chemically active as catalyst. Moreover, TMO materials explore different regimes depending on pressure and temperature, or due to variations of the chemical composition as well as formation of defects [10]. Many oxides exhibit also ferroic properties, such as ferroelectricity, ferromagnetism and ferroelasticity. Therefore, TMO's constitute a rich playground for the scientific investigation of many physical and chemical phenomena. The academic interest for oxide materials is accompanied by a large number of established and emerging technologies, based on the TMO functionalities. Finally, the characterization of TMO properties is useful also to understand the functionality of other classes of materials, such as metals. In fact, almost every metal gets oxidized while exposed to ambient conditions, forming an oxide at the surface, which could alter the device functioning [8, 11].

[1.1.1] TiO_2

Titanium dioxide, TiO_2, is one of the most studied transition metal oxides. It is relatively easy to obtain high quality crystals, well suited for many experimental techniques, making the basic properties of this material well characterized [12]. A wide range of applications makes use of TiO_2 as catalyst and photocatalyst, as white pigment in paints and cosmetic products, as gas sensor, as optical and corrosion-protecting coating, as varistor in electric devices, for the purification of contaminated water, and in solar cells.

[1.1.2] Rutile

TiO_2 exists in various crystal structures. Rutile is one of the most common and stable polymorphs. As shown in Fig. 1.1, the rutile TiO_2 owns a tetragonal symmetry with lattice vectors $a = b = 4.584$ Å and $c = 2.953$ Å [12] [Fig. 1.1(a)]. Each Ti atom is surrounded by six O atoms in a distorted octahedral configuration. Four oxygens lying on the equatorial plane are at a Ti-O distance of 1.944 Å while the two apical oxygens show a longer Ti-O separation of 1.988 Å [13, 14]. Neighboring octahedra along $\langle 110 \rangle$-type directions share one corner and are rotated by 90° [Fig. 1.1(b)]. The oxygen atoms are in a planar-trigonal coordination symmetry. The titanium atoms own a nominal 4+ oxidation state (Ti^{4+}), while the oxygens are in a 2− state

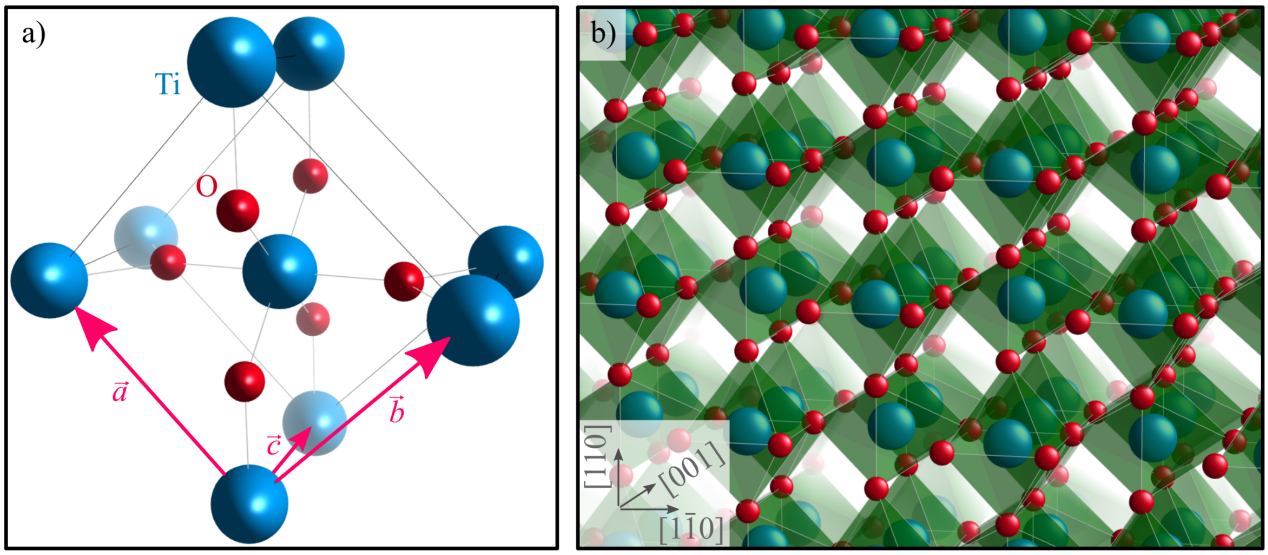

Figure 1.1: The rutile TiO_2 crystal structure. Perspective views of the primitive cell (a) and the octahedron stacking in the bulk (b). *[Unpublished Figure]*

(O^{2-}). Although TiO_2 is a semiconductor, bulk defects can modify drastically its electronic properties. The n-type doping resulting from the intrinsic defects, such as interstitial Ti atoms (Ti_{int}) and oxygen vacancies (V_O), can determined a sensible decrease of the resistivity, accompanied by a color change, from transparent to blue [15].

[1.1.3] The (110) surface

The most stable surface of rutile TiO_2 is the (110) surface, shown in Fig. 1.2. It consists of a bulk-terminated (1×1) surface, with large relaxations of the atoms on the surface layers, predominantly along [110]. The TiO_2(110) is a Tasker-type 2 surface [16], *i.e.*, it is constituted by charged planes parallel to the surface, with no dipole moment because of the symmetrical stacking sequence. One plane is constituted by an equal number of Ti^{4+} and O^{2-} atoms (a Ti_2O_2 $+4e$-positively charged layer per bulk Ti_2O_4 unit cell), and it lies between two layers of oxygen atoms (including a single O^{2-} atom per layer per bulk Ti_2O_4 unit cell). Therefore, these tri-layer units have no dipole moment.

The (110) surface is very corrugated since it terminates with a layer of undercoordinated oxygens (O_{2c}), arranged in rows along [001], above a Ti_2O_2 layer. The Ti_2O_2 layer below the O_{2c} rows is constituted by tri-fold coordinated oxygen [001] rows alternated to six-fold coordinated (Ti_{6c}) and five-fold coordinated (Ti_{5c}) titanium [001] rows. Therefore, the surface breaks the symmetry of the Ti and O atoms: In particular, beyond the evident difference between

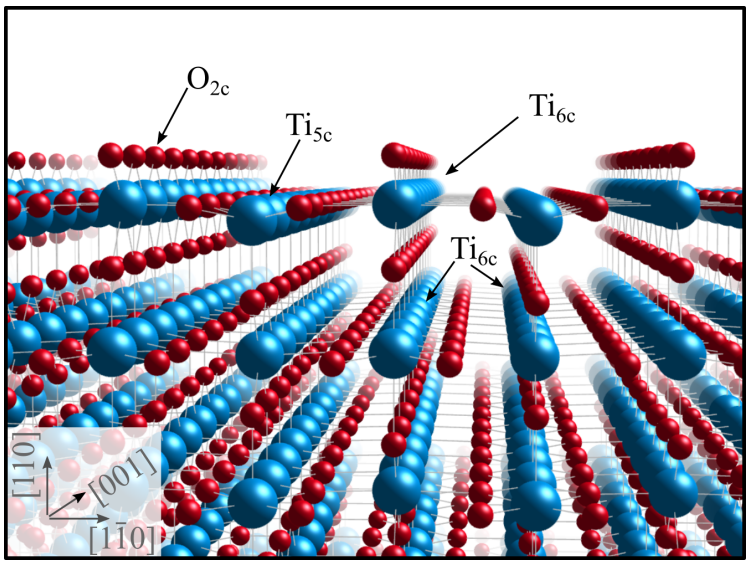

Figure 1.2: The rutile TiO_2(110) surface. The surface O_{2c}, Ti_{5c} and Ti_{6c} [001] rows are indicated in the figure, as well as the Ti_{6c} rows on the subsurface layer. *[Unpublished Figure]*

Ti_{5c} and Ti_{6c} atoms on the surface tri-layer, the Ti_{6c} atoms on the subsurface tri-layer undergo different degree of structural relaxations, depending on their position (that is below the surface Ti_{6c} or Ti_{5c} rows).

The O_{2c} atoms on the (1×1) surface are relatively easily removed by thermal annealing, irradiation, electron bombardment, or sputtering, due to their coordinative undersaturation. These experimental techniques are able to control the amount of oxygen vacancies and, consequently, the reduction level of the system. At extreme reducing conditions, TiO_2(110) undergoes a structural reconstruction, from the (1×1) to a (1×2) phase, doubling the periodicity along [1$\bar{1}$0]. Many models have been proposed to describe the atomic structure of the (1×2) phase, and the debate is still open. The added Ti_2O_3 row model [17–19] seems to be the best candidate, supported by recent experimental data [20] and systematic simulations [21]. The (1×2) reconstructed structure is further discussed in Chapter 4.

[1.1.4] Polarons in TiO_2

TiO_2 bears the formation of polarons (see Sec. 1.2 for a detailed introduction on the polaron concept) [22–33]. An overview on the polaronic properties of TiO_2 is elaborated in Sec. 1.3, together with a description of the experimental observations of polarons in other materials. Charge trapping and the formation of polarons is a pervasive phenomenon in transition metal oxide compounds, in particular on the surface. Polaron formation influences the fundamental physical and chemical properties of materials: The local alteration of the lat-

tice bond lengths, the change of the formal valence at the specific polaronic site, and the emergence of a characteristic peak in the TMO-semiconductor energy gap are typical manifestations of polarons [34–37]. These changes affect virtually all functionalities of the material in practical applications.

The experimental and computational methods usually adopted to study the formation of polarons in oxides are described in Chapter 2. Chapter 3 is devoted to the detailed characterization of the polarons on rutile $TiO_2(110)$, as this is one of the most important aspects of this doctorate project. The effects of the polarons on the stability and on the chemical reactivity of the surface are discussed in Chapter 4 and Chapter 5, respectively.

1.2 Polarons

Electrons in perfect crystals are typically adequately described in terms of periodic wave functions. However, rather than being constituted by a perfect lattice, real materials are often characterized by the presence of defects, such as impurities, grain boundaries, and dislocations [38, 39]. Defects in the crystal break the periodicity of the electronic charge density. They can lead to the formation of localized states [40–42], which affect the materials properties and, thus, their performance in applications. Less intuitively, such localized states could exist also in the absence of any defects in the crystal, *i.e.*, they can form in perfect lattices. This phenomenon is referred to as polaron. A polaron is a quasiparticle originating from the interactions between charge carriers (*i.e.*, electrons or holes) and lattice ion vibrations [43]. The charge carrier is surrounded by local lattice distortions, and this polarized cloud follows the charge carrier as it moves through the crystal (see Fig. 1.3). Such quasiparticles differ from lattice defect states: They own peculiar properties, described by well developed quantum field theories [43, 44] as summarized in the following.

Formation of polarons is particularly favorable in polar semiconductors and transition metal oxides owing to the strength of the electron-phonon interaction, and it is further promoted in the vicinity of a surface, where the crystal lattice is more flexible and the necessary lattice relaxations cost less energy [45–49]. Polarons play a decisive role in a wide range of phenomena, including electron transport [29, 50], optical absorption, and chemical reactivity, and have crucial implications in high-T_c superconductivity [51], colossal magnetoresistance [52, 53], thermoelectricity [54], photoemission [55], and photochemistry [56].

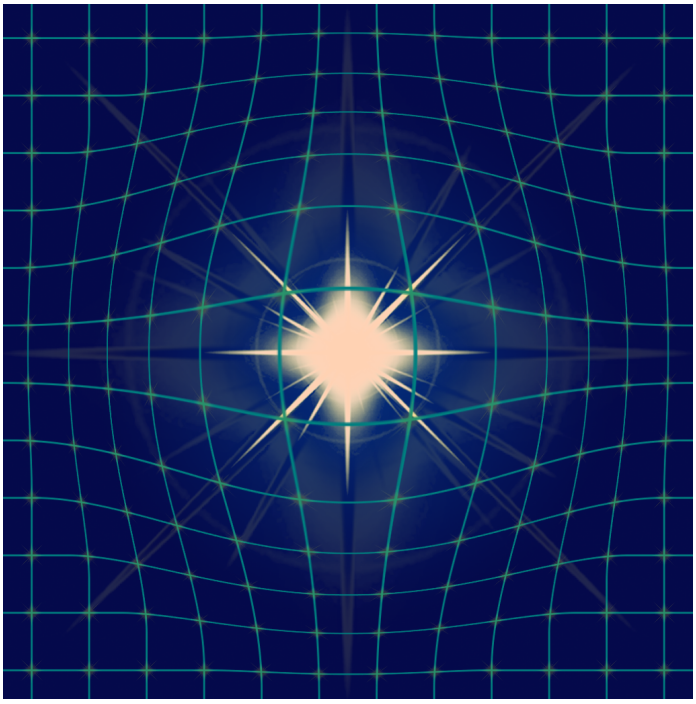

Figure 1.3: Pictorial view of a polaron. An excess charge is trapped in a lattice site (bright) and distorts the surrounding lattice. *Figure adapted from Springer ©2018 Handbook of Materials Modeling* [1].

[1.2.1] Origins

The emergence of the polaron theory can be traced back to 1933, when Landau elaborated on the possibility for lattice distortions to trap electrons, via modifications of the lattice phonon field induced by the electron itself [57]. The resulting electron-phonon quasiparticle was later called polaron, a coupled electron-phonon system in which the polarization generated by the lattice distortions acts back on the electron renormalizing the electronic properties (such as the effective mass). An analogous discussion is valid for holes rather than electrons.

A first formal description of the polaron problem was published in 1946 by Pekar [58], who considered a free electron interacting with lattice deformations in the continuum approximation. Therefore, Pekar's study is limited to the case of polarons with a size larger than the lattice constant, so that the atomic discreteness is negligible [59]. With the ionic lattice described as a polarizable dielectric continuum, the ion displacements contribute to the charge trapping. As a result, the lattice polarization enhances the charge carrier mass m, with respect to the solely contribution of the valence electrons [60].

During the 1950s, the second quantization formalism was used to refine the description of the polaron problem in terms of quantum effective Hamiltoni-

ans including an electronic term (H_e), a phonon term (H_{ph}) and the electron-phonon coupling term (H_{e-ph}). The $e-ph$ term is of fundamental importance for understanding the polaronic states, since it takes into account the type (e.g. short- or long-range) and intensity (weak to strong) of the mutual interactions between charge carriers and lattice vibrations. However, a complete analytic solution of the polaron Hamiltonian cannot be achieved and approximations are needed. Fröhlich [61] and Holstein [43] separately addressed different aspects of the problem and proposed two different pictures, as described in the following.

[1.2.2] Fröhlich polaron

In the Fröhlich picture [44, 61], the electron-phonon coupling is considered in its weak limit. Therefore, perturbation theory can be applied to solve the quantum Hamiltonian [59]:

$$H = \sum_{\mathbf{k}} \frac{k^2}{2} c^\dagger_{\mathbf{k}} c_{\mathbf{k}} + \sum_{\mathbf{q}} b^\dagger_{\mathbf{q}} b_{\mathbf{q}} + \sum_{\mathbf{k},\mathbf{q}} \left[V_d(\mathbf{q}) b^\dagger_{\mathbf{q}} c^\dagger_{\mathbf{k}-\mathbf{q}} c_{\mathbf{k}} + V^\dagger_d(\mathbf{q}) b_{\mathbf{q}} c^\dagger_{\mathbf{k}+\mathbf{q}} c_{\mathbf{q}} \right] , \quad (1.1)$$

where $c_{\mathbf{k}}$ and $b_{\mathbf{q}}$ are annihilation operators for a particle with wave vector $\mathbf{k}$ and a phonon with wave vector $\mathbf{q}$, respectively. $V_d(\mathbf{q})$ is the electron-phonon coupling function for a system in d dimensions; in 3 dimensions, it reads:

$$V_3(\mathbf{q}) = i \left(\frac{2\sqrt{2}\pi\alpha}{V} \right)^{\frac{1}{2}} \frac{1}{q} . \quad (1.2)$$

Here, V is the volume of the system and α is the dimensionless Fröhlich electron-phonon coupling constant defined in terms of the reduced Plank constant $\hbar$, the charge carrier charge e, the phonon frequency ω of the long-wavelength optical-longitudinal phonon, and the material's static and high-frequency dielectric constants ϵ_0 and ϵ_∞, respectively (ϵ_0 includes ionic relaxation effects, whereas the ion-clamped ϵ_∞ accounts only for electronic contributions):

$$\alpha = \frac{e^2}{\hbar} \sqrt{\frac{m}{2\hbar\omega}} \left(\frac{1}{\epsilon_\infty} - \frac{1}{\epsilon_0} \right) . \quad (1.3)$$

The material dependent constant α represents the phonon cloud thickness of the polaron. In fact, for a polaron at rest, the number of phonons (N_{ph}) in the cloud is half the value of α, *i.e.*, $N_{\text{ph}} = \alpha/2$. In real materials α ranges typically between 0.02 (InSb) to 3.8 ($SrTiO_3$).

The electron-phonon interactions are too weak to trap the charge carrier in a lattice specific site. The spatial extension of the Fröhlich polaron is larger than the lattice constant, and a phonon cloud accompanies the charge carrier

motion, enhancing its mass [62, 63]:

$$m^* = \frac{m}{1-\alpha/6} \simeq (1+\alpha/6)\, m \ . \tag{1.4}$$

[1.2.3] Holstein polaron

Holstein considered the polaron determined by a strong electron-phonon coupling, such that the spatial confinement reduces up to the order of the lattice constant [43, 64]:

$$H = -t \sum_{<ij>} c_i^\dagger c_j + \omega \sum_i b_i^\dagger b_i + g \sum_i n_i (b_i^\dagger + b_i) \tag{1.5}$$

where t is the hopping amplitude between neighboring sites, c_i (b_i) and $c_i^\dagger$ ($b_i^\dagger$) are fermionic (bosonic) creation and annihilation operators acting on the site i, ω the phonon frequency, g the electron-phonon coupling strength, and $n_i = c_i^\dagger c_i$ is the fermionic particle number operator.

In the simplified case of a polaron trapped in a linear molecule and hopping between different molecular sites [43, 65], Eq. 1.5 reduces to a two-site Hamiltonian describing the electron hopping between the two sites, interacting with the vibrational modes of an ion placed in between [59]:

$$H = t(c_1^\dagger c_2 + c_2^\dagger c_1) - \frac{1}{2M}\frac{\partial^2}{\partial x^2} + \frac{\gamma x^2}{2} + gx(c_1^\dagger c_1 + c_2^\dagger c_2) \tag{1.6}$$

with M the ion mass, $\gamma = M\omega^2$ the spring constant and x the linear ion displacement from the equilibrium position. The state $|\psi\rangle$ with an extra electron introduced into the unperturbed system $|0\rangle$ and localized at the site 1 or 2 with amplitude probability $u(x)$ and $v(x)$, respectively, is written as

$$|\psi\rangle = \left[u(x)c_1^\dagger + v(x)c_2^\dagger\right]|0\rangle \ . \tag{1.7}$$

Despite the simplicity of this model, an analytic solution for the Schrödinger equation $H\psi = E\psi$ can be found only in special cases (e.g. ionic vibration perpendicular to the hopping direction), and one has to rely on numerical approximations or restrict the study to the nonadiabatic ($t \ll \omega$) or adiabatic ($t \gg \omega$) limits.

[1.2.4] Lattice defects

At this point, the distinction between polarons and electrons trapped at lattice defect sites stands out clearly by inspecting the Fröhlich's and Holstein's analysis. First of all, as mentioned above, polaron formation occurs even in the absence of lattice defects, *i.e.*, in the perfect crystal. Moreover, polarons are not stuck to a specific lattice site, rather they can move around through the system. Both these characteristics, *i.e.*, spontaneous localization and mobility, were pointed out by Holstein, who summarized the concepts in few brilliant sentences [43]:

> "Let us imagine that an electron is momentarily fixed at some point of the crystal. As a result of electron-lattice interaction, the surrounding lattice particles will be displaced to new equilibrium positions [...] such as to provide a potential well for the electron. If the well is sufficiently deep, the electron will occupy a bound state, unable to move unless accompanied by the well, that is to say, by the induced lattice deformation."

Conversely, the physics of an electron attached to a defect is rather different, as it is typically not mobile and its characteristics strongly depend on the type of defect [10, 37].

[1.2.5] Large VS small

Many other theoretical studies have further developed the original pictures elaborated by Fröhlich and Holstein, commonly referred to as large and small polaron, respectively [66].

Large Polaron	Small Polaron
Polaron radius $\gg$ lattice parameter	Polaron radius $\simeq$ lattice parameter
Shallow state ($\sim$ 10 meV below CBM)	In-gap state ($\sim$ 1 eV below CBM)
Coherent motion (scattered occasionally by phonons)	Incoherent motion (assisted by phonons)
Mobility $\mu \gg 1$ cm^2/Vs	Mobility $\mu \ll 1$ cm^2/Vs
Decreasing mobility with increasing temperature	Increasing mobility with increasing temperature

Table 1.1: General properties of large and small polarons.

Table 1.1 summarizes the main distinctions between the large and the small polaron [63]. Their names reflect the length scale of the spatial localization: while the small-polaron electronic charge is usually confined in the primitive cell (a few Å), the large polaron extends over several lattice sites (typically about 20 Å). Also, the two types of polaronic states exhibit distinct energy scales. The large polaron is usually a shallow state, few tens of meV below the conduction band minimum (CBM). Conversely, the small polaron is firmly trapped by local distortions in a stronger potential well, which determines the formation of a deeper in-gap state well localized around 1 eV below the CBM.

The localization process is also different: a charge carrier introduced into a system can quickly equilibrate with the lattice and form a large polaron, whereas the formation of a small polaron occurs only after overcoming an energy barrier [67, 68]. Finally, the two types of polarons are characterized by

very different transport properties. The large polaron, a heavy quasiparticle, is weakly scattered by phonons. This weak scattering can compensate the large mass, resulting in a large mobility for the large polaron. A small polaron instead hops between trapping sites with a lower mobility. Since its motion is assisted by phonons, the mobility of small polarons increases with increasing temperature.

Both large and small polarons have been observed in several experiments, as reported in the next section, and studied by different theoretical and computational schemes (Sec. 1.4). Historically, large polarons have been investigated mostly via effective Hamiltonians, in particular by means of variational treatments solved by Feynmann's path integral techniques (able to extend the Fröhlich's Hamiltonian from the weak to the so-called all electron-phonon coupling regime), and by diagrammatic Monte Carlo [69–75] approaches. First principles techniques are more suitable for the description of the small polaron, but successful attempts to address the large-polaron case have been presented in the last few years [35, 48, 76].

1.3 Observations of polarons

Several years after the first theoretical predictions, experiments had started to observe polarons in real materials [25]. Nowadays, it is a common practice to complement experimental data with theoretical interpretations based on electronic structure simulations. Details regarding the computational techniques are reported in Sec. 1.4. Table 1.2 lists significant experimental studies on polaronic materials. This list also represents the variety of experimental techniques used to observe both small and large polarons, formed by both negative (electron) and positive (hole) excess charges in oxide materials. The injection of extra carriers (eligible to form polarons) into the system is obtained by different approaches. Analogously, the observations of polarons is achieved by measuring different quantities.

[1.3.1] Conductivity exp.

The first observation of polarons is attributed [82] to an experimental study published in 1963 [34]. Experiments on oxidized uranium dioxide reported an increasing hole conductivity with raising temperature, following a behavior well described by the formula:

$$\mu \sim \frac{1}{T} \exp\left(-\frac{\Delta E}{k_B T}\right) , \tag{1.8}$$

indicating small polaron hopping from U^{5+} to U^{4+} sites upon thermal activation [77, 83, 84]. This interpretation is further substantiated by a decreasing activation energy ΔE with increasing oxygen concentration.

Type	Material	Source	Exp. technique	Publication
hole, small polaron	UO_2	oxidation	conductivity measurement	1963 [34]
hole, small polaron	MnO	Li doping	conductivity measurement	1970 [50]
electron, small polaron	CeO_2	O vacancies	conductivity and Seebeck	1977 [77]
electron, small polaron	$BaTiO_3$	Nb doping	EPR	1994 [78]
electron, small and large polaron	a-TiO_2 and r-TiO_2	Nb doping	conductivity and optical measurements	2007 [79]
electron, small polaron	r-TiO_2	O vacancies	Resonant photoelectron diffraction	2008 [80]
electron, small polaron	r-TiO_2	O vacancies	EPR	2013 [27]
electron, large polaron	a-TiO_2	O vacancies	ARPES	2013 [29]
electron, small polaron	r-TiO_2	O vacancies	STM and STS	2014 [48]
electron, small polaron	r-TiO_2	UV irradiation or H adatom	IR spectroscopy	2015 [36]
hole, small polaron	$LiNbO_3$	Visible light	IR spectroscopy	2016 [37]
electron, small polaron	r-TiO_2	O vacancies	IR spectroscopy on adsorbates	2017 [81]
electron and hole, large polaron	lead halide perovskites	laser pulse	TR-OKE	2017 [76]

Table 1.2: List of significant experimental studies on polaronic materials.

Experimental confirmations of Eq. 1.8 were obtained for a wide range of materials, with charge carriers injected by different types of defects. Examples are given by the hole small polarons observed in Li-doped MnO [50], and by the electron small polarons in oxygen deficient cerium dioxide [77]. In the latter

example, two excess electrons originate from every oxygen vacancy present in the system. Each excess electron localizes at one Ce^{4+} site forming a Ce^{3+} ion. Hopping is activated by temperature, and the conductivity measurements confirmed the expected trend for polarons (Eq. 1.8). Moreover, by measuring the Seebeck coefficient for thermo-electricity, the number of carriers was found to be temperature independent. This is in contrast with the band model for the conductivity, which predicts an increasing number of charge carriers with raising temperature. On the contrary, according to the polaron hopping model, the charge carriers are introduced in CeO_2 only by defects, and the mobility increases with raising temperature due to the increased phonon populations.

[1.3.2] EPR

The electron paramagnetic resonance (EPR) technique is able to identify lattice ions with unpaired electrons, a distinct feature of the polaron state. In EPR experiments, an external magnetic field splits the energy level of the unpaired electrons (Zeeman effect), thus determining energy levels available by emitting or absorbing a photon at a specific frequency: the sample is illuminated by light, typically at constant frequency, while the magnetic field varies and the resonance peaks are measured as function of the magnetic field when the conditions for the level transitions are satisfied. The shape, intensity and energy values of the resonance peaks determine the electronic states of the atoms in the sample, making possible to detect charge trapping. Small polarons were identified by EPR in Nb doped $BaTiO_3$ samples [78, 85], and other materials including oxygen-deficient rutile TiO_2 samples [27].

[1.3.3] Optical measurements

The difference between small and large polarons manifests itself prominently in the optical properties of materials. An example is the response of two different polymorphs of TiO_2, rutile and anatase, to (electron) doping with Nb, reported by Zhang *et al.* [79]. By substituting 4-valent Ti with 5% of 5-valent Nb, electrons were added to the system. The two types of films showed contrasting behavior in conductivity measurements: anatase films were metallic while rutile films semiconducting. This is consistent with the formation of large and small electron polarons, respectively. The optical transmittance of 80% in the visible range for epitaxial anatase films shows that these films can be characterized as transparent conductive oxides [86].

[1.3.4] Resonant photoelectron diffraction

The charge distribution in reduced rutile $TiO_2(110)$ single crystals was first determined by Krüger *et al.* [80, 87]. Their experiment is based on angle-resolved x-ray photoemission (XPS). Intensity variations in a specific photoelectron peak (here Ti-2*p*) are recorded while changing the polar and azimuthal emission angle. Since forward-focusing dominates the scattering of electrons with kinetic energies of a few hundred eV, the configuration of near-range atomic neighbors can be accessed in a rather direct manner, and modeled in

a simple cluster geometry [88]. In their work, the authors took advantage of the fact that the Ti-2*p* XPS peak shows a clear shoulder that is attributed to Ti^{3+}; the intensity of this feature was additionally increased by tuning the photon energy to a resonance condition [89]. The photoelectron diffraction pattern of the Ti^{4+} peak (from Ti^{4+} at regular lattice sites) and the reduced Ti^{3+} signature turned out to be drastically different, and the best fit was obtained by attributing the excess electrons to the subsurface Ti atoms. This is true independently of the way the excess electrons are introduced into the lattice, either by creating O vacancies [80] or by adding electrons via Na deposition [87]. This points to the fact that the location of polarons in subsurface sites is an intrinsic feature of rutile TiO_2.

[1.3.5] ARPES

TiO_2 has been investigated by numerous different experimental techniques in addition to the methods mentioned above. Angle resolved photoemission spectroscopy (ARPES) [29] was used to identify the presence of large polarons in the anatase polymorph of titanium dioxide. The energy dispersion close to the Fermi level measured by ARPES experiment shows satellite (shallow) states below the conduction band, corresponding to large electron polarons, brought about by the oxygen vacancies present in the sample. By tuning the amount of oxygen vacancies (via UV irradiation [90]), the density of charge carriers can be controlled. At high vacancy concentrations, the satellite states disappear, due to the overlap of the polaronic wavefunctions, giving rise to a metallic behavior indicated by the crossing of the conduction band with the Fermi energy.

[1.3.6] STM and STS

A direct view at the polaronic states in TiO_2 can be achieved by using scanning tunneling microscopy (STM) and spectroscopy (STS) [48]. These techniques are based on the electronic tunneling occurring between the sample and a tip. By controlling the voltage bias between the sample and the tip, the tunneling can be tuned to occur at various energy ranges around the Fermi energy. By measuring whether the tunneling current at a given sample-tip distance (constant height mode) or the sample-tip distance for a given tunneling current (constant current mode), one can obtain accurate information on the energy-resolved dispersion (in the STS) and on the spatial distribution (in the STM) of the electronic states.

In-gap states stand clearly from the STM and STS studies on rutile TiO_2. The charge carriers (electrons), induced by oxygen vacancies, form polaronic states at deep energy (approximatively 1 eV below the conduction band minimum) [48]. The spatial distribution of the polaronic charge measured by the STM confirms the small polaron formation on the subsurface Ti sites.

[1.3.7] IR spec.

Small polaron states have been detected in rutile TiO_2 also by absorption infrared (IR) spectroscopy experiments [36]. The vibrational energies of the lattice bonds are typically in the infrared regime. Therefore, by exposing the sample to IR light, resonance peaks appear in the transmitted and reflected beams. In presence of small polarons, the localized charge together with the local lattice distortions contribute to form resonant peaks at characteristic vibrational frequencies. Interestingly, the polaron peaks in TiO_2 were found to be independent of the source of charge carriers, H adsorption and UV irradiation, a strong evidence of the polaronic nature of the peaks. The characteristic vibrational spectra of a defect state would, in fact, be susceptible to the type of donor.

Infrared spectroscopy can also be used to detect polarons indirectly, by inspecting the vibrational properties of bonds in the vicinity of the trapping site. Electron small polarons were found to redshift the stretching frequency of NO molecules adsorbed on reduced TiO_2 surfaces with respect to the pristine samples [81]. Analogously, hole small polarons modify the vibrational frequency of the OH impurities at Li vacancies in $LiNbO_3$ samples [37]. In the latter study, irradiation in the visible region was used to generate hole small polarons at O sites, and electron polarons at Nb sites. The hole polarons localize in the vicinity of the Li vacancies, due to the a more favorable electrostatic potential, and therefore strongly contribute to the frequency shift of the OH impurities. Once the source is turned off, hole and electron polarons recombine, since their mobile character, and the original vibrational frequency is restored.

[1.3.8] Kerr effect

Recently, the time-resolved optical Kerr effect (TR-OKE) was used to investigate polaron formations in $CH_3NH_3PbBr_3$ and $CsPbBr_3$ perovskites [76]. In a TR-OKE experiment, a laser pulse is sent to the material and the polarization rotation is detected. With laser pulses of energy larger than the energy-gap value, the experiment probes the TR-OKE response upon charge injection. In these lead halide perovskites, the detected signals are compatible with a description of the altered phonon dynamics in terms of the formation of hole and electron, large polarons in the $PbBr_3$ sublattice. This TR-OKE study reported also interesting insights on the polaron-formation dynamics. In fact, the two materials show different rates for the polaron formation. This is attributed to the reorientations of the cations in $CH_3NH_3PbBr_3$, which determine a polaron formation faster than in $CsPbBr_3$.

1.4 Modeling small polarons by first principles

The terms in the Fröhlich and Holstein Hamiltonians (Eqs. 1.1 and 1.5) can be determined for real materials by first-principles density-functional theory (DFT) calculations [35, 91]. Especially, the solution of the Fröhlich model can be fairly straightforward [48]: All one needs to determine is the effective mass, the phonon frequency, and the dielectric constant of the system hosting the large polaron. Nevertheless, the modeling of polarons in real materials by means of the Fröhlich and Holstein Hamiltonians constructed via first principles has hereto hardly been attempted [25]. In many cases, the restriction to a single band and a single phonon mode (see Eqs. 1.1 and 1.5) is a too severe simplification [59].

The situation is even more complicated for small polarons. The Holstein model seems to be a too simplistic approach: For a small polaron, the lattice distortions are usually large around the polaronic site, and it is not obvious how to map the distortions to a single effective mode. However, small polarons often involve fairly large energy scales, around 1 eV [24, 25, 92]. In this case, one might consider the ionic degrees of freedom as classical particles, since the typical vibrational frequencies are relatively small. The second crucial approximation is to treat the electronic degrees of freedom via using a mean field theory, such as DFT. Therefore, one might (and usually does) adopt a full first-principles approach, which seems to be a valid approximation for polarons in transition metal oxides [93], although it gives up on the quantum nature of the ions and restricts the treatment of the electrons to a mean field level. The full first-principles approach consists of few simple steps: One chooses a large unit cell, adds a charge carrier, and investigates the ground state of the system (see the detailed description of the computational methods in Chapter 2). However, polarons pose particular technical challenges in DFT calculations, since they imply localization of the electrons, which many density functionals fail to describe accurately, as discussed in the following.

[1.4.1] DFT

The electronic structure community has been indeed quite active in the study of polarons in real materials, and density functional theory has been largely employed. Simulations can be helpful to understand and interpret the experimental findings, as well as to predict the formation of polaronic states. However, as already mentioned, common schemes used to describe the exchange-correlation functional in DFT simulations, such as the local density and generalized gradient approximations (LDA and GGA, respectively), fail to describe properly the charge localization at atomic sites. By using LDA or GGA, the excess charges are delocalized through the lattice and partial occupations of the electronic levels is favored against integer occupations. Therefore,

the modeling of polarons requires a correction able to overcome the drawback of standard local and semilocal exchange-correlation approximations.

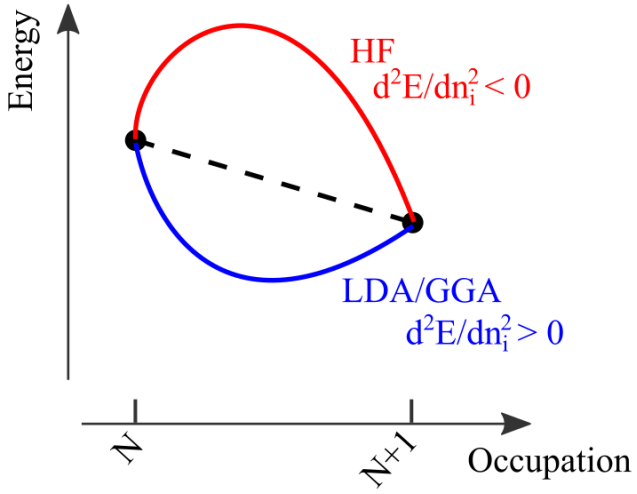

Figure 1.4: Total energy vs. occupation in DFT and HF. Total energy as a function of the electronic occupation in DFT (convex function) and HF schemes (concave function). *Figure adapted from Springer ©2018 Handbook of Materials Modeling* [1].

According to the Janak's theorem [94], variations of the total energy E due to the electronic occupation (n_i) of the state i are given in terms of the DFT Hamiltonian eigenstates ϵ_i as $\mathrm{d}E/\mathrm{d}n_i = \epsilon_i$, independently of the exchange-correlation approximation. The expected behavior of the exact total energy is a piecewise linear function of the electronic occupation, with discontinuities in the first derivative for integer values ($n_i = N$) [95, 96], that is $\mathrm{d}^2E/\mathrm{d}n_i^2 = 0$ except at integer occupancies. Therefore, the energy of the state i remains constant during electron addition or removal.

At variance with the expected behavior, LDA and GGA generally result in a convex function for the total energy, *i.e.*, $\mathrm{d}^2E/\mathrm{d}n_i^2 > 0$. This is schematically shown in Fig. 1.4. The energy change of the state i upon its own occupation reflects a spurious self-interaction effect, introduced by the type of exchange-correlation approximation. As a consequence of the convexity of the calculated energy, partial occupations are preferred over integer occupations. This leads to well known failures of DFT simulations including the underestimation of the energy band gaps, the description of strongly-correlated insulators as metals, and the difficulty to account for charge localization.

[1.4.2] **Hybrid DFT**

The tendency of DFT to delocalize charge can be corrected via modifications of the exchange-correlation approximations [97]. An effective approach is to construct hybrid functionals by mixing LDA or GGA with the Hartree Fock (HF) exchange [98], as in the following formula

$$E_{XC}^{\text{Hybrid}} = \alpha_1 E_X^{\text{HF}} + \alpha_2 E_X^{\text{LDA/GGA}} + \alpha_3 E_C^{\text{LDA/GGA}}. \tag{1.9}$$

The mixing ratios α_i (and, eventually, other parameters not discussed here, such as the screening length) related to the exchange (E_X) and correlations (E_C) terms can be tuned to match physical quantities determined empirically, such as the energy band gap [99]. Alternatively, the hybrid-functional parameters can be determined *ab initio* by requiring the linearity of the total energy [100, 101], or by following a self-consistent procedure [102], or by fitting the parameters to the dielectric function of the material [103, 104].

The piecewise linearity of the total energy can be effectively restored by the hybrid functional approach, since the HF theory predicts an opposite result as compared to DFT: The energy change upon electronic occupation is described by a concave function of the electronic occupation, $\mathrm{d}^2E/\mathrm{d}n_i^2 < 0$, thus, the charge localization is overestimated by HF. This overestimation is due to neglecting screening effects, which are usually not negligible in solids.

[1.4.3] **DFT+U**

As alternative to hybrid functionals, which are usually computationally quite demanding, different corrections can be applied to the standard formulation of the density functional theory in order to restore the expected behavior for the charge localization [105–107]. To this class of methods belongs the DFT+U approach, which includes an additional term to the expression for the total energy. The DFT+U total energy $E_{\text{DFT+U}}$ is given by

$$E_{\text{DFT+U}} = E_{\text{DFT}} + E_{\text{U}}(U, J) \ , \tag{1.10}$$

where E_{DFT} is the energy obtained by standard DFT, while E_{U} is an on-site correction arising from a local Hubbard-like Coulomb repulsion (U) and an Hund's parameter (J), including double-counting corrections. Various expressions for E_{U} have been proposed [108–112], such that the integer occupation of electronic states is energetically favored. Clearly, the results depend on the choice of U and J, which is not trivial. As a matter of fact, these quantities are typically treated as fitting parameters, by adjusting their values such that a specific quantity (*e.g.*, the band gap) is predicted accurately. In order to maintain the *ab initio* character of DFT, various procedures have been defined to calculate the DFT+U parameters from first principles such as the constrained local-density approximation [113, 114], where the interaction parameters are obtained by considering the total-energy variation with respect

to the occupation number of localized orbitals, and the constrained random-phase approximation (cRPA), which allows for an explicit calculation of the matrix element of the screened interactions U and J [115]. Alternatively, in the specific case of excess charge introduced by impurities, the $E_{\mathrm{U}}(U, J)$ term can be substituted by an on site angular dependent potential that does not affect the states of the defect-free system; this potential depends on parameters which are tuned to restore the expected linearity of the total energy [116, 117].

Chapter 2

Methods

The modeling of polarons by first principles techniques requires a careful consideration on the adopted methodologies. In fact, the possibility for small polarons to localize at various lattice sites determines the existence of many local minima on the energy surface. In order to achieve a reliable physical description of the polaronic materials, it is indeed essential to properly take under consideration this aspect.

The methodology adopted within this doctorate project proved to be adapt to achieve an exhaustive characterization of the polaronic properties of TiO_2(110) [3], as well as of the surface stability [4] and reactivity [2] of this material. This chapter describes the adopted computational setup, presenting a more detailed description as compared to the works previously published in scientific journals. The crucial experimental aspects are also briefly reported here.

Contents

2.1 Computational Methods

[2.1.1] DFT+U

The study of polarons on transition-metal oxide surfaces [specifically, small polarons on rutile TiO_2(110)] was conducted in the framework of the density functional theory (DFT), by using the Vienna *ab initio* simulation package (VASP) [118, 119]. The generalized gradient approximation (GGA) within the Perdew, Burke, and Ernzerhof parametrization (PBE) [120] was adopted. As discussed in Sec. 1.4, GGA fails to account for the charge localization at atomic sites, and various solutions have been proposed and commonly used in numerous studies. In this study, the exchange-correlation approximation was corrected in the DFT+U framework, *i.e.*, by introducing an additional term (E_{U}) in the DFT Hamiltonian (see Eq. 1.10). E_{U} takes into account the on-site Coulomb repulsion and the exchange interaction expressed by the Hubbard parameter (U) and the exchange parameter (J), respectively, and contains double-counting corrections. Several expressions for E_{U} have been proposed in literature. In this study, the Dudarev rotationally invariant approach was adopted [111], thus, E_{U} takes the following form:

$$E_{\mathrm{U}} = \frac{U-J}{2} \sum_{\sigma} \left[\left(\sum_{m_1} n^{\sigma}_{m_1,m_1} \right) - \left(\sum_{m_1,m_2} n^{\sigma}_{m_1,m_2} n^{\sigma}_{m_2,m_1} \right) \right] , \tag{2.1}$$

where $n^{\sigma}_{m_1,m_2}$ represents the m_1 and m_2 elements of the on-site occupancy matrix $\hat{n}^{\sigma}$ related to the electronic states m_1 and m_2 with spin σ. This term forces the on-site occupancy matrix in the direction of idempotence [121], *i.e.*, $\hat{n}^{\sigma} = \hat{n}^{\sigma}\hat{n}^{\sigma}$. Therefore, the occupancy matrix is pushed to assume eigenvalues equal to either 1 or 0, which correspond to fully occupied or fully unoccupied states, respectively. In this approach, E_{U} depends only on the difference between the U and J parameters, and can be written in terms of an effective $U' = U - J$.

An effective U' of 3.9 eV was adopted for the Ti-d orbitals in rutile TiO_2. This value was previously determined by constrained random-phase approximation (cRPA) calculations in bulk rutile [48]. It has to be notice that atoms close to the surface could be more reliably described by using a U' different than the value calculated for the bulk. However, typical values of U' for d orbitals in rutile TiO_2 are around 4 eV. The effect of changing the value of U' is reported in the Appendix A.3. Moreover, the DFT+U results were compared to test calculations based on the hybrid-functional approach, for selected representative cases concerning the spatial extension of the electronic charge density of polarons (details in Sec. 2.1.2). As discussed in Sec. 1.4, hybrid-DFT calculations are able to reproduce the charge localization effects, at much higher computational costs than DFT+U.

The DFT+U approach was used to perform $T = 0$ K calculations, including relaxations of the lattice stress (via optimizations of the ionic positions) and, alternatively, calculations at fixed geometries (useful to investigate the polaron energetics, see Sec. 2.1.4). Moreover, first-principles molecular dynamics (FPMD) DFT+U calculations at $T = 700$ K were also performed, in order to investigate the mobile character of polarons (see Sec. 2.1.6).

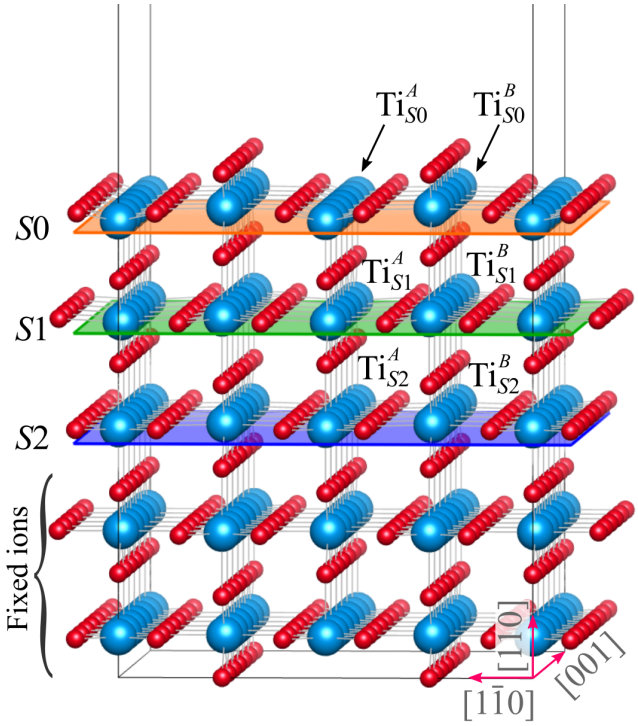

Figure 2.1: The rutile TiO_2(110) slab. The pristine 6×2-large 5-tri-layer-deep slab is shown. The $S0$, $S1$ and $S2$ layers are outlined by solid planes. *[Unpublished Figure]*

[2.1.2] TiO_2 structural models

The structure of the pristine (*i.e.*, stoichiometric, with no lattice defects) rutile TiO_2(110) is shown in Fig. 2.1. In order to address different aspects of the polaron formation and dynamics, the (1×1) phase of the rutile surface was modeled by constructing asymmetric slabs of various sizes, as summarized in Table 2.1. The number of TiO_2 tri-layers varied from 4 to 8, with the bottom two layers kept fixed at bulk positions, whereas all other atomic sites where relaxed. The unit cells including a large number of layers (up to 8) with small lateral dimensions (5×2 and 3×2) were useful to inspect the convergence of the results (see Appendix A.1) and to investigate the polaron formation as a function of the localization depth.

lateral size	tri-layers	system	scope
9×2	5	(1×1)	polaron $T = 0$ K hopping, $T = 700$ K FPMD, polaronic ground-state analysis, surface stability, polaron-polaron interaction, polaron-V_O interaction, CO adsorption
6×2	5	(1×1)	hybrid-DFT tests, polaron $T = 0$ K hopping, polaronic ground state, CO adsorption, interstitial Ti (also by FPMD)
5×2	8	(1×1)	layer resolved analysis polaron $T = 0$ K hopping,
3×2	8	(1×1)	layer resolved analysis polaron $T = 0$ K hopping,
3×2	4 to 8	(1×1)	size tests
9×2	5	(1×2)	$T = 700$ K FPMD, polaronic ground-state, surface stability
3×2	5	(1×2)	hybrid-DFT tests

Table 2.1: Structural models used in the calculations for the rutile TiO_2(110).

Most of the calculations were performed by adopting large 9×2 and 6×2 unit cells, including five TiO_2 tri-layers. The large lateral dimensions reduce the interaction between a localized charge and its periodical image. Therefore, this setup was useful to study the properties of isolated polarons, together with the distance-dependent interaction between two polarons and between a polaron and point defects, *i.e.*, oxygen vacancies (V_O), Ti interstitials (Ti_{int}), and also adsorbates (CO molecules). Moreover, this setup was used to analyze the polaron dynamics via two different approaches, that are the $T = 700$ K FPMD calculations and the $T = 0$ K simulations at fixed geometries simulating the polaron hopping between two lattice sites (details in Sec. 2.1.6). Finally, the analysis of the energy stability of a large number of polaronic configurations allowed to determine the polaronic ground state among the considered configurations.

The properties of the spatial extension of the electronic charge densities of the small polarons where investigated in both the thick (5×2 and 3×2, 8-layer deep) and the large (9×2 and 6×2, 5-layer deep) slabs. Scanning tunneling microscopy (STM) simulations were performed, in order to achieve a description of the polaronic charge above the surface, directly comparable with the experimental images. The STM data obtained by DFT+U were also compared to hybrid-DFT calculations, showing analogous results.

A similar analysis was conducted for the (1×2) reconstructed phase, constructed according to the Onishi Ti_2O_3 model [17, 20, 21] by placing reconstructed asymmetric rows on top of the five tri-layers of the (1×1) phase (as described in detail in Sec. 2.1.9).

[2.1.3] Charge injection

Formation of defects, such as oxygen vacancies, is one of the various approaches able to introduce excess charge eligible to form polarons, as discussed in Chapter 1 [92]. The (1×1) phase of rutile TiO_2(110) is prone to V_O formation at the undercoodinated O_{2c} sites (see Sec. 1.1). Each V_O supplies two excess electrons, eligible to form two small polarons [48]. Therefore, oxygen vacancies were homogeneously included in the slabs by removing the O_{2c} atoms on the surface layer, at different concentrations (c_{V_O}= 5.6%, 8.3%, 11.1%, 16.7%, 22.2%, 33.3%, 38.9%, and 50.0%) [122, 123].

In the (1×2) phase, the reconstructed Ti_2O_3 rows can be considered as Ti_2O_4 units with c_{V_O}= 50.0%. This deviation of 50% from the stoichiometric formula provides the slab with two excess electrons per 1×2 unit cell.

These slabs modeling the (1×1) phase with oxygen vacancies and the reconstructed (1×2) phase are overall neutrally charged. In addition to the charge-neutral slabs, charged systems with an altered number of electrons were considered, in order to disentangle and investigate individually the key quantities driving the polaron formation. The following charged configurations were modeled for the (1×1) phase, eventually including oxygen vacancies:

(*i*) No oxygen vacancies and one excess electron (−1 charged system, obtained by adding one valence electron to the stoichiometric system). This setup is useful to study individual polarons, with no perturbations coming from the V_O.

(*ii*) One oxygen vacancy with one excess electron (+1 charged system, *i.e.*, one of the two excess electrons provided by the V_O is neutralized by the manual removal of one valence electron). The effect of V_O on the polaronic properties is conveniently inspected via this setup.

(*iii*) No oxygen vacancies and two excess electrons (−2 charged system, obtained by adding two valence electrons to the stoichiometric system), to study the polaron-polaron interaction.

(*iv*) One oxygen vacancy and no excess electrons (+2 charged system, obtained by removing the two excess electrons provided by the V_O), to study the intrinsic effects of the V_O in the absence of excess charge.

It has to be noticed that the charged systems are automatically neutralized by a homogeneous background charge, which is essential in order to perform DFT calculations in periodic boundary conditions.

[2.1.4] Polaron formation

In the framework of DFT, regardless of the type of correction to the local/semi-local exchange-correlation approximation (DFT+U or hybrids), the stability of polarons can be analyzed in terms of a set of different energies. The important ingredients to consider in order to characterize a polaron system are:

1. The type of electronic state: excess charge localized in a lattice site (polaron solution), or delocalized throughout the slab (no polaron, fractional electronic occupation on several lattice sites).

2. The type of structural solution: local distortions at the trapping site (polaron-induced distortions) or absence of polaron-induced distortions (uniform lattice except for the deformations induced by the lattice defects, such as V_O). The polaron-induced lattice distortions are obtained fully self-consistently, via the minimization of the forces acting on the ions.

A given material, suitable for the formation of polarons, can be forced to have only delocalized charge carriers (electrons and holes), by performing non spin-polarized calculations. In this delocalized solutions, none of the charge carriers is localized at any atomic site, and no polaronic state exists. By selectively switching on or off the charge localization in combination with the polaronic lattice distortions, it is possible to compute the total energy for a given system in different regimes:

- $E_{\text{dist}}^{\text{loc}}$, *i.e.*, the total energy of the system in the polaronic solution, including localized excess charge and polaron-induced lattice distortions (ionic positions relaxed in the presence of polarons);

- $E_{\text{unif}}^{\text{deloc}}$, *i.e.*, the total energy of the system forced to have only delocalized charge carriers, in the lattice structure without polaron-induced distortion (ionic positions relaxed in the presence of delocalized charge carriers);

- $E_{\text{dist}}^{\text{deloc}}$, *i.e.*, the total energy of the system forced to have only delocalized charge carriers and constrained into the polaron-distorted structure (the structure is obtained by relaxing the ionic positions in the presence of polarons).

In order to compare these energies with each other, many parameters, such as the number of electrons, the unit-cell size and the value of the U' parameter in the DFT+U (or the mixing parameter Hybrid-DFT) approach, are kept constant.

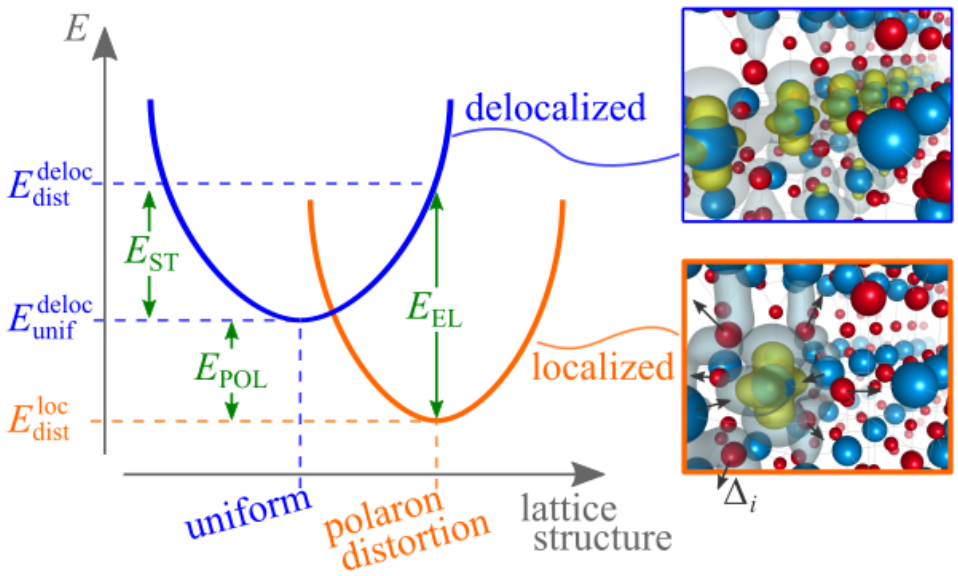

Figure 2.2: Polaron energies. Sketch of the polaron formation energy (E_{POL}), the structural energy cost (E_{ST}) and the electronic energy gain (E_{EL}) obtained as combinations of the calculated total energies in the localized and delocalized solutions ($E^{\mathrm{loc}}_{\mathrm{dist}}$, $E^{\mathrm{deloc}}_{\mathrm{unif}}$ and $E^{\mathrm{deloc}}_{\mathrm{dist}}$). The delocalized and localized electronic charge densities are also shown for rutile TiO_2, together with the polaronic lattice distortions Δ_i. *Figure adapted from Springer ©2018 Handbook of Materials Modeling* [1].

Figure 2.2 sketches the energy diagram for the delocalized and localized solutions, considering an harmonic (parabolic) dispersion as a function of the lattice distortions. Valuable insights on the formation of polarons can be obtained by combinations of the $E^{\mathrm{loc}}_{\mathrm{dist}}$, $E^{\mathrm{deloc}}_{\mathrm{unif}}$ and $E^{\mathrm{deloc}}_{\mathrm{dist}}$ total energies, that lead to a set of polaronic energies. Unfortunately, the definition of polaronic energies is not well standardized, and it varies according to the authors' preferences. The polaron formation energies (E_{POL}), the strain cost (E_{ST}) and the electronic gain (E_{EL}) are often defined as:

$$E_{\mathrm{POL}} = E^{\mathrm{loc}}_{\mathrm{dist}} - E^{\mathrm{deloc}}_{\mathrm{unif}} \ , \tag{2.2}$$

$$E_{\mathrm{ST}} = E^{\mathrm{deloc}}_{\mathrm{dist}} - E^{\mathrm{deloc}}_{\mathrm{unif}} \ , \tag{2.3}$$

$$E_{\mathrm{EL}} = E^{\mathrm{loc}}_{\mathrm{dist}} - E^{\mathrm{deloc}}_{\mathrm{dist}} \ . \tag{2.4}$$

The stability of a polaron solution can be analyzed in terms of the polaron

formation energy. A negative E_{POL} stands for stable polarons, *i.e.*, the polaronic solution is energetically more convenient than a system with delocalized charge carriers. E_{ST} quantifies the structural cost needed to distort the lattice in order to accommodate the excess charge to form a polaron, whereas E_{EL} is the electronic energy gained by localizing the charge in the distorted lattice via the electron-phonon interaction. The values of E_{ST} and E_{EL} depend on the degree of charge localization and the size of the lattice distortion (see the horizontal shift of the parabolas in Fig. 2.2), and on the curvature of the parabola in Fig. 2.2. The three polaronic energies are strongly connected. For instance, E_{POL} can be interpreted as the result of the competition between the structural cost E_{ST} and the electronic energy E_{EL} [48]:

$$E_{\mathrm{POL}} = E_{\mathrm{EL}} + E_{\mathrm{ST}} \ . \tag{2.5}$$

The contribution of the electrostatic potential on the polaron formation was also analyzed, by inspecting the volume-averaged electrostatic potential energy for the electrons (E_{pot}) at each atomic site [124].

The polaronic energies and the electrostatic potential energy were calculated also for the charged-state systems (see items *i*-*iv* in the list in Sec. 2.1.3). Since the polaronic energies are defined as differences (between localized and delocalized solutions at constant number of electrons), adopting charged systems does not substantially alter the results, regardless of the surface extension of the slabs, as tested for the 3×2, 5×2, and 9×2 slabs. Conversely, the electrostatic potential energy strongly depends on the charge state of the system. Adding (and, similarly, removing) electrons to the neutral system alters the value of E_{pot}, obviously because of the presence of the additional charge. The energetics of adsorbates on the surface is also affected by the charge state of the system (see discussion in Sec. 5.3).

In order to measure the degree of local structural distortions, an average bond-length distortion D_{O} for the oxygen atoms O_i coordinated to the polaronic Ti site was calculated:

$$D_{\mathrm{O}} = \frac{1}{N_{\mathrm{O}}} \sum_{i=1,N_{\mathrm{O}}} |\Delta \mathrm{O}_i| \tag{2.6}$$

where N_{O} is the number of O atoms coordinated to the Ti site, and $\Delta \mathrm{O}_i = \delta^{loc}_{\mathrm{O}_i} - \delta^{del}_{\mathrm{O}_i}$ is the distortion of the bond length δ at each atomic site O_i between the localized (polaronic) and delocalized solution.

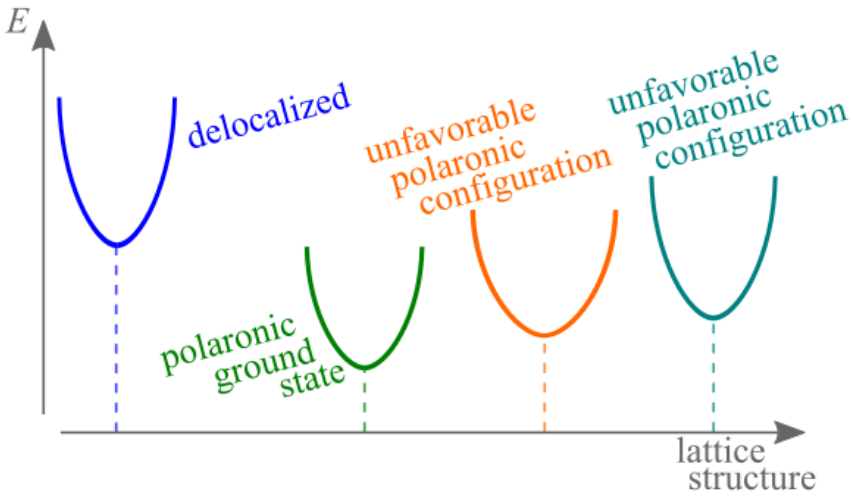

Figure 2.3: Local energy minima in polaronic systems. Sketch of the energy in a polaronic system. Several minima exist: the ground state is given by a specific polaronic configuration, while other minima exist for charge trapping occurring in other spatial configurations or not occurring at all. *[Unpublished Figure]*

[2.1.5] Site-controlled localization

Typically, charge trapping can occur at various sites. Obviously, the distinct polaronic configurations result in different lattice distortions and different energies. As a function of the lattice structure, the energy curve of a single polaronic system shows multiple local minima, corresponding to the various polaronic configurations (see diagram in Fig. 2.3). In general, there is no guarantee that a standard, self-consistent DFT+U (or hybrid-DFT) calculation leads to the global energy minimum of the polaronic system. In fact, the formation of polarons could spontaneously occur at less favorable lattice sites, or not occur at all (*i.e.*, the DFT self-consistent routine, aiming to minimize the system energy, could get stuck in a local energy minimum). Therefore, it is extremely important to inspect the formation of polarons at different sites and to compare the relative formation energies. For this purpose it is essential to establish a protocol capable to selectively control the charge trapping at specific sites.

Since charge localization strongly depends on the initial conditions (input) of the calculation, a selective charge trapping can be achieved by forcing initial perturbations in form of structural distortions or strong on-site Coulomb energy [47, 125, 126]. Starting from a biased setup, it is easier for the system to relax into one desired configuration at the end of the electronic and structural self-consistent calculation (output). Structural perturbations can be introduced manually by distorting the local structure around a given atomic site, resembling the expected polaron-induced lattice distortions. Alternatively, the

initial perturbation can be achieved by chemical substitution, as explained below:

Step 1: Chemical substitution at the selected site where charge trapping should occur with an atom containing one more electron than the original native atom (*e.g.*, Ti → V). Structural relaxation performed at spin-polarized DFT+U level will yield local lattice distortions around the chosen site.

Step 2: The original element is reinserted at its original position (*e.g.*, V → Ti). It is often necessary to use a larger value of U at the selected site, while the other atoms keep the original value of U. The manual initialization of the local magnetic moment has to take into account the presence of the localized electron at the selected site. A new relaxation is performed starting from the optimized structure obtained in Step 1. The self consistent run should be able to maintain the polaron solution obtained in Step 1.

Step 3: A final step is necessary, performed by using the original value U for all atoms. In this case it is recommended to initialize the orbitals with those obtained by Step 2. In fact, by using a random initialization it can happen that the self-consistent loop will end up in a different polaron solution (different polaron site) or in a delocalized solution [45, 127–129].

The effective final localization of the electron at the end of each step can be verified by analyzing the local magnetic moment at the selected site. Step 2 (*i.e.*, using a larger U) usually helps to localize the electron at the selected site. However, it is possible, in simple problems, to skip this step and obtain charge localization at the selected site by simply performing steps 1 and 3. This strategy can be extended to the hybrid-DFT level, by using the orbitals and the optimized structure obtained in step 3 as an input for the hybrid functional calculations. In case more than one electron needs to be localized at selected sites, the steps 1 to 3 can be performed for every selected site separately, one after the other, or, alternatively, at the same time. A systematic use of this strategy allows the identification of the polaronic ground state (global energy minimum) of the system [130].

This strategy was applied to a large number of polaronic configurations, in order to determine the polaronic ground state of the (1×1) phase, at weakly reducing conditions (one to four polarons in the slab). The polaronic configurations differ from each other in terms of the polaron positions (as a function of the depth and with respect to the lattice defects), and in terms of the polaron-polaron distances. Strongly reduced surfaces, including also the (1×2) phase require instead a different approach, since the large number of excess electrons complicates the selective control of the charge trapping. This approach

is based on the polaron distributions obtained by the FPMD calculations, as described in detail in the following section.

[2.1.6] Polaron dynamics

Besides the selectively-controlled-charge-localization strategy, a large variety of polaron configurations was obtained via first-principle molecular dynamics (FPMD) DFT+U calculations [131]. The ion motion was simulated by Nosé dynamics at fixed temperature ($T = 700$ K) [132]. In the FPMD run, the thermal vibrations of the ions perturb the polaron-induced lattice distortions. This perturbation weakens the charge trapping, ultimately undermining the polaron stability. As a result, these vibrations occasionally induce polaron hopping [126]: A polaron is transfered from a lattice site to another one, resulting in a different polaronic configuration. This process takes place several times in long FPMD runs (approximatively 1 hopping event per polaron every 100 fs), providing a large set of different polaronic configurations. The corresponding ionic structures are characterized by thermally-induced lattice distortions, which can be removed by performing $T = 0$ K DFT+U relaxations: The lattice stress is relaxed, and the system shows only polaron-induced lattice distortions. Finally, it is possible to determine the polaronic ground state of the system by comparing the E_{POL} values (obtained by $T = 0$ K DFT+U calculations) for the various configurations explored in the FPMD. This strategy was performed for the rutile TiO_2(110) surface, in the (1×2) and (1×1) phases (with c_{V_O}= 5.6%, 11.1%, 16.7%, 22.2%, 33.3%, 38.9%, and 50.0%, or with Ti_{int} atoms).

A statistical analysis was also performed on the polaron dynamics obtained by the FPMD calculations. The polaron hopping was analyzed as a function of the distance from the surface, by determining the average occurrences of charge trapping on each layer. The polaron-polaron site correlation function $S_{\mathrm{pol-pol}}$ was also calculated, in order to investigate the effects of the polaronic interactions on the polaron dynamics. $S_{\mathrm{pol-pol}}$ is defined as the distribution of the site distance i along [001] between two polarons at a given time-step t, averaged over the complete FPMD interval τ:

$$S_{\mathrm{pol-pol}}(i) = \frac{1}{N}\frac{1}{\tau}\sum_{t}\sum_{j}\rho_j(t)\rho_{j+i}(t) \ , \tag{2.7}$$

where N is the number of Ti sites, and $\rho_j(t)$ indicates the polaronic site density at time t, and it is equal to 1 for the j-th Ti site hosting a polaron, and 0 otherwise. Analogously, the polaron-polaron $R_{\mathrm{pol-pol}}$ and vacancy-polaron $R_{\mathrm{V_O-pol}}$

radial correlation functions were calculated, as a function of the distance r:

$$\begin{aligned} R_{\mathrm{pol-pol}}(r) &= \frac{1}{\tau}\sum_{t}\sum_{(q,p)}\delta(|\mathbf{r}_q-\mathbf{r}_p|,r,t)\ , \\ R_{\mathrm{V_O-pol}}(r) &= \frac{1}{\tau}\sum_{t}\sum_{(V_\mathrm{O},p)}\delta(|\mathbf{r}_{V_\mathrm{O}}-\mathbf{r}_p|,r,t)\ , \end{aligned} \tag{2.8}$$

where the variables $\delta(|\mathbf{r}_{V_\mathrm{O}}-\mathbf{r}_p|,r,t)$ and $\delta(|\mathbf{r}_q-\mathbf{r}_p|,r,t)$ assume the value 1 if, at time t, the polaron p is at distance r from the V_O at position $\mathbf{r}_{V_\mathrm{O}}$ or from the polaron q at position $\mathbf{r}_q$, respectively, and are 0 otherwise.

The polaron dynamics was investigated also by computing the energy barrier for the polaron hopping between two Ti sites, in the $T = 0$ K DFT+U framework [133]. A polaron was localized alternately in one of the two sites (the initial and final Ti sites) by performing the procedure described in Sec. 2.1.5. Clearly, the polaronic distortions depend on the polaron localization site. The corresponding structures (hosting a polaron either in the initial or final Ti site) were used to obtain a set of intermediate lattice structures, by linear interpolation of the ionic positions. The energy barrier for polaron hopping can be estimated by evaluating the energy of every intermediate structure. Therefore, electronic self-consistent calculations at fixed geometry were performed. Two solutions were obtained for every intermediate structure, which exhibit the excess electron localized either on the initial or final Ti site[1]. This set of calculations was performed with large 9×2 and 6×2 slabs, as well as by using thick slabs with 8 tri-layers. The former were useful to describe intra-layer hopping, and also to consider the effects of defects (such as oxygen vacancies) and adsorbates on the surface. The latter were used to analyze the inter-layer hopping. It is important to note that, unfortunately, different functionals can lead to a different description of the polaron transfer process. In fact, DFT+U and hybrid functional approaches lead to qualitative different results [134]. In DFT+U, partial localization is unfavorable, and the excess charge is strongly localized in one site only; therefore, the interaction between the initial and final configurations is weak and the hopping occurs typically diabatically. Conversely, hybrid functionals predict usually an adiabatic hopping, with a gradual transfer of the electronic charge from one trapping site to the other one.

[1] The excess electron localization in the intermediate structures was selectively controlled. The electronic wavefunctions were calculated for a polaron in the initial structure, and, separately, for a polaron in the final structure. The electronic wavefunctions for the intermediate structures were initialized to the two polaronic wavefunctions, alternately.

[2.1.7] Surface stability

The stability of the (1×2) and (1×1) phases was inspected by constructing a surface phase diagram, using standard *ab initio* atomistic thermodynamics [135]. The total energies of the most stable polaronic configurations, at given phase and c_{V_O}, were used. By neglecting configuration entropy and phonon contributions the surface free energy ΔG can be approximated as follows:

$$\Delta G = \frac{1}{A}\left[E^{\text{loc}}_{\text{dist}} - n_{\text{Ti}} E^{\text{bulk}}_{\text{TiO}_2} + \mu_{\text{O}}(2n_{\text{Ti}} - n_{\text{O}})\right] \ , \tag{2.9}$$

where $E^{\text{loc}}_{\text{dist}}$ is the total energy for the surface slab with trapped polarons (as described above), and $E^{\text{bulk}}_{\text{TiO}_2}$ is the energy for the TiO_2 bulk. The adimensional prefactor $1/A$ scales the energy to the (1×1) surface cell. The weighted difference between the number of Ti (n_{Ti}) and O (n_{O}) atoms accounts for the deviation from the stoichiometric formula. The chemical potential μ_{O} of oxygen atoms was considered in terms of its deviation $\Delta\mu_{\text{O}}$ from the total energy E_{O_2} of an isolated oxygen molecule:

$$\mu_{\text{O}} = \left(\frac{1}{2}E_{\text{O}_2} + \Delta\mu_{\text{O}}\right) \ . \tag{2.10}$$

An additional phase diagram describing the stability of TiO_2(110) surfaces forced to have all the electrons delocalized was also constructed, by substituting $E^{\text{deloc}}_{\text{unif}}$ to $E^{\text{loc}}_{\text{dist}}$ in Eq. 2.9.

[2.1.8] Molecular adsorption

The interplay between polarons and adsorbates was investigated by modeling the adsorption of CO molecules on the polaronic TiO_2(110) surface. Several configurations of polarons were considered, in combination with CO molecules adsorbed on various surface sites and at different coverage. Therefore, the adsorption energy per CO molecule (E_{ads}) was computed according to the formula

$$E_{\text{ads}} = E^{P}_{\text{TiO}_2+\text{CO}} - (E^{CGS}_{\text{TiO}_2} + E_{\text{CO}}) \ , \tag{2.11}$$

where $E^{P}_{\text{TiO}_2+\text{CO}}$ is the total energy of the TiO_2(110) surface with adsorbed CO and an arbitrary configuration of polarons (P), $E^{CGS}_{\text{TiO}_2}$ is the total energy of the clean (*i.e.*, without adsorbates) TiO_2(110) with polarons in the clean-surface-ground-state configuration (CGS), and E_{CO} represents the energy of the CO molecule in the gas phase.

In addition to E_{ads}, the adsorption energy of CO molecule was compared also with respect to the clean surface including excess electrons in configurations different than the polaronic CGS ground state. In this case, the adsorption energy E^{*}_{ads} reads

$$E^{*}_{\text{ads}} = E^{P1}_{\text{TiO}_2+\text{CO}} - (E^{P2}_{\text{TiO}_2} + E_{\text{CO}}) \ , \tag{2.12}$$

where the labels $P1$ and $P2$ refer to arbitrary polaronic configurations. By fixing $P1 = P2$, E^*_{ads} evaluates the adsorption energy at a fixed polaronic configuration. Additionally, $P1$ and $P2$ could refer also to systems with delocalized excess electrons (obtained by non spin-polarized calculations).

[2.1.9] Further technical details

The structural models were built by using the low-temperature experimental values for the lattice parameters: $a = b = 4.584$ Å and $c = 2.953$ Å [12]. The effects of the thermal expansion on the polaronic properties were also investigated (see Appendix A.2). Since the periodical boundary conditions used by VASP, a large region of vacuum (about 30 Å long) was included in the surface models, in order to separate the rutile surface from its the periodic repetition. Ionic relaxations were performed by using standard convergence criteria with a plane-wave energy cutoff of 300 eV. The density of states (DOS) and the distribution of the polaronic charge density in real space were obtained by using a large plane-wave energy cutoff (700 eV). The Tersoff-Hamann approach was used to simulate the STM images [136]. The FPMD was conducted using Nosé dynamics [132], with a lower energy cutoff of 250 eV, at a simulation temperature of 700 K, with a timestep of 1 fs, for 10 ps (except 17 ps for the $c_{V_O} = 5.6\%$ slab, and 5 ps for slabs containing $\mathrm{Ti_{int}}$).

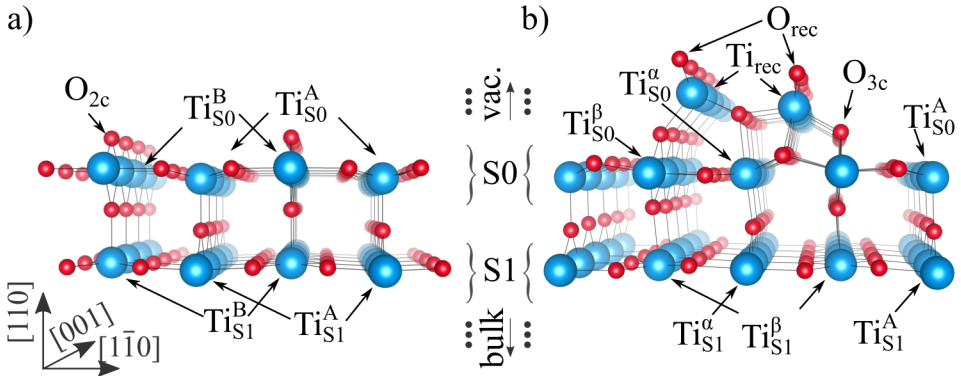

Figure 2.4: The rutile (1×1) and (1×2) surface phases. The stoichiometric (1×1) (a) and the reconstructed (1×2) (b) surfaces are shown, by indicating the nomenclature adopted for the various sites. *Figure adapted from Physical Review X ©2017 American Physical Society* [4].

The study of the molecular adsorption on the rutile TiO_2(110) surface was conducted by using a larger energy cutoff for the ionic relaxation (400 eV) and including van der Waals corrections, adopting the optimized PBE [137] functional as proposed by Dion *et al.* [138] (reliability among various methods is discussed in the Appendix A.4).

The notation adopted for the atomic sites is illustrated in Fig. 2.4. The A sites are the five-fold coordinated Ti atoms ($\mathrm{Ti_{5c}}$) on the top layer $S0$ and

all six-fold (octahedrally) coordinated Ti_{6c} atoms at deeper layers ($S1$, $S2$, etc...) below the Ti^{A}_{S0} row. The B sites are the Ti_{6c} atoms bonded to the two-fold coordinated O_{2c} atoms and/or V_O in the $S0$ layer and all Ti_{6c} atoms at deeper layers below the Ti^{B}_{S0} row. For the (1×2) reconstruction, the Ti sites below the reconstructed rows are named by using Greek symbols, with α and β replacing A and B, respectively. The symmetry of the d orbitals is defined in terms of the x, y and z directions which correspond to [001], [1$\bar{1}$0] and [110], respectively.

2.2 Experiments

The detection of polarons on TiO_2(110) was performed by combining atomic force and scanning tunneling microscopy (AFM and STM, respectively) measurements. These experiments were performed by research partners, and here briefly summarized.

Synthetic single-crystal TiO_2 samples were cleaned in a preparation chamber, by repeated sputtering with 1 keV Ar^+ ions, and annealing to 1000 K. The rutile TiO_2(110) surface was reduced by more than 100 cycles of prior sputtering and annealing.

The combined STM and AFM measurements (in constant-height mode) were performed at low temperature (T = 78 K or lower) in an adjoining ultrahigh vacuum (UHV) chamber with a base pressure below 2×10^9 Pa. Tuning-fork-shaped AFM sensors with a separate wire for the tunneling current were used [139]. Glued to each tuning fork was an electrochemically-etched W tip, which was cleaned in situ by field emission and self-sputtering in 10^{-4} Pa argon [140]. The tips were purposely functionalized by either an O adatom or CO.

Both the O-terminated and CO-terminated tips allow the imaging of the surface oxygen atoms, with excellent lateral resolution. Best images were obtained with O-functionalized tips having negligible attractive force towards the surface O_{2c} atoms.

The AFM imaging has significant advantages compared to more commonly employed empty-states STM imaging, especially for investigating the molecular adsorption. First, imaging at zero bias (without tunneling current) is possible in AFM experiments. This eliminates the possibility of adsorbate hopping induced by the tunneling electrons. Certain adsorption configurations are more affected by the tunneling electrons, therefore the imaging by STM perturbs the system and alters the configuration balance. Second, AFM imaging provides a more reliable picture of the adsorption geometry (electronic effects are eliminated).

The STM measurements are instead essential to investigate the polaron formation. In fact, the in-gap states can be detected by the filled-state STM technique. This technique has been largely employed in this project, has shown in the next chapters.

Chapter 3

Properties of polarons on the rutile TiO_2(110) surface

Polaron formation plays a major role in transition metal oxides, determining the structural, electrical and chemical properties, associated to a significant impact on the functionalities of these materials.

This Chapter reports the systematic analysis of the polaronic properties of rutile TiO_2(110) surface that has been carried on within this doctorate project [3]. This systematic analysis revealed to be fundamental to disclose the crucial mechanisms behind various processes occurring at the surface, such as structural reconstructions [4] and molecular adsorption [2].

Contents

3.1 The excess electrons

A wide range of transition metal oxides, including TiO_2, bears the formation of polaronic in-gap states upon injection of extra charge, as the excess electrons or holes couple with the lattice phonon field (as described in Chapter 1) [22–33]. The formation of polarons alters the properties of the system [59, 82, 141], and it can prevent doping-driven insulator-to-metal transition.

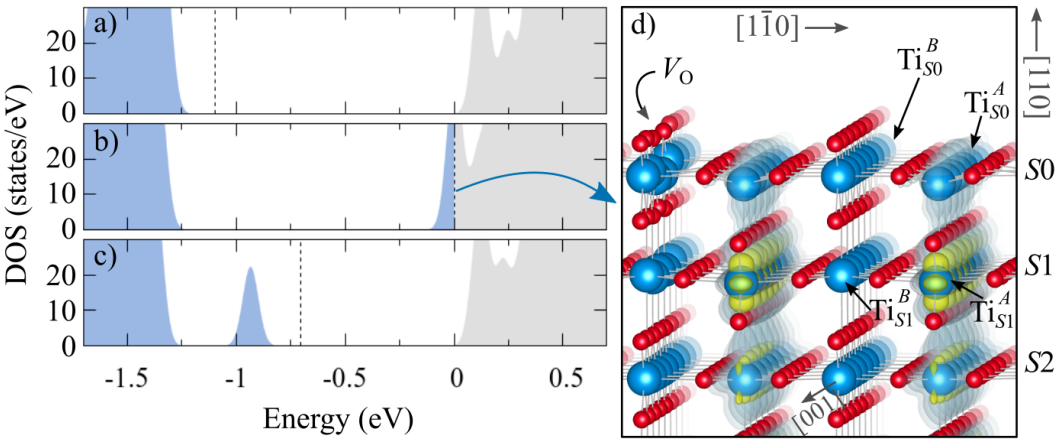

Figure 3.1: Excess electrons on rutile TiO_2(110). The density of the filled (blue) and empty (gray) states around the Fermi energy (dashed lines) are shown for the stoichiometric (a) and V_O-reduced (b,c) slabs. The reduced slab is modeled by using a 6×2-large cell with one surface oxygen vacancy (corresponding to c_{V_O}= 8.3%); the DOS for both the delocalized (b) and polaronic (c) solutions are shown. Panel (d) shows the spatial extension of the delocalized electrons at the bottom of the conduction band of panel (b); high (yellow) and low (gray) isosurface levels of the charge density are shown. *[Unpublished Figure]*

The pristine rutile TiO_2(110) surface is insulating, as shown by the density of states (DOS) in Fig. 3.1(a). However, rutile TiO_2 samples are often characterized by the presence of intrinsic defects, such as oxygen vacancies (V_O) and interstitial titanium atoms (Ti_{int}) [142], which reduce the system. In particular, one V_O and one Ti_{int} introduce two and four excess electrons into the system, respectively. In Fig. 3.1, the DOS of the pristine surface [Fig. 3.1(a)] is compared to the electronic properties of a reduced TiO_2(110) slab, modeled by the inclusion of a surface V_O [Fig. 3.1(b,c,d)]. Analogous results can be obtained by reducing the slab via the inclusion of a Ti_{int} atom or by manually modifying the number of electrons in the system (by adding one or more extra electrons to the stoichiometric slab). By selectively switching on or off the spin polarization (see Chapter 2), it is possible to study via DFT+U calcula-

tions both the localized (polaronic) and delocalized excess electron solutions, respectively. In the delocalized solution, the excess electrons spread throughout the crystal rather than being localized at any specific lattice site. The spatial distribution of the excess charge in the delocalized solution is shown in Fig. 3.1(d). Most of the charge lies on the subsurface Ti^{A}_{S1} sites and on deeper A-type Ti atoms. The Ti^{A}_{S0} sites appear to host a minor amount of excess charge: This is likely due to the presence of a higher electronic density on $S0$ as compared to the density on $S1$ and deeper layers, originating from the broken bonds at the surface, which repels the excess charge.

The density of state obtained in the delocalized solution in Fig. 3.1(b) reveals an insulator-to-metal transition. In fact, the delocalized excess electrons lie at the bottom of the conduction band, driving the system into a metallic state. This result contradicts the experiments: Weakly reduced samples are found to be insulators, and the excess charge forms in-gap states, as clearly evidenced by STM/STS experiments [48]. The agreement with the experimental measurements is restored by performing spin polarized calculations, which enable the formation of polarons. The polaronic solution is energetically more favorable than the delocalized electron solution. By using this setup, the conduction band remains entirely unoccupied, while polaronic states form within the energy band gap [see Fig. 3.1(c)]. Therefore, in the reduced system, the insulating state characteristic of the pristine system is preserved through the formation of polaronic states.

The modeling of the excess electrons is a delicate task, since the energy surface is characterized by numerous local minima, due to the the various sites available for the localization of the excess electrons (see Fig. 2.3) [130]. It is necessary to adopt specific procedures in order to identify the global minimum (as discussed in Sec. 2.1.5 and 2.1.6). In fact, an improper modeling of the polaron formation could lead to an incorrect account of the physical properties of polaronic materials. The fundamental properties of small polarons on TiO_2(110) are described in the following sections.

3.2 Isolated polarons

A systematic characterization of the intrinsic properties of isolated polarons on TiO_2(110) was achieved by controlling the numbers of electrons in the DFT calculations, as described in Sec. 2.1.3. Thick slabs including 8 TiO_2 tri-layers were used. The excess charge was introduced into the system by manually adding one electron to the stoichiometric slab. The site-controlled localization strategy (see Sec. 2.1.5) was used to trap the excess electron in various Ti sites.

Figure 3.2 shows the charge densities for isolated polarons at various Ti

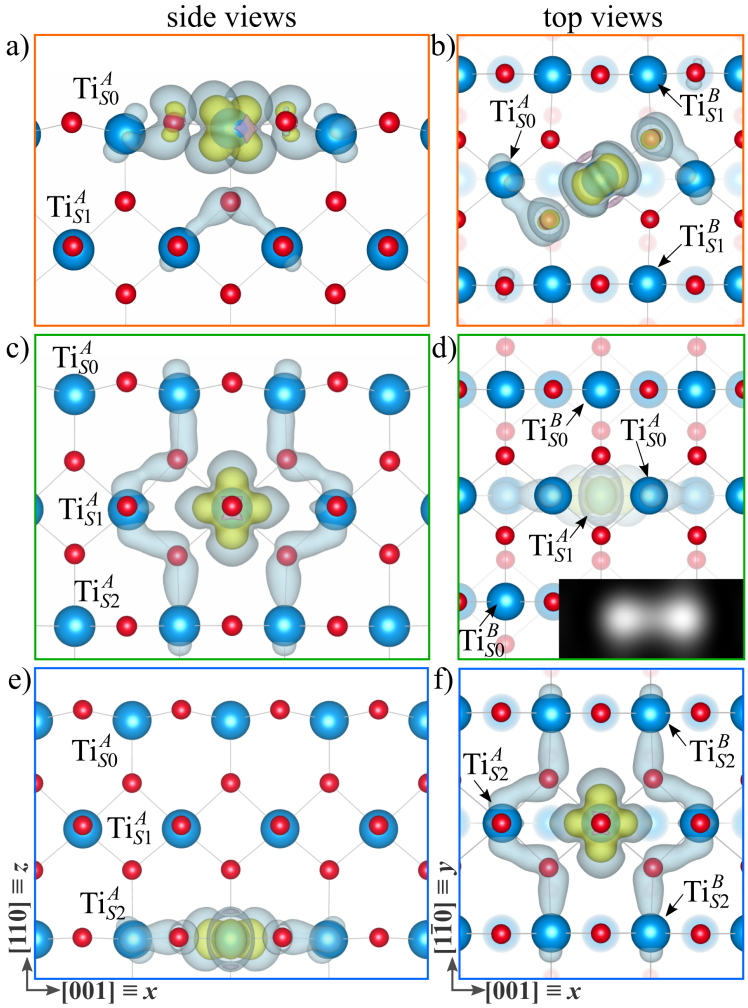

Figure 3.2: Polaron charge density. The side and top views of the Ti^A_{S0} polaron (a,b), Ti^A_{S1} polaron (c,d) and Ti^A_{S2} polaron (e,f) are shown. The inner and outer isosurfaces represent different levels of the charge density of the polaronic states. Faded spheres represent deeper atoms in top-view images [$S0$ and $S1$ atoms not shown in panel (f)]. The inset in panel (d) shows the simulate filled-state STM image of the Ti^A_{S1} polaron. *Figure adapted from Physical Review B ©2018 American Physical Society* [3].

sites (Ti^A_{S0}, Ti^A_{S1} and Ti^A_{S2}), which exhibit distinct orbital topologies, degree of localization and structural distortions. The corresponding orbital-projected analysis is reported in Table 3.1. The symmetry of the d orbitals is defined in terms of the x, y and z directions which correspond to [001], [1$\bar{1}$0] and [110], respectively. A description of the polaronic lattice distortions is reported in Table 3.2.

Polaron	d_{xy}	d_{xz}	d_{yz}	$d_{x^2-y^2}$	d_{z^2}	non local
Ti^A_{S0}	-	22	48	-	-	30
Ti^A_{S1}	-	-	-	14	57	28
Ti^A_{S2}	-	-	-	71	-	29

Table 3.1: **Polaronic orbitals.** The orbital character is reported (in percentage) for the Ti^A polarons in the $S1$, $S2$ and $S3$ layers; the column 'non local' refers to the amount of charge (in percentage) non localized at the Ti site hosting the polaron. Data obtained for independent polarons in the 5×2 large, 8-layer deep, stoichiometric slab.

Polaron	Δz_{Ti}	D_{O}	$\delta_{\mathrm{Ti-Ti}}$
Ti^A_{S0}	0.14	+0.10	+0.02
Ti^A_{S1}	0.03	+0.07	-0.03
Ti^A_{S2}	0.00	+0.07	-0.02

Table 3.2: **Polaronic distortions.** Displacement (Δz_{Ti}) of the Ti site hosting the polaron, with respect to the delocalized solution (in Å); the average bond-length distortion of the surrounding O atoms (see Eq. 2.6) is also indicated (in Å per atom); the bond-length distortion $\delta_{\mathrm{Ti-Ti}}$ indicates (in Å) the variation in the bond-legth between the polaronic Ti site and its nearest neighbor along [001] due to the presence of the polaron. Data obtained for independent polarons in the 5×2 large, 8-layer deep, stoichiometric slab.

[3.2.1] The Ti^A_{S0} polaron

The Ti^A_{S0} polaron is characterized by a predominant d_{yz} orbital character, mixed with a smaller d_{xz} contribution, well recognizable from the polaronic isosurfaces displayed in Fig. 3.2(a,b). Remarkably, only two thirds of the polaronic charge density is localized at the Ti site. The remaining 30% spreads away from the central Ti, and hybridizes asymmetrically with the in-plane oxygen atoms along the xy directions, the two nearest-neighbor Ti atoms along [001], and atoms below the $S0$ layer. Polaron formation on Ti^A_{S0} induces large structural distortions, mostly localized around the polaron site, quantified by an average bond-length distortion D_{O} of 0.10 Å per O atom. The Ti site hosting the polaron relaxes outwards along [110] by 0.14 Å. The in-plane nearest-neighbor Ti-O bond-lengths involving the O atoms hybridized with the polarons increase by 0.05 Å with respect to the positions in the non-polaronic cell, while the remaining two in-plane O are pushed away by 0.11 Å. The distortions involve also the nearest-neighbor Ti atoms on the [001] row, which move away from the polaronic site by approximately 0.02 Å.

[3.2.2] The Ti^A_{S1} polaron

The Ti^A_{S1} polaron is instead characterized by a dominant d_{z^2} symmetry together with a smaller $d_{x^2-y^2}$ contribution [143] [Fig. 3.2(c,d)]. Almost one third of the polaronic charge density spreads away from the hosting Ti atom: The hybridization with two Ti atoms in $S0$ determines the dimer-like signal typically observed by STM simulations and experiments [144] [see the inset in Fig. 3.2(d)]. The hybridization with the two nearest-neighbor Ti atoms along [001] affects the polaron-polaron interaction and stabilizes a 3×1 ordering of polarons at high c_{V_O}, which leads to a surface reconstruction (discussed in Sec. 3.3 and Chapter. 4). The Ti^A_{S1} polaron is coupled with small lattice distortions. The polaronic Ti site is displaced towards the surface by only 0.03 Å; the Ti atoms in the same [001] row move towards the polaronic site by 0.03 Å; the six octahedrally coordinated O atoms move away by about 0.04-0.08Å, resulting in rather different in-plane and out-of-plane Ti-O bond-lengths ($D_O = 0.07$ Å).

[3.2.3] The Ti^A_{S2} polaron

Finally, on the $S2$ layer [Fig. 3.2(e,f)], the Ti^A_{S2} polaron shows a clear $d_{x^2-y^2}$ symmetry. Due to the 90° rotation of the coordination octahedron around the Ti^A_{S2} site with respect to the Ti^A_{S1} site, the polaronic cloud resembles the symmetry of the Ti^A_{S1} but extends on a plane parallel to the (110) surface rather than the $(1\bar{1}0)$ plane. Distortions for the Ti^A_{S1} polaron are small: The polaron site is very close to the original non-polaronic Ti position, the closest Ti sites move towards the polaronic site by 0.01 Å, whereas the Ti-O bond-lengths undergoes changes of about 0.02-0.09 Å ($D_O = 0.07$ Å).

[3.2.4] Ti^B polarons

The formation of polarons on B sites on $S1$ and $S2$ (not shown) was also explored. The corresponding polaronic charge have orbital symmetries very similar to those forming at the A sites: Ti^B_{S1} and Ti^B_{S2} polarons exhibit a $d_{x^2-y^2}$ and d_{z^2}-$d_{x^2-y^2}$ symmetry, respectively, consistently with the orientation of the coordination octahedron of the hosting site. Localization of electrons at Ti^B sites on the surface $S0$ layer is very unstable, and it was not achieved on the stoichiometric slabs.

[3.2.5] The octahedral coordination

It has to be noticed that, in any case, the polaronic orbitals show a t_{2g} character, determined by the octahedral environment around the Ti atom hosting the polaron. In the setup used for the calculations, both the combination of d_{xz}-d_{yz} orbitals of the Ti^A_{S0} polaron, and the combination of d_{z^2}-$d_{x^2-y^2}$ orbitals (such as for the Ti^A_{S1} polaron), and a pure $d_{x^2-y^2}$ orbital (such as for the Ti^A_{S2} polaron), are t_{2g} orbitals. The d orbitals of the six-fold coordinated Ti^{4+} atoms in rutile TiO_2(110) are unoccupied, and split into e_g orbitals, lying along the Ti-O bonds, and t_{2g} orbitals, with lower energies, at the bottom of the conduction band [48]. When an excess electron is introduced into the system, a t_{2g} polaronic state is formed. Interestingly, on $S1$ and deeper layers, the orbital

characters, d_{z^2}-$d_{x^2-y^2}$ or purely $d_{x^2-y^2}$, vary alternately along the [110] and [1$\bar{1}$0] directions, following the orientation of the octahedral orientation around the hosting site.

The inner charge of the $S1$ [Fig. 3.2(c,d)] and $S2$ [Fig. 3.2(e,f)] polarons shows two lobes extending along [001], towards the two nearest-neighbor Ti^{4+} atoms, with a consequent decrease of the Ti-Ti bond-length, by a different extent due to the local lattice stiffness. The characteristics of polarons on the $S0$ layer are substantially different, due to the broken symmetry at the surface. The broken bonds at the surface make the Ti^{A}_{S0} atoms more negatively charged. Excess charge avoids these sites, as observed for the delocalized solution shown in Fig. 3.1. As a result, the inner lobes of $S0$ polarons do not extend along [001], and the two neighbor Ti^{A}_{S0} sites move away from the polaronic Ti site [Fig. 3.2(a,b)], in contrast to the behavior observed for polarons localized at deeper layers. Therefore, the surrounding atoms exert a compressive stress on the Ti^{A}_{S0} polaron: This aspect becomes crucial while considering the molecular adsorption on the surface, as discussed in Chapter 5 and Appendix A.2. Moreover, due to the broken bonds surrounding the polaronic Ti^{A}_{S0} site, the symmetry of the $S0$ polarons can be easily modified: Local distortions of the lattice, such as those produced by a surface oxygen vacancy, are indeed able to move the d_{xz}-d_{yz} orbitals to different characters, accompanied by slight energy variations (see discussion in Sec. 3.4).

[3.2.6] Polaronic energies

The polaron stability strongly depends on the type of polaronic Ti site. This is shown in Fig. 3.3, where the polaron formation (E_{POL}), structural (E_{ST}) and electronic (E_{EL}) energies as well as the electrostatic potential energy E_{pot}, are reported for one excess electron in the 3×2, 8-layer-deep slab with and without V_{O} (qualitatively similar behaviors are obtained at lower polaronic density, *i.e.* one excess electron in a 5×2 cell, not shown). The convergence of the E_{POL} as a function of the number of tri-layers included in the slabs is discussed in Appendix A.1.

The Ti^{A}_{S1} site results to be the most favorable one for charge trapping. In absence of oxygen vacancies, polaron formation at the $S1$ A site is about 300 meV more convenient as compared to the other layers [see E_{POL} curve in Fig. 3.3(a)]. When polarons are trapped in A-type sites on $S0$ or $S2$, the energy of the localized polaronic solution $E^{\mathrm{loc}}_{\mathrm{dist}}$ is almost identical to $E^{\mathrm{deloc}}_{\mathrm{relax}}$ (the energy of the system with the excess electron delocalized in the conduction band), resulting in essentially no energy gain, *i.e.*, $E_{\mathrm{POL}} \approx 0$. Despite the very large energy gain provided by E_{EL}, the formation of a $S0$ polaron is contrasted by a large structural cost E_{ST} [Fig. 3.3(b,c)]. This is due to the large lattice distortions of the undercoordinated atoms around the Ti^{A}_{S0} polaron (see Table 3.1) and to the reduced electron screening at the surface, which leads

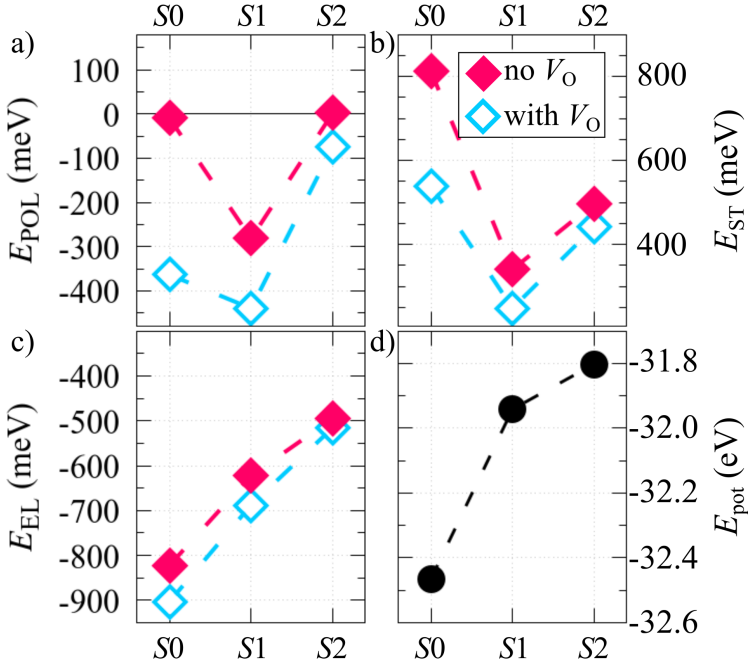

Figure 3.3: Polaronic energies of isolated polarons. Polaron formation energy E_{POL} (a), strain energy E_{ST} (b), and electronic energy E_{EL} (c) of a polaron localized at Ti^A sites at various depths (from $S0$ to $S2$). Results of stand-alone DFT+U calculations on a 8-layer deep, 3×2-large slab with one excess electron considering both the cases of one and no V_{O} in the cell. Ti^A sites closest to the V_{O} at the $S1$ and $S2$ layers were considered, while the next-nearest neighbor to the vacancy at $S0$ is shown. The electrostatic potential energy for the electrons E_{pot} (d) was obtained on a neutral, pristine, 3×2-large, 8-layer deep slab. *Figure adapted from Physical Review B ©2018 American Physical Society* [3].

to an unfavorable $E_{\mathrm{dist}}^{\mathrm{deloc}}$ energy (*i.e.*, an unfavorable energy for the delocalized solution constrained in the distorted structure). On the $S2$ layer (and also in deeper layers, reported in Fig. C.1), the polaron formation is unfavorable due to a reduction of E_{EL} and a still larger structural cost owing to the increased rigidity of the deep layers. Conversely, charge trapping on $S1$ is preferable due to the relatively small structural cost compared to the the electronic energy gain E_{EL}. Remarkably, E_{EL} follows the trend of the electrostatic potential energy E_{pot} [calculated for the neutral slab, see Fig. 3.3(d)], which is very negative on $S0$ sites (*i.e.*, more adapt to attract excess negative charge), and gradually increases at deeper layers (finally saturating at $S2$).

The presence of oxygen vacancies on the surface alters this picture. The polaron formation in $S1$ is further stabilized ($E_{\mathrm{POL}} \approx -450$ meV); moreover, the reduced structural cost to distort the lattice on $S0$ (from 800 meV to

500 meV) results in a rather large E_{POL}, making polaron formation on $S0$ a more favorable process as compared to the vacancy-free situation. This strong reduction of the structural costs does not involve sub-surface layers, where E_{ST} changes only slightly (in the range of 20 meV), which is however sufficient to maintain $S1$ the most favorable site for polaron trapping. The effect of the oxygen vacancies on the polaronic states are discussed in detail in Sec. 3.4.

Therefore, Ti^{A}_{S1} atoms represent the most convenient trapping sites [47]. Conversely, polarons localized at B sites on any layer (including $S1$) are not energetically convenient (discussed in detail in Sec. 3.4). Despite the similarity of the octahedral environments around the Ti^{A}_{S1} and Ti^{B}_{S1} sites, different relaxations of the oxygen octahedra occur due to the surface symmetry breaking, which leads to different charge trapping capabilities. At deeper layers, the energy difference between B and A sites becomes negligible, since these sites become structurally equivalent at large distance from the surface.

The technical setup adopted in the calculations can drastically affect the polaron stability, for instance favoring the formation of Ti^{A}_{S0} polarons rather than Ti^{A}_{S1} polarons. In particular, the stretching of the lattice parameter along [001] and larger (physically unjustified) values for the U parameter make the $S0$ polarons more stable. This effect is discussed in detail in the Appendix A. The choice of the computational setup is indeed crucial in order to describe successfully the physical phenomena occurring in the real polaronic systems.

3.3 Polaron-polaron interaction

This section focuses on the quantitative analysis of the polaron-polaron interaction and its effect on the overall energetics. Figure 3.4 collects the results obtained by using a stoichiometric 9×2, 5-layer-deep slab containing two excess electrons (manually added to the slab). One polaron is kept fixed on a Ti^{A}_{S1} site, while the second one is systematically localized on different Ti^{A} sites in $S1$ and $S0$ (see Fig. C.3 for the Ti^{B} sites). In agreement with the results obtained by using deeper slabs (presented in Sec. 3.2), the energy is lower if polarons reside on $S1$ sites (down-pointing triangles). However, the energy depends strongly on the polaron-polaron distance. The polaron formation becomes progressively more favorable by increasing the polaron-polaron distance. Clearly, two polarons interact via Coulomb repulsion: A polaron affects the electrostatic potential on the surrounding atoms (see Fig. C.2), contrasting the formation of other polarons nearby. The details of the polaron-polaron interactions are described in the following.

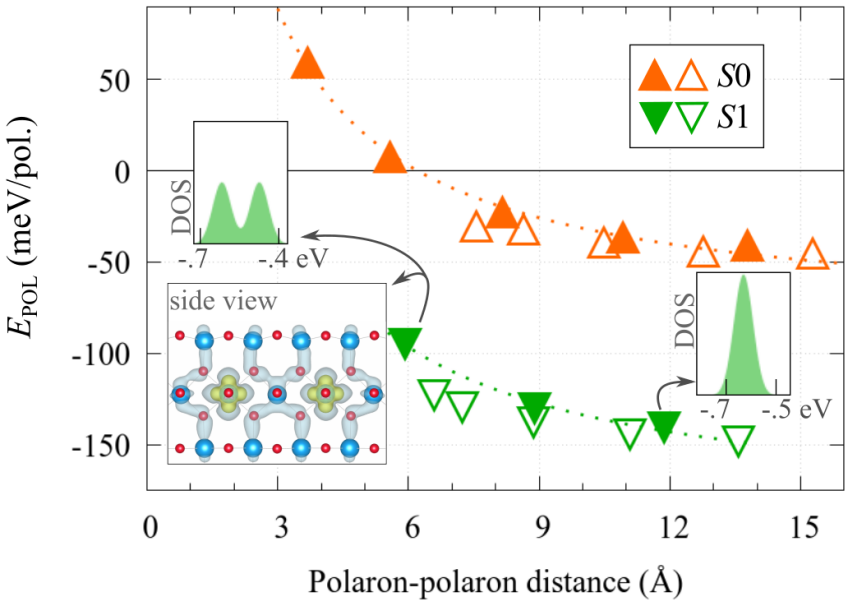

Figure 3.4: Polaron-polaron interaction. E_{POL} (in meV per polaron) as a function of the distance between two polarons in the stoichiometric 9×2 slab (−2 charged slab). One polaron is fixed on a Ti^A_{S1} site; the second polaron explores Ti^A sites on $S0$ (up-pointing triangles) and $S1$ (down-pointing triangles). Filled (empty) symbols are used for polarons lying on sites with the same (different) y coordinate(s). The insets show the in-gap DOS polaronic peaks for two particular configurations (energy values in eV units, with respect to the bottom of the conduction band). The spatial distribution of the polaronic charge is also shown for polarons located on two next-nearest neighbor Ti^A_{S1} sites (two lattice constants apart, approximatively 6Å). *Figure adapted from Physical Review B ©2018 American Physical Society* [3].

[3.3.1] $S1$-$S1$ polaron pair

The most spatially-confined configuration for the polaron pair is given by two polarons localized on adjacent Ti sites along [001] (d_1-Ti^A_{S1}, corresponding to a polaron-polaron distance of $d_1 \simeq 3$ Å). However, it was not possible to obtain this d_1-Ti^A_{S1} configuration in the stoichiometric cell, unless forcing large local lattice distortions by using a larger U' of 5 eV (see the discussion on the effects of the U' values in Appendix A.3). In fact, the configuration with the two polarons separated by two lattice sites (d_2-Ti^A_{S1}), corresponding to a polaron-polaron distance of $d_2 \simeq 5.9$ Å, is the most spatially-confined configuration along [001] obtained by using the standard value of $U' = 3.9$ eV (calculated by cRPA) [48] and a stoichiometric cell.

The energy gained by separating the two polarons from the d_2-Ti^A_{S1} configuration to a distance of four lattice constants (11.87 Å) on the [001] row (filled

$S1$ triangles) is quite large, ΔE_{POL}= 46 meV, clearly indicating that polarons prefer to be spatially separated. Figure C.3 helps to clarify the reason of the E_{POL} trend, by considering the E_{ST} and E_{EL} components. The d_2-Ti^A_{S1} configuration is energetically unfavorable due to the overlap of the electronic charge of the two polarons (shown in the inset in Fig. 3.4). In fact, as described in Sec. 3.2, a considerable part of the Ti^A_{S1}-polaron charge extends on the Ti^A_{S1} atoms aside. Therefore, the charge overlap affects mostly d_1-Ti^A_{S1} and d_2-Ti^A_{S1} polarons, while it vanishes for polarons separated by three or more lattice constants. The charge overlap results in a strong polaron-polaron repulsion, quantified by the weaker E_{EL} energy of the d_2-Ti^A_{S1} configuration as compared to polarons at large separation (see Fig. C.3). On the other hand, the trend of E_{ST} is opposite to E_{EL}: The structural cost to form polarons in the d_2-Ti^A_{S1} configuration is smaller, since the two polarons induce similar lattice distortions on shared atoms (*i.e.*, a smaller degree of distortions can accommodate both the two polarons in the d_2-Ti^A_{S1} configuration). However, the reduction in E_{ST} is smaller than the variation in E_{EL}. Therefore, the E_{POL} is driven essentially by E_{EL} and it is overall less favorable to form d_2-Ti^A_{S1} polarons than polarons at larger separation.

The trend of E_{POL} as a function of the polaron-polaron distance is useful also to determine the minimal setup to adopt in simulations aiming to describe isolated polarons: By using less than three lattice sites along [001], the overlap of the polaronic charge is large, and the spurious interactions between a polaron and its periodical image are not negligible [145]. Conversely, polarons separated by three lattice sites show an E_{EL} energy converged to the large-distance value (see Fig. C.3).

If the two polarons are localized on two different Ti^A_{S1} [001] rows (empty $S1$ triangles in Fig. 3.4), the E_{POL} variations are rather small (25 meV), and mostly attributable to the structural E_{ST} contribution, while E_{EL} varies only slightly, due to the small overlap of the polaron charge densities (see Fig. C.3).

Importantly, the polaronic energy trend reflects the location of the polaronic state in the energy gap region, shown in Fig. 3.5. At large separation, the polarons do not interact strongly and form independent polaron peaks, which are degenerate in energy [see Fig. 3.5(a-e) for polarons on different Ti^A_{S1} rows, and Fig. 3.5(g,h) for polarons on the same row]. Conversely, spatially confined polaronic pairs split this degeneracy and give rise to a double-peak structure due to the enhanced polaron-polaron interaction via the charge overlap [see Fig. 3.5(f)]. As mentioned above, three lattice sites along [001] are enough to separate two polaronic charges and obtain degenerate polaronic states [Fig. 3.5(g)].

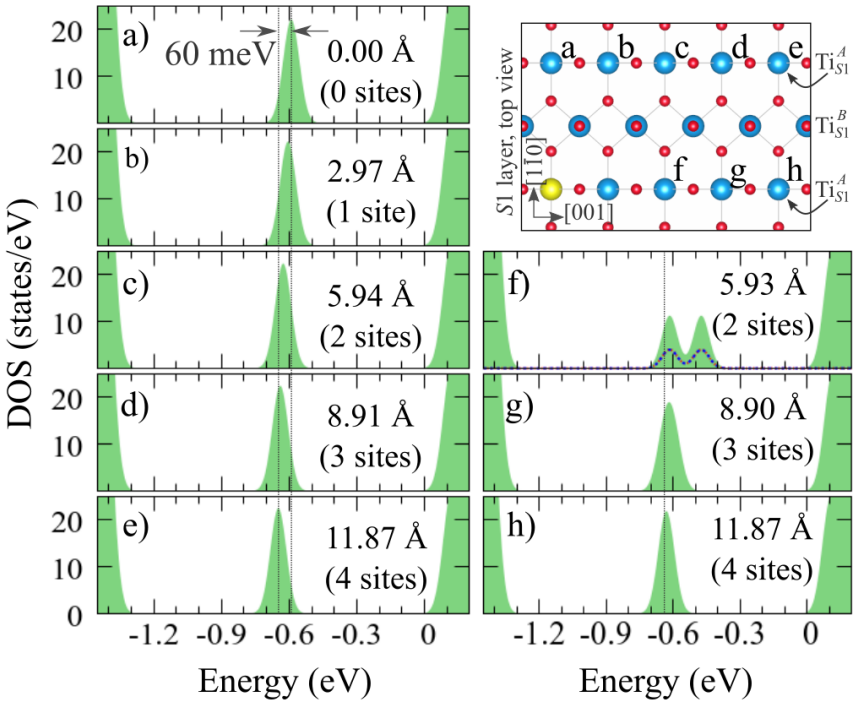

Figure 3.5: The Ti^{A}_{S1} polaron in-gap state. Two polarons are localized on different (a-e) Ti^{A}_{S1} [001] rows, or on the same (f-h) row, as sketched in the inset (the yellow sphere represents the position of one polaron, while the position of the second polaron is indicated by the a-h labels). The [001] component of the polaron-polaron distance is reported in each panel (in both Å and lattice site units). These results were obtained by using a $-2e$-charged, 9×2-large, stoichiometric slab. *[Unpublished Figure]*

[3.3.2] $S1$-$S0$ polaron pair

An analogous trend is observed when the two polarons are localized on different layers, on Ti^{A}_{S1} and Ti^{A}_{S0} sites (up-pointing triangles in Fig. 3.4). In this case, it is possible to form a polaron-polaron pair confined within a distance of less than 4 Å (one polaron above the other). Nevertheless, the resulting E_{POL} is positive (in the computational setup used here)[1], indicating an intrinsic instability of this solution. This is due to the repulsive interaction between the $S0$ polaron with the electronic charge of the $S1$ polaron, which spreads towards the surface Ti^{A}_{S0} sites right above. The electronic energy gain

[1]The polaron formation energy depends strongly on the computational setup (*e.g.*, the E_{POL} convergence requires an high number of TiO_2 layers, as reported in Appendix A.1). However, energy variations between different polaronic configurations are satisfyingly converged in the computational setup used here. Therefore, only the energy trends can be safely addressed and analyzed, while the analysis of the absolute values would require a more refined computational setup, hardly possible for such large slabs.

E_{EL} is largely affected by this overlap, and it is not compensated by a the smaller reduction of the structural energy (see Fig. C.3), even though smaller lattice distortions are required to accommodate spatially confined polaron-pairs.

By separating the two polarons along [001] (filled $S0$ triangles in Fig. 3.4), the polaron formation becomes progressively more convenient: the energy gain is 100 meV at the maximum distance considered (15 Å). Similarly to the $S1$-$S1$ case, the variation of E_{POL} is small (15 meV) if the two polarons are located on different [001] rows (empty $S0$ triangles).

3.4 Polaron-V_O interaction

The removal of an O_{2c} atom from the surface creates a positively charged vacancy [146], which is expected to behave as an attractive center for the negatively charged polarons. Figure 3.6 reports the most interesting effects of V_O on the polaron formation (the complete data set is shown in Fig. C.4). A 9×2, 5-layer-deep slab, containing one single V_O was used in the calculation; one of the two excess electrons provided by the V_O was removed manually, in order to investigate the formation of one polaron only. These data confirm that polaron formation is energetically favored in proximity of the vacancy [Fig. 3.6(a)] [147, 148]. Forming a polaron at the Ti^A_{S1} site closest to the V_O is 95 meV more favorable than for large (14.54 Å) polaron-V_O distances.

[3.4.1] The Ti^B_{S1} polaron

The polaron-V_O attractive interaction influences particularly the propensity of Ti^B_{S1} sites to host polarons. As already mentioned in Sec. 3.2, in the stoichiometric cell the formation of polarons in B sites is unstable ($E_{POL} > 0$ in the adopted computational setup)[2]. The presence of a surface vacancy reduces the strain cost and increases the electronic gain [shown in Fig. C.4(b,c)] associated with the Ti^B_{S1} polarons, making polaron formation at B sites possible (negative E_{POL}) for polaron-V_O distances smaller than approximatively 8 Å.

The trend of E_{POL} correlates well with the electrostatic potential. This is shown in Fig. 3.6(b) by comparing the electrostatic potential energy E_{pot} for Ti A and B sites in S1. At long distance from the V_O, E_{pot} is largely more negative at Ti^A_{S1} sites (more suitable for polaron formation) as compared to Ti^B_{S1} sites, due to a different degree of local-structure distortions induced by the broken symmetry at the surface. By decreasing the distance from the V_O, E_{pot} decreases quickly at Ti^B_{S1} sites, and stabilizes the polaron formation (negative

[2] As already mentioned in Footnote 1, the polaron formation energy depends strongly on the computational setup, and well converged E_{POL} values would require an higher number of TiO_2 layers

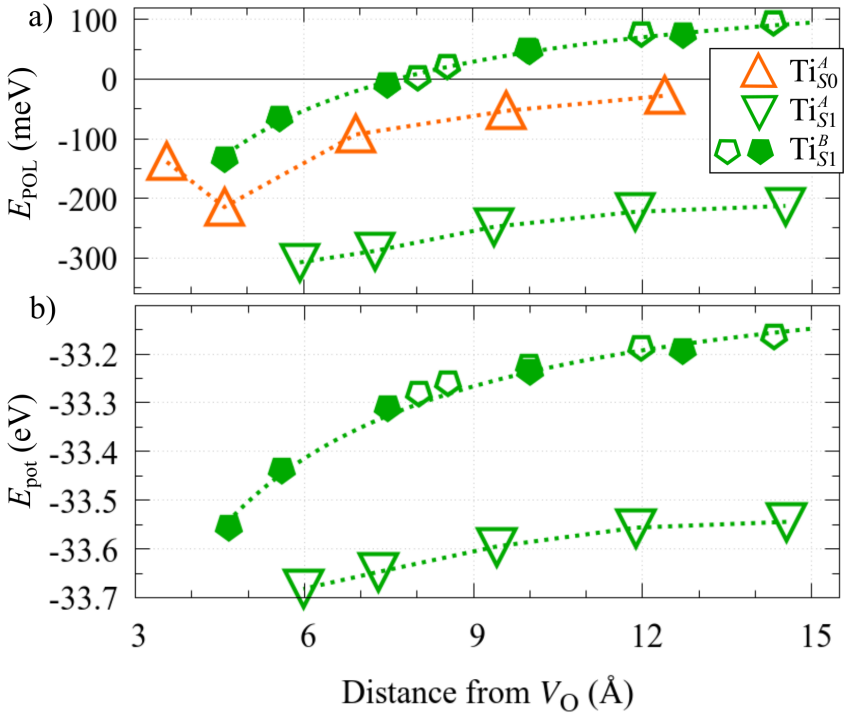

Figure 3.6: Polaron-vacancy interaction. Panel (a): E_{POL} as a function of the distance between the oxygen vacancy and the polaron, included in the 9×2 slab (*i.e.* $c_{V_O} = 5.6\%$, +1 charged system). The polaron explores the Ti^A_{S0}, Ti^A_{S1} and Ti^B_{S1} sites. Defect states at Ti^B_{S0} sites adjacent to the V_O (not reported) show a large positive E_{POL} ($\simeq$ 300 meV). Panel (b): E_{pot} on Ti^A_{S1} and Ti^B_{S1} sites as a function of a distance from the oxygen vacancy, in the +2 charged slab (one V_O and no excess electrons). In both panels, filled and empty symbols represent polaron positions with the same or different $[1\bar{1}0]$ coordinate with respect to V_O, respectively. *Figure adapted from Physical Review B ©2018 American Physical Society* [3].

E_{POL}). The trend of E_{pot} determines the E_{EL} energy gain [Fig. C.4(c)], and, finally, affects the E_{POL}. Therefore, despite being similar in terms of the local structural coordination and possibly geared to host polarons with similar orbital symmetry (d_{z^2}-$d_{x^2-y^2}$ and $d_{x^2-y^2}$, respectively), Ti^A_{S1} and Ti^B_{S1} sites do show different E_{POL} values as a consequence of the different electrostatic potential [Fig. 3.6(b) and Fig. C.4(c)] and structural flexibility [Fig. C.4(b)].

[3.4.2] V_O effects on $S0$ polarons

The E_{POL} calculated for $S0$ polarons follows a similar trend, with the polaron formation favored on sites closer to V_O. This trend can be understood in terms of the E_{ST} and E_{EL} contributions [Fig. C.4(b,c)], as discussed above for the $S1$ polarons.

However, besides the general trend of E_{POL}, the Ti^A_{S0} site nearest neighbor to V_O (NN-Ti^A_{S0}) is energetically less favorable than the next nearest neighbor one (NNN-Ti^A_{S0}) [47], as evidenced by the kink at about 4.5 Å. Therefore, the overall attractive trend is perturbed at the NN-Ti^A_{S0} site. The deviation from the overall trend of the energy is accompanied by a change of the orbital symmetry, due to local lattice distortions induced by the oxygen vacancy (shown in Fig. C.5). In fact, the V_O moves the nearest Ti^B_{S0} atoms downwards, which become aligned with the Ti^A_{S0} atoms along the [001] direction. This alignment facilitates the formation of polarons with a dominant $d_{x^2-y^2}$ orbital character (52%) on NN-Ti^A_{S0} sites, at variance with all other Ti^A_{S0} polarons, which show a d_{xz}-d_{yz} symmetry [Fig. 3.2(a,b)]. Therefore, the NN-Ti^A_{S0} polaron shows an orbital character similar to polarons on deeper layers (*e.g.*, Ti^B_{S1} and Ti^A_{S1} sites), due to the alignment with the surrounding atoms.

Flavor	E_{POL}	d_{xy}	d_{xz}	d_{yz}	$d_{x^2-y^2}$	d_{z^2}	nonlocal
d_{xz}-d_{yz}	−359	0	**24**	**41**	0	0	36
$d_{x^2-y^2}$	−337	0	10	1	**50**	3	36
d_{yz}	−322	0	6	**58**	0	0	36

Table 3.3: **Flavors of the NNN-Ti^A_{S0} polaron.** The polaron formation energy (in meV) and the orbital character (in percentage) are reported here for three different variations of the $S0$ polarons localized on the NNN-Ti^A_{S0} site, with different dominant characters (d_{xz}-d_{yz}, d_{yz} and $d_{x^2-y^2}$); the column 'non local' refers to the amount of charge (in percentage) non localized on the Ti site hosting the polaron. Data obtained by using the 6×2 large, 5-layer deep slab, with two oxygen vacancies (c_{V_O}= 16.7%), one $S0$ polaron on the NNN-Ti^A_{S0} site, and three $S1$ polarons in a fixed configuration.

As already mentioned, at variance with the NN-Ti^A_{S0} polaron, the NNN-Ti^A_{S0} polaron retains the d_{xz}-d_{yz} symmetry typical of the isolated $S0$ polarons. However, it is possible to obtain solutions with different orbital characters, which show slightly less favorable energies. This can be achieved by initializing different structural distortions during the polaron localization process (see Sec. 2.1), which drive the electronic and ionic relaxations towards different energy minima. The characteristics of the various flavors obtained for the NNN-Ti^A_{S0} polaron are summarized in Table 3.3 (see also Fig. C.6). In analogy with the NN-Ti^A_{S0} case, the $d_{x^2-y^2}$ flavor for the NNN-Ti^A_{S0} polaron is stabilized by the hybridization with the Ti^B_{S0} atoms, pushed downwards by the V_O. A

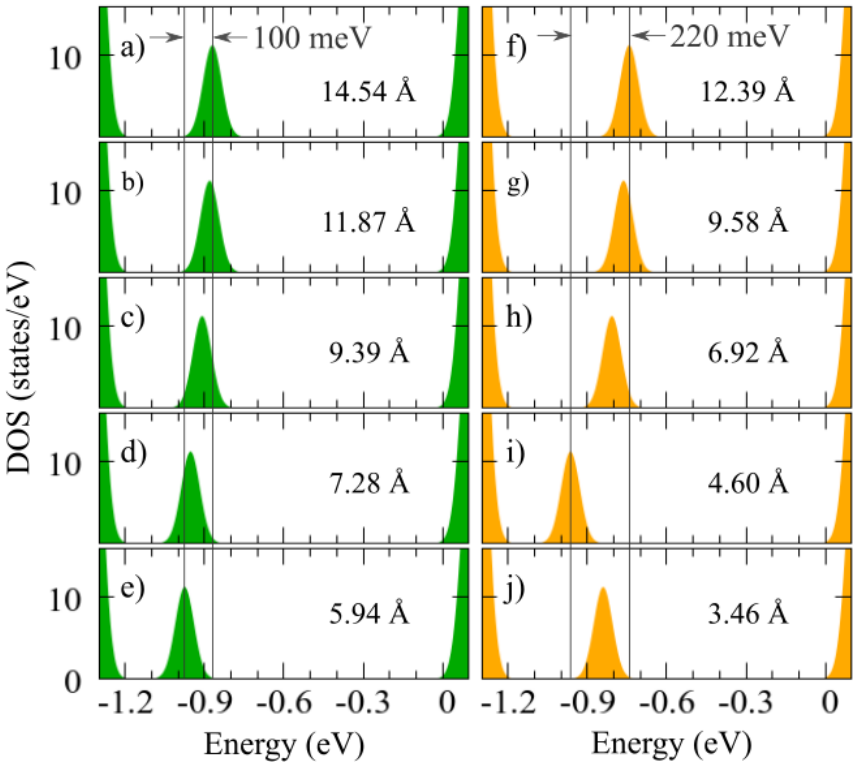

Figure 3.7: The polaronic in-gap state versus the V_O-polaron distance. DOS calculated for a polaron on Ti^A_{S1} (a-e) and Ti^A_{S0} (f-j) sites, in the 9×2-large slab with one oxygen vacancy (c_{V_O}= 5.6%). The V_O-polaron distance is shown in each panel. *[Unpublished Figure]*

third flavor is found, which owns a large d_{yz} (58%) orbital character, and it tends to extend along [1$\bar{1}$0]. These two additional flavors are less convenient in energy by about 20 meV and 40 meV, respectively.

Therefore, it is important to keep the orbital character of polarons under control while evaluating the energy of the system (since simulations could eventually lead to the less stable NNN-Ti^A_{S0} polaron flavors). Moreover, the orbital symmetry plays an important role in molecular adsorption calculations. In fact, simulations are able to reproduce the filled-state STM measurements only if the most favorable orbital character for $S0$ polarons is considered in the calculations (details in Chapter 5).

[3.4.3] DOS

The $S0$ polaron states lie at different energies in the gap region, as shown in Fig. 3.7, following the trend of E_{POL}. In fact, the polaronic state depends on the type of the hosting site and on the mutual interaction among polarons as well as on the interaction between polarons and V_O, which strongly depend on the relative positions [149]. Therefore, modifications on the energy of

the polaronic in-gap state, observed in experiments for Ti^{A}_{S1} polarons, should be interpreted as a result of the interaction with other polarons and oxygen vacancies, rather than an intrinsic property of the isolated polaron [36].

3.5 Combined V_O-polaron and polaron-polaron effects

This section focuses on the combined polaron-polaron-vacancy effects in the charge-neutral system, containing one V_O and two Ti^{A}_{S1} polarons, modeled by a 9×2, 5-layer-deep slab.

Besides facilitating individual charge trapping at the surface and subsurface sites, as reported in Sec. 3.4, the presence of an oxygen vacancy weakens the strong repulsion between polaron pairs localized at adjacent Ti^{A}_{S1} sites along [001] (d_1-Ti^{A}_{S1}, with $d_1 \simeq 3$ Å). This allows the study of the evolution of the polaronic properties as a function of the polaron-polaron distance from very short to large separation. The results are collected in Figure 3.8.

[3.5.1] d_1-Ti^{A}_{S1} polarons

The formation of d_1-Ti^{A}_{S1} polarons is clearly not a favorable configuration [see Fig. 3.8(a,b)]. The E_{POL} value is influenced by the alignment of the polaronic spin [47, 149–151]. In fact, when the distance between polarons is small, it is important to take into account the magnetic ordering of the polaron complexes. Two different spin configurations, parallel and antiparallel, were tested, and are reported here. As expected, when the spins are separated by only one lattice constant, the antiferromagnetic state (resulting in a zero total magnetization) is the energetically most favorable solution. Two polaronic peaks appear at the same energy, approximatively 0.65 eV below the bottom of the conduction band [two-spin channel DOS in Fig. 3.8(a)]. In contrast, the parallel alignment induces a large splitting between the two polaronic peaks of about 0.6 eV [Fig. 3.8(b)]. The two distinct spin-polarized solutions exhibit different orbital symmetries, as graphically visualized in the spin-dependent isosurfaces shown in Fig. 3.8(f-i). In the anti-parallel spin case, the orbital occupation of one polaron is not drastically altered by the overlap with the electronic cloud of the other polaron in the neighboring site, which belongs to a different spin channel. Therefore, the two polarons individually retain the d_{z^2}-$d_{x^2-y^2}$ orbital character, typical of isolated Ti^{A}_{S1} polarons [Fig. 3.8(f,g)]. Conversely, within the parallel-spin configuration, a hybridization of the polaronic state occurs, which causes a spread of the polaron charge across both adjacent sites: The polarons are no longer fully localized in one specific Ti site, rather, the polaronic charge is shared between the two adjacent sites in a sort of bonding/anti-bonding configuration [see partial DOS in Fig. 3.8(b) and

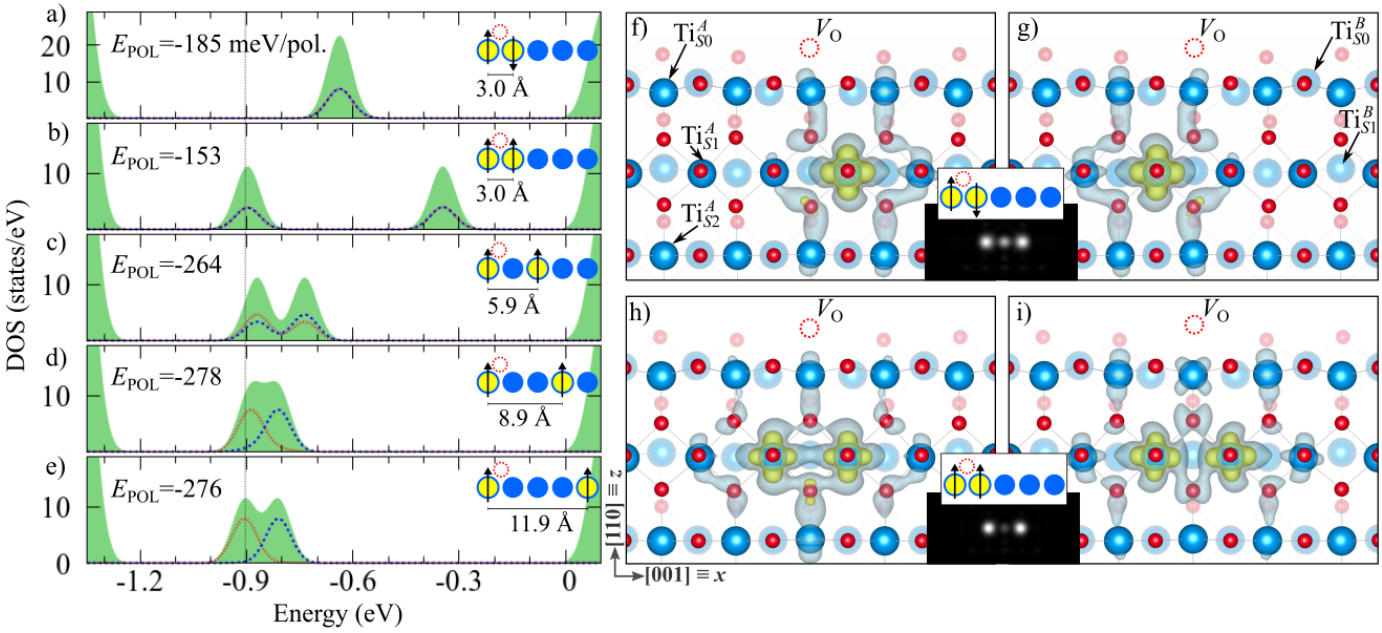

Figure 3.8: V_O-polaron and polaron-polaron combined effects (Ti^A_{S1} sites). Panels (a-e): DOS calculated for two polarons at various distances with opposite (a) and parallel (b-e) spins. The total DOS and the projection on the two polaronic sites are shown with filled and dotted curves, respectively. One polaron is fixed at the Ti^A_{S1} closest to V_O while the other one is localized at various sites of the same [001] Ti row. The respective E_{POL} is indicated on each panel (in meV per polaron). Panels (f-i): spatial charge density of the polaronic states for two adjacent polarons with opposite (f,g) and parallel (h,i) spins. Each state is shown separately: Spin up (f) and spin down (g) charge densities for the antiferromagnetic configuration, and the charge densities of the −0.90 eV (h) and −0.35 eV (i) energy states for the parallel-spin configuration. The insets show the simulated STM resulting from the in-gap states. *Figure adapted from Physical Review B ©2018 American Physical Society* [3].

isosurfaces in Fig. 3.8(h,i)]. The spin-integrated STM signals of the adjacent polaron-pairs are qualitatively similar for the two spin alignments [insets in Fig. 3.8(f,g) and Fig. 3.8(h,i)], both very different from a superposition of two double-lobed shape typical of individual polarons [compare with the inset in Fig. 3.2(d)]. They are characterized by a weak spot in the middle between two bright ones, separated by two lattice constants. Only spin-dependent STM measurements would be able to experimentally detect the difference between the parallel and antiparallel orderings. In fact, the two brightest spots in the antiparallel case come from one specific spin channel [compare the polaron isosurfaces in the top layer in Fig. 3.8(f,g)]. However, as already highlighted,

this is not a likely polaronic configuration in TiO_2(110), while it was experimentally observed in materials with a high density of polarons and a similar lattice structure. [152]

[3.5.2] d_2-Ti^A_{S1} polarons

The spin-dependent splitting of the polaronic state vanishes very rapidly with the distance, due to the reduction of the overlap of the polaronic clouds. For next-nearest-neighbor d_2-Ti^A_{S1} polarons (*i.e.*, two Ti^A_{S1} atoms 5.9 Å apart) the energy difference between parallel and antiparallel spin orderings reduces to less than 1 meV. Therefore, only the parallel spin solution is discussed in the following.

By separating the polarons from d_1-Ti^A_{S1} configuration to d_2-Ti^A_{S1}, the energy splitting reduces to 0.1 eV and the spin-dependent polaron charge is almost equally distributed between the two Ti sites [see Fig. 3.8(c) and the charge density in Fig. C.7]. As compared to the analogous configuration of two polarons located 5.9 Å apart without oxygen vacancy (inset in Fig.3.4), the energy separation between the two polaron peaks is not largely affected by the introduction of the V_O, confirming that the nature of the splitting should be attributed to the polaron-polaron hybridization. However, in the presence of a V_O, both states are shifted towards deeper energy by 0.3 eV, leading to an enhanced E_{POL} (-264 meV rather than -94 meV observed in the slab without V_O, see Fig. 3.4), with a major contribution arising from the electrostatic potential, and only a slight reduction of the structural cost.

[3.5.3] Large distance

By further increasing the distance along [001], the two polarons can be effectively considered as independent from each other. In fact, the charge overlap is negligible for inter-polaron distances of at least three Ti^A_{S1} sites, with a consequent reduced repulsion between the polarons. The splitting is strongly reduced, and each polaron is localized around its Ti^A_{S1} trapping center [Fig. 3.8(d,e)]. It is important to note that the residual splitting between the two peaks for a distance of 8.9 Å and 11.9 Å does not originate from hybridization effects, but from electrostatic effects due to the fact that polarons are trapped in inequivalent positions with respect to the V_O (as discussed in Fig. 3.7). E_{POL} saturates to a value of about -280 meV, since both attractive (V_O-polaron) and repulsive (polaron-polaron) interaction decay rapidly with increasing separations. Consistently, the deepest polaronic peak remains located at about -0.9 eV, the typical energy level associated to individual polaronic states in proximity to a V_O. As mentioned before, the polaron is less stable in defect-free samples, and the characteristic polaronic peak is instead typically located approximatively 0.6 eV below the bottom of the conduction band.

3.6 Polaron dynamics

[3.6.1] Hopping energy barrier

When thermally activated, small polarons are able to hop to surrounding Ti^{4+} sites [46, 126, 153, 154]. The energy barrier for the polaron hopping can be calculated in the framework of DFT, by interpolation of ionic positions between the initial and final polaronic configurations (see Chapter 2). However, the commonly employed correlation-exchange functionals drastically influence the physical description of this process [134]. In fact, hybrid functionals favor an adiabatic process, and the polaron migrate gradually from the initial site to the final one. Conversely, the DFT+U approach leads to a diabaticlike hopping, where the polarons is strongly localized in whether one site or the other. In the latter case, the hopping barrier value is determined by the intersection of two energy curves, which describe the variations of the total energy as a function of the structural distortions. The results for the energy barrier in the DFT+U approach are described in the following. Due to the conceptual and technical limitations, the conclusions have qualitative validity only.

The energy barrier for polaron hopping along the Ti^A_{S1} row (that includes the most favorable sites for charge trapping, as discussed in Sec. 3.2), was investigated by using a 9×2, 5-layer-deep slab, including one excess electron and one oxygen vacancy (+1 charged slab). As shown in Fig. 3.9(a-d), polarons hop easily between adjacent sites along the Ti^A_{S1} row [155], with an energy barrier lower than 200 meV. The energy barrier is not strongly dependent on the position of the initial and final Ti sites with respect to the position of the oxygen vacancy. The same setup was adopted also to analyze the $S1$-to-$S0$ polaron hopping. In this case, the calculations yield an energy barrier of approximately 350 meV for a polaron hopping from a Ti^A_{S1} to a NNN-Ti^A_{S0} site (not shown).

The inter-layer hopping was investigated also by using thicker slabs (3×2 slabs with 8 tri-layers). The results are shown in Fig. 3.9(e-h). The $S1$-to-$S0$ barrier obtained in this setup, 327 meV, is consistent with the result of the thinner slab [Fig. 3.9(e)]. Hopping towards deeper layers is more difficult, as the energy barrier for the $S1$-to-$S2$ polaron hopping is 479 meV [Fig. 3.9(g)]. The different lattice distortions induced by the $S1$ and the $S2$ polarons contribute to disfavor $S1$-to-$S2$ hopping. In fact, the total amount of ionic displacements (*i.e.*, the variation of the ionic positions between the structure with a Ti^A_{S2} polaron and the structure with a Ti^A_{S1} polaron) is about 3.2 Å, much larger than for the $S1$-to-$S0$ hopping (2.7 Å).

The inter-layer polaron hopping is influenced strongly by the oxygen vacancy, playing the role of an attracting center for polarons. In fact, in case of a defect free surface with one excess electron (a −1 charged slab, with 8

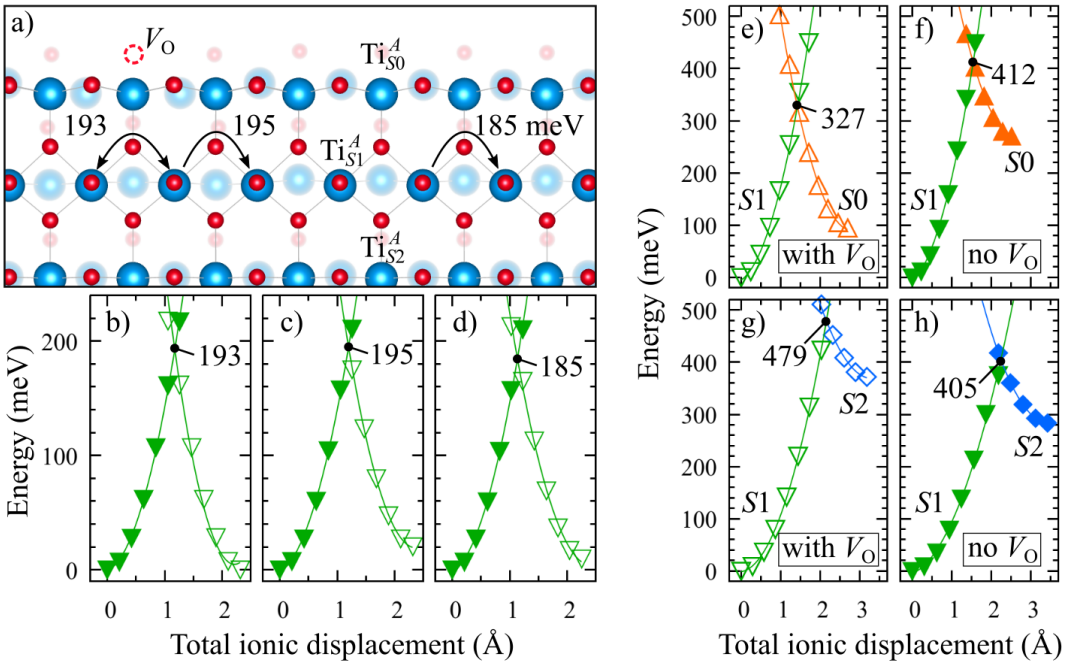

Figure 3.9: Energy barrier for the polaron hopping. Panel (a): polaron hopping among various Ti^A_{S1} sites, with values of the energy barriers reported for each case (in meV). Panels (b-d): detail of the polaron hopping energies for the cases sketched in panel a, as obtained by DFT+U calculations on 9×2 slabs with 5 tri-layers, one vacancy and one excess electron (+1 charge state system). Filled and empty triangles refer to the two different hosting sites. Panels (e-f): inter-layer polaron hopping, obtained by using 3×2 slabs with 8 tri-layers and one excess electron, with and without oxygen vacancies. The values of the energy barriers is indicated in meV. In panels (b-f), the ionic total displacement refer to the sum of the distortions of each ion with respect to the position in the starting configuration. *[Unpublished Figure]*

tri-layers), the energy barrier for the $S1$-to-$S0$ hopping is definitively higher [412 meV, compare Figs. 3.9(e,f)]. Moreover, the absence of oxygen vacancies lowers the $S1$-to-$S2$ barrier by approximatively 70 meV [compare Fig. 3.9(g,h)].

[3.6.2] FPMD on the (1×1) phase

The polaron dynamics was investigated also by performing FPMD calculations [126, 131, 132, 156] on 9×2, 5-layer-deep slabs. Both the (1×2) and (1×1) phases of rutile TiO_2(110) surface, at various oxygen-vacancy concentration levels (c_{V_O}= 5.6%, 11.1%, 16.7%, 22.2%, 33.3%, 38.9%, and 50.0%), were considered. The excess electrons are introduced into the system by modifying the TiO_2 stoichiometry: two excess electrons per V_O in the (1×1) phase, and

two excess electrons per Ti_2O_3 unit in the (1×2) phase. Therefore, each system is in a neutral charge state. The polaron dynamics in the presence of Ti interstitials was investigated in separate FPMD calculations, and the results are discussed in Sec. 3.7.

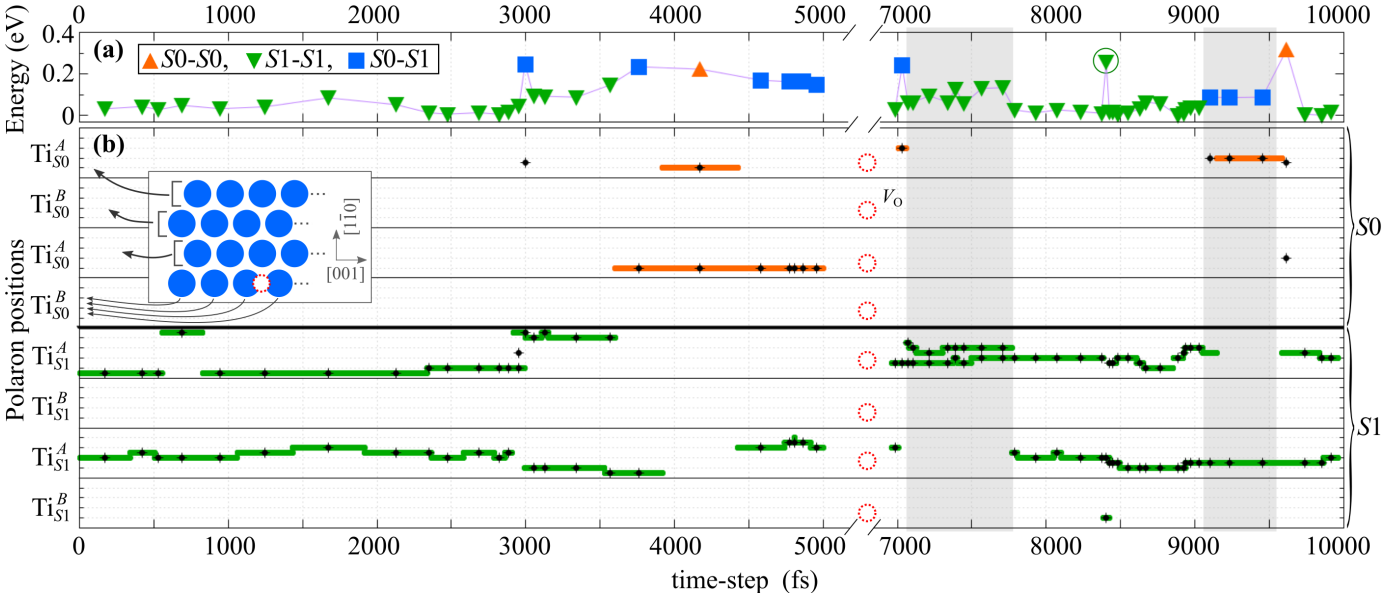

Figure 3.10: FPMD polaron hopping. A representative part of the results for the (1×1) surface with one oxygen vacancy in the 9×2 slab (c_{V_O}= 5.6%) is shown. The gray rectangles highlight data discussed in detail in the main text. Panel (a): DFT+U energies (based on the structures obtained by FPMD at 700 K and relaxed to the local equilibrium). The most stable polaronic configuration is taken as a reference. The up-pointing triangles, down-pointing triangles and squares refer to configurations with the two excess electrons in the slab localized both on the $S0$ layer, both on the $S1$ layer and one polaron per $S0$ and $S1$ layer, respectively. The circled value indicates the case of a polaronic Ti^B_{S1} site. Panel (b): polaron positions at every FPMD step. The y-axis indicates the polaron positions along each Ti^A and Ti^B [001] row (as sketched in the inset). The thick lines indicates the polaron positions as obtained by the FPMD runs at T = 700 K, whereas crosshairs are the corresponding post-FPMD polaron configurations obtained by the relaxation. The position of V_O projected along the various [001] rows is shown by dashed circles. *Figure adapted from Physical Review B ©2018 American Physical Society* [3].

Figure 3.10 shows the results for the lowest V_O concentration analyzed, c_{V_O}= 5.6% (one V_O on the 9×2 slab). Figure 3.10(b) reports the polaron lo-

calization site at every FPMD time step. Two polarons are initially localized on two sub-surface Ti^{A}_{S1} sites, and hop to different Ti sites on the $S0$ and $S1$ layers, in particular sub-surface Ti^{A}_{S1} sites and surface Ti^{A}_{S0} sites [46, 48] [Fig. 3.10(b)]. The distinctly different configurations assumed by the polarons during the FPMD run were further analyzed by performing $T = 0$ K DFT+U relaxations (*i.e.*, the ions were relaxed to the equilibrium positions determined by the given polaronic configuration, see Chapter 2). The resulting total energies are shown in Fig. 3.10(a), while E_{POL} is reported in Fig. 3.11(a) for the whole set of configurations of this FPMD run at $c_{V_{\mathrm{O}}}$= 5.6%. It has to be noticed that in a few cases, during the $T = 0$ K relaxation calculations, the polaronic configuration changes as compared to the initial FPMD configuration: The energies reported in Fig. 3.10(a) refer to the final $T = 0$ K configurations [represented by the crosshairs in Fig. 3.10(b)]. The specific arrangement of small polarons plays a crucial role in determining the energy of TiO_2(110). The results are in line with the analysis reported in Sec. 3.2, 3.3 and 3.4.

The most recurring and most stable configurations are those hosting both polarons on Ti^{A}_{S1} sites, located in different [001] rows [47, 80, 157]. Formation of two Ti^{A}_{S1} polarons on the same [001] row has a high energy cost, about 150 meV with respect to the most stable configuration, and it is indeed a relatively rare event (see gray area around 7500 fs in Fig. 3.10). Moreover, during the FPMD run at $c_{V_{\mathrm{O}}}$= 5.6%, polarons were never found on two adjacent Ti-sites (about 3 Å) [as evident from Fig. 3.11(a), which shows no data at short distance].

The polaron-vacancy interaction is another factor which influences the energy of the system. Figure 3.11(b) shows the total energy of the most favorable Ti^{A}_{S1}-polaron configurations with respect to the distance from the surface oxygen vacancy. In the most stable configuration both polarons (labeled p_1 and p_2) lie on the nearest Ti^{A}_{S1} sites to the V_{O} (black triangle, set to $E = 0$ eV). The energy increases progressively with increasing polaron-vacancy distance. Therefore, the total energy of a Ti^{A}_{S1}-polaronic configuration depends on the polaron-polaron repulsion, and on the polaron-V_{O} attraction.

Polaron formation on $S0$ sites [filled squares and up pointing triangles in Fig. 3.10(a) and Fig. 3.11(a)] is unfavorable, characterized by an energy increase of about 200 meV. However, depending on the specific location of polarons on $S0$, significant energy changes occur. As an example, the gray area around 9000-9500 fs in Fig. 3.10 highlights a $S0$-$S1$ configuration which is only 90 meV less stable than the optimal Ti^{A}_{S1} arrangement. This behavior can be traced back to the relative distance and interaction between the $S0$ and $S1$ polarons as well by their interaction with the V_{O}, as discussed in Sec. 3.3 and 3.4. At variance with charge trapping on Ti^{A}_{S1} sites, polaron formation on Ti^{B}_{S1} sites occurs very rarely [80]: only one event observed during the en-

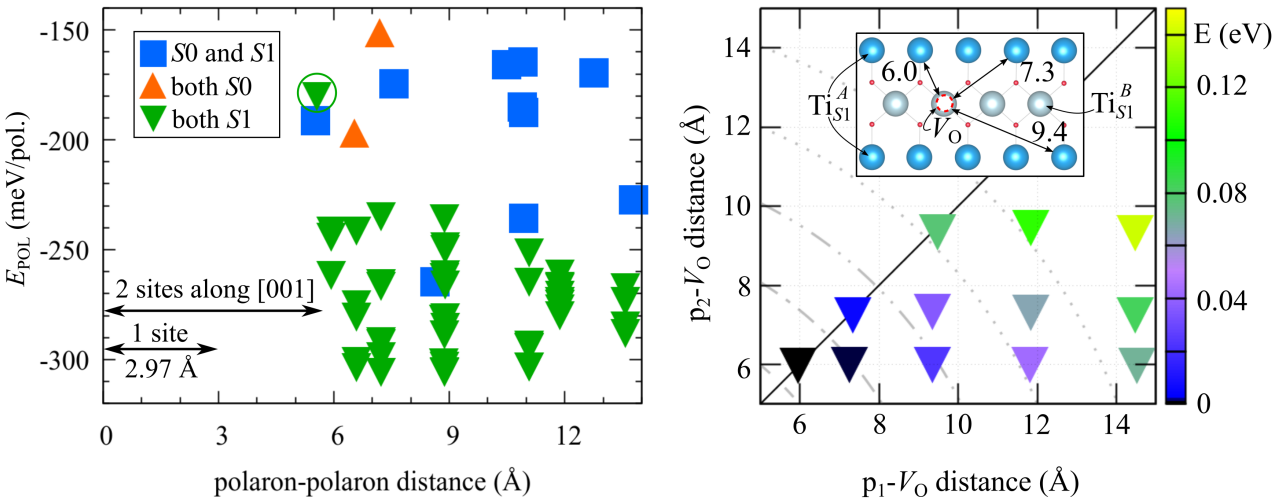

Figure 3.11: Energetics of the FPMD configurations. The 9×2-large slab, with one V_O (*i.e.*, c_{V_O}= 5.6%, two excess electrons) is considered here. Panel (a): E_{POL} as a function of the polaron-polaron distance, for configurations hosting both polarons on the $S0$ layer (up-pointing triangles), or on $S1$ (down-pointing triangles), or one polaron on $S0$ and one on $S1$ (squares). The circled triangles represents the configuration with a Ti^B_{S1} polaron. The typical size of the [001] lattice vector is also reported (2.97 Å) Panel (b): Energy (with respect to the most favorable configuration) as a function of the distance of two Ti^A_{S1} polarons (labeled p_1 and p_2) from the V_O site. The inset sketches the geometry used (the distances between the V_O and the Ti^A_{S1} sites are shown in Å). *Figure adapted from Physical Review X, Supplemental Material ©2017 American Physical Society* [4].

tire FPMD run, which shows an energy comparable to the $S0$-configurations [circled triangle in Fig. 3.10(a)].

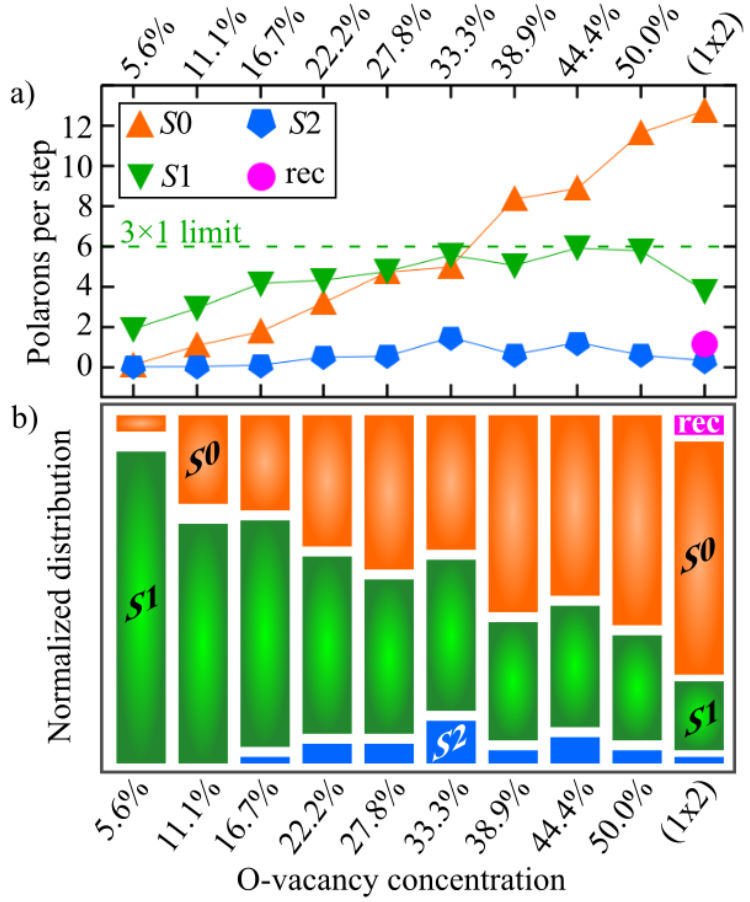

Figure 3.12: FPMD layer-resolved statistical analysis. Panel (a): Average number of polarons on the various layers, per FPMD time step. The dashed line represents the number of polarons (*i.e.*, six polarons) sustained by the 3×1 pattern in our 9×2 slab. Panel (b): Overall occurrences of polaron formation on the various layers. For the (1×1) phase, the histogram bars represent from top to bottom the $S0$, $S1$ and eventually $S2$ layers, while for the (1×2) phase the topmost bar refers to the reconstructed layer. *Figure adapted from Physical Review B ©2018 American Physical Society* [3].

[3.6.3] FPMD statistical analysis

The polaron dynamics obtained by the FPMD were further analyzed by means of a quantitative analysis of the polaron distribution. Figure 3.12 shows the layer-resolved polaronic distribution for all oxygen-vacancy concentrations considered. At c_{V_O}= 5.6%, polaron hopping occurs mainly among Ti sites on the $S1$ layer [see Fig. 3.12(b)]. At higher V_O concentrations, the polarons populate more often the $S0$ layer, and also the $S2$ layer becomes sporadically populated by polarons. At large c_{V_O}, polaron localization in $S0$ becomes progressively predominant.

The trend of the layer-resolved polaron occupancy observed in the FPMD runs is due to the balance between two opposite effects: The energetic convenience to host polarons on the sub-surface $S1$ layer, and in particular on Ti^A_{S1} sites (dominant at low c_{V_O}), and the strong repulsion between nearby polarons (dominant at high c_{V_O}), discussed in Sec. 3.2 and 3.3. As a result, polarons tend to assume an optimal arrangement involving 1 polaron every 3 Ti sites along the Ti^A_{S1} rows. In fact, as discussed in detail in Sec. 3.3 and 3.5, the overlap of polaronic clouds for two polarons localized 3 sites apart along a [001] row is small, as well as the resulting polaron-polaron repulsion. This defines a maximum density for the Ti^A_{S1} polarons (that is 6 polarons in the 9×2 slab), arranged in a 3×1 pattern. Indeed, Fig. 3.12(a) shows that the average polaron density on $S1$ does not exceed this limit, at any V_O concentration. At large c_{V_O}, polarons prefer to populate $S0$ rather than undermining the favorable 3×1 pattern on the Ti^A_{S1} rows. The localization on $S0$ sites at large c_{V_O} is also favored by the relatively small structural costs to distort the lattice at the surface, due to the presence of a large number of oxygen vacancies. In contrast to Ti^A_{S1} polarons, excess electrons on $S0$ reach higher densities on the Ti^A_{S0} rows, and localize also on the Ti^B_{S0} atoms near the V_O. The increasing polaron-polaron repulsion gradually weakens the stability of the surface and ultimately leads to a (1×2)-Ti_2O_3 structural reconstruction, which is able to accommodate a large amount of excess electrons at easily reducible Ti_{S0} sites. The details of this reconstruction are discussed in Chapter 4.

Therefore, the trend of the distribution of polarons among various layers, observed in the FPMD runs, is consistent with the analysis on the energetics for isolated polarons, reported in Sec. 3.2, and for the polaron-polaron and polaron-vacancy interactions, as discussed in Sec. 3.3 and 3.4, respectively. It has to be mentioned that the FPMD runs were conducted on 5-layer deep slabs (with the 2 layers at the bottom kept fixed). This setup weakens E_{POL} and restrains the formation of polarons in deep layers. However, this is a physically valid choice due to the inconvenience to form polarons on layers deeper than $S1$ (discussed in Sec. 3.2).

Figure 3.13 collects information on the statistical analysis of the polaron-

polaron and polaron-vacancy interactions, which are the key quantities for achieving further insights on the formation and dynamics of polarons. The correlation function $R_{\mathrm{pol-pol}}$ displayed in Fig. 3.13(a-c) shows that polarons on nearest-neighbor sites along the [001] Ti^{A}_{S1} row (*i.e.*, d_1-Ti^{A}_{S1}-polarons, at a polaron-polaron distance of 2.97 Å) are extremely rare. Instead, polarons prefer to maximize the distance between them as manifested by the strong peak at 9 Å and 12 Å, corresponding to a 4×1 and 3×1 periodicity in the 9-sites long Ti^{A}_{S1} row at c_{V_O}= 5.6%-11.1% and c_{V_O}= 16.7%, respectively.

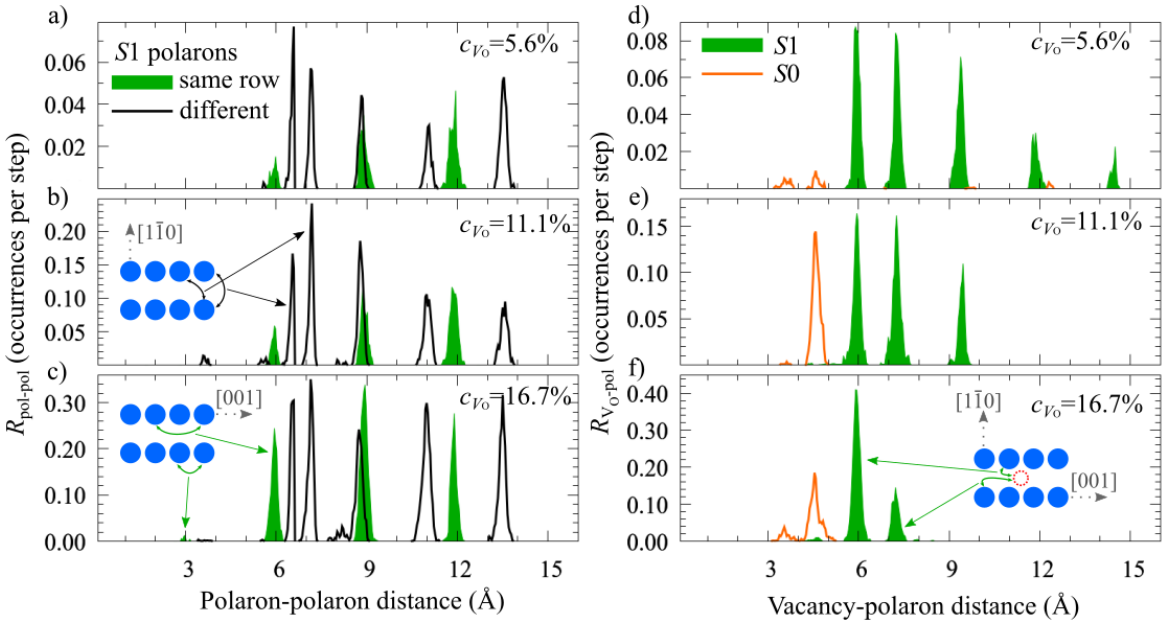

Figure 3.13: FPMD correlation. The radial distribution functions of the correlation between polarons (a,b,c) and between a polaron and the nearest oxygen vacancy (d,e,f) are shown for the systems with c_{V_O}= 5.6%, 11.1% and 16.7%. Filled and empty curves refer to the correlation between two $S1$ polarons in the same and different [001] rows, respectively, (a,b,c), and to the correlation between the oxygen vacancy and the $S1$ and $S0$ polaron, respectively, (d,e,f). The positions of the Ti^{A}_{S1} (filled circles) and V_O (empty circle) sites are sketched. *Figure adapted from Physical Review B ©2018 American Physical Society* [3].

The correlation between polarons lying on different [001] Ti^{A}_{S1} rows is rather homogeneous with a larger probability to find polaron pairs at short distances, approximately corresponding to the inter-row distance of 6.6 Å [Fig. 3.13(a,b)]. This implies that inter-row polaron-polaron repulsion is essentially ineffective. The nature of these peaks at short distances becomes clear by considering the contribution of the vacancy, which is summarized in Fig. 3.13(d-f), in terms of the correlation function $R_{\mathrm{V_O-pol}}$. These data show a polaron-V_O attraction,

which clearly influences the polaron distribution. In fact, R_{V_O-pol} decreases with increasing polaron-V_O distance, at any reported c_{V_O}, indicating the overall tendency of polarons to occupy the Ti^A_{S1} sites nearest to the V_O, which is consistent with the experimental observations [144] and with the analysis on the energetics reported in Sec. 3.4. This polaron-V_O attraction counteracts the polaron-polaron repulsion and facilitates the short-range arrangement between polarons on different rows, evidenced by the large peaks in $R_{pol-pol}$ at 6.6 Å and 7.0 Å, as well as in the same row, manifested by the peak at 6 Å (revealing polarons at next-nearest neighbor Ti^A_{S1} sites) [see empty and filled peaks in Fig. 3.13(a-c)]. On the $S0$ layer, the V_O-polaron correlation function shows that the preferred site is the Ti^A_{S0} site next nearest neighbor to V_O (NNN-Ti^A_{S0}), at 4.7 Å. Finally, even though polaron-polaron repulsion hinders the formation of a Ti^A_{S0} polaron directly above a Ti^A_{S1}, the presence of an oxygen vacancy mitigates the polaron-polaron repulsive interaction, and formation of such $S0$-$S1$ polaron-complex sporadically occurs (not shown in the figure).

[3.6.4] FPMD averaged STM

At this point it is interesting to compare the computational results with available experimental data, in particular to acquire some insights on the possible existence of surface $S0$ polarons. Surface sensitive experimental probes like scanning tunneling microscopy (STM) and scanning tunneling spectroscopy (STS) provide clear evidence of the formation of $S1$ polarons, but do not report any direct indication of $S0$ polaronlike in-gap states, at least at low temperature. Similarly to STM/STS, resonant photoelectron diffraction performed at room temperature supports the formation of sub-surface $S1$ polarons, but some broadened signals coming from surface Ti atoms are detected, which were tentatively assigned to $S0$ polarons [80]. Therefore, one might argue that $S0$ polarons might be activated by temperature. As already mentioned, the FPMD runs are done at 700 K, a choice motivated by the need of increasing the statistics by accelerating the polaron hopping. As a coupled effect, high-temperature enables $S1$ polarons to overcome the energetic barrier and hop on the $S0$ layer. At low temperature, the appearance of $S0$ polarons in FPMD would be a much rarer event, which would require very long time-intervals to be observed.

The presence of $S0$ polarons and their influence on experimentally measurable quantities is well described by the simulated filled-state STM images shown in Fig. 3.14. Figure 3.14(a) is obtained as a time average of the charge of the polaronic states at each FPMD step at the representative concentration c_{V_O}= 16.7%. The time average is performed in order to mimic the experimental conditions: In fact, the exposure time of the STM measurements is much longer than the typical lifetime of any given polaronic configuration. The $S0$ polarons appear in the simulated STM image as particularly bright and diffuse

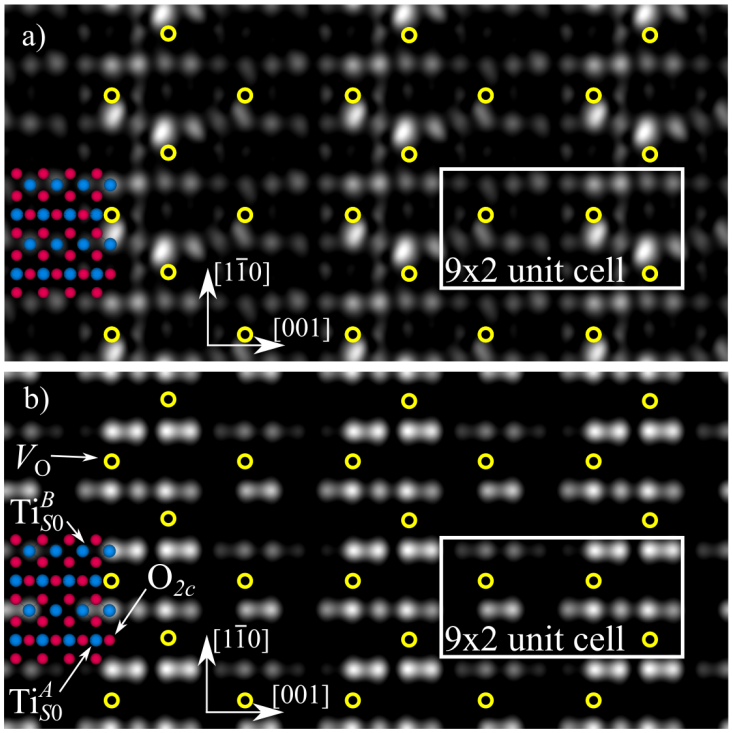

Figure 3.14: Simulated filled-state STM (c_{V_O}= 16.7%). Time-averaged simulated STM images of the in-gap states for the whole FPMD run (a) and for configurations (1168 time steps) with polarons only on $S1$ (b). Empty circles mark the positions of the oxygen vacancies. Ball models representing the $S0$ surface layer are also shown. *Figure adapted from Physical Review B ©2018 American Physical Society* [3].

spots above the Ti^A_{S0} sites nearest neighbor to V_O (each V_O is indicated by a circle). The less intense and generally circular spots arise from Ti^A_{S1} polarons.

In low-temperature experimental STM images [48], it is well-established that Ti^A_{S1} polarons exhibit a dimerlike shape, in apparent disagreement with the high-T-FPMD STM images. To recover the dimerlike feature peculiar of low temperature experiments, an STM image was constructed, by averaging the polaronic states over all FPMD-derived configurations characterized by $S1$ polarons only. The resulting image, shown in Fig. 3.14(b), is in excellent agreement with the low-temperature experiments and, at the same time, it satisfies the energetic requirements for favorable Ti^A_{S1} polarons (*i.e.*, proximity to the vacancy, and 3×1 pattern that maximizes the polaron-polaron distance).

[3.6.5] FPMD on the (1×2) phase

As already mentioned, also the (1×2) phase was inspected by FPMD. The Ti_2O_3 reconstructed row on the 9×2 slab introduces 18 excess electrons, corresponding to a deviation from the TiO_2 stoichiometry of 50%. While most of the results are discussed in detail in Chapter 4, it is interesting to mention here about the statistical analysis, due to the similarity between the (1×1) and (1×2) phases.

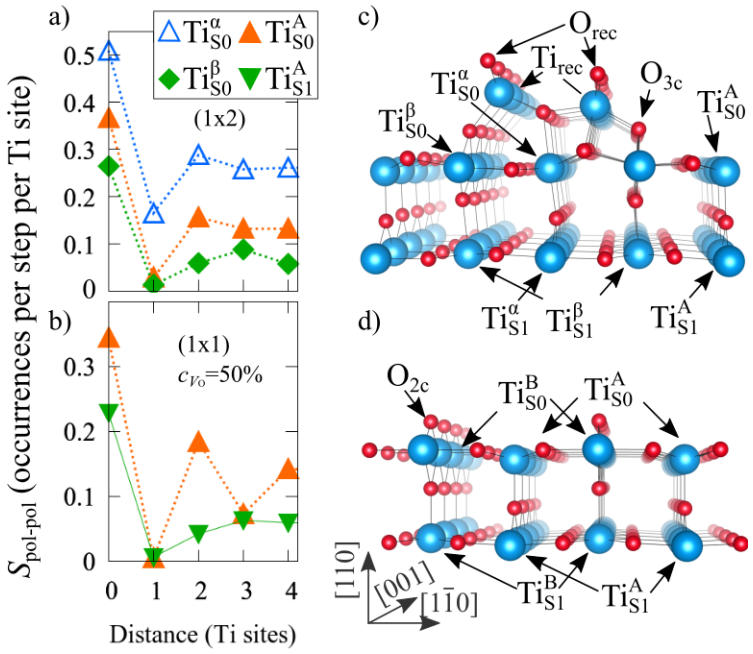

Figure 3.15: FPMD correlation for the (1×2) phase. The site-resolved polaron-polaron correlation function along [001] is shown for the (1×2) and (1×1) (c_{V_O} = 50%) cases (a,b). The site-resolved correlation at zero distance indicates the density of polarons per step. The (1×2) and (1×1) models from Fig. 2.4 are reported here for clarity (c,d). *Figure adapted from Physical Review B ©2018 American Physical Society* [3].

In fact, the (1×2) reconstructed phase shows polaron distributions similar to those obtained for the unreconstructed (1×1) phase at strongly reducing conditions (see Fig. 3.12): Charge trapping takes place predominantly on $S0$ rather than $S1$. Moreover, the Ti atoms on the reconstructed Ti_2O_3 layer (Ti_{rec}) are found to host on average only 1 of the 18 excess electrons available per time step, due to the energetic instability of polarons trapped on the reconstructed sites (see analysis on the energy stability for the reconstruction in Chapter 4).

However, the specific site-resolved polaron distribution shows specific differences between the (1×1) and (1×2) phases. Figure 3.15 reports the polaron-

polaron correlation $S_{\mathrm{pol-pol}}$ obtained for the reconstructed Ti_2O_3 phase and the unreconstructed (1×1) surface with c_{V_O}= 50%. Since these slabs are characterized by the same deviation from the stoichiometric formula (50%), they include the same amount of excess electrons. The $S_{\mathrm{pol-pol}}$ data at zero distance indicate the density of polarons localized on a specific site type per FPMD step. In the (1×1) slab, polaron localization on the $S0$ layer is predominant, showing a density of approximatively 0.34 polarons per Ti^A_{S0} site per FPMD time step [Fig. 3.15(b)]. Both Ti^A_{S0} and Ti^A_{S1} polarons tend to avoid localization on sites adjacent to other polarons (the $S_{\mathrm{pol-pol}}$ correlation is essentially zero at one Ti site distance). Considering the Ti^A_{S1} polarons, $S_{\mathrm{pol-pol}}$ becomes progressively larger for increasing distance, indicating that the Ti^A_{S1} polarons tend to maximize the polaron-polaron distance.

The (1×2) reconstruction does not substantially alter the density of polarons on the Ti^A_{S0} rows on the surrounding (1×1) terrace [compare the Ti^A_{S0} data at zero distance in Figs. 3.15(a,b)]. However, excess electrons prefer to localize on the Ti^α_{S0} sites underneath the reconstructed rows: Excess electrons on Ti^α_{S0} sites (empty triangles) are able to reach higher densities (approximatively 0.5 polarons per site per step), by localizing on sites adjacent to each other (see data at 1 Ti site distance).

Interestingly, the Ti^β_{S0} polarons on the (1×2) phase [Fig. 3.15(a)] tend to adopt the 3×1 pattern characteristic of the Ti^A_{S1} polarons. This similarity can be understood by considering that Ti^β_{S0} and Ti^A_{S1} sites show similar structural properties: The coordination octahedra are oriented along the same direction, and all the coordinated O atoms are three-fold coordinated. The Ti^β_{S0} sites in the (1×2) phase correspond to Ti^B_{S0} sites on the (1×1) terrace [Fig. 3.15(c,d)]. However, the Ti^B_{S0} sites are coordinated to two-fold coordinated O_{2c} atoms, and polaron formation is unfavorable (see Sec. 3.2). Therefore, the (1×2) reconstructed row stabilizes the formation of polarons on the Ti^β_{S0} sites by saturating the bonds of the O_{2c} atoms, ending up with three-fold coordinated O_{3c} [indicated in Fig. 3.15(c)]. Due to the structural similarities, polaron formation on Ti^β_{S0} and Ti^A_{S1} occurs with a similar spatial extension of the electronic charge, the key quantity driving the polaron-polaron repulsion and the polaronic 3×1 pattern (Secs. 3.3 and 3.5).

3.7 Interstitial Ti atoms

Typical point defects on rutile TiO_2(110), in addition to the surface vacancies, are the Ti interstitials (Ti_{int}). In the following, the rutile TiO_2 containing only interstitial Ti atoms is referred to as $Ti_{1+x}O_2$, while TiO_{2-y} is used for slabs including only oxygen vacancies. The Ti_{int} atoms introduce excess electrons to

the system, which are eligible to form polarons [158]. Therefore, it is interesting to compare the V_O-induced polarons to the Ti_{int}-induced polarons. As reported in this section, the polarons show similar characteristics, regardless of their origin. However, understanding the role of Ti_{int} in TiO_2 is more complicated than for the V_O.

First, at low temperature, oxygen vacancies are known to form on specific surface sites, *i.e.*, the two-fold coordinated oxygen O_{2c}. These defects can be experimentally detected relatively easily by AFM or empty-states STM imaging. Conversely, the position of interstitial Ti atoms is more difficult to detect. However, experiments and simulations agree that, at low-temperature, Ti_{int} atoms are located in deep bulklike positions, far below the (110) surface.

Second, as already mentioned, both oxygen vacancies and interstitial titaniums contribute to reduce the TiO_2 rutile. However, one V_O introduces two excess electrons, while one Ti_{int} introduces four electrons. The localization of this excess charge is not trivial. The systematic analysis reported in the previous sections shows that on TiO_{2-y}(110) surfaces, the two V_O-induced excess electrons form polarons, preferentially localized on the $S1$ layer, in the proximity of the V_O. The V_O, immobile at the temperature explored in this study, acts as an attractive center for the polarons. On the other hand, the interaction between polarons and interstitial titaniums has not been systematically investigated yet, and it represents a challenge for theory and experiment.

[3.7.1] Ti_{int} energetics

The study on $Ti_{1+x}O_2$ starts by inspecting the formation of interstitial Ti atoms. Figure 3.16 reports the computational results for the energy stability analysis of possible Ti_{int} positions. The system is modeled by using a 6×2 slab both without any oxygen vacancies, and with one V_O. An interstitial Ti atom is introduced into the system at various positions, as explained in the following. From a top view of the rutile TiO_2(110) surface, it is possible to identify pentagons whose corners lie in correspondence of three Ti and two O atoms on the $S0$ layer [159]. The interstitial Ti atom are inserted on the center and on the $[1\bar{1}0]$ edge of the pentagon, between the $S0$ and $S1$ layers, and between the $S1$ and $S2$ layers (labeling every interstitial site as $S0S1$-center, $S0S1$-edge, $S1S2$-center and $S1S2$-edge, as sketched in the insets of Fig. 3.16).

There is no systematic study accounting for the free energy variations of the $Ti_{1+x}O_2$ system brought about by the localization of polarons in different configurations. Similarly, there is no study aiming to deliver an exhaustive description of the individual contribution of the various interactions at play, such as the Ti_{int}-polaron and the polaron-polaron interactions. A recent work investigated the dynamics of polarons in presence of interstitial Ti atoms [160], and obtained patterns revealing an attractive Ti_{int}-polaron interaction, in combi-

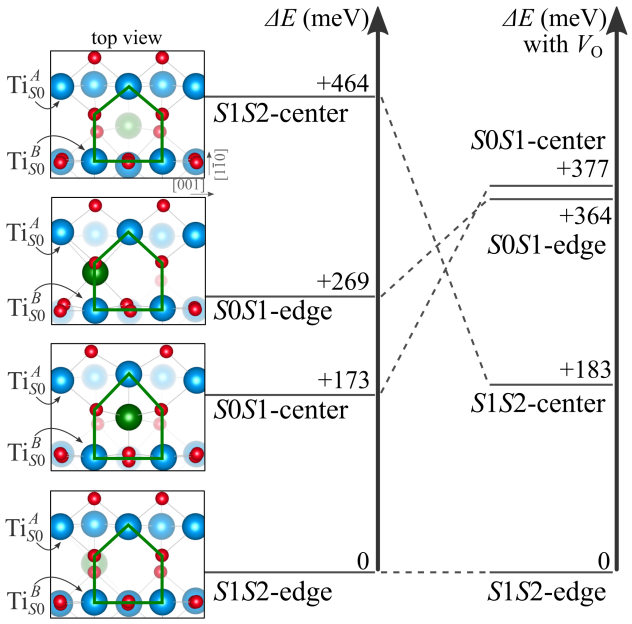

Figure 3.16: Stability of the Ti_{int}. A 6×2-large slab contains a Ti_{int} atom modeled in the $S0S1$-center, $S0S1$-edge, $S1S2$-center and $S1S2$-edge positions. The insets sketch the geometry used (Ti_{int} is in green; faded spheres represent atom deeper into the slab; the reference pentagon is individuated by a green line). The energy of each system is calculated in the non spin-polarized setup and shown with respect to the most stable case, that is $S1S2$-edge. Both the energy values obtained by using slabs with and without surface V_O are reported. *[Unpublished Figure]*

nation with the formation of $S1$ polarons (it has to be noted that the stability of $S1$ polarons could be here fictitiously overestimated by the computational setup, which models interstitial Ti atoms only at deep layers, where polaron formation is inhibited by the crystal stiffness). Consequently, the most convenient polaronic configuration is unknown for the TiO_2(110) surface with interstitial Ti atoms (at variance with the TiO_{2-y} system).

As a starting-point, the stability of Ti interstitials was studied in the delocalized electron solution (the excess electron localization is inhibited by performing non spin-polarized calculations, see Sec. 2.1). In the delocalized electron solution, the Ti_{int} preferentially form in the $S1S2$-edge position, while shallower positions are energetically less favorable (Fig. 3.16), in agreement with literature [160, 161].

The V_O and Ti_{int} show a strong repulsive interaction [162]. This repulsion stands out clearly from the delocalized-electron calculations, since the formation of interstitial Ti atoms in $S1S2$ positions is favored by the presence of a surface V_O (Fig. 3.16). Therefore, it makes sense to study the properties of

Ti_{int} by considering $Ti_{1+x}O_2$ slabs without any surface V_O, since the oxygen vacancy would repel the Ti interstitials towards the bulk, thus, reducing the impact of the Ti_{int} on the surface properties.

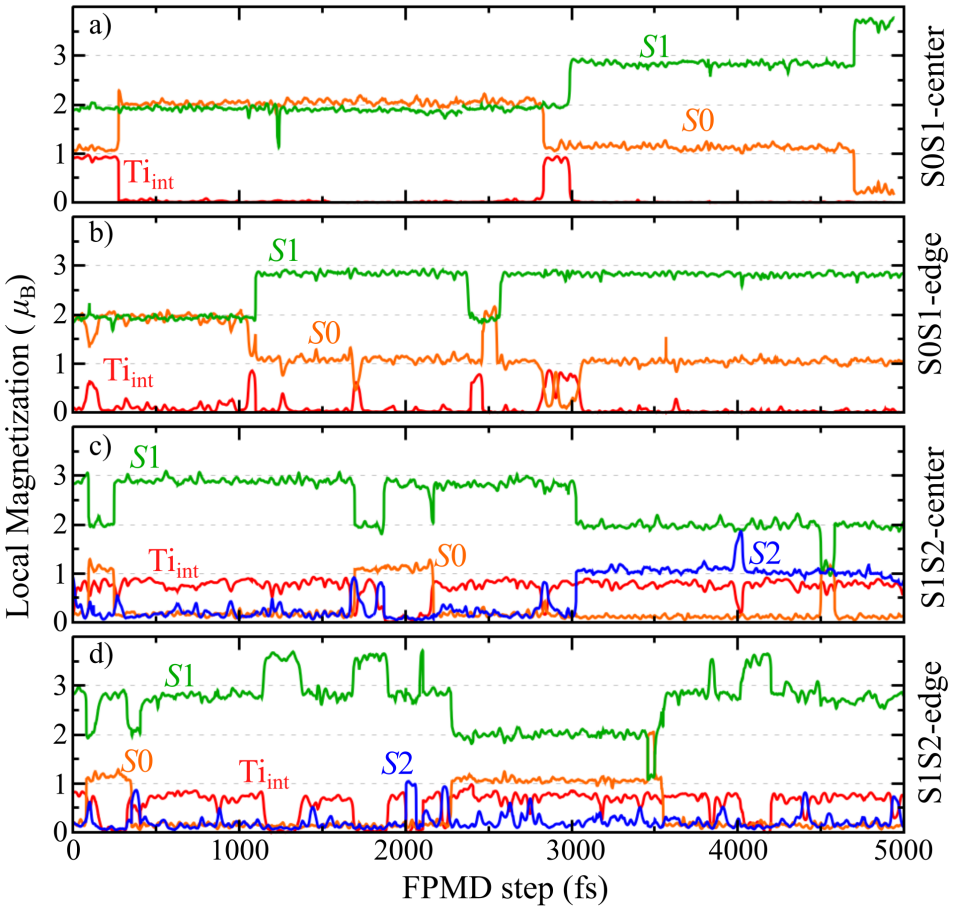

Figure 3.17: Polaron FPMD hopping (Ti_{int} excess electrons). A pristine 6×2-large slab contains a Ti_{int} atom (introducing four excess electrons) modeled in the $S0S1$-center (a), $S0S1$-edge (b), $S1S2$-center (c) and $S1S2$-edge (d) positions. The local magnetization is shown for the Ti_{int} atom (red line) and the $S0$ (orange), $S1$ (green) and $S2$ (blue) layers. *[Unpublished Figure]*

[3.7.2] Ti_{int} polarons

The polaron formation in the $Ti_{1+x}O_2$ system was studied by performing FPMD calculations, on the four different geometries considered ($S0S1$-center, $S0S1$-edge, $S1S2$-center and $S1S2$-edge). At the simulating temperature of 700 K, the interstitial Ti does not diffuse through the crystal, and it maintains its original position in the whole FPMD run (approximatively 5000 fs), with minor deviations from the equilibrium position. The four excess elec-

trons introduced by the Ti_{int} atom form polarons, which hop among the Ti sites. The 6×2 slab used in the calculations is large enough to accommodate all four polarons on a single layer and, simultaneously, to guarantee a minimum polaron-polaron distance of three lattice sites along [001]. It is important to recall that a smaller distance results in a strong polaron-polaron repulsion (see Sec. 3.3); therefore, smaller slabs could affect the polaron formation by penalizing configurations with high polaron density on a single layer. The polaron hopping is tracked by inspecting the local magnetic moment on every site. In fact, in the absence of polarons, every Ti atom would have a zero magnetic moment; one polaron determines a local magnetic moment of approximatively 1 μ_B. Figure 3.17 shows the amount of local magnetic moment on the Ti_{int} atom and on the $S0$, $S1$ ad $S2$ layers.

For a Ti_{int} at $S0S1$ positions [Fig. 3.17(a,b)], the polarons lie preferentially on $S1$, analogously to the TiO_{2-y} FPMD at low c_{V_O} presented in Sec: 3.6. However, hopping towards the $S0$ layer occurs frequently, confirming the attractive character of the Ti_{int} sites for the polarons (*i.e.*, the Ti_{int} seems to reduce the energy cost required by the $S0$ polarons). Consistently, hopping towards the $S2$ and deeper layers was not observed. Polaron localization at the Ti_{int} site occurs sporadically, and it could lead to a polaron transfer between the $S1$ and $S2$ layers [see the magnetization switching around 3000 fs in Fig. 3.17(a), which shows one $S0$ polaron moving to the Ti_{int} and, finally, to $S1$].

The hopping pattern appears different for a Ti_{int} at the $S1S2$ positions [Fig. 3.17(c,d)]. The $S1$ layer plays again the major role for the polaron localization. Interestingly, one polaron is strongly trapped at the Ti_{int} site: Few hopping events from the Ti_{int} towards any other Ti site are observed. The attractive interaction with the Ti_{int} atoms also drives the polaron hopping towards the $S2$ layer, depleting the $S0$ layer (especially in the $S1S2$-center geometry).

In addition to the data shown in Fig. 3.17 for the layer-resolved distribution of polarons, it is important to mention that the Ti_{int} seems to stabilize the charge trapping at specific Ti sites (not shown). In fact, in the $S0S1$ geometries, the nearest Ti^A_{S0} atoms from Ti_{int} host frequently polarons. Moreover, at any considered geometry, the Ti_{int} favors the polaron formation on the Ti^A_{S1} sites nearby; this attraction makes polarons lie on two nearest and next nearest Ti^A_{S1} sites along [001] (d_1-Ti^A_{S1} and d_2-Ti^A_{S1} sites), in particular in the $S1S2$ geometries. Therefore, the polaron-Ti_{int} attractive interaction appear to be able to overtake the short-range polaron-polaron repulsion, resembling the effect of the polaron-V_O interaction (discussed in Sec. 3.6)

The polaron hopping observed during the FPMD runs provides a set of polaronic configurations, which can be analyzed via $T = 0$ K DFT+U relaxations

$S0S1$-center					
Amount of polarons					Total
$S2$	$S1$	$S0$	Ti_{int}	ΔE (meV)	E_{POL} (meV)
0	2	1	1	0	-1564

$S0S1$-edge					
Amount of polarons					Total
$S2$	$S1$	$S0$	Ti_{int}	ΔE (meV)	E_{POL} (meV)
0	2	2	0	+17	-1642
0	3	1	0	+26	-1633

$S1S2$-edge					
Amount of polarons					Total
$S2$	$S1$	$S0$	Ti_{int}	ΔE (meV)	E_{POL} (meV)
0	2	1	1	+514	-876
0	3	0	1	+338	-1053

Table 3.4: **Ti_{int} polaron energetics.** Free energy (ΔE, referenced to the $S0S1$-center system) and total E_{POL} for the $Ti_{1+x}O_2$ system. The calculations are performed by using given FPMD configurations (the amount of polarons on the Ti_{int} site and $S0$, $S1$ and $S2$ layers is reported for each case).

in analogy with the study for the V_O-induced polarons in Sec. 3.6. The analysis of the polaronic configurations was performed by using only a small subset of the FPMD configurations. As discussed in the following, this restriction allowed for the explanation of some aspects of the Ti_{int}-polaron interaction, while some issues are left open for future studies. A deeper analysis, extended to more FPMD configurations (and, eventually, longer FPMD runs), seems to be required in order to achieve a comprehensive understanding of the Ti_{int} role, which was beyond the scope of this work.

Table 3.4 summarizes the results of the analysis on the energetics of the $Ti_{1+x}O_2$ system, in the presence of polarons. Only the values related to the most favorable polaronic configurations are reported. The layer-resolved polaron occupation is reported for each entry in the table, together with the energy of the system (referenced to the $S0S1$-center geometry) and the polaron formation energy. The considered polaronic configuration in the $S0S1$-center geometry seems to represent the ground state of the $Ti_{1+x}O_2$ system ($\Delta E = 0$). The stability of this configuration originates from an E_{POL} energy particularly

strong for the $S0S1$ geometries in comparison to the $S1S2$. For the Ti_{int} in the $S1S2$-edge geometry in the considered polaronic configurations, the system turned to be largely less stable ($\Delta E = +338$ meV). At variance with the data obtained for the delocalized solutions, the results seem to contradict the low-temperature experimental observations, which report Ti_{int} atoms preferentially at deeper positions [19, 142, 163]. This discrepancy could be due to several reasons, such as the small variety of polaronic configurations examined in this work, and the setup used to model the structure, which includes only three mobile layers in the slab. These open issues will be examined in future works.

Despite the open doubts regarding the Ti_{int} stability, the employed computational setup seems to deliver a consistent picture regarding the polaron-Ti_{int} interaction. The attractive nature of the Ti_{int} atoms stands out clearly from the ΔE and E_{POL} values reported for two pairs of configurations in the $S0S1$-edge and $S1S2$-edge geometries. Each configuration differs from the second configuration in the pair by the position of only one polaron. In the $S0S1$-edge geometry, by moving one polaron from $S1$ to $S0$, the energetic variation is small, due to the attractive interaction of the Ti_{int} at short distance, compensating the larger cost usually required to form $S0$ polarons (see Sec. 3.2). Accordingly, moving one polaron from $S1$ to $S0$ costs more energy in the $S1S2$-edge geometry. Moreover, the most stable polaronic configurations for the $S1S2$-edge geometry are obtained by localizing one excess electron on the Ti_{int} site, as expected from the FPMD hopping analysis.

In summary, the excess electrons introduced by the Ti_{int} form polarons on TiO_2(110), similarly as for the excess charge originating from V_O. However, the attractive interaction with the Ti_{int} is stronger: it could lead to the formation of polarons at short inter-polaronic distance (overtaking the polaron-polaron repulsion), and on the surface $S0$ layer at low energy cost. Moreover, the defect point is found to host polarons itself, without compromising the polaron mobility (*i.e.*, the polaron is able to escape the Ti_{int} site).

3.8 Outline of the polaron formation and dynamics

The conditions for the formation of polarons and their dynamics on the reduced rutile TiO_2(110) surface were analyzed by using first principles static and dynamic calculations, in the framework of DFT+U and FPMD (at $T = 700$ K). The excess electrons were obtained by removal of oxygen atoms from the surface layer of the (1×1) phase, and a wide range of V_O concentrations were

considered from $c_{V_O} = 0$ to $c_{V_O} = 50\%$. The analysis was also partly extended to TiO_2 slabs reduced by Ti interstitials and to (1×2) surfaces modeling the Ti_2O_3 reconstruction.

During the FPMD runs, the thermally activated hopping drives the polarons to a wide variety of configurations. At low c_{V_O}, polarons reside predominantly on the $S1$ sub-surface layer, which is energetically favored. At $c_{V_O} = 16.7\%$, the polarons tend to populate the $S1$ layer with an optimal 3×1 pattern, which avoids the repulsive interaction of the negatively charged electronic clouds (particularly strong at short polaron-polaron distance). At higher concentrations ($c_{V_O} > 16.7\%$), the distribution of polarons in the system is too high to preserve the 3×1 pattern on $S1$, and polarons start to form often on $S0$ sites. At this high concentrations, the high density of polarons on the surface and subsurface layers destabilizes the 1×1 surface and the systems undergoes a (1×2) structural reconstruction (details in Chapter 4), which is able to host a larger number of polarons.

Each inequivalent polaronic configuration observed in the FPMD was further analyzed by $T = 0$ K DFT+U relaxations, in order to calculate E_{POL} and inspect the energy balance. To disentangle the different effects contributing to the degree of stability of the various polaron configurations, and to address the role of polaron-polaron and polaron-vacancy interactions, DFT+U calculations were conducted also by selectively controlling the polaron position in the slab. Engineering the polaron position was useful in order to selectively vary the relative distance of polarons and oxygen vacancies in the (1×1) system. The resulting picture appears to be comprehensive and consistent with the FPMD results.

Various Ti sites are able to host polarons, which differ by their specific location in the slab and by the different local chemical and structural environment. This gives rise to different types of polarons with distinct characteristics in terms of orbital symmetry, spatial localization and local structural distortions. In the (1×1) phase, polaronic Ti^A_{S0} sites are accompanied by larger local distortions of the lattice, with a polaronic cloud exhibiting preferentially a d_{xz}-d_{yz} orbital. At deeper layers, A and B Ti sites are able to host d_{z^2}-$d_{x^2-y^2}$ and $d_{x^2-y^2}$ polarons, alternately in the [110] and [1$\bar{1}$0] directions (due to the orientation of the coordination octahedron surrounding the polaronic Ti site). The Ti^A_{S1} atoms are the most energetically stable sites for isolated polarons, in agreement with experimental observations. The electrostatic potential at Ti^A_{S1} sites is stronger, owing to the local-structure distortions induced by the broken symmetry at the surface, and determines an electron energy gain E_{EL} large enough to overcome the small strain energy cost E_{ST} required to locally distort the lattice and accommodate a polaron. Conversely, the Ti^A_{S0} sites suf-

fer from a large strain energy cost E_{ST} to distort the lattice in the defect-free surface, while formation of polarons at Ti^{B}_{S1} sites is hindered by an unfavorable electrostatic potential. The presence of a vacancy on the surface increases the flexibility of the lattice, thereby lowering the E_{POL} in both surface and sub-surface Ti sites. In general, oxygen vacancies act as attractive centers for polarons (a situation also observed in other oxides [164–167]), reduce E_{ST}, increase the electronic gain E_{EL} (due to an attractive electrostatic potential), and can influence the orbital symmetry of the neighboring polarons. Similarly, Ti interstitials show attractive interactions with polarons, and the polaronic pattern depends on the specific position assumed by the $\mathrm{Ti}_{\mathrm{int}}$.

The polaron-polaron interaction is clearly repulsive, and particularly effective at small distances. Polaron pairs at nearest-neighbor Ti^{A}_{S1} sites along [001] only form in proximity of a Ti interstitials or an oxygen vacancy, whose electrostatic potential mitigates the strong polaron-polaron repulsion enhanced by the overlap of the polaronic charges. In this configuration, the energy level of the characteristic in-gap polaron peak as wells as its shape depend significantly on the spin alignment of the two polarons. The antiferromagnetic configuration is energetically more favorable and results in polarons at degenerate energy levels, with electronic clouds resembling the features of isolated Ti^{A}_{S1} polarons. Conversely, for ferromagnetically aligned spins, the two polarons are shared equivalently by the two hosting Ti^{A}_{S1} sites, and the polaronic orbitals undertake a substantial hybridization, with a bonding/anti-bonding splitting of about 0.6 eV. At larger polaron-polaron distance (*i.e.*, more than 2 sites apart along the [001] row), the charge overlap becomes negligible: antiferro and ferro solutions are degenerate in energy and the polaron charge remains distinctively localized in one single Ti^{A}_{S1} sites.

In conclusion, the results presented here offer a valid key to interpret the behavior of small polarons in TiO_2, and likely represent the general behavior of polaron in oxides. In particular, on oxide surfaces, the site-specific polaron characteristic is expected to influence the interaction with adsorbates and to play a crucial role in catalysis (details in Chapter 5).

From a technical point of view, the results presented here confirm the need to control the charge trapping process in simulations rather than relying on the spontaneous electron localization, which, in same cases, could not lead to the global energy minimum of the system. Finally, adopting large supercells is advised for calculations on polaronic systems, in other to minimize the spurious overlap among polaronic orbitals, as well as to avoid rigid constrains on the polaron-induced lattice relaxations.

Chapter 4

Surface stability and structural reconstruction

Solid surfaces, even at the thermodynamic equilibrium, experience a structural and electronic stress (due to, e.g., unsaturated bonds and/or intrinsic polarity), undermining the surface stability. Spontaneous geometrical reconstructions, generally associated with charge transfer, occur to overtake this instability.

An alternative and radically different reconstruction mechanism based on charge trapping (i.e., polarons) rather than charge transfer was proposed and investigated within this doctorate project, by combining first principles calculations and surface sensitive experiments [4]. This mechanism explains the debated (1×1)-to-(1×2) transition on the polaronic rutile TiO_2(110) surface.

Contents

4.1 The Ti_2O_3 reconstruction

[4.1.1] Surface reconstructions

The majority of surfaces undergo significant structural and electronic modifications with respect to the ideal bulk phase in order to minimize their surface free energy [168]. Typical mechanisms reduce the number of surface dangling bonds, compensate intrinsic polarity, or decrease the lattice stress [17, 168–170]. Prototypical examples are the Si(111)-(7×7) reconstruction [171, 172], and the (n×1) and (2×n) reconstructions occurring on the $SrTiO_3$(110) surface [173, 174]. A complex example of polarity compensation mechanism in transition metal oxides is reported in Appendix B for the $KTaO_3$(001) perovskite.

Unraveling the mechanism that drives the surface reconstructions is essential to understand the physical and chemical properties of surfaces, and it can serve to optimize applications in microelectronics, catalysis, and surface engineering [175]. The stabilization process typically involves the displacements of surface atoms and electronic charge transfer between surface atoms, and often results in non-stoichiometric reconstructions; this mechanism can be affected by defects, heating treatments, and by the interaction of orbitals, lattice and spins [168, 176, 177]. In addition to the well studied reconstructing processes, charge trapping can cause surface reconstructions as well: The following discussion focuses on the role of polarons on the surface stability and its structural reconstruction, by considering the archetypal TiO_2(110) surface.

[4.1.2] The TiO_2 (1×2) phase

TiO_2 single crystals are often reduced by formation of surface oxygen vacancies. At strongly reducing conditions, the surface assumes a (1×2) reconstruction rather than the (1×1) termination that is observed on more stoichiometric crystals [17, 178, 179]. This (1×2) structure is then the low-temperature phase; it can reversibly switch to the (1×1) phase when the sample temperature is raised above ≈1000 K [180], and the transition is facilitated by the surface-to-bulk mass flow [181].

The large-area STM image in Fig. 4.1(a) shows a surface typical for a strongly reduced TiO_2(110) sample. The bulk-terminated (1×1) structure with isolated oxygen vacancies (V_O) coexists with stripes of the (1×2) reconstruction. When a pristine (stoichiometric) TiO_2 sample is introduced into UHV, it shows only the (1×1) surface. Standard sample treatments, consisting of sputtering and high-temperature annealing, reduce the crystals and, at first, result in the appearance of isolated surface oxygen vacancies at the 2-coordinated oxygen (O_{2c}) sites. Eventually the (1×2) stripes shown in Fig. 4.1(a) appear; their density increases upon further reduction until they cover the whole surface [178]. This phase separation into (1×1) and (1×2) regions allows for an accurate determination of the critical concentration of oxygen vacancies at

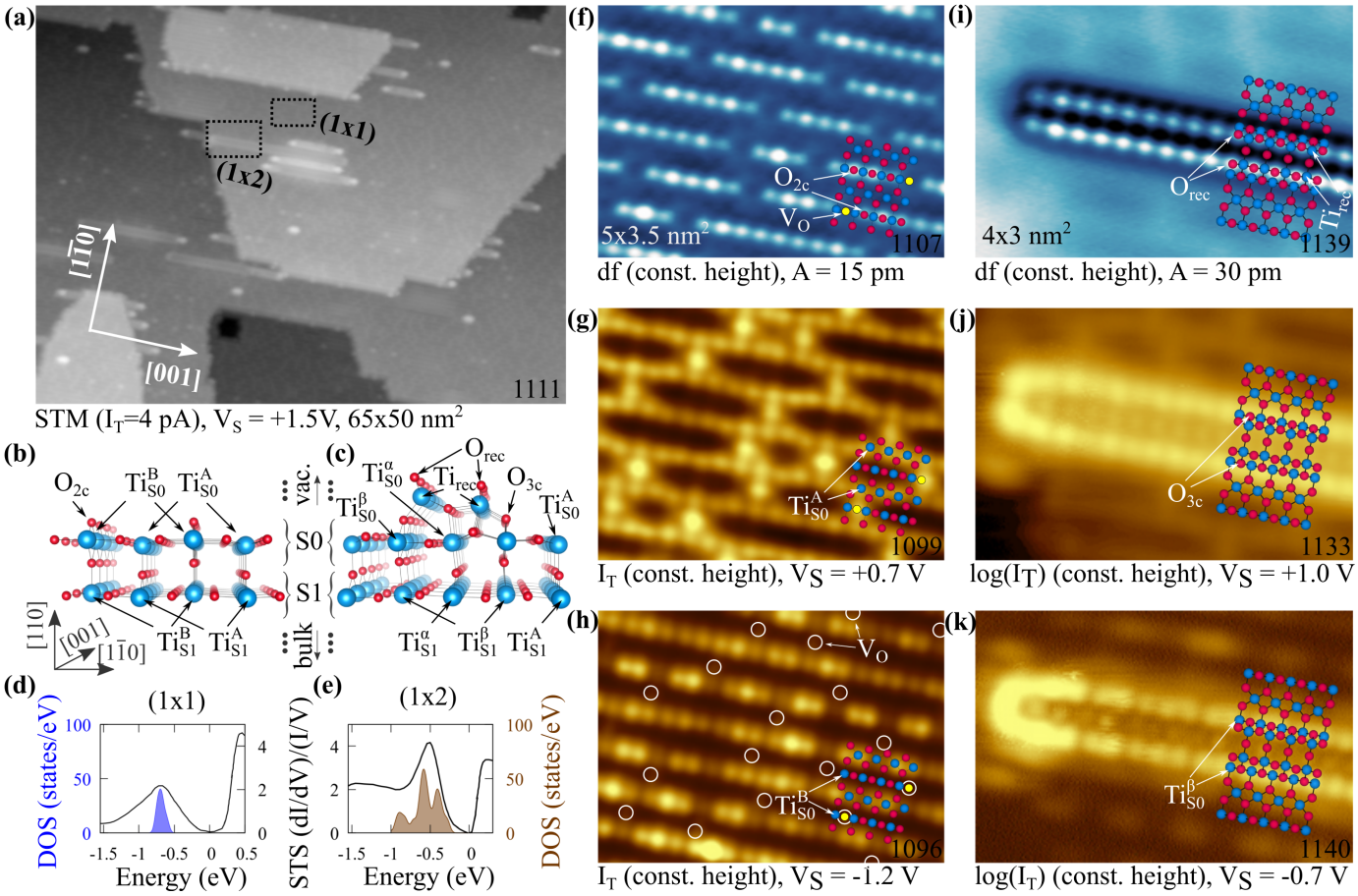

Figure 4.1: The (1×1) and (1×2) surface phases of TiO_2(110). Panel (a): Large-area STM image of a reduced rutile (110) single crystal. Unreconstructed (1×1) regions with single oxygen vacancies appear together with reconstructed (1×2) Ti_2O_3 stripes. Panels (b, c): Structural models of the (1×1) and (1×2) phases, as shown also in Fig. 2.4. Panels (d, e): STS spectra (line) taken above (1×1) and (1×2) together with calculated polaronic gap states (filled area), shifted upwards by ≈0.25 eV to align the polaronic peaks with the experiment. Panels (f-k): High-resolution images of the (1×1) and (1×2) regions marked in panel (a), overlaid with the respective structural models. AFM images (i, f) show the highest O atoms (O_{2c} and O_{rec}) on the surface, and STM images the empty (g, j) and filled (h, k) states. *Figure adapted from Physical Review X ©2017 American Physical Society* [4].

which the transition occurs. In the samples considered here it is measured as $16.7 \pm 0.2\%$ (≈1/6) monolayer.

[4.1.3] AFM

A zoom-in of the (1×1) phase and a detail of the (1×2) reconstruction are shown in Figs. 4.1(f-h) and Figs. 4.1(i-k), respectively. The O sublattice is revealed by AFM. On the well-known (1×1) phase [Fig. 4.1(f)], the image shows the O_{2c} atoms in the regime of repulsive forces; oxygen vacancies appear as missing spots in the rows. This imaging mode is particularly useful for the (1×2) reconstruction [Fig. 4.1(i)], since the structural model is still under debate [17, 20, 21, 182–185]. The AFM allows a precise measurement of the positions of the surface O atoms on the $[1\bar{1}0]$-[001] plane, which contributes to exclude most of the proposed structures. These results confirm the Ti_2O_3 model [sketched in Fig. 4.1(c)], initially proposed by Onishi and Iwasawa [17], recently refined by Wang *et al.* [21] via DFT-based genetic algorithms, and supported by a total-reflection high-energy positron diffraction study [20]. Here the stripes have a Ti_2O_3 stoichiometry, *i.e.*, their composition can be viewed as Ti_2O_4 with 50% of oxygen vacancies.

[4.1.4] STM

While STM images [Figs. 4.1(g,h) and Figs. 4.1(j,k)] provide supplementary information about the geometric structure, their importance resides in unraveling the electronic structure of the two phases. In the empty-state STM images of the (1×1) phase [the imaging mode most-widely employed in the literature, Fig. 4.1(g)] the oxygen vacancies appear as bright spots between the surface Ti^{A}_{S0} rows. More interesting, however, are the filled-states STM images, which collect the gap states seen in STS [Fig. 4.1(d)]; the image in Fig. 4.1(h) directly shows the polaron spatial distribution on the (1×1) phase (here the excess electrons originate from the surface oxygen vacancies). The lattice of the (1×2) reconstruction is very flexible [see the DFT ground-state structural model shown in Fig. 4.1(c)]: Both experiment and DFT find competing structures with different degree of buckling (discussed in details in Sec. 4.2). When the buckling is small, like in Fig. 4.1(i-k), the STM signal comes from the O_{3c} [empty-states, Fig. 4.1(j)] and $Ti^{\alpha,\beta}_{S0}$ [in-gap states, Fig. 4.1(k)] atoms; the latter is attributed to Ti^{3+} polaronic-like states. The DFT calculations show that the reconstructed Ti_2O_3 (1×2) surface hosts two polarons per (1×2) unit cell, in accord with a nominal V_O concentration of 50% (*i.e.*, 1 missing oxygen per unit cell). This value is also in agreement with the electronic structure results shown in Fig. 4.1(e): The significant jump in the off-stoichiometry from the (1×1) to (1×2) reconstruction, 16.7% to (locally) 50%, implies a high concentration of polarons and causes the broadening of the in-gap peak in the DOS and filled state STS [186–188] of the reconstructed surface [see Figs. 4.1(d,e)].

4.2 The buckling of the Ti_2O_3 stripes

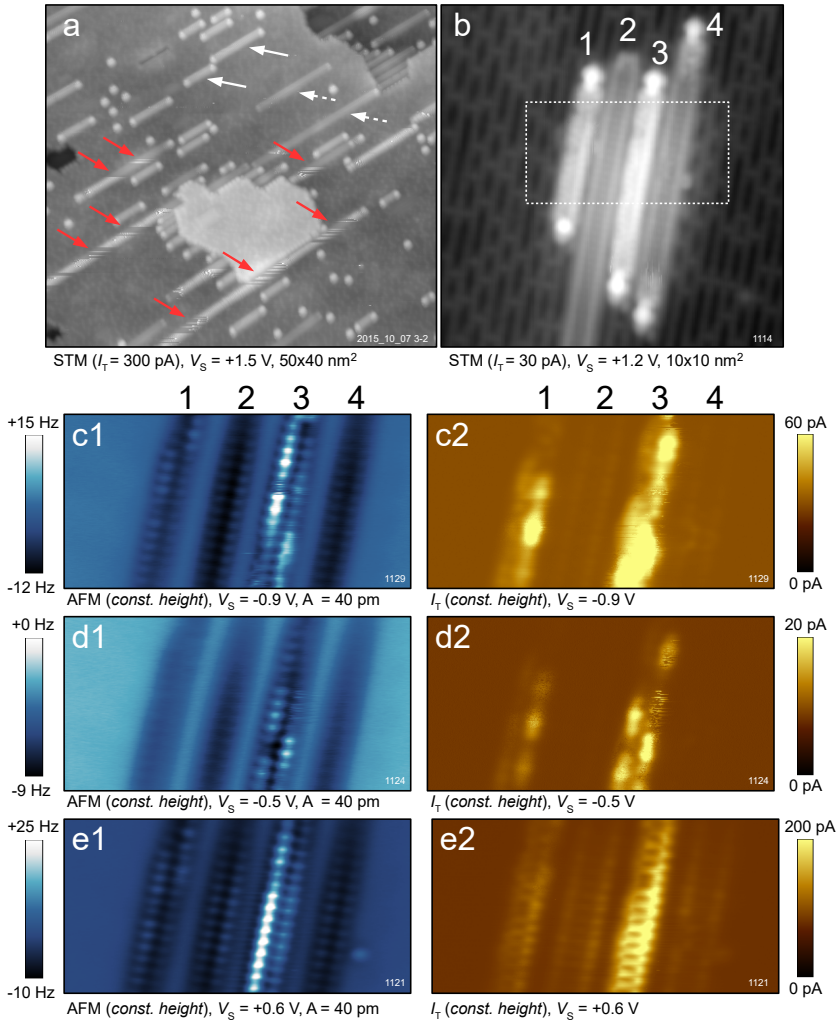

Figure 4.2: The buckling (1×2) reconstruction. Panel (a): A large-area STM image of a strongly reduced rutile (110) surface. There are brighter and less bright stripes of the (1×2) reconstruction, marked by solid and dashed white arrows. Red arrows mark tip-induced switching between these two configurations. Panel (b): A region with four adjacent stripes of the (1×2) reconstruction. The stripes are labeled by numbers 1 to 4. Panels (c-e): Simultaneous AFM (c1-e1) and STM (c2-e2) images of the selected region. *Figure adapted from Physical Review X, Supplemental Material ©2017 American Physical Society* [4].

[4.2.1] **Experiments**

The (1×2) reconstruction appears in the STM images via two distinctly different signals, as shown in Fig. 4.2. Fig. 4.2(a) shows a large-area STM

image of the rutile (110) surface, with stripes of the (1×2) reconstruction. Some of the (1×2) stripes are brighter (marked by solid white arrows), while others are darker (marked by dashed white arrows), as shown in detail in Fig. 4.2(b). A switching between the brighter and darker contrast occurs frequently on the surface (marked by red arrows). This switching is induced by the STM tip, and depends on both the sample bias and the tunneling current.

The brighter and darker stripes have the same atomic structure, and the STM contrast-switch is related to the buckling of the (1×2) stripe. The area surrounded by a rectangle in Fig. 4.2(b) is imaged in Figs. 4.2(c-e) at different conditions. There are four (1×2) stripes, labeled by numbers (1 to 4). The detailed AFM images (c1-e1) reveal that the lines 1 and 3 are buckled, while lines 2 and 4 are almost symmetric. The different AFM contrasts in c,d,e stems from a varying tip-sample distance. The buckling of line 3 was switched between images d1 and e1, by changing the sample bias polarity. The buckling is stable when the surface is imaged by AFM at zero sample bias. On the other hand, tunneling current and applied bias induce often tip-induced buckling switches.

Therefore, the STM signal from the (1×2) reconstruction originates from different atoms in the buckled and non-buckled cases. For the buckled chains, the tunneling current flows mainly from the surface O_{rec} and Ti_{rec} atoms; the stripes 1 and 3 in Fig. 4.2 are a bit narrower in both filled and empty states. In contrast to this, the non-buckled stripes are a bit broader in both filled- and empty-states STM images: The empty states fit with the positions of the reconstruction O_{3c} atoms, while the filled states are centered on the Ti^{α}_{S0} and Ti^{β}_{S0} atoms of the surface layer below the reconstruction.

[4.2.2] DFT simulations

The Ti_2O_3 stripes were analyzed also in the DFT framework, by exploring a large set of polaronic configurations. The first-principles molecular dynamics was used to obtain the most favorable polaron spatial localization. The statistical analysis on the FPMD calculations for the Ti_2O_3 reconstructed surface [reported in Fig. 3.15(a)] reveals that the excess electrons are preferentially localized on Ti^{α}_{S0} and Ti^{β}_{S0} sites. This configuration (without polarons on the reconstructed Ti_{rec} row) is the most energetically favorable (details in Sec. 4.3). The corresponding electronic charge density is shown in Fig. 4.3(c). The DFT polaron positions closely resemble the positions deduced by the experimental filled-state STM images on the non-buckled Ti_2O_3 stripes [compare Fig. 4.3(c) with the experimental STM in Fig. 4.3(a)]. However, the direct comparison between experimental and simulated filled-state STM image is unsatisfying [compare Fig. 4.3(a) and 4.3(b)]: In the calculations, the polaronic states typically hybridizes with the atoms of the reconstructed rows [see Fig. 4.3(d)], thus,

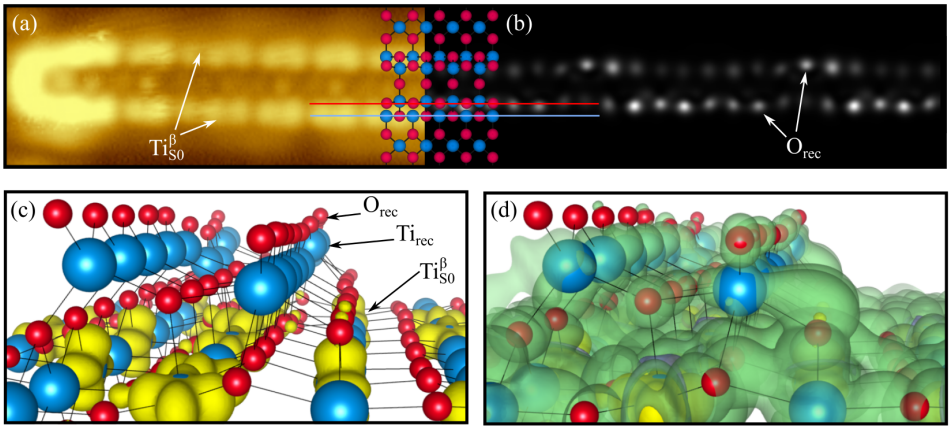

Figure 4.3: In-gap states on the Ti_2O_3 stripes. Panel (a): Experimental filled-state STM image for a non-buckled Ti_2O_3 row (almost symmetric in AFM). Panel (b): Simulated filled-state STM image corresponding to the lowest energy configuration from the FPMD run. The top-view of the Ti_2O_3 model in the inset in panel (a) and (b) compares the positions of the bright spots in the experimental and calculated STM images. Panel (c): Detail of the corresponding charge density isosurfaces in Ti_2O_3, showing that polarons are localized at the $S0$ layer level. Panel (d): Same as panel (c), but for a lower isosurface density. *Figure adapted from Physical Review X, Supplemental Material ©2017 American Physical Society* [4].

the calculated filled-state STM images show bright spot above the top-layer atoms. Conversely, filled-state STM experiments show bright signals above the $Ti^{\alpha,\beta}_{S0}$ atoms. This misalignment between simulations and experiments could be due to the limitation of the Tersoff-Hamann approach, which neglects the tip-sample interaction.

Interestingly, the polarons occasionally hop to the Ti_{rec} sites. In fact, on average 6% of the total polaronic charge is located on these sites during the FPMD run (which corresponds to one electron among the eighteen excess electrons introduced by the stoichiometry deviation of the Ti_2O_3 rows in the 9×2 slab used for the FPMD), as shown in Fig. 3.12. The presence of polarons on the Ti_2O_3 rows results in a strong buckling. Figure 4.4(a) shows the in-gap charge density for the buckled Ti_2O_3 stripes, with polarons trapped on Ti_{rec} sites. The corresponding in-gap STM image is shown in Fig. 4.4(b): the brightest and broadest spots are related to the polarons on the Ti_{rec} sites, while, the remaining visible charge comes from the hybridization between polarons on $S0$ and O_{rec} atoms (similar hybridization as for the non-buckled stripes). The calculated STM images for the polaronic buckled stripes closely resemble the experimental results [compare Fig. 4.4(b) and 4.4(c)].

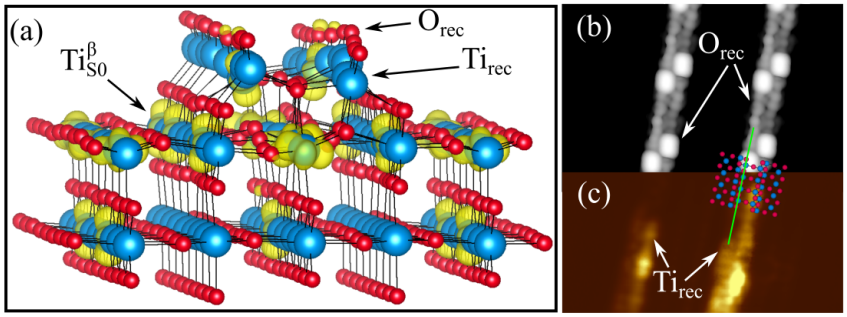

Figure 4.4: Polaron trapping at Ti_{rec} sites. Panel (a): Isosurface charge density for the Ti_2O_3 stripe, hosting polarons also at Ti_{rec} sites. Panel (b): Simulated filled-sate STM image for the same structure as in panel (a). Panel (c): Experimental filled-state STM image. The top-view model facilitates the comparison between the simulated and experimental STM images. *Figure adapted from Physical Review X, Supplemental Material ©2017 American Physical Society* [4].

4.3 Surface thermodynamic stability

In the (1×1) phase, the surface free energy ΔG (defined in Eq: 2.9) strongly depends on the reduction level of the TiO_2(110) surface. The thermodynamic stability of the surface was studied as a function of the c_{V_O} level by constructing 9×2 and 6×2 large, 5 tri-layer deep slabs.

[4.3.1] The V_O distribution

The vacancies were homogeneously distributed on the surface, to mimic the experimental situation, as explained and justified in the following. The oxygen vacancies are nominally positively charged, and exhibit a mutual repulsive interaction on TiO_2(110) [189]. This repulsion can be analyzed via both theoretical and experimental approaches. Figure 4.5(a) shows the contribution of the V_O distribution to the total energy of the slab as obtained by non-spin-polarized DFT+U calculations (precluding polaron formation). Two oxygen vacancies were included on the 9×2 surface (corresponding to c_{V_O}= 11.1%), varying the V_O-V_O distance. The calculated total energies are compared with the autocorrelation function [Fig. 4.5(c)] extracted from the experimental empty-state STM image [Fig. 4.5(b)]. Both, theoretical and experimental data indicate a strong repulsion between the oxygen vacancies along the [001] direction, and a significantly weaker repulsion along the $[1\bar{1}0]$ direction. Specifically, the experimental images suggest that the two oxygen vacancies hardly form at nearest and next-nearest O_{2c} sites along a [001] row; these V_O distributions are indeed characterized by highly unfavorable energies (≈ 800 meV larger than the reference case). In the perpendicular $[1\bar{1}0]$ direction there is a visible repulsion only for the first nearest neighbor positions. As a result, the experimental AFM

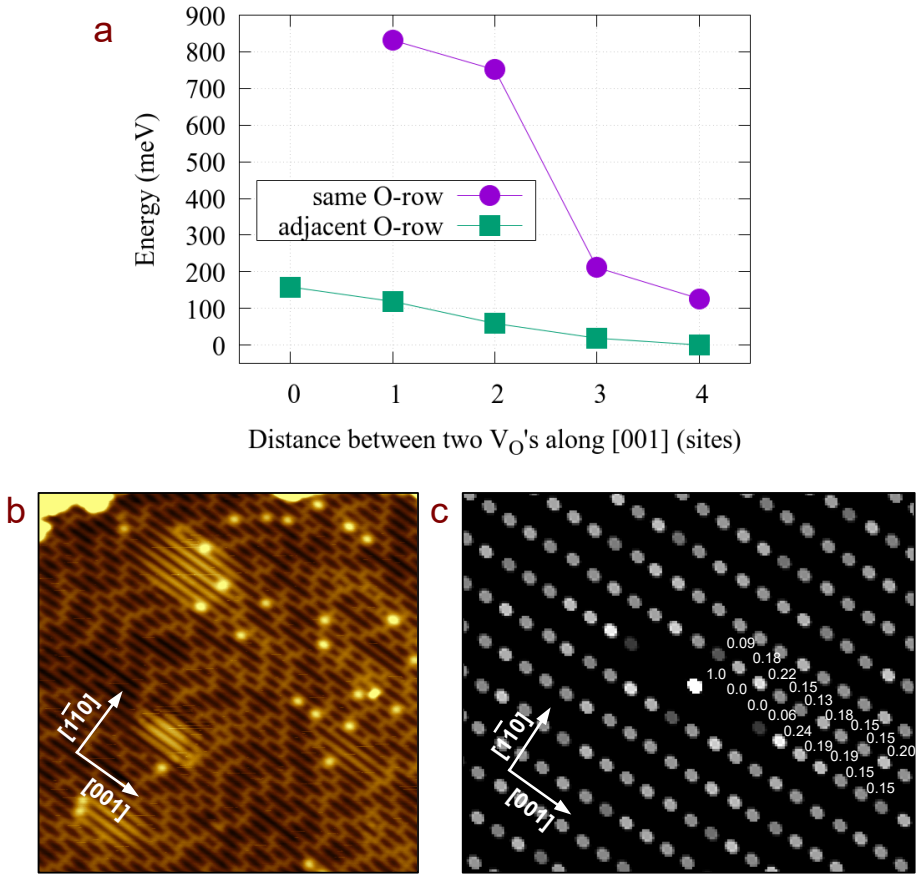

Figure 4.5: Oxygen vacancy distribution. Panel (a): Calculated total energy of the 9×2 slab with two surface oxygen vacancies ($c_{V_O} = 11.1\%$). The oxygen vacancies are placed at different sites in the same or in adjacent O_{2c} rows. To avoid the additional complication of V_O-polaron interactions, polaron formation is here inhibited by performing non spin-polarized calculations. Panel (b): Experimental empty-state STM image of a surface with approximatively 15% V_O, used for calculating the V_O autocorrelation function. A few bright V_O-free areas are attributed to subsurface argon bubbles left over from sputtering. Panel (c): Experimental autocorrelation function of the V_O positions. The numbers denote values of the autocorrelation for selected points. *Figure adapted from Physical Review X, Supplemental Material ©2017 American Physical Society* [4].

and STM images acquired on the reduced (1×1) phase show a clear tendency towards a homogeneous distribution of the oxygen vacancies.

Consistently, in order to study the stability of TiO_2(110), the oxygen vacancies were placed homogeneously on the surface. Clearly, using energetically

unfavorable (*i.e.*, inhomogeneous) V_O distributions would fictitiously change the thermodynamic stability of the surface, and alter the overall thermodynamic phase diagram. The lateral dimensions of 9×2 surface unit cells used to perform the simulations, are compatible with the optimal arrangement for the oxygen vacancies at any relevant concentration here investigated, except c_{V_O}= 16.7%. In this latter case, the homogeneous distribution of oxygen vacancies is achieved by constructing a 6×2 slab with two oxygen vacancies (one V_O per O_{2c} row).

[4.3.2] Polaronic configurations

The configurations assumed by the polarons play a crucial role for the surface stability. In the (1×1) structure, the V_O-induced excess electrons form polarons preferentially located on the subsurface Ti^A_{S1} atoms (as described in Chapter 3). These can easily hop to surface sites when thermally activated [46, 48, 127, 147, 190, 191], while a polaron trapping deeper in the bulk is energetically significantly less favorable, as well as delocalized electrons [27]. The hopping was simulated by FPMD calculations (discussed in detail in Sec. 3.6), at various polaron densities, by constructing 9×2 slabs with an increasing amount of homogeneously distributed oxygen vacancies (c_{V_O} ranging from 5.6% up to 50.0%). At the smallest concentration, c_{V_O}= 5.6%, the polarons are located on the $S1$ layer 95% of the time, and undergo inter- and intra-Ti^A_{S1} row hopping [histogram bar of Fig. 4.6(a)]. Hopping towards surface sites is very rare, with polarons being trapped on $S0$ for 5% of the time only. By increasing c_{V_O} [histogram bars of Figs. 4.6(b-d)], *i.e.*, by increasing the amount of excess electrons, hopping towards $S0$ sites becomes more likely.

The configurations obtained by FPMD were further analyzed to determine the most stable structure at low temperature: Each polaronic FPMD configuration was relaxed at the DFT+U level, according to the methodology detailed in Sec. 2.1.6. Figure 4.6 shows the charge density isosurfaces of polarons, as obtained for the energetically most favorable configuration for each c_{V_O}. The stable configurations at relatively low V_O concentration ($c_{V_O} \leqslant$ 16.7%) are characterized by polarons trapped only on $S1$ sites [Figs. 4.6(a-c)]. At higher concentrations ($c_{V_O} \geqslant$ 22.2%), it is energetically more favorable to host polarons also on $S0$ sites rather than increasing their density in the $S1$ layer [Fig. 4.6(d)], in agreement with the energetic analysis of the polaronic interactions illustrated in Chapter 3. Interestingly, the calculated c_{V_O}= 16.7% maximum value for polaron formation exclusively on the $S1$ layer coincides with the experimental critical V_O concentration at which the (1×1) and (1×2) phases coexist. Therefore, the (1×1)-to-(1×2) transition seems to be related to the limited capacity of the subsurface layer to accommodate large amounts of polarons.

The polaron-polaron electrostatic repulsion is the mechanism pushing po-

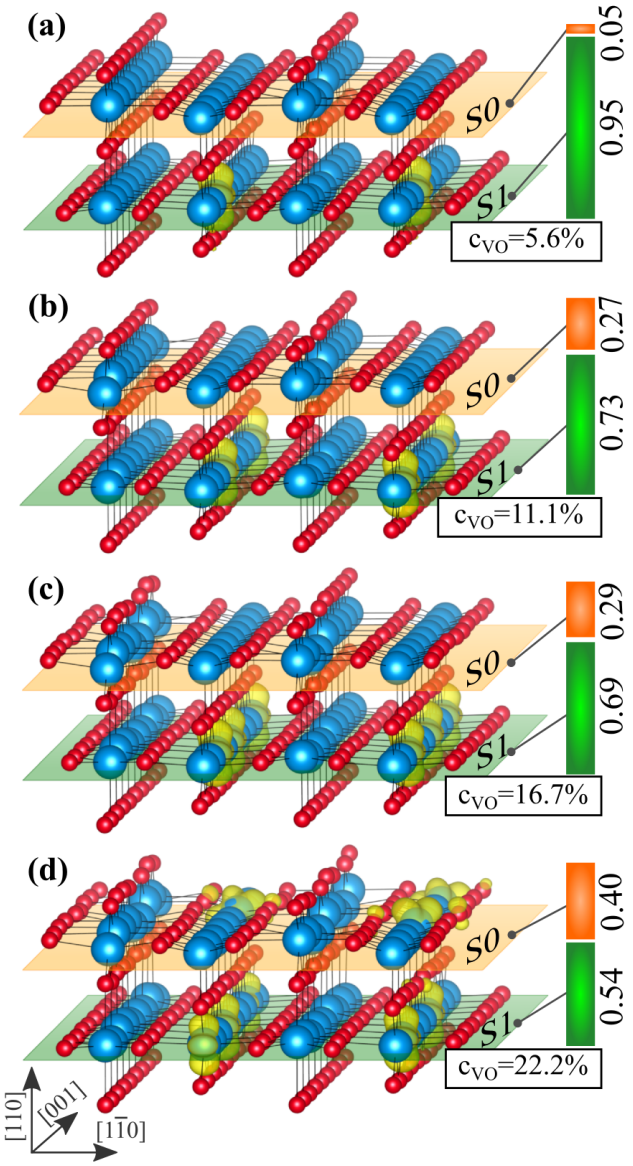

Figure 4.6: Polaron distribution in the (1×1) TiO_2(110). (a-d), Most stable polaron configurations obtained by FPMD and subsequent relaxations. 9×2 large slabs with various V_O concentrations (specified in each panel) were used. The histograms illustrate how often the polarons are found on $S0$ (orange) and $S1$ (green) Ti sites during the FPMD runs. *Figure adapted from Physical Review X ©2017 American Physical Society* [4].

larons towards the $S0$ layer. As reported in Sec. 3.6, the probability of finding

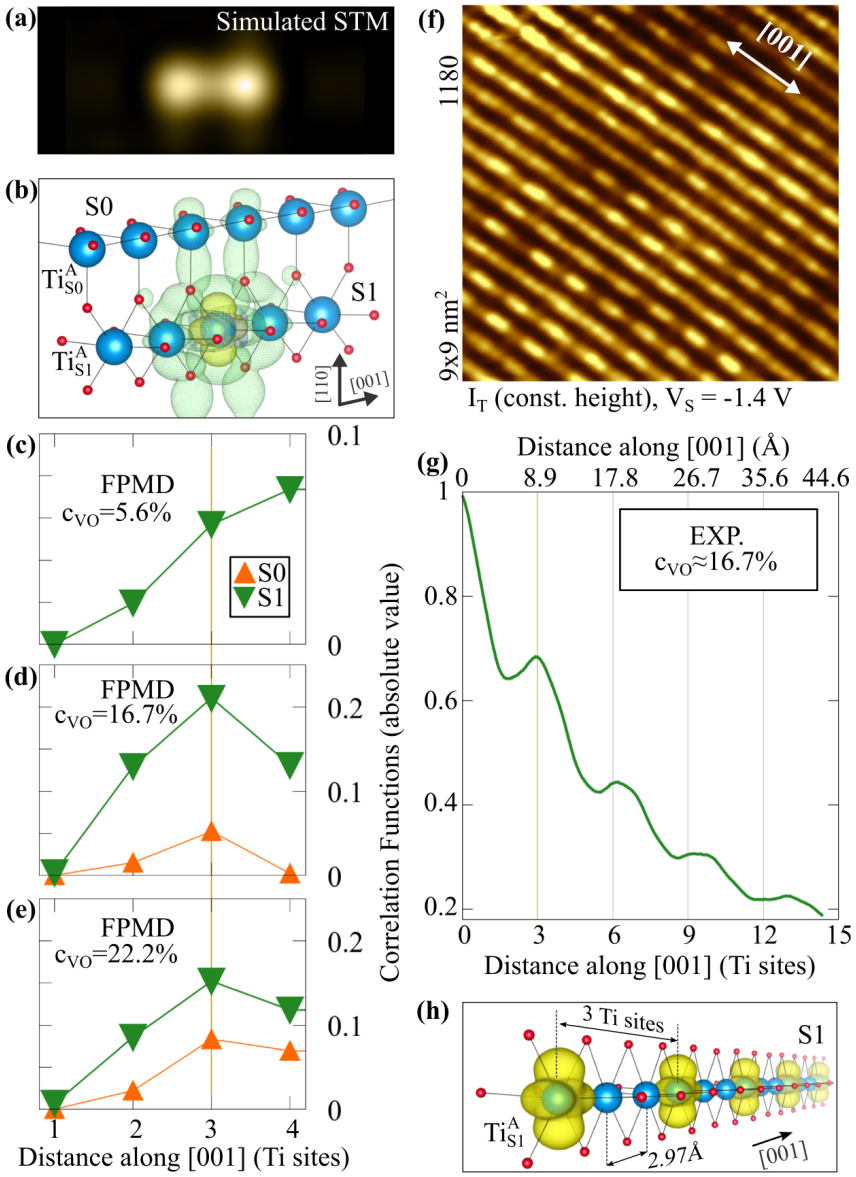

Figure 4.7: Polaron distribution along the Ti^A_{S1} row. Panel (a): Simulated filled-states STM of an isolated polaron around a Ti^A_{S1} site. Panel (b): The corresponding charge density isosurface shows the high-density d_{z^2}-like orbital localized at Ti^A_{S1} (yellow) and the large, low-density cloud extending across the nearby Ti^A_{S1} and Ti^A_{S0} sites. Panels (c-e): Calculated polaron-polaron autocorrelation functions along Ti^A_{S1} and Ti^A_{S0} rows extracted from FPMD runs at c_{V_O}= 5.6%,16.7%,and 22.2%. Panels (f,g): Experimental filled-state STM image at c_{V_O}= 16.7% (f) and corresponding polaron-polaron autocorrelation function along the [001]-rows (g). Panel (h): Sketch of the 3×1 periodicity on the Ti^A_{S1} row. *Figure adapted from Physical Review X ©2017 American Physical Society* [4].

two polarons at adjacent Ti^{A}_{S1} sites in the FPMD runs is very low at any c_{V_O}. Figure 4.7(c-e) summarizes the results for the polaron-polaron autocorrelation functions along the Ti^{A}_{S1} rows. The highest probability is found for values that maximize the distance between polarons in the row, corresponding to 3 or 4 lattice constants apart, depending on the c_{V_O} level [Fig. 4.7(c-e)]. This result is in excellent agreement with the experiment, in particular at c_{V_O}= 16.7% where a clear 3×1 periodicity is observed in the autocorrelation analysis of filled-states STM images [Fig. 4.7(g)]. At larger V_O concentration ($c_{V_O} \geqslant$ 22.2%), the peak of the calculated correlation function is not shifted to smaller distances, notwithstanding the increased amount of polarons in the system: Instead, the 3×1 pattern in $S1$ is preserved [Fig. 4.7(e)] and polarons populate the $S0$ layer more often [histogram bar of Fig. 4.6(d)]. The robustness of the 3×1 pattern is explained by the spreading of the Ti^{A}_{S1} polaron charge density. While most of the polaron charge has d_{z^2} symmetry [see inner yellow isosurface in Fig. 4.7(b)], a non negligible amount of charge spreads across the surrounding Ti^{A}_{S0} and Ti^{A}_{S1} atoms [see external isosurface in Fig. 4.7(b)]. This extended cloud gives rise to the characteristic double lobes [Fig. 4.7(a)] observed in STM experiment [Fig. 4.7(f)]. The 3×1 periodicity of polarons along the Ti^{A}_{S1} row [sketched in Fig. 4.7(h)] avoids the overlap of two adjacent extended repulsive polaron clouds [Fig. 4.7(b)], thereby reducing the polaron-polaron repulsion (see the analysis in Sec. 3.8) [125]. In the FPMD runs at higher V_O concentrations, polarons are pushed towards $S0$ sites in order to preserve the optimal pattern on the $S1$ layer. It has to be noticed that the polaron-polaron repulsion is perturbed by the attracting interaction between polarons and the V_O centers [26, 192], which modifies the optimum patterns.

[4.3.3] Polaron driven transition

The polaron hopping towards the $S0$ layer results into an energetic instability. In fact, as discussed in detail in Chapter 3, Ti^{A}_{S0} polarons are energetically less favorable than Ti^{A}_{S1} polarons. Conversely, the Ti_2O_3 reconstructed surface is able to accommodate a larger amount of excess electrons (corresponding to a reduction level of 50%), with a sensible energy gain. Therefore, the instability is overtaken by the structural (1×1) to (1×2) reconstruction, rather than a migration of the excess electrons to the bulk as recently suggested in literature [125]. Figure 4.8 summarizes the evolution of the TiO_2(110) surface energy as the reduction level is increased. The phase diagram in Fig. 4.8(b) was obtained by considering the surface free energy ΔG for the most stable polaronic configuration for the (1×1) phase at each c_{V_O} and for the Ti_2O_3 reconstruction. By increasing the reduction level of the system, the Ti_2O_3 reconstruction becomes the most stable structure above the critical V_O concentration of 22.2%. This value is slightly larger than the critical concentration measured experimentally (16.7%); this deviation could be attributable to effects not included

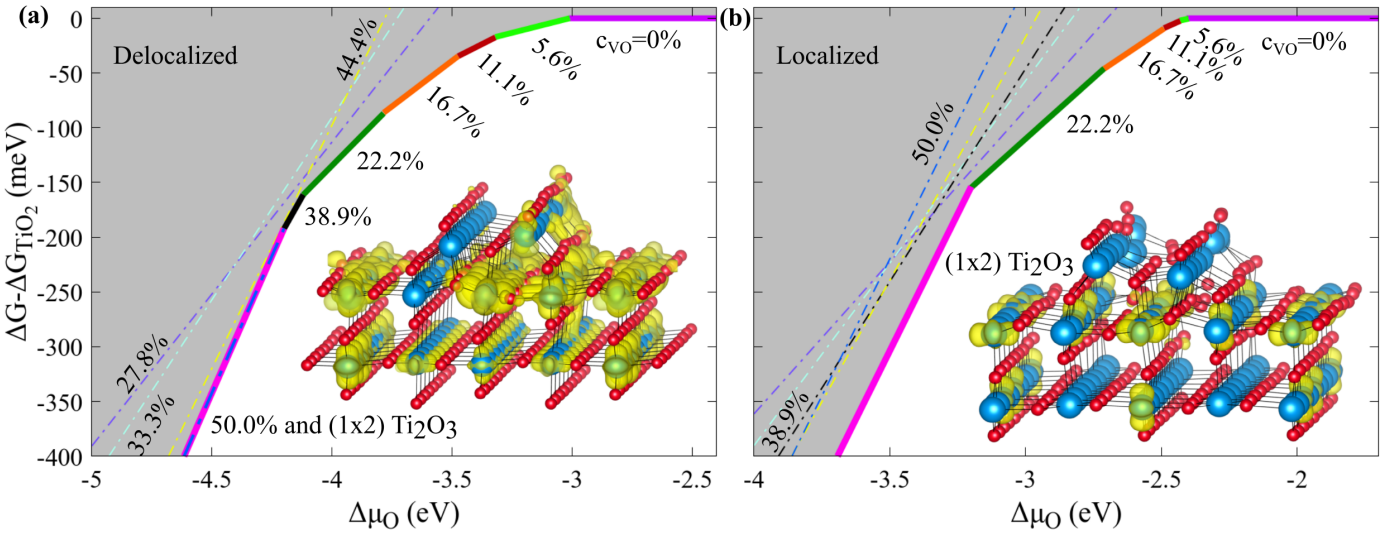

Figure 4.8: TiO_2(110) surface phase diagram. Surface free energy (ΔG) for the most stable configurations obtained from the FPMD for the reduced (1×1) structures at different V_O concentrations (all lines except magenta) and for the (1×2) Ti_2O_3 reconstruction (magenta line) as a function of the chemical potential $\Delta\mu_O$ with respect to the stoichiometric (1×1) phase. All the calculations were performed in 9×2 large, 5 tri-layer deep slabs, except the $c_{V_O} = 16.7\%$ modeled by a 6×2 slab with a selective control of the polaron formation. Panel (a): Delocalized solution (excess electrons are spread across all lattice sites and delocalized at the bottom of the conduction band). At $c_{V_O} = 50.0\%$ the (1×1) structure is degenerate with the (1×2) Ti_2O_3 reconstruction (Ti_2O_4 with 50% of V_O). Panel (b): Localized solution (the excess electrons are trapped in distinct Ti sites, mostly located in $S0$). The insets show the distribution of excess electrons in the (1×2) structure. *Figure adapted from Physical Review X ©2017 American Physical Society* [4].

in the calculations, such as the presence of additional dopants (e.g., interstitial Ti [142]), the contribution of different V_O distributions, and the specific type of approximation (DFT+U) chosen to treat the localization effect [143] (see also discussion in Appendix A.3).

The polarons play a crucial role in the determination of the surface stability. In fact, calculations are able to simulate the (1×1) to (1×2) transition only if the polaron states are included in the slab [126]. The phase diagram in Fig. 4.8(a) was obtained by considering the surface free energy for the unrealistic case of excess electrons delocalized in the conduction band. The delocalized calculations predict that the reduced (1×1) phase remains the most

stable structure even at high V_O concentrations: The Ti_2O_3 reconstruction with delocalized electrons [shown in the inset in Fig. 4.8(a)] is just as stable as the (1×1) at c_{V_O}= 50.0%.

4.4 Details of the polaronic contributions to the surface stability

To understand the polaron-mediated change of the surface stability, it is instructive to analyze the trend of the energy gained upon polaron formation, that is described by E_{POL}. Figure 4.9(a) shows E_{POL} for the most stable configuration at each considered c_{V_O}. For low concentrations, up to $c_{V_O} \simeq$ 20% in the (1×1) phase, E_{POL} decreases with increasing concentration (it becomes more favorable to form polarons in the system). For $c_{V_O} >$ 22.2%, E_{POL} remains initially constant, and ultimately increases. Figure 4.9(a) also includes the polaron energy for the reconstructed Ti_2O_3 surface. It has the largest negative value of all the configurations considered, and the resulting convex hull shows that the reduced (1×1) phases are unstable for $c_{V_O} >$ 22.2%. The surface undergoes a structural reconstruction above this critical value.

The trend of E_{POL} as a function of c_{V_O} becomes clear if one considers the energy cost that is required to locally distort the lattice in order to accommodate an electron and the energy gained by localizing an electron in such a lattice. Figure 4.9(b) reports this strain energy E_{ST} for the most stable configuration at each considered c_{V_O}. E_{ST} decreases with increasing c_{V_O}, but shows a distinct discontinuity at the critical c_{V_O}= 22.2% (ΔE_{ST}=E_{ST}(22.2%)−E_{ST}(16.7%) = 65 meV). The isosurfaces plotted in Figure 4.6 are helpful to understand this trend. At low concentrations, up to c_{V_O}= 16.7%, the polarons reside preferentially along the Ti^A_{S1} [001] row. Once the lattice in the $S1$ layer is distorted, it is progressively easier to form more polarons. The $S0$ layer is kept essentially unperturbed. At c_{V_O}= 22.2%, however, the polarons start to populate also the $S0$ layer: The breaking of the symmetry of the top layer results in a large energy cost (as analyzed in Sec. 3.2). As pointed out in Sec. 4.3, hopping towards $S0$ sites happens in order to preserve the optimum 3×1 pattern on $S1$ (reached at c_{V_O}= 16.7%), since a larger polaron density in $S1$ would result in the overlap of the polaronic cloud, and in a strong Coulomb repulsion (see also Sec. 3.5). While hosting polarons on both the $S1$ and $S0$ layers reduces the charge overlap, it simultaneously requires a distortion of the lattice around both the Ti^A_{S1} and Ti^A_{S0} sites. Apparently a structural switch to a local (1×2) structure happens instead. The Ti_2O_3 reconstruction exhibits a high degree of structural flexibility, expressed in terms of a low energy cost E_{ST} [Fig. 4.9(b)]

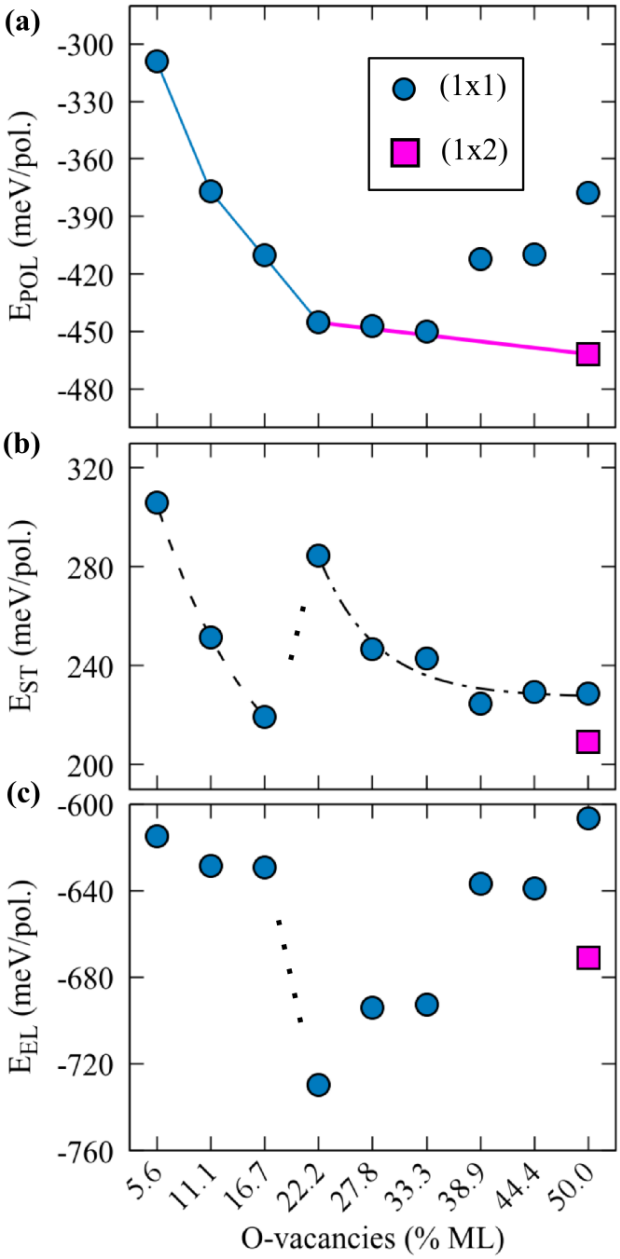

Figure 4.9: Polaron energies (meV/polaron) as a function of c_{V_O}. Polaron formation energy E_{POL} (a), strain energy cost E_{ST} (b) and electronic energy gain E_{EL} (c) for the (1×1) (circles) and (1×2) (squares) phases. *Figure adapted from Physical Review X ©2017 American Physical Society* [4].

needed to accommodate a large concentration of polarons (as large as in the (1×1) c_{V_O}= 50% case).

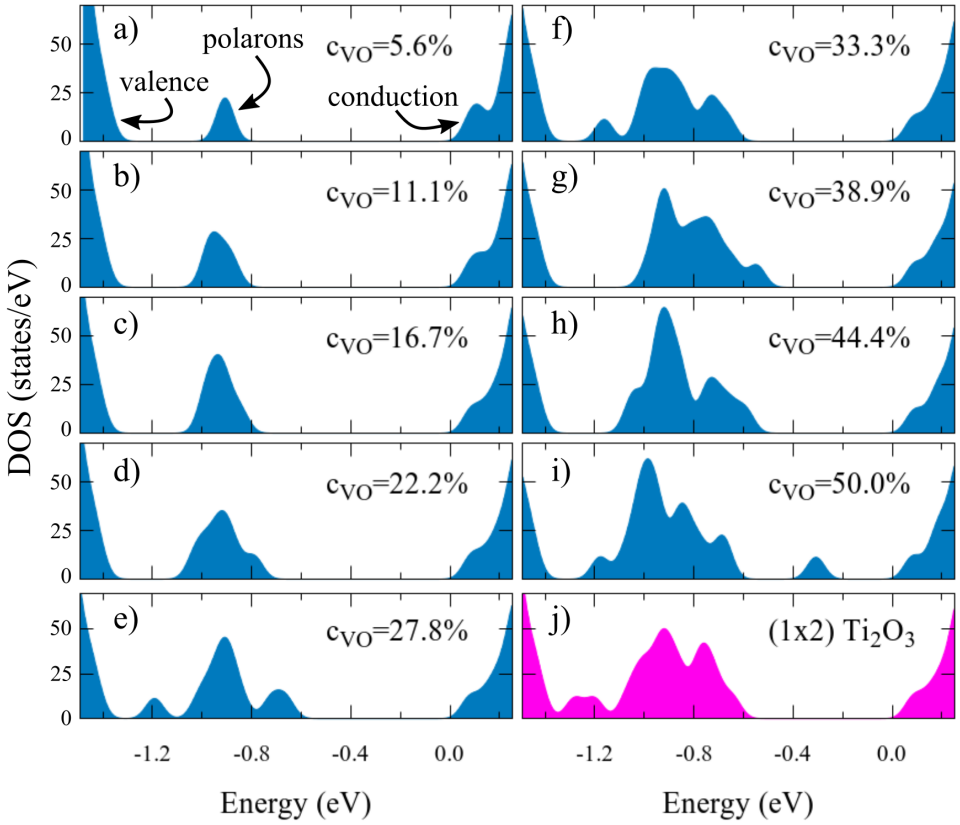

Figure 4.10: The polaron state as a function of c_{V_O}. Calculated electronic density of states showing the top of the valence band, the polaronic peak and the bottom of the conduction band, in the reduced (1×1) surfaces, at various V_O concentrations (a-i), and in the (1×2) phase (j). *Figure adapted from Physical Review X, Supplemental Material ©2017 American Physical Society* [4].

Finally, Figure 4.9(c) shows the evolution of E_{EL} as a function of $c_{V_{\mathrm{O}}}$. E_{EL} is overall about twice as larger as E_{ST} and leads to a large polaron formation energy at any V_{O} concentration. The trend of E_{EL} correlates with the $c_{V_{\mathrm{O}}}$-dependent change in the polaron DOS [Fig. 4.1(d,e) and Fig. 4.10]. The energy value and broadening of the polaronic in-gap state depends on the position of the polarons in the crystal, and on the polaron-polaron and polaron-vacancy interactions, as detailed in Sec. 3.3 and Sec. 3.5. At low $c_{V_{\mathrm{O}}}$ the polarons form a well localized peak below the Fermi energy [Fig. 4.1(d) and Fig. 4.10(a-c)], corresponding to $E_{\mathrm{EL}} \simeq -620$ meV [Fig. 4.9(c)]. At $c_{V_{\mathrm{O}}} = 22.2\%$, E_{EL} jumps downwards by approximatively 100 meV, and the polaronic peak broadens significantly [Fig. 4.10(d)]. For larger $c_{V_{\mathrm{O}}}$, the peak exhibits a progressive broadening towards higher energies, accompanied by a progressively weaker E_{EL} [Fig. 4.10(e-i)].

The combined action of both the low strain cost E_{ST} and the favorable electronic localization energy E_{EL} determines the thermodynamic stability of the (1×2) phase, which overtakes the electrostatic instability brought about by the trapped charges on the (1×1) surface. The $\mathrm{Ti}_{S0}^{\alpha,\beta}$ sites on the reconstructed Ti_2O_3 surface are easily reducible and can conveniently host polarons [see the advantageous formation energy E_{POL} in Fig. 4.9(a)]. The (1×2) phase is more stable than the highly reduced ($c_{V_{\mathrm{O}}} = 50\%$) (1×1) surface, by about $\Delta E_{\mathrm{POL}} =$ 84 meV. This energy gain arises predominantly from the difference in E_{EL} between the two phases ($\Delta E_{\mathrm{EL}} = 64$ meV, while $\Delta E_{\mathrm{ST}} = 20$ meV).

4.5 Outline of the polaron driven reconstruction

In conclusion, polarons play a fundamental role for the stability of rutile surfaces. At low reducing conditions, polarons trap in the sub-surface sites of the (1×1) TiO_2 surface, with the optimal polaron-polaron distance being 3 lattice sites. As the polaron density increases, polarons are pushed to the less favorable Ti surface sites as well. This, however, costs energy, so that ultimately a transition to a strongly reduced (1×2) reconstruction occurs. If one neglects the formation of polaron in the description of the process, the reconstructed phase would turn to be unstable.

The results reported here for the rutile TiO_2 (1×1) to (1×2) transition could present a new paradigm for surface reconstructions that involve trapped charges and the interaction among them. Polaron formation is ubiquitous in transition-metal oxides and is typically propelled by oxygen vacancies and doping [147]. Possible examples of other materials in which polaron-mediated re-

constructions could be operational are oxide perovskites, in particular $SrTiO_3$ [126, 174, 193], as well as popular oxides like ceria [194–196] and hafnia [82]. Therefore, this polaron-mediated mechanism is likely to be a pervasive phenomenon that could explain structural, electronic and magnetic reconstructions at surfaces and interfaces [197] and could be employed to tune surface properties and to control the surface geometry. For instance, it is known that Nb-doping, V-doped or Cr-doped TiO_2 samples form the (1×2) reconstruction much easier, even when the surrounding (1×1) phase has much lower V_O concentrations [198–200]. Finally, the control of charge trapping could provide a way to optimize the functionality of TiO_2-based memristors [201] and to facilitate charge transfer in catalytic processes [202] (see also the discussion in Chapter 5).

Chapter 5

Adsorbates and polarons: CO on TiO_2(110)

On weakly reduced TiO_2(110) surfaces, polarons lie preferentially on the sub-surface layer. Due to the vicinity to the surface, polarons strongly interact with adsorbates, as explored within this doctorate project for the CO adsorption, by first-principles modeling, with the support of surface sensitive experiments [2]. CO adsorbates are indeed able to alter the polaron stability, destabilizing the typical polaronic ground-state configuration, and forcing the polarons to localize on surface sites. In turn, polarons affect the energetics and the geometry of the adsorption process.

Contents

5.1 The effects of adsorbates on polarons

The ground state of weakly reduced rutile TiO_2(110) surfaces exhibits polarons lying on the sub-surface layer $S1$, in proximity of the oxygen vacancies (see discussions in Chapter 3 and Sec. 4.3). Due to the vicinity to the surface, one could expect polarons to interact with adsorbates on the surface [177, 203–206]. Despite this obvious consideration, the interaction between polarons and adsorbates has been amply neglected in literature. This has led to contrasting physical interpretations: One prototypical example is given by the CO adsorption on TiO_2(110). In fact, beyond a generic consensus on the local geometric properties (CO molecules adsorbs vertically at low coverage) [12, 207, 208], conflicting outcomes have been reported which either suggest [209] or exclude [81, 210, 211] the possibility of CO adsorption at V_O sites, in the latter case endorsing a major role played by the fivefold-coordinated Ti^A_{S0} sites. These apparent disagreements can be solved by taking into account the interplay between adsorbates and polarons.

[5.1.1] The NNN-Ti^A_{S0} site

This section focuses on the effects of the CO adsorbate on the polaronic states. The discussion illustrates initially CO adsorption on the five-fold coordinated Ti^A_{S0} atom, one lattice site distant from the V_O along [001] (NNN-Ti^A_{S0}). This is a convenient choice for many reasons: First, NNN-Ti^A_{S0} is considered to be a favorable site for CO adsorption, as reported by many experiments [209, 210]. Second, on clean TiO_2(110) surfaces (*i.e.*, surfaces without adsorbates), the NNN-Ti^A_{S0} atom represents the most favorable site for polaron formation on the $S0$ layer. Finally, it lies right above the most stable $S1$ polarons (Ti^A_{S1} polarons in proximity of the V_O, which define the ground-state polaronic configuration). Therefore, it is a reasonable choice to select the NNN-Ti^A_{S0} atom as the adsorption site for the investigation of the effects of CO on polarons. Nevertheless, other geometries are also tested and presented in the following.

Figure 5.1 reports the results obtained by modeling the system at low c_{V_O}= 5.6% (a 9×2-large slab with one oxygen vacancy). A polaron is selectively localized either on the $S1$ layer in proximity of the V_O (CO+$S1$-polaron complex) or at the NNN-Ti^A_{S0} site (CO+$S0$-polaron complex). The spatial extension of the $S1$ and the $S0$ polaron electronic charge is shown in Fig. 5.1(a) and 5.1(b), respectively. The $S1$ polaron retains its characteristic spatial distribution as in the absence of adsorbates [143], with a d_{z^2}-$d_{x^2-y^2}$-like orbital character at the hosting Ti^A_{S1} site, and about one third of the charge distributed on the surrounding atoms [compare Fig. 5.1(a) with Fig. 3.2(c,d)]. The CO does not substantially alter this situation, and only a very small amount (0.1%) of the polaronic charge is transfered to the CO molecule. Conversely, the po-

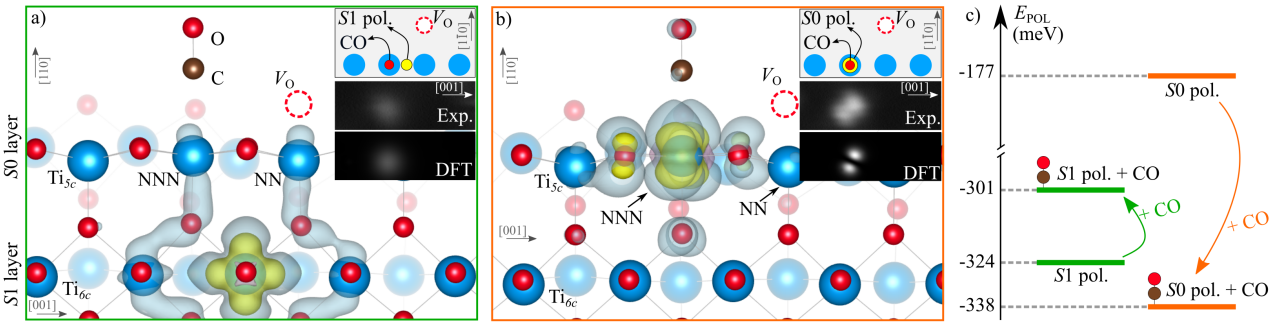

Figure 5.1: Effects of a CO molecule on polaronic states. The CO is modeled to adsorb on the NNN-Ti^A_{S0}, on a weakly reduced surface (c_{V_O} = 5.6%, *i.e.*, one V_O on a 9×2-large slab). Panels (a,b): Electronic charge density of the $S1$ (a) and $S0$ (b) polarons in the presence of CO. Atoms at the back are depicted by faded spheres. The insets sketch a top view of the considered geometry and report the experimental and simulated STM images. Panel (c): Polaron formation energy of $S0$ and $S1$ polarons, both in the absence and presence of a CO molecule on the NNN-Ti^A_{S0} site. *Figure adapted from Physical Review Letters ©2018 American Physical Society* [2].

laron at the NNN-Ti^A_{S0} site is strongly affected by the CO molecule [Fig. 5.1(b)]. The NNN-Ti^A_{S0} polaron acquires a stronger d_{yz} character (54%) as compared to the case with no adsorbates (43%), and a non negligible portion of the polaronic charge (1%) is transfered to the $2\pi^*$ antibonding orbital of the adsorbed CO [212, 213].

[5.1.2] The double lobed STM spots

The charge transfer to the $2\pi^*$ orbitals causes the formation of a double-lobed polaronic cloud above the CO molecule, detected as a double-lobed signal in the simulated and experimental filled-state STM images [see inset in Fig. 5.1(b)]. Interestingly, if the CO+$S0$-polaron complex at the NNN-Ti^A_{S0} site is modeled in the $d_{x^2-y^2}$ $S0$-polaron flavor (energetically less favorable, see Table 3.3), then the simulated STM signal would result in a single bright spot (not shown), contradicting the experimental evidence. Remarkably, the double-lobed spot above the CO+$S0$-polaron complex at the NNN-Ti^A_{S0} site is tilted with respect to the [001] direction, while the dimerlike $S1$ STM signal on the clean surface lies along [001] [see inset in Fig. 3.2(d)]. The experimental investigations can benefit from this different orientation of the filled-state STM signals, since it allows to distinguish between CO+$S0$-polaron complexes and $S1$ polarons.

The effects of CO on the $S0$ polarons was studied also by considering different geometries: The CO adsorption was modeled at other available Ti^A_{S0} sites, in combination with the formation of an $S0$ polaron at the same Ti^A_{S0}

site. Likewise the NNN-Ti^{A}_{S0} case, for Ti^{A}_{S0} sites at larger distance from V_O, the polaronic charge is partially transferred to the CO orbitals, giving rise to similar bright double-lobed spots in the filled-state STM simulations. On the other hand, when the CO+$S0$-polaron complex is modeled at the NN-Ti^{A}_{S0} site, then the double-lobed spot is oriented perpendicularly to [001], *i.e.*, along $[1\bar{1}0]$ (shown in Fig. C.8). This rotation is due to the different symmetry of the polaronic charge density at the NN-Ti^{A}_{S0} (a fully d_{yz} orbital character, 67% of the total charge), a distinctive feature for the NN-Ti^{A}_{S0}-polaron also on the clean surface (described in Sec. 3.4).

The characteristic double lobes would in principle make the CO+$S0$-polaron complexes at any Ti^{A}_{S0} site well detectable by filled-state STM experiments. However, the double-lobed spot is experimentally observed only above the NNN-Ti^{A}_{S0} site. This is in agreement with the energetic analysis (discussed below), which predicts a particularly convenient polaron formation energy only for the CO+$S0$-polaron complex at NNN-Ti^{A}_{S0}.

[5.1.3] The weak STM spots

The CO+$S1$-polaron is instead detected by filled-state STM experiments and simulations as a weak circular spot [see inset in Fig. 5.1(a)]. Figure 5.2 provides interesting insights on the polaron charge density for various adsorption geometries, complementing the data presented in Fig. 5.1(a). The weak spot in Fig. 5.1(a) originates from the extension of the polaronic charge density above the CO molecule as shown in the upper part of Fig. 5.2 (labeled as "CO at NNN"). A similar weak circular spot is also obtained for a CO molecule adsorbed in the proximity of an $S1$ polaron, rather than directly above the polaronic Ti^{A}_{S1} (see the charge density spreading over the CO molecule on the right side of Fig. 5.2). Conversely, the filled-state STM measurements on a clean TiO_2(110) surface detect the $S1$ polarons as dimerlike signals, oriented along the [001] direction [see the inset in Fig. 3.2(d)]. However, the $S1$ polaron charge density (labeled as "no CO" in Fig. 5.2) extends less towards the vacuum as compared to the spreading over the CO molecules, thereby impeding a precise detection by filled-state STM experiments on samples covered by CO.

Figure 5.3 shows an alternative origin for the weak circular spots imaged by filled-state STM. In fact, a weak signal is measured when an additional CO molecule is adsorbed on top of the Ti^{A}_{S0} site near the CO+$S0$-polaron complex. The CO+$S0$-polaron complex is well identified by the characteristic double-lobed signal, and an additional weaker circular spot appears one lattice site away: The $S0$ polaron charge density partly spreads over the additional CO molecule, consistent with the picture discussed for one single CO-molecule [see Fig. 5.2(b)]. This STM signal is similar and less intense as compared to the spot characteristic of the CO molecule adsorbed above an $S1$ polaron (shown in Fig. 5.3 for a direct comparison).

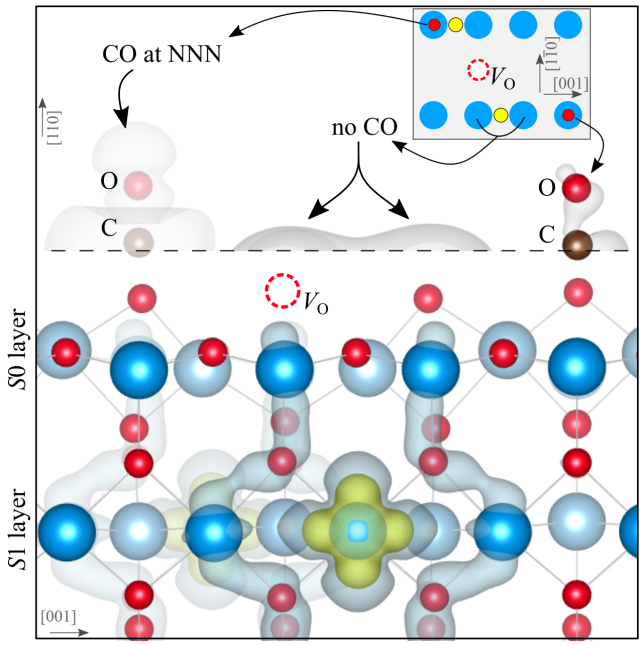

Figure 5.2: Detail of the $S1$-polaron-charge spatial extension. Two polarons are localized on Ti^A_{S1} sites in the proximity of the oxygen vacancy, as sketched in the inset (yellow and red circles represent polarons and CO molecules, respectively, and dashed circles indicate the position of the V_O); one CO molecule is adsorbed on the NNN-Ti^A_{S0} site (*i.e.*, above one $S1$ polaron), and a second CO molecule is adsorbed two lattice site away the V_O along [001]. The charge density of the two $S1$ polarons is shown for high (bottom part of the figure) and low (upper part) isosurface levels: Low isosurface levels are not included in the bottom part for a better readability of the image. Faded spheres represent atoms in the back (corresponding to the upper row in the inset). *Figure adapted from Phys. Rev. L, Supplemental Material ©2018 American Physical Society* [2].

[5.1.4] A new ground-state

The CO-polaron interaction affects strongly the polaron formation energy (E_{POL}), as shown in Fig. 5.1(c) for a CO on the NNN-Ti^A_{S0} site and a polaron in the proximity. While the formation energy of an $S1$ polaron is only marginally destabilized by the CO adsorbate ($\Delta E^{S1}_{POL} = +23$ meV), the formation of an $S0$ polaron becomes remarkably more favorable ($\Delta E^{S0}_{POL} = -161$ meV), due to a significant reduction of the structural energy cost E_{ST}. The variations in the E_{POL} energy are consistent with the shifts of the polaron state in the energy gap region (as evident from the density of states shown in Fig. C.9).

Figure 5.4 shows the effects of the CO adsorption on the polaron formation by considering different configurations. A CO molecule is adsorbing on the

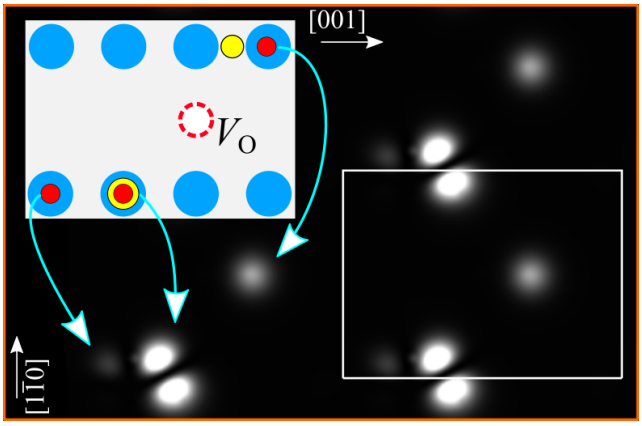

Figure 5.3: The CO+$S0$-polaron complex charge tail. STM simulation of three CO molecules, one adsorbing above an $S1$ polaron, a second one forming a CO+$S0$-polaron complex, and a third one adsorbing on a site adjacent to the $S0$ polaron. The inset sketches the geometry used (top view). The white rectangular line defines the unit cell used in the simulations. The symbols are used in the same way as in Fig. 5.2. *Figure adapted from Phys. Rev. L, Supplemental Material ©2018 American Physical Society* [2].

NNN-Ti^A_{S0} site [Fig. 5.4(a)] or on a Ti^A_{S0} four lattice-site distant from the V_O [Fig. 5.4(b)], and E_{POL} is shown as a function of the polaron localization site. As already mentioned above, the CO molecule adsorbed on the NNN-Ti^A_{S0} site favors the formation of an $S0$ polaron, which shows the strongest E_{POL}. Other Ti^A_{S0} sites are characterized by unfavorable E_{POL} values, even in combination with CO adsorption (not shown). The CO adsorption contrasts the formation of polarons in $S1$; the corresponding E_{POL} value gets reduced by about 20 meV (see differences between the two panels in Fig. 5.4), in agreement with the energy diagram in Fig. 5.1(c).

The attractive interaction between polarons and V_O facilitates the formation of $S1$ polaron at Ti^A_{S1} sites close to the oxygen vacancy, and compensates easily the weak polaron-CO repulsion. Therefore, the trend for the $S1$ polaron formation energy is qualitatively equivalent to the behavior observed for the clean surface (presented in Fig. 3.6). As far as only the $S1$ layer is considered, the CO molecule does not affect the distribution of the polarons; however, the formation of $S0$ polarons becomes largely more convenient due to the CO molecule. In fact, the formation of an $S0$ polaron coupled to a CO at a NNN-Ti^A_{S0} site results in the strongest E_{POL}. The adsorbate changes the polaronic ground state of the system, an effect that was overlooked in previous studies [159, 214]. The study of CO adsorption on rutile TiO_2(110) must consider

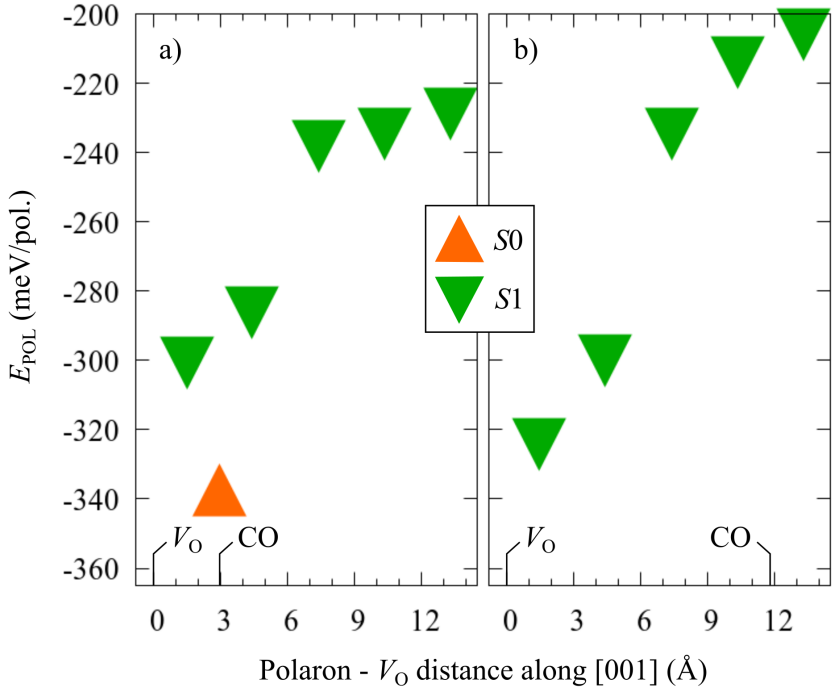

Figure 5.4: Polaron formation in various geometries. Calculations were performed by using a 9×2-large slab, including one V_O (c_{V_O}= 5.6%), with one excess electron (corresponding to a +1 charge state, *i.e.*, one electron removed from the system). A CO molecule is adsorbed either on the NNN-Ti^A_{S0} site (a) or on a Ti^A_{S0} four lattice-site away from the V_O along [001] (b). A polaron is localized on the $S1$ layer at various distances from the V_O (down pointing triangles), or on the NNN-Ti^A_{S0} site (up pointing triangle). *Figure adapted from Phys. Rev. L, Supplemental Material ©2018 American Physical Society* [2].

the change of stability of the polaronic configurations due to the presence of adsorbates.

[5.1.5] Polaron hopping

The presence of CO perturbs the dynamics of polarons. Figure 5.5 collects the results regarding the hopping process of an $S1$ polaron towards an adjacent Ti^A_{S1} site or towards the $S0$ layer. The calculations simulating the polaron hopping are performed according to the setup and procedure described in Chapter 2, at a low concentration of oxygen vacancy (c_{V_O}= 5.6%). In the absence of adsorbates, the $S1$-to-$S1$ polaron hopping is characterized by an energy barrier of 193 meV [Fig. 5.5(a)], much smaller than for the $S1$-to-$S0$ hopping (322 meV) [Fig. 5.5(b)]. Moreover, smaller ionic displacements occur for the $S1$-to-$S1$ hopping (1.2 Å), as compared to the $S1$-to-$S0$ hopping

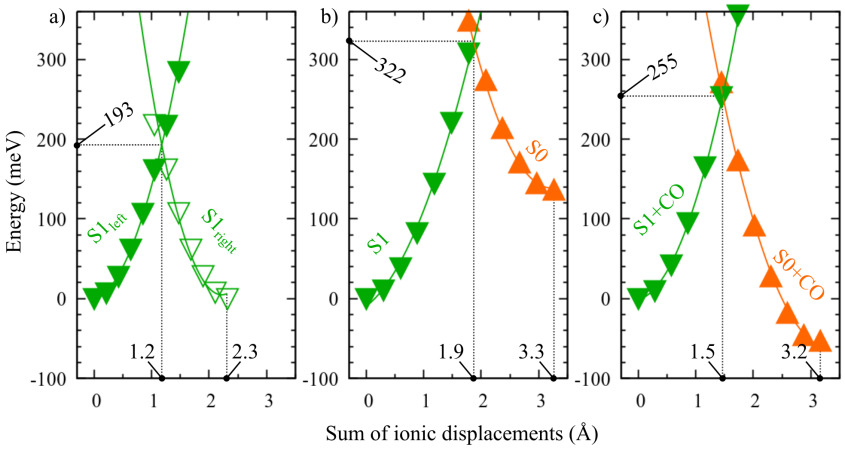

Figure 5.5: Effects of the adsorbates on the polaron hopping. Polaron hopping in the absence (a,b) and presence (c) of an adsorbed CO molecule. The electronic charge in the displaced structures maintains the electronic localization of either the initial or final state. The CO molecule is adsorbed on the NNN-Ti^{A}_{S0} site, and the $S1$ and $S0$ polarons are localized below the molecule (as in Fig. 5.1). The slab is modeled by using the experimental values of the lattice parameters at high temperature (see discussion in Appendix A.2). The $S1_{\text{left}}$ and $S2_{\text{left}}$ labels in panel (a) refer to $S1$ polarons localized on equivalent Ti^{A}_{S1} sites, in proximity of the oxygen vacancy. The values of the energy barriers are reported in meV, while the total amount of ionic displacements with respect to the initial structure is reported in Å. *Figure adapted from Phys. Rev. L, Supplemental Material ©2018 American Physical Society* [2].

(1.9 Å). In the presence of a CO molecule on the NNN-Ti^{A}_{S0} site, the energy barrier for the polaron hopping from the $S1$ to the $S0$ state is reduced by only 70 meV [Fig. 5.5(c)], while the effects on the $S1$-to-$S1$ hopping are negligible (not shown). Therefore, at weakly reducing conditions, the $S1$-to-$S1$ polaron hopping exhibits a lower energy barrier than the $S1$-to-$S0$ hopping.

5.2 The effects of polarons on the adsorbates: Unrevealing the CO adsorption on TiO_2(110)

This section focuses on the evolution of the CO adsorption as a function of the CO coverage (θ_{CO}) and of the V_O concentration (c_{V_O}).

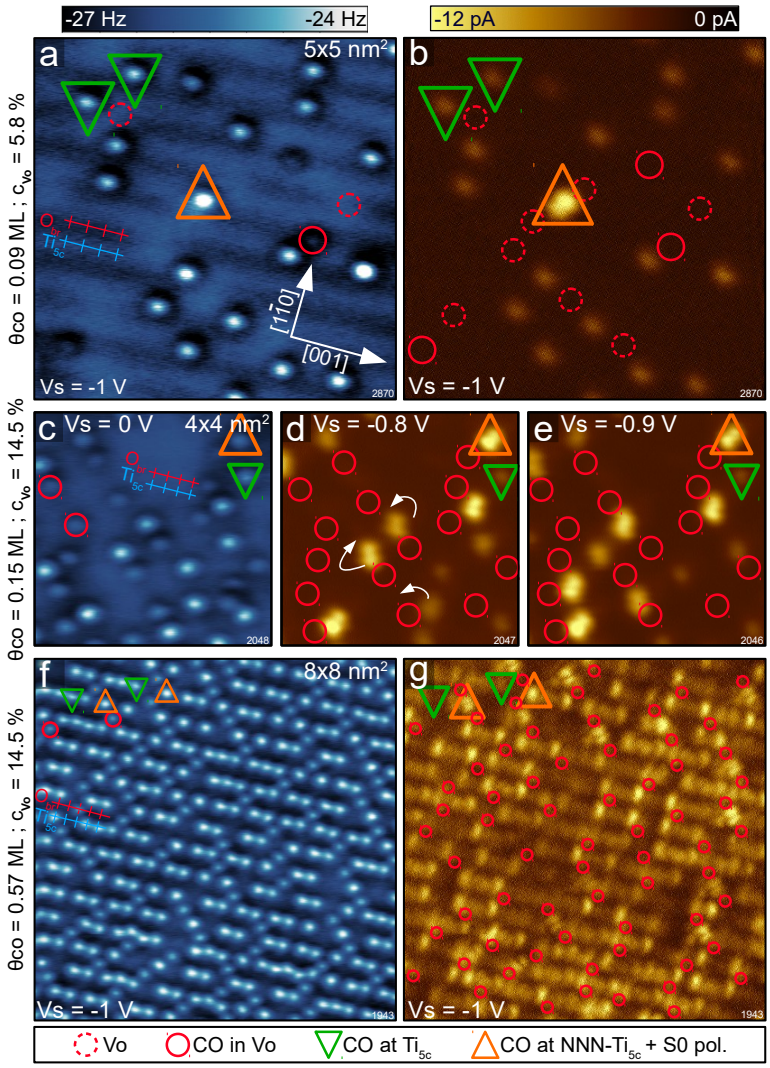

Figure 5.6: Experimental AFM and filled-state STM images. Dashed circles indicate the positions of some oxygen vacancies, solid circles indicate the positions of some vacancies with an adsorbed CO molecule, triangles show some CO molecules adsorbed on Ti^{A}_{S0} atoms. Down-pointing triangles indicate coupling with $S1$ polarons, up-pointing triangles indicate coupling with $S0$ polarons. Panels (a,b): Low CO coverage and low reduction level (θ_{CO} = 0.09 ML and $c_{V_{\mathrm{O}}}$= 5.8%). Panels (c,d,e): moderate CO coverage and high reduction level (θ_{CO} = 0.15 ML and $c_{V_{\mathrm{O}}}$= 14.5%). The STM images (d,e) were measured sequentially, and the arrows indicate the diffusion of CO along Ti_{5c} sites, accompanied by polaron hopping. Panels (f,g): High CO coverage and high reduction level (θ_{CO} = 0.57 ML and $c_{V_{\mathrm{O}}}$= 14.5%). *Figure adapted from Physical Review Letters ©2018 American Physical Society* [2].

[5.2.1] Experiments (low c_{V_O})

Figure 5.6 shows the AFM and STM experimental images for θ_{CO}= 0.09 ML, 0.15 ML and 0.57 ML at different reduction levels (c_{V_O}= 5.8% and 14.5%). At low coverage (θ_{CO}= 0.09 ML) and low oxygen vacancy concentration (c_{V_O}= 5.8%), the AFM identifies CO molecules predominantly adsorbed on Ti^{A}_{S0} sites and less frequently on V_O sites [CO+V_O, see Fig. 5.6(a)]. The filled-state STM image shows an isolated bright double-lobed feature (up pointing triangle) and weaker circular spots (some indicated by down pointing triangles) [Fig. 5.6(b)]. The single lobes of feeble intensity are assigned to the electronic cloud of $S1$ polarons in the vicinity of the CO, in analogy to those shown in Fig. 5.1(a) and Fig. 5.2. The intense double-lobed feature is attributed to an $S0$ polaron bound to a CO at the NNN-Ti^{A}_{S0} site, sandwiched by two oxygen vacancies, analogous to the signal shown in Fig. 5.1(b). The CO adsorbed on V_O sites (some indicated by solid circles), observed by the AFM, carry no in-gap state, and are invisible to the filled-state STM investigation. Therefore, the filled-state STM technique alone would not be capable to identify the totality of the adsorption sites.

[5.2.2] Experiments (high c_{V_O})

At strongly reducing conditions, the number of polarons increases, and polaron hopping towards $S0$ sites become progressively more probable. In fact, polaron hopping within the $S1$ plane is inhibited by the repulsive polaron-polaron interaction. Conversely, the $S1$-to-$S0$ polaron hopping is favored by the attractive interaction between polarons and the abundant positively charged V_O centers. The increased hopping rate to $S0$ sites favors the formation of a larger number of CO+$S0$-polaron complexes at NNN-Ti^{A}_{S0} sites. This is confirmed by the experimental data shown in Fig. 5.6(c,e), measured at c_{V_O}= 14.5% and θ_{CO}= 0.15 ML. The AFM image [Fig. 5.6(c)] displays a larger number of CO+V_O spots, and the corresponding STM image [Fig. 5.6(d)] shows an increased occurrence of double-lobed features at the Ti^{A}_{S0} sites, which identify CO+$S0$-polaron complexes. Figs. 5.6(d,e) are two filled state STM images of the same area, recorded consecutively in time, which show the diffusion of some CO molecules accompanied by polaronic hopping.

Finally, by increasing further the CO concentration up to θ_{CO}= 0.57 ML at strongly reducing condition (c_{V_O}= 14.5%), the AFM image [Fig. 5.6(f)] clearly shows that CO tends to avoid adsorption sites nearest neighbor to the oxygen vacancies (NN-Ti^{A}_{S0}), and preferentially populates NNN-Ti^{A}_{S0} sites in combination with the $S0$ polaron [double-lobed features in Fig. 5.6(g), particularly intense when the CO is adsorbed at a NNN-Ti^{A}_{S0} site sandwiched between two oxygen vacancies]. Adsorption on oxygen vacancies occurs frequently, again with no in-gap state reported. CO molecules adsorb also on other Ti^{A}_{S0} sites, characterized by weaker STM signals. These weak STM signals originates from $S1$ polarons and also from the long-range tail of the polaronic cloud of

the CO+$S0$-polaron complexes at NNN-Ti^{A}_{S0} (as explained in Fig. 5.3). At this strongly reducing condition and high CO coverage, most of the polarons form CO+$S0$-polaron complexes: The amount of bright double lobes is quite high (it tends to twice the number of oxygen vacancies), thus, there remain few $S1$ polarons in the samples (in addition to the excess electrons originating eventually from any other electron dopant, such as interstitial Ti atoms).

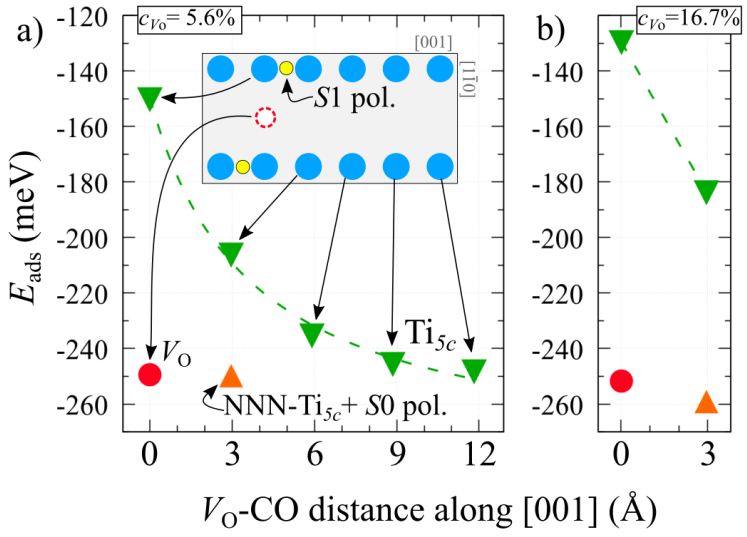

Figure 5.7: Site dependent adsorption energy. A CO molecule is modeled to adsorb on Ti^{A}_{S0} sites at various distances from the oxygen vacancy (down pointing triangles), and on the V_O site (circles), in presence of polarons localized on the $S1$ layer in reduced slabs with c_{V_O}= 5.6% (a) and c_{V_O}= 16.7% (b). The inset sketches the considered geometry. The E_{ads} values for for the adsorption on the NNN-Ti^{A}_{S0} site hosting an $S0$ polaron are also shown (up pointing triangles). *Figure adapted from Physical Review Letters ©2018 American Physical Society* [2].

[5.2.3] Simulations (low c_{V_O})

The interpretation of the experimental data is supported by the trend of the adsorption energy (E_{ads}, see Eq. 2.11) computed by DFT at c_{V_O}= 5.6% and 16.7%, with homogeneous distributions of oxygen vacancies. Various scenarios are considered for modeling the CO adsorption. The CO molecule is modeled to adsorb on either V_O or Ti^{A}_{S0} sites, while the polarons are kept in the polaronic ground-state configuration of the clean surface (*i.e.*, on Ti^{A}_{S1} sites in proximity of the oxygen vacancy). Moreover, in case of a CO molecule adsorbing on the NNN-Ti^{A}_{S0} site, one polaron is localized on the Ti^{A}_{S0} adsorption site, in order to study the CO+$S0$-polaron complex. The data, collected in Fig. 5.7, confirm the essential role played by polarons and their interaction with CO. For a weakly reduced surface [c_{V_O}= 5.6%, Fig. 5.7(a)], in the presence of $S1$ polarons

arranged as in the clean-surface ground-state configuration, the stability of the CO adsorption on Ti^{A}_{S0} sites (down pointing triangles) increases with increasing distance from the V_O, in accordance with the experiments [Fig. 5.6(a,b)]. CO adsorptions on V_O or on polaronic NNN-Ti^{A}_{S0} (CO+$S0$-polaron complex) are essentially degenerate in energy, comparable to the most favorable CO+$S1$-polaron configurations; the smaller rate of double-lobed CO+$S0$ spots and CO+V_O features in the experimental images [Figs. 5.6(a,b)] are due to a smaller number of available adsorption sites, as compared to the non-polaronic Ti^{A}_{S0} sites combined with $S1$ polarons [209].

[5.2.4] Simulations (high c_{V_O})

By increasing the V_O concentration [c_{V_O}= 16.7%, Fig. 5.7(b)], the adsorption on Ti^{A}_{S0} sites in combination with $S1$ polarons becomes significantly less favorable, mainly due to the absence of available Ti^{A}_{S0} sites at large distances from the V_O, whereas the CO+$S0$-polaron and CO+V_O configurations retain their strong stability and represent the most stable solutions. This is in excellent agreement with the experimental STM measurements, indicating a progressive increase of double-lobed spots arising from CO+$S0$ complexes with increasing c_{V_O} [see Figs. 5.6(c,d,g)] combined with a large density of CO+V_O features [see Figs. 5.6(c,f)].

Figure 5.8 shows the results for the adsorption energy obtained by using a slab with a different (*i.e.*, inhomogeneous) distribution of oxygen vacancies. The two vacancies are separated by two lattice sites rather than three (6×2 slab, c_{V_O} = 16.7%). Although the homogeneous distribution of oxygen vacancies (separated by three lattice sites) is more stable (as found by calculations and experiments, reported in Fig. 4.5 in Sec. 4.3), small deviations (typically of one lattice site) occurring on the sample might determine the formation of particularly convenient adsorption sites. In fact, a NNN-Ti^{A}_{S0} site becomes sandwiched between two oxygen vacancies, simultaneously, due to this inhomogeneous V_O distribution. The adsorption via a CO+$S0$-polaron complex on the sandwiched Ti^{A}_{S0} site is largely stable, more favorable than the adsorption on the NNN-Ti^{A}_{S0} site on a homogeneous slab (see up pointing triangle in Fig. 5.8). This stability explains the signals of CO molecules on sandwiched Ti^{A}_{S0} sites observed by the AFM and STM experiments (see Fig. 5.6).

[5.2.5] The CO vibrations

The polarons affects not only the energetics and the spatial localization of the CO adsorbates, but also internal molecule properties. Figure 5.9 shows the computational analysis of the vibrational frequency of the CO bond. The vibration of a CO molecule adsorbed at the NNN-Ti_{5c} site depends strongly on the position of the polarons. Due to the different amount of charge transfer to the CO orbitals, the CO+$S0$-polaron and CO+$S1$-polaron complexes are characterized by different C-O bond lengths (as discussed in Appendix A.4) and different vibrations. The frequency of the CO+$S0$-polaron complex (up

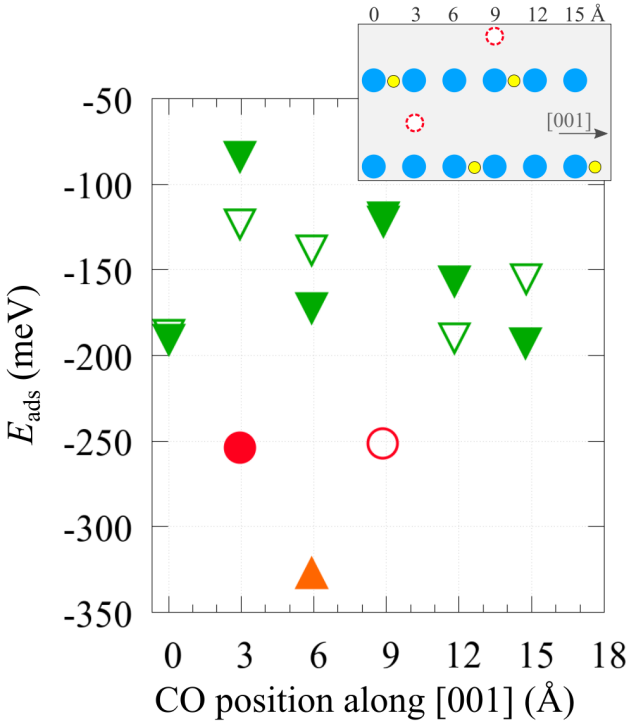

Figure 5.8: Effects of an inhomogeneous distribution of oxygen vacancies on the CO adsorption. The E_{ads} is calculated either for a CO forming a sandwiched CO+$S0$-polaron complex (upper pointing triangle), or for a CO adsorbed on the V_O (circles) and Ti^A_{S0} (down pointing triangles) sites in combination with $S1$ polarons (localized on the most stable Ti^A_{S1} sites). The inset sketches the geometry of the system (top view), modeled by using a 6×2-large slab (c_{V_O}= 16.7%). The filled (empty) symbols refer to the lower (upper) sites in the inset. *Figure adapted from Phys. Rev. L, Supplemental Material ©2018 American Physical Society* [2].

pointing triangle in Fig. 5.9) is very similar to the value obtained for the adsorption on the V_O site (circle). Conversely, an $S1$ polaron below the CO molecule on the NNN-Ti_{5c} site leads to a larger vibrational frequency. The vibrational frequency becomes progressively larger as the separation from the V_O increases (down pointing triangles), approaching the value obtained for the pristine slab (square).

Based on these data, one expects the vibrational spectra to be constituted by two main peaks: one peak attributable to the CO adsorption at large distances from the oxygen vacancies (similar to pristine samples) and the second one arising from the adsorption on V_O sites and via CO+$S0$-polaron complexes.

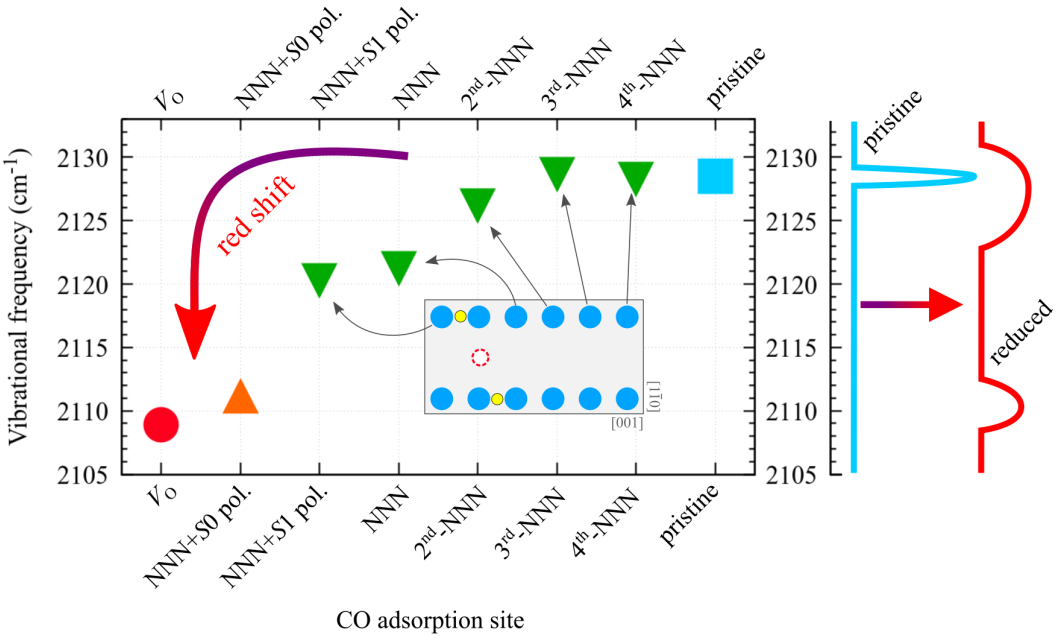

Figure 5.9: Vibrational frequency of the CO bond. Various adsorption geometries are considered: Formation of a CO+$S0$-polaron complex on the NNN-Ti^{A}_{S0} site (labeled as NNN+$S0$); adsorption on V_O and on various Ti^{A}_{S0} sites in combination with $S1$ polarons in proximity of the V_O; the CO on the Ti^{A}_{S0} sites either directly above an $S1$ polaron (labeled as NNN+$S1$), or away from the polarons (NNN, 2$^{\mathrm{nd}}$-NNN, 3$^{\mathrm{rd}}$-NNN, 4$^{\mathrm{th}}$-NNN); also the adsorption on a Ti^{A}_{S0} site on the pristine slab (labeled as pristine) is considered. The arrow indicates the red shift occurring on reduced surfaces. The sketch on the right sides shows a pictorial view of the expected infrared adsorption spectra on the pristine and reduced surfaces. Data obtained by using a 9×2-large slab (c_{V_O}= 5.6%), in the optPBE-DF setup mode (see Appendix A.4), without any renormalization. *Figure adapted from Phys. Rev. L, Supplemental Material ©2018 American Physical Society* [2].

All other configurations are expected to play a minor role (i.e., broadening of the peaks in the vibrational spectra), as they are energetically less stable.

These results are in nice qualitative agreement with infrared spectroscopy experiments showing a sharp single peak for CO adsorbing on a pristine sample (at 2188 cm^{-1}), and two broadened peaks for the reduced samples (at 2188 and 2178 cm^{-1}) [211].

5.3 Individual contributions to the CO adsorption

This section outlines the individual role of the multiple interactions contributing to the CO adsorption. Figure 5.10 shows the main contributions to the adsorption process, arising from the interaction between CO and (a) an oxygen vacancy, (b) another CO molecule or (c) an $S1$ polaron, separately.

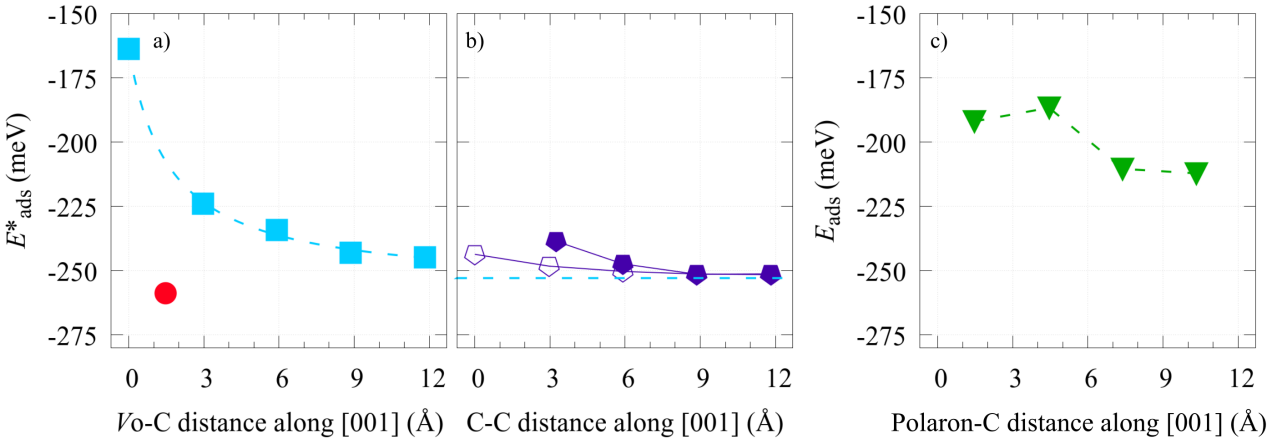

Figure 5.10: Individual contributions to the CO adsorption energy. E^*_{ads} is calculated in the absence of polarons, *i.e.*, by substituting $E^{S1}_{TiO_2}$ with $E^{deloc}_{TiO_2}$ (the energy of the clean surface without localized electrons) in Eq. 2.11 (see Eq. 2.12). Panel (a): The E^*_{ads} energy is shown for a CO molecule adsorbed on a weakly reduced slab (c_{V_O}= 5.6%) on various Ti^A_{S0} sites (squares) and on the V_O site (circle); the two excess electrons originating from the V_O are forced to be delocalized (by performing non-spin-polarized calculations). Panel (b): E^*_{ads} energy for two CO molecules adsorbed on various Ti^A_{S0} sites, on a pristine cell, as a function of the C-C distance; the energy of a single CO adsorbed on a pristine slab is also reported for comparison (dashed horizontal line); filled (empty) symbols refer to CO molecules on the same (different) Ti^A_{S0} [001] row(s); excess electrons are not present in the pristine system. Panel (c): E_{ads} energy for one CO molecule adsorbed on Ti^A_{S0} sites on a stoichiometric slab, as a function of the polaron-C distance; an excess electron is manually introduced into the system, which forms an $S1$ polaron on a given Ti^A_{S1} site. *Figure adapted from Phys. Rev. L, Supplemental Material ©2018 American Physical Society* [2].

[5.3.1] V_O-CO

The data in panel Fig. 5.10(a) are obtained by modeling a CO molecule adsorbed on the V_O and Ti^A_{S0} sites, at weakly reducing conditions (c_{V_O}= 5.6%). The two excess electrons originating from the V_O are forced to form delocalized states at the bottom of the conduction band (by performing non spin-polarized

calculations, as explained in Sec. 2.1). The adsorption energy decreases with increasing V_O-C distance, with an overall energy gain of about 80 meV as compared to the adsorption on the NN site. The adsorption at the V_O site (red circle) shows a favorable energy, comparable to the adsorption on Ti^A_{S0} sites at large distance. By removing one or both excess electrons (corresponding to a +1 and +2 charged system, respectively) the adsorption energy data rigidly shit downwards by about 40 meV per removed electron (not shown).

[5.3.2] CO-CO

The CO-CO interaction affects only marginally the CO adsorption energy [Fig. 5.10(b)]. In fact, even if two CO molecules are modeled to adsorb on the same Ti^A_{S0} [001] row, the energy varies by only 15 meV as a function of the CO-CO distance. Remarkably, by increasing the C-C distance, the CO-CO adsorption energy approaches quickly the energy of an isolated CO molecule (modeled by a CO on a 9×2 pristine slab). It has to be noticed that, in this setup, the two CO molecules are able to bend along [001]; this bending reduces the energy cost of CO molecules adsorbing on adjacent Ti^A_{S0} sites; on the other hand, at high CO coverage this route to reduce the energy is hindered, resulting in stronger repulsions (not analyzed in this work).

[5.3.3] Polaron-CO

The data in Fig. 5.10(c) are obtained by adding an excess electron to a 9×2 stoichiometric slab, with a CO molecule adsorbing on various Ti^A_{S0} sites. Similarly to the CO-CO repulsion, the $S1$ polaron affects only slightly the adsorption energy. In fact, E_{ads} varies in a small range of about 30 meV as a function of the polaron-CO distance. It has to be noticed that here the the system is −1 charged, due to the manually added excess electron. Due to this charge state, an energy shift of 40 meV affects the calculated values, as it stands out by comparing the E_{ads} for large polaron-CO separation in Fig. 5.10(c) and Fig. 5.7(a). This is consistent with the shift described above for the +1 and +2 charged system with one V_O.

[5.3.4] Balance

Therefore, at weakly reducing conditions, it is the V_O-CO interaction that plays a primary role in the CO adsorption process. In fact, adsorption on V_O and on distant Ti^A_{S0} sites is favored at weakly reducing conditions [see Fig. 5.6(a,b)] and driven by the V_O-CO interaction. Only the strong stability of the CO+$S0$-polaron complexes at NNN-Ti^A_{S0} sites can overtake the V_O-CO interaction. In fact, the adsorption on the NNN-Ti^A_{S0} site becomes very stable, as soon as the formation of $S0$ polarons and CO+$S0$-polaron complexes is enabled by strongly reducing conditions [see Fig. 5.6(c-g) and Fig 5.7(b)].

5.4 Ti interstitials and CO adsorption

Rutile TiO_2(110) is able to oxidize CO molecules into CO_2. The O_2 is also involved in the process: An O_2 molecule adsorbs on the surface, and dissociates into two O atoms; the CO molecule adsorbs beside an O adatom; the O adatom and the CO bond together, forming a CO_2 molecule which desorbs from the TiO_2(110) surface. Unfortunately, the second O adatom which is left behind, oxidizes the TiO_2(110) surface by filling an oxygen vacancy [159]. Therefore, the CO oxidation cannot be promoted continuously on TiO_{2-y} samples.

Conversely, samples reduced by interstitial Ti atoms (here referred to as $Ti_{1+x}O_2$ samples) can sustain steady CO oxidation cycles [159]. In fact, the O adatoms do not deplete the in-gap states on the TiO_2(110), thus, O_2 adsorption and CO oxidation can occur repeatedly. This section summarizes the main features of the Ti_{int}-CO interaction, also considering the effects of polarons. The oxygen vacancies are not included in the slabs, due to the effects of the repulsive interaction, which pushes the Ti_{int} atoms towards the bulk (see discussion in Sec. 3.7).

	$\Delta E^{\text{deloc}}_{TiO_2}$ (meV)	
	no CO	with CO
$S0S1$-center	+173	**-39**
$S0S1$-edge	+269	+155
$S1S2$-center	+462	+464
$S1S2$-edge	**0**	0

Table 5.1: **The CO effects on the Ti_{int} stability.** Comparison of the (delocalized-electron solution) free energy for the TiO_2(110) surface with an interstitial Ti atom (at various positions, namely $S0S1$-center, $S0S1$-edge, $S1S2$-center, $S1S2$-edge). The "no CO" data were obtained for the clean slab (reported already in Fig. 3.16), while "with CO" refers to data with CO adsorbed on the Ti^A_{S0} site nearest to the Ti_{int} atom. The most favorable energies are printed in magenta. The energy value of the $S1S2$-edge system is taken as a reference.

[5.4.1] Ti_{int} and CO

The presence of CO on the surface, seems to affect drastically the Ti_{int} stability. Table 5.1 reports the energy value of the $Ti_{1+x}O_2$ system, comparing different positions for the Ti_{int} ($S0S1$-center, $S0S1$-edge, $S1S2$-center, $S1S2$-edge, described in detail in Sec: 3.7). Excess electrons were forced into delocalized states, by performing non spin-polarized calculations. In the absence of adsorbates, the $S1S2$-edge geometry is the most stable, thus, Ti_{int} is

preferentially located at deep positions. [160, 161] By including CO, the energy balance changes and the most favorable site become $S0S1$-center, closer to the surface. Therefore, the delocalized-electron analysis suggests that the diffusion towards the surface of the interstitial Ti could be promoted by the adsorbates [161].

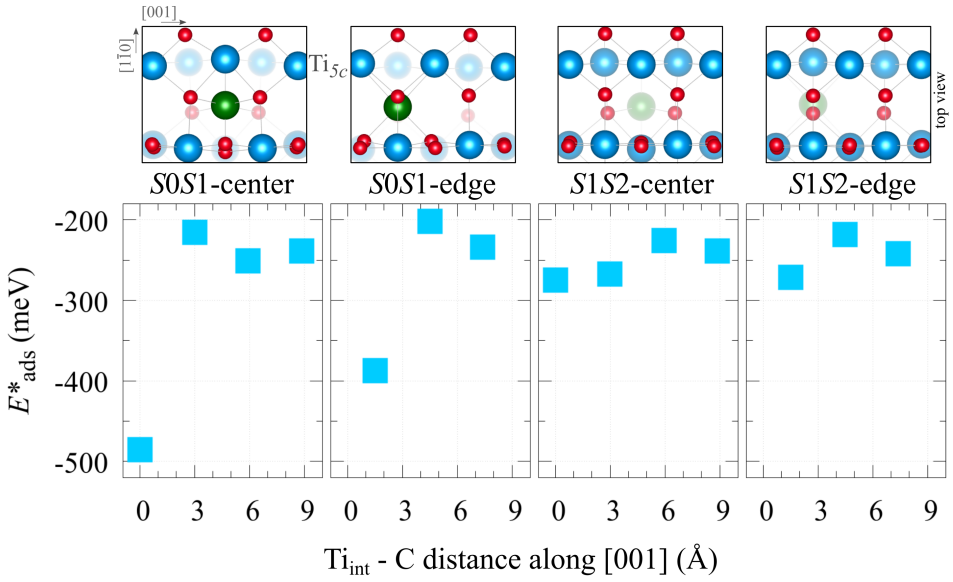

Figure 5.11: CO adsorption on the Ti_{int}-reduced TiO_2(110). Adsorption energy E^*_{ads} (in the delocalized-electron solution) calculated for one CO molecule adsorbed on various Ti^A_{S0} sites, as a function of the distance along [001] from the Ti_{int} (considering various geometries, as indicated in the insets). *Figure adapted from Phys. Rev. L, Supplemental Material ©2018 American Physical Society* [2].

Figure 5.11 shows the trend of the adsorption energy as a function of the Ti_{int}-CO distance. The adsorption is clearly more favorable at small Ti_{int}-CO distance, for any geometry investigated. This attraction is particularly strong for the $S0S1$ geometries (hundreds of meV), which show the most stable adsorption energies.

[5.4.2] Ti_{int} polarons and CO

By turning on the charge localization (*i.e.*, by performing spin polarized calculations), the role of polarons in the CO adsorption on the $Ti_{1+x}O_2$ system can be investigated. This analysis was performed on the most favorable polaronic configurations, according to the FPMD analysis on the clean $Ti_{1+x}O_2$ surface, as described in Table 3.4. As a general important result, the CO+$S0$-polaron complex is found to play a primary role, also in the Ti_{int} reduced systems.

$S0S1$-center					
Amount of polarons				ΔE	E_{ads}
$S2$	$S1$	$S0$	Ti_{int}	(meV)	(meV)
0	2	1	1	0	-516

$S0S1$-edge					
Amount of polarons				ΔE	E_{ads}
$S2$	$S1$	$S0$	Ti_{int}	(meV)	(meV)
0	2	2	0	+138	-396
0	3	1	0	+270	-264

$S1S2$-edge					
Amount of polarons				ΔE	E_{ads}
$S2$	$S1$	$S0$	Ti_{int}	(meV)	(meV)
0	2	1	1	+828	-27
0	3	0	1	+602	-253

Table 5.2: **CO adsorption on the polaronic $\mathbf{Ti_{1+x}O_2}$.** Most favorable polaronic configurations for different Ti_{int} geometries ($S0S1$-center, $S0S1$-edge, $S1S2$-edge, as in Table 3.4) and corresponding free (ΔE, referred to the $S0S1$-center) and adsorption (E_{ads}) energies. The CO is adsorbed on the Ti^{A}_{S0} site nearest to the Ti_{int}, eventually forming a CO+$S0$-polaron complex.

The $S0S1$-center geometry was found to be the most stable geometry for the polaronic surface, in the absence of adsorbates (see Table 3.4): The polaronic $S0S1$-edge shows a similar energy ($\Delta E = +17$ meV), while the $S1S2$-edge geometry is largely less stable ($\Delta E = +338$ meV). As reported in Table 5.2, the CO adsorption further stabilizes the $S0S1$-center geometry in comparison to the $S0S1$-edge and $S1S2$-edge, which show higher free energy ($\Delta E = +138$ meV and $\Delta E = +602$ meV, respectively).

The enhancement of the $S0S1$-center stability is due to the formation of the CO+$S0$-polaron complex, which is particularly strong in this geometry. In the $S0S1$-edge geometry, it was possible to evaluate the strength of this complex, by moving the $S0$ polarons to the $S1$ layer. As for the surfaces reduced by the oxygen vacancies, breaking the CO+$S0$-polaron complex by moving the polaron costs energy ($E_{\text{ads}}= -396$ meV $\rightarrow -264$ meV).

The $S1S2$-edge geometry shows an opposite behavior. In this case, the Ti_{int} is not near the surface, thus, the energy cost required to form an $S0$ polaron is higher. In fact, the CO+$S0$-polaron complex does not conveniently

form (E_{ads}= −27 meV instead of −253 meV).

In conclusion, the CO+$S0$-polaron complexes are energetically favorable only if the adsorption takes place in the proximity of the interstitial Ti atom. This is in agreement with the results achieved in the case of oxygen vacancies, where only the NNN-Ti^{A}_{S0} site allows for the formation of the CO+$S0$-polaron complex. The formation of $S0$ polarons seems to require not only the presence of the CO adsorbate but also the attractive interaction of either an oxygen vacancy or Ti interstitials.

The CO+$S0$-polaron complexes show the characteristic double-lobed signature in filled-state STM simulations on any considered slab (see Fig. C.10 comparing the STM signals in proximity of Ti_{int} and V_{O}). Similar results can be obtained also for CO+$S0$-polaron complexes away from lattice defects (not shown). Therefore, the double-lobed STM spots and the associated electronic charge transfer towards the CO $2\pi^*$ orbitals seem to be an intrinsic characteristics of $S0$ polarons, independent of the specific type of defect responsible for the electronic reduction. Importantly, the low-temperature filled-state STM measurements in Fig. 5.6 detect the double-lobed spots only in correlation with the oxygen vacancies, precisely, only on NNN-Ti^{A}_{S0} sites. This is an indication that interstitial Ti atoms are not present in shallow ($S0S1$) positions near oxygen vacancies, mostly due to the V_{O}-Ti_{int} electrostatic repulsion [162].

5.5 Outline of the adsorption on polaronic TiO_2(110)

The interplay between polarons and adsorbed CO molecules significantly influences the adsorption scheme: It affect the adsorption energies, the bonding distances from the surface as well as the C-O bond length (Fig. A.9). The various polaron-CO coupling schemes presented here are consistent with reported experimental data on the CO adsorption: In temperature programmed desorption (TPD), the TPD spectra measured on the rutile (110) surface [208] are complex, with multiple desorption peaks. Contrary, the same experiment performed on the anatase TiO_2(101) surface [215] shows a single desorption peak only. This can be associated with the absence of small polarons on the anatase (101) surface [48], which simplifies the adsorption scheme in comparison to the polaronic rutile. In a similar way, infrared absorption spectra of CO on the anatase (101) surface always exhibits a single absorption peak [215], while the rutile (110) surface shows either one or two vibrational states, depending on the reduction level of the crystal [211].

In turn, polaronic states are drastically affected by the presence of CO molecules on the surface. The CO adsorption promotes polarons transfer from subsurface to surface sites, in particular at strongly reducing conditions, thus

reinforcing the reactivity of surface Ti_{5c} sites. Three distinct types of adsorption can occur, with well-defined distinctive characteristics: CO on V_O sites, CO on Ti_{5c} sites weakly coupled with polarons in the subsurface (manifested by weak circular features in filled-state STM images), and strongly coupled CO+$S0$-polaron complexes on NNN-Ti_{5c} sites (appearing as double-lobes in filled-state STM images). The coupling between CO and polarons and its interaction with the defective lattice effectively influences the dynamics of the CO+polarons complexes, enabling breaking and recombination of the CO-$S0$/$S1$ complexes.

This comprehensive picture of the CO adsorption process on the polronic TiO_2(110) surface solves long-standing ambiguities and conflicting interpretations, and set the path for revisiting the interpretation of adsorption processes in polar semiconductors and transition metal oxides.

Chapter 6

Conclusions

This doctorate project has investigated fundamental aspects regarding polarons in TiO_2, an archetypal transition-metal oxide, revealing their impact on the material properties and functionalities. The rutile $TiO_2(110)$ and the electron small polarons have been at the core of the study, performed by density-functional theory calculations, supported by surface sensitive experiments.

The systematic analysis of the polaron properties presented in Chapter 3 represents the keystone for the interpretation of the phenomena occurring on polaronic oxide surfaces. The energetics of small polarons can be considered in terms of essentially three aspects. First, charge trapping occurs more favorably on specific lattice sites on the subsurface layer of $TiO_2(110)$, due to the local electrostatic potential and to the crystal structure flexibility. Second, the polaron-polaron repulsive interaction is particularly strong at small distances, and configurations with polarons on nearest sites are unfavorable. Third, positively-charged point defects, such as oxygen vacancies and Ti interstitials, attract the (negatively charged) small polarons. Therefore, small polarons are expected to form preferentially on subsurface sites in the proximity of these defects, and maximizing the polaron-polaron distance, simultaneously.

The investigation on the spatial extension of the polaronic charge density shed further lights on the polaron properties. Small polarons show specific orbital symmetries, depending on the trapping site and the local lattice distortions. Despite subsurface sites host most of the polaronic charge, a considerable amount of charge density spreads over neighbor sites and towards the surface. This spatial extension allows to detect the subsurface polarons by filled-state STM measurements. Moreover, the charge density overlap between two polarons is energetically unfavorable, since it enhances the short-range polaron-polaron repulsion, and it affects significantly the polaron distribution. Consistently, small polarons tend to form a characteristic 3×1 pattern on the

subsurface sites (one polaron every three lattice sites along the [001] direction) in order to minimize the charge overlap.

Chapter 4 relates the polaron properties to the surface thermodynamic stability. On strongly reduced samples, experiments observe a phase transition from the (1×1) TiO_2(110) surface to a (1×2) Ti_2O_3-reconstructed surface. The (1×1) phase is not able to conveniently host large amounts of excess electrons, since polarons preserve the 3×1 pattern even at strongly reducing conditions. Conversely, the (1×2) reconstruction can accommodate larger amount of excess electrons, providing easily reducible sites for polaron formation. As a consequence, the (1×2) phase becomes energetically more favorable on strongly reduced samples.

The impact of polarons on the material properties is outlined also in Chapter 5, considering the CO adsorption process. CO molecules can adsorb on the oxygen vacancies and on the five-coordinated Ti sites on TiO_2(110). Subsurface polarons show repulsive interaction with the CO adsorbates. Nevertheless, on samples with high concentration of surface oxygen vacancy, CO molecules can promote polaron transfer from subsurface to surface sites. Surface polarons show a different behavior and couple with the adsorbates, strengthening the CO adsorption by partial transfer of the polaronic charge towards the CO orbitals. The study of the formation of polaron-CO complexes solves long-standing ambiguities and conflicting interpretations of experimental results on the CO adsorption process.

As a general conclusion, polarons are, clearly, extremely important in the physics and chemistry of oxides. Polarons are indeed determinant in order to correctly understand the phenomena presented here. Theoretical studies overlooking polaron formation would predict inadequate thermodynamic phase diagrams for TiO_2(110). Similarly, interpretations disregarding the polaron dynamics from subsurface to surface sites are unable to explain the CO adsorption process. The apparent contradictions are fully solved in the polaronic picture.

Importantly, the study of polarons in the density-functional theory framework requires careful considerations on technical aspects (as discussed in detail in Chapter 2 and Appendix A). In fact, the charge localization brings complications in the calculations, which can lead to unrealistic results. The crucial step is figuring out which polaronic configuration determines the ground state of the system under consideration. Quite some efforts need to be spent by comparing the energetics of different configurations, which can be obtained by controlling selectively the polaron localization or by relying on molecular dynamics calculations. There is no guarantee that the spontaneous charge localization obtained by single shot calculations represents the ground state.

Polarons certainly play primary roles in numerous physical and chemical processes taking place on transition-metal oxide surfaces. Fascinating investigation areas include catalysis, electron transport, optical absorption, thermoelectricity, magnetoresistance, and high temperature superconductivity. In order to analyze diverse phenomena, it would be interesting to extend the systematic study of the polaron properties reported here for $TiO_2(110)$ to other materials (including ceria compounds, $SrTiO_3$, $KTaO_3$ and $LaMnO_3$ perovskites).

Appendix A

Polarons in TiO_2: Crucial aspects of the computational setup

The study of polaron states by first principles calculations is a delicate task. Results are affected by the computational setup, and the risk of achieving unrealistic outcomes is high.

It is therefore essential to investigate the dependence of crucial quantities at play on the approximations and parameters adopted in the calculations. This Appendix reports some of the most relevant aspects to consider while studying polarons on TiO_2(110) in the DFT+U framework.

Contents

A.1 Slab thickness convergence

The modeling of TiO_2(110) requires careful technical considerations. The DFT calculations are usually performed by using slabs which consist of few TiO_2 layers (ranging typically between four and ten), embedded in periodic boundary conditions, alternated with a thick vacuum region of about 10–20 Å. It is well known that the surface energy [216], the adsorption energy [217, 218] and the energy band gap [219] show slowly-converging oscillations as a function of the number of layers used to model the stoichiometric TiO_2 slab. The oscillations are due to a pairing of the TiO_2 layers, which lowers the energy of slabs with an even number of layers.

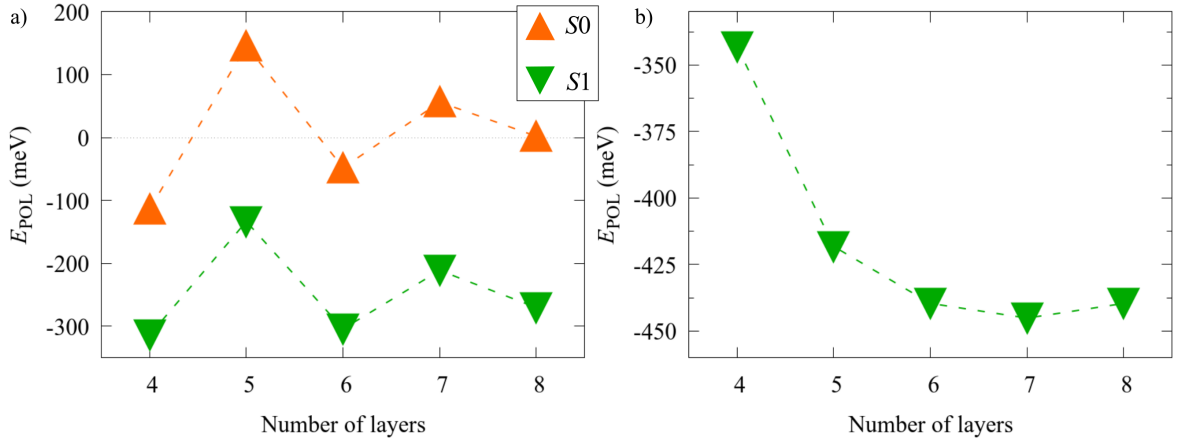

Figure A.1: Slab thickness and polaron formation energy Polaron formation energy for Ti^A_{S0} (up pointing triangles) and Ti^A_{S1} (down pointing triangles) polarons as a function of the slab thickness (number of TiO_2 layers). The results were obtained by using 3×2 slabs with zero (panel a) or one (panel b) V_O and one excess electron, corresponding to a +1 and −1 charged system, respectively. *[Unpublished Figure]*

The polaron formation energy obtained for a stoichiometric TiO_2 slab presents a similar oscillating behavior, as shown in Fig. A.1(a). The formation of polarons on the $S1$ layer is more favorable than on the $S0$ layer, as expected (Sec. 3.2). Both the $S1$ and $S0$ polarons are characterized by oscillating E_{POL} energies, which converge only at 7 layers with a precision of 100 meV. Importantly, the E_{POL} difference between the two types of polarons seems to be independent of the number of layers.

The formation of oxygen vacancies on the rutile surface, drastically change the E_{POL} trend. As shown in Fig. A.1(b), an $S1$ polaron is characterized by E_{POL} values which are converged within 25 meV by using only 5 layers, without any strong oscillation.

The following sections discuss additional aspects, such as the effects of the lattice strain (Sec. A.2), and the effects of the approximations for the exchange-correlation DFT term (Sec. A.3 and A.4). Future studies could be pointed into the direction of investigating the dependence of E_{POL} on other relevant computational parameters, such as the lateral size of the unit cell.

A.2 Lattice strain

The polaronic properties presented in the main text are quite robust upon variations of the computational setup. However, some particular parameters used for the simulations may affect the description of the system, in specific cases. In fact, inappropriate technical choices can favor the formation of $S0$ polarons instead of $S1$ polarons.

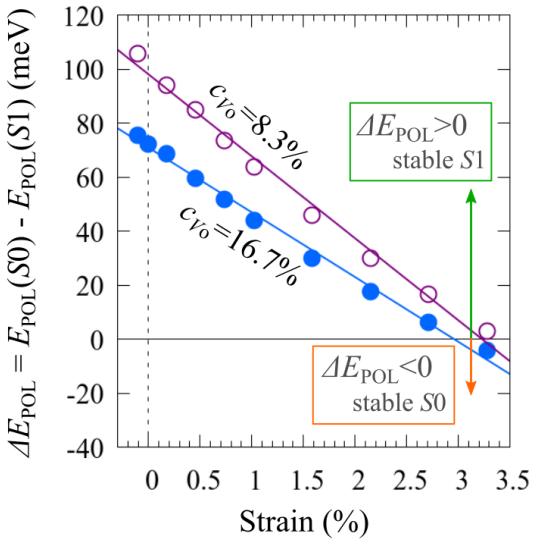

Figure A.2: The strain dependence of the $S0$ and $S1$ polaron stability. The graph shows the energy difference (ΔE_{POL}) for the formation of an $S0$ and an $S1$ polaron, as a function of the lattice strain along [001]. The calculations are performed by using a 6×2-large slab, including two (one) vacancies on the surface, corresponding to $c_{V_{\mathrm{O}}}$= 16.7% ($c_{V_{\mathrm{O}}}$= 8.3%), together with four (two) polarons. One of the polarons is localized selectively on an $S0$ or $S1$ site, while the others are kept fixed in energetically favorable $S1$ sites. *[Unpublished Figure]*

[A.2.1] Polaron stability vs strain

As discussed in Sec. 3.2, polarons localized on Ti^A_{S1} and Ti^A_{S0} sites are characterized by different lattice distortions. In particular, a Ti^A_{S1} polaron tends to attract the nearest-neighbor Ti atoms along [001] towards the polaronic site. Conversely, the Ti^A_{S0} polaron increases the distance of the hosting site with the nearest-neighbor Ti atoms along [001]. In other words, the $S0$ polaron is subjected to a compressive strain, while the $S1$ polaron experiences a tensile strain.

As a consequence of the opposite behavior of the polaronic distortions, the $S1$ and $S0$ polarons are affected by the strain along [001] to a different extent. Figure A.2 summarizes the comparison between Ti^A_{S1} and Ti^A_{S0} polarons. A tensile strain along [001] strengthens the formation of $S0$ polarons and weakens the stability of $S1$ polarons, due to the increase of the bond lengths. The difference (ΔE_{POL}) between the E_{POL} energy values for the $S0$ and $S1$ polarons decreases with increasing tensile strain, thus reducing the stability of $S1$ polarons, especially on strongly reduced surfaces ($c_{V_{\mathrm{O}}}$= 16.7%). Ultimately, for very large values of the strain (over about 3%) the Ti^A_{S0} sites become the most favorable sites for polaron formation ($\Delta E_{\mathrm{POL}} < 0$).

[A.2.2] The strain and the (1×2) phase

Therefore, samples under tensile strain along [001] favor the polaron hopping towards the $S0$ surface, as compared to samples with the low-temperature experimental lattice constant c = 2.953 Å [12]. The [001] lattice parameter chosen to model the TiO_2(110), thus, plays a crucial role. A large lattice parameter would favor the energetic stability of the $S0$ polarons in the simulations. Even tough for reasonable amounts of strain (up to $\approx$ 3%) the $S1$ polarons still remain the most favorable ones, some specific properties, as the surface energy, might change sensibly.

As discussed in details in Chapter 4, the (1×1) phase of the rutile TiO_2(110) surface is found to reconstruct into a (1×2) structure. The experimental observations show that the (1×1)-to-(1×2) transition takes place on highly reduced (1×1) surfaces, specifically for $c_{V_{\mathrm{O}}}$= 16.7%. This phenomenon was investigated by computational techniques, modeling the TiO_2 system with an expanded [001] lattice parameter (about 0.5%) in order to mimic the high temperature (T = 700 K) features of the compound. However, this choice overestimates the stability of the $S0$ polarons, leading to a slightly larger critical concentration ($c_{V_{\mathrm{O}}}$= 22%). By using the low temperature lattice parameters, the comparison with the experiment is expected to improve.

[A.2.3] Strain and adsorption

An additional important consequence of the strain effect on the polaron stability regards the study of the molecular adsorption. In particular, as detailed described in Chapter. 5, the adsorption energy and the spatial configuration of the CO molecules strongly depends on the presence of polarons. As observed in STM and AFM experiments at low reducing conditions, the CO molecules

preferably adsorbs at large distances from the oxygen vacancy. Conversely, at high reducing conditions, adsorption on NNN-Ti^{A}_{S0} sites is more convenient, due to the formation of CO+$S0$-polaron complexes. These results are in excellent agreement with the simulations, as far as the low-temperature [001] lattice parameter is used in the calculations.

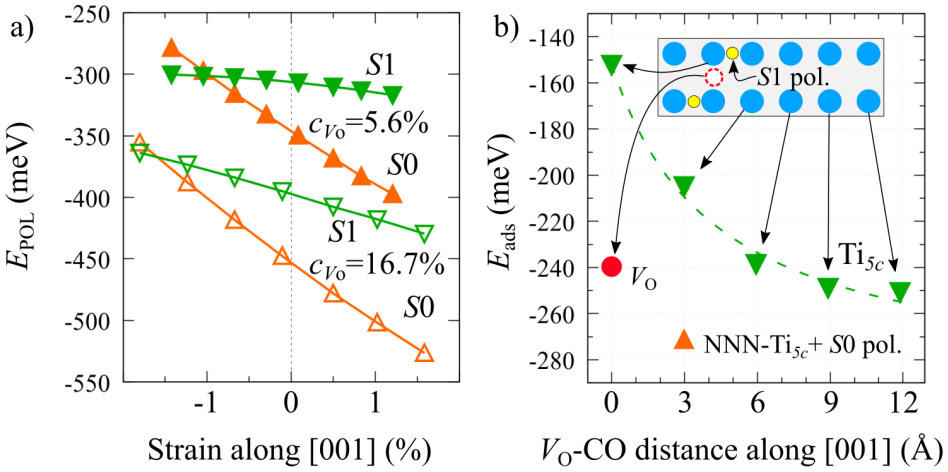

Figure A.3: Strain effects on the adsorption process. Panel (a): The polaron formation energy E_{POL} is reported as a function of the strain along [001] with respect to the low-temperature lattice parameter (c = 2.953 Å). One CO molecule is adsorbed on the NNN-Ti^{A}_{S0} site. Filled and empty symbols correspond to c_{V_O}= 5.6% and 17.6% reduced slabs, respectively. Down-pointing triangles indicate the presence of an $S1$ polaron below the CO molecule, while the up-pointing triangles represents the CO+$S0$-polaron complex. Panel (b): The adsorption energy E_{ads} is reported for a CO molecule adsorbed on various sites, on a c_{V_O}= 5.6% reduced slab, as indicated by the sketch. This figure is analogous to Fig. 5.7, but a strain of about 0.5% is applied along [001]. *[Unpublished Figure]*

Figure A.3 shows the effects of the strain on the polaron formation and CO adsorption energies. The E_{POL} data in Fig. A.3(a) are obtained by using a 6×2 slab and varying the lattice parameter along [001]. A CO molecule is adsorbed on the NNN-Ti^{A}_{S0} site, and a polaron is localized below the CO, on the $S0$ or $S1$ layer. At zero strain, the formation of a $S0$ polaron is more favorable than $S1$ polarons, at any reducing condition. By applying a tensile strain, $S0$ polaron formation becomes further favorable. This result is in agreement with the data show in Fig. A.2 for the clean (*i.e.*, no adsorbates) surface.

Interestingly, the increased stability of the $S0$ polaron upon strain affects the CO adsorption and worsen the comparison with the experiment. In fact, as shown in Fig. A.3(b), a tensile strain of 0.5% stabilizes CO+$S0$-polaron

complexes, even on weakly reduced surfaces. This is clearly in disagreement with the experimental observation, since the CO+$S0$-polaron complexes are observed only on strongly reduced surfaces (see Fig. 5.6). The agreement with experiment is recovered by using the low-temperature lattice parameter (see Fig. 5.7).

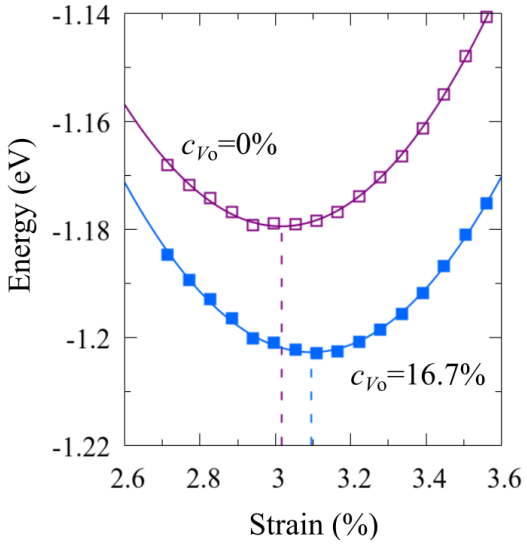

Figure A.4: Dependence of the c lattice vector on the amount of surface oxygen vacancies. The energy of the system in the delocalized solution, modeled by a 6×2-large slab, including two (zero) surface vacancies, corresponding to c_{V_O}= 16.7% (c_{V_O}= 0%), is reported as a function of the strain along the c lattice vector, *i.e.*, along [001]. Both the energy and the strain are given in terms of the low temperature system (c = 2.953 Å), used as a reference. The dashed lines indicate the amount of strain minimizing the energy. *[Unpublished Figure]*

[A.2.4] The c lattice vector

Therefore, a careful setup of the [001] lattice vector is required in order to obtain accurate and reasonable results. However, typically, DFT+U calculations based on GGA functionals overestimate the lattice vectors with respect to the experiments, which is the case also for the c lattice parameter along [001] of TiO_2(110). The value of the c lattice vector predicted by the simulation corresponds to a strain of about 3% with respect to the experimental value (c = 2.953 Å [12]), as shown in Fig. A.4. As described above, this large overestimation of the lattice parameter drastically affects the stability of the polarons, favoring, unrealistically, the formation of $S0$ polarons. By using the low-temperature experimental parameters to describe the geometrical properties of the lattice, the results on the polaronic properties are more reasonable.

Interestingly, as shown in Fig. A.4 for both the stoichiometric and strongly

reduced surfaces, the calculated [001] lattice parameter becomes larger as the concentration of oxygen vacancies increases, due to the broken bonds on the surface, at the V_O sites. This trend of the lattice parameter, obtained by forcing the excess electrons into the delocalized solution, sheds some light on the propensity of the strongly reduced samples to host $S0$ polarons. In fact, the $S0$ polarons are revealed in AFM and STM experiments on sampled exposed to CO, but only at strongly reducing conditions. The propensity of strongly reduced TiO_2(110) surfaces to host $S0$ polarons can be related to this stretching of the lattice vector along [001]: A large V_O concentration not only attracts polarons towards the surface via electrostatic interaction, but also stretches the lattice parameter, which in turns reduced the compressive strain and favors the formation of $S0$ polarons.

A.3 The U

The stability of the $S0$ and $S1$ polarons depends strongly on the choice of the U parameter adopted in the DFT+U calculations. Figure A.5 shows the comparison of the E_{POL} energy for $S0$ and $S1$ polarons as a function of U'. By setting U' to the value $U^{cRPA} = 3.9$ eV obtained from cRPA calculations [48], $S1$ polarons are largely more favorable (by approximatively 100 meV) than $S0$ polarons, even at strongly reducing conditions [Fig. A.5(a)]. By adopting a smaller U' value, the stability of the $S1$ polarons is further reinforced with respect to the $S0$ ones. On the other hand, larger U' values favor the formation of $S0$ polarons: At $U' \simeq 5$ eV (approximatively 1 eV above the U^{cRPA} value) formation of $S1$ polarons becomes energetically less favorable. The linear trend shown in Fig. A.5(a) indicates an extraordinary stability for the $S0$ polarons if a very large U' is used. Since the stability of the $S0$ polarons is not supported by the experimental observations (at least at low temperature), these large U' values should be avoided in the calculations.

Moreover, the trend of E_{POL} shown in Fig. A.5(b) for the $S0$ and $S1$ polarons, individually, shows a discontinuity of the linear trend (at around $U' \simeq 7$ eV). Therefore, the interpretation of the stabilization process of $S0$ polarons upon increase of the U' value is not trivial. Certainly, a larger U' value determines a stronger polaronic-charge localization at the hosting site (which can be evaluated by inspecting the local magnetization). The trend of the magnetic moment of the hosting Ti^A_{S1} site is shown in the inset in Fig. A.5(b). At large U' values, the magnetic moment is large (approximatively 1 μ_B), while at small U' values, the charge localization decreases rapidly.

The discontinuity in the E_{POL} trend seems to be related to the energy value characterizing the polaronic state with respect to the valence band. Figure A.6

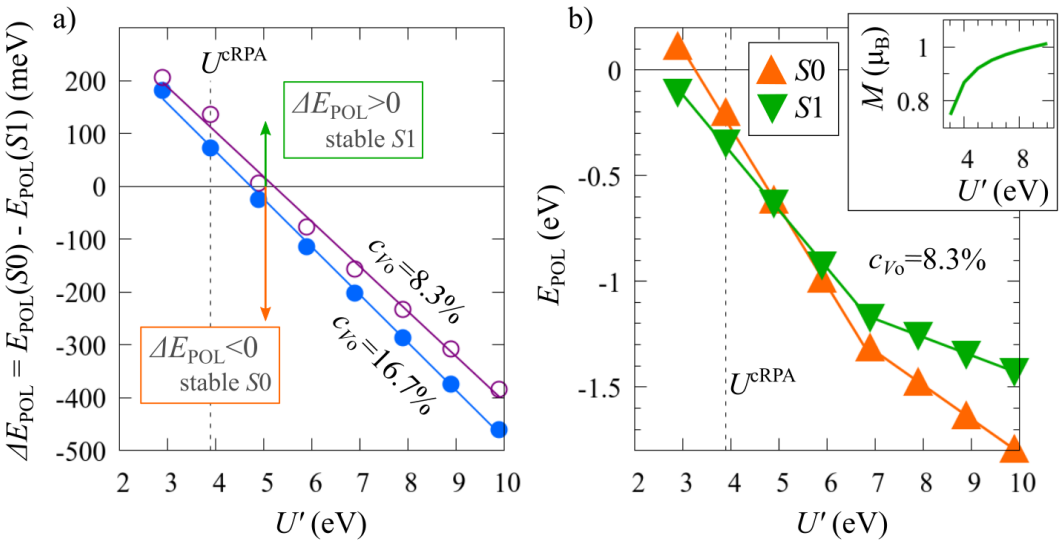

Figure A.5: Dependence of the $S0$ and $S1$ polaron stability on the U parameter. Energy difference (ΔE_{POL}) for the formation of an $S0$ and an $S1$ polaron, as a function of the effective $U' = U - J$ parameter (a). One polaron is localized selectively on an $S0$ or $S1$ site, while the others are kept fixed on energetically convenient $S1$ sites, in a 6×2-large slab with c_{V_O}= 16.7% and 8.3%. The E_{POL} is shown for the $S0$ and $S1$ polarons, individually, for a 6×2-large slab with one V_O (c_{V_O}= 8.3%) and one excess electron, *i.e.*, +1 charge state (b). The inset shows the trend for the local magnetic moment M of the Ti atom hosting the $S1$ polaron. *[Unpublished Figure]*

show the density of states obtained in a slab with an $S1$ polaron, by using various values for U'. At low U' values ($U' \lesssim 4.5$ eV), the polaronic state is sharply located in the energy gap region. Around $U' \simeq 4.5$ eV, the polaronic state overlaps with the valence band. It has to be noticed that these data were obtained by using a slab in a +1 charge state; as a consequence, the energy band gap is modified by the extra positive charge, thus, the DOS-polaron overlap could occur for slightly different U' values (*i.e.*, few tenths of eV) in the neutral slab. The d states of the hosting Ti site show no sharp features at $U' \simeq 7$ eV, that is in correspondence of the discontinuity in E_{POL} [Fig. A.5(b)].

The U parameter affects also the polaronic distortions. Figure A.7 shows the trend of the polaronic distortions as obtained for a Ti^A_{S1} polaron, considering the six coordinated O atoms (two apical along [1$\bar{1}$0], two equatorial above and two equatorial below the reference Ti) and the two nearest Ti atoms along [001]. As one might expect, the bonds of the polaronic Ti^A_{S1} atom with the octahedrally coordinated O atoms increase as U' increases [Fig. A.7(a-c)], due to the enhanced charge localization (in agreement with the inset in Fig. A.5).

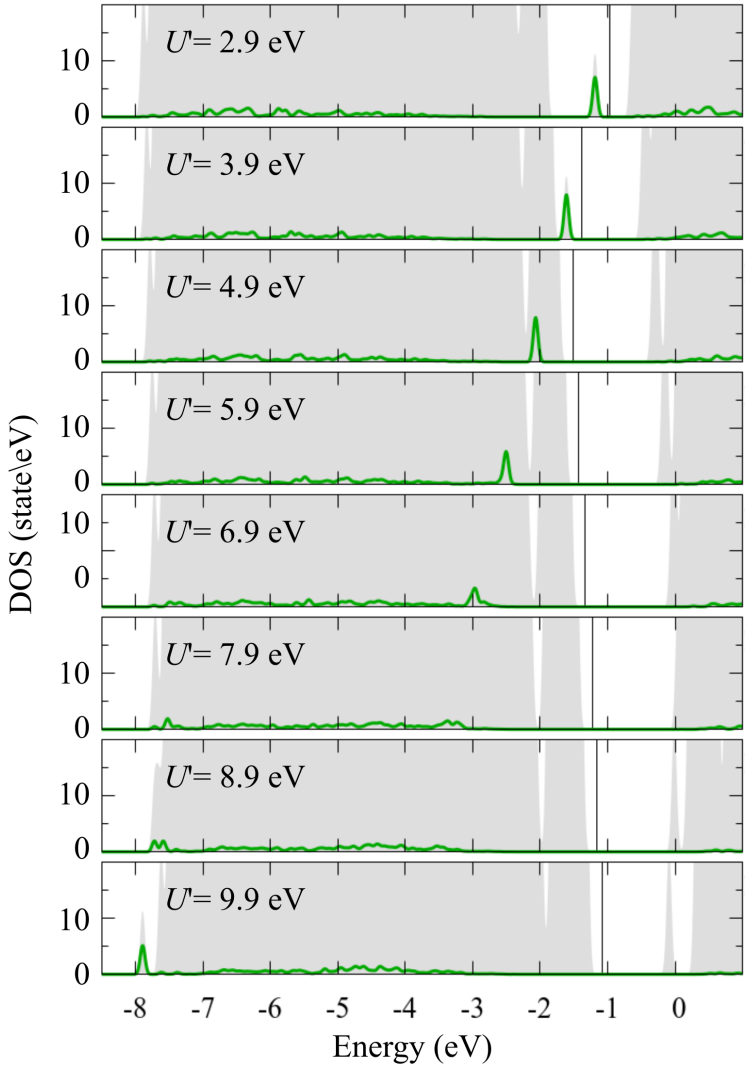

Figure A.6: The dependence of the polaron state on the U parameter. The total DOS (filled area) and the partial DOS projected on the Ti^{A}_{S1} atom hosting the polaron (solid line) are reported for various values of U' (as indicated in the image). The vertical line represents the value of the Fermi energy. These data were obtained by using a 6×2-large slab, with one V_O (c_{V_O}= 5.6%) and one excess electron only (+1 charge state). *[Unpublished Figure]*

A similar trend is observed also for the system constrained in the delocalized electron solution. A comparison of the trend of the distortion between the localized and delocalized solutions is shown in Fig. A.7(e-g): The bonds of the polaronic Ti site with the two apical O atoms increase less in the polaronic solution than in the delocalized solution. Conversely, the bonds with the

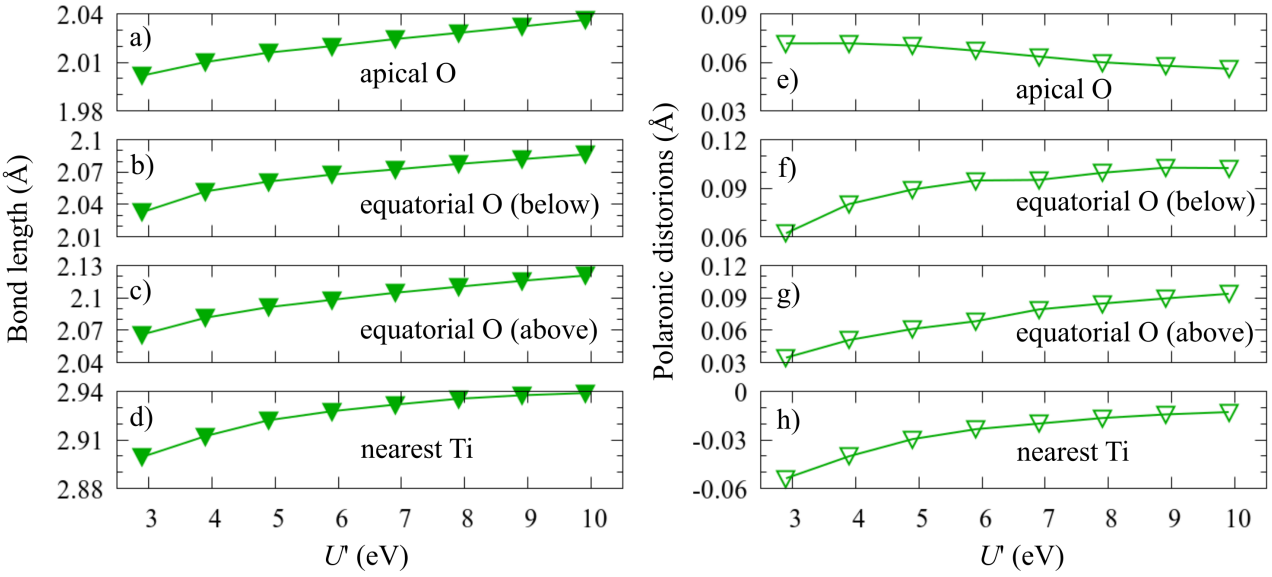

Figure A.7: Dependence of the bond lengths and the polaronic distortions on the U parameter. The bond lengths for a polaronic Ti^{A}_{S1} atom (a-d) and the variations with respect to the delocalized solution (*i.e.*, the polaronic lattice distortions, e-h) are shown for the octahedrally coordinated O atoms (a-c, and e-g) and the nearest Ti atom along [001] (d and h). The two apical O atoms are along $[1\bar{1}0]$, while the four equatorial O atoms can be either closer to the surface or deeper towards the bulk than the polaronic Ti^{A}_{S1} (*i.e.*, above and below, respectively). *[Unpublished Figure]*

equatorial O atoms are stretched more in the localized solution. This different behavior between the equatorial and apical O atoms could be attributed to the spatial extension of the electronic charge of the Ti^{A}_{S1} polaron, which develops more along the [110] and [001] directions, rather than $[1\bar{1}0]$.

Figure A.7(d,h) shows the distortions involving the nearest neighbor Ti atoms along [001]. Being positively charged (nominally Ti^{4+}), the nearest Ti atoms are expected to move towards the Ti^{3+} polaronic site, as observed indeed at $U' = U^{\mathrm{cRPA}}$ (see Sec. 3.2). Surprisingly, larger values of U' push the neighbor Ti sites away from the polaronic Ti^{A}_{S1}. In fact, the Ti-Ti distance increases upon increase of U' [Fig. A.7(d)] and tends to the value obtained in the delocalized solution [the polaronic distortion tends to zero Fig. A.7(h)]. This behavior is not trivial, and its interpretation would require additional efforts. To this aim, it could be helpful to disentangle the various contributions at play, such as the amount of charge localization and the degree of lattice distortions. Therefore, an efficient strategy would be to explore various values of U' and relax only the electronic states, using a fixed lattice structure.

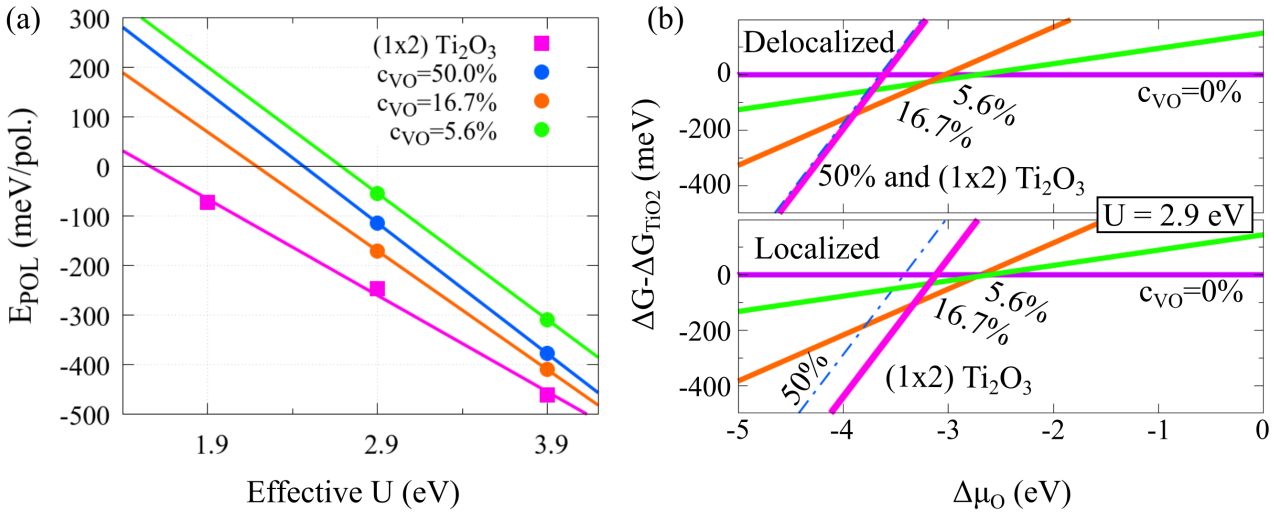

Figure A.8: Effect of the U parameter on the TiO_2(110) surface reconstruction. (a), Polaron formation energy E_{POL} calculated by using different values of U' (*i.e.*, the effective U parameter). (b) TiO_2(110) surface phase diagram; surface free energy ΔG (calculated using $U' = 2.9$ eV) for the most stable configurations obtained from the MD (by using $U' = U^{\mathrm{cRPA}} = 3.9$ eV) for the reduced (1×1) structures at different V_{O} concentrations (all lines except magenta) and for the (1×2) Ti_2O_3 reconstruction (magenta line) as a function of the oxygen chemical potential $\Delta\mu_{\mathrm{O}}$. The delocalized and localized solutions are presented in the upper and lower panel, respectively. *Figure adapted from Physical Review X, Supplemental Material ©2017 American Physical Society* [4].

[A.3.1] The (1×2) surface

As discussed above, the choice of the U' value characterizes the polaronic properties of TiO_2, thus one might wonder about the stability of the polaronic (110) surface. As discussed in Chapter 4, the (1×1)-to-(1×2) phase transition of the TiO_2(110) surface is well described by DFT only if polaron formation is accounted in the calculations. In fact, simulations with the system constrained in the delocalized electron solution disagree with the experimental observations of a structural reconstruction occurring at $c_{V_{\mathrm{O}}} = 16.\%$.

However, the physical description obtained for the localized solution holds qualitatively for any amount value of U'. Figure A.8 shows the results for the polaron formation energy and the stability of the TiO_2(110) surface, obtained considering various values of U'. It has to be noticed that these data were obtained by fixing the lattice structure at the polaronic solution obtained by using $U' = U^{\mathrm{cRPA}} = 3.9$ eV, while only the electronic states were relaxed at the given U'.

Clearly, the (1×2) reconstruction favors polaron formation more than the (1×1) phase, as the reconstruction provides larger polaronic energy at any

value of U'. Specifically, Figure A.8(a) shows the behavior of the polaron formation energy E_{POL} as a function of U'. The energy gain in the (1×2) reconstruction with respect to the reduced (1×1) surfaces is only slightly dependent on the U (*i.e.*, the various $E_{\mathrm{POL}}(U)$ lines are essentially parallel). Furthermore, the polarons remain localized (*i.e.*, $E_{\mathrm{POL}} < 0$) even at very low values of U' (down to $\simeq 2.3$ eV) at the optimal concentration of oxygen vacancies $c_{V_{\mathrm{O}}} = 16.7\%$ and (down to $\simeq 1.5$ eV) in the reconstructed phase. Moreover, the choice of U' is not crucial in changing the physics of the (1×1) to (1×2) transition. In fact, the phase diagram obtained for $U' = 2.9$ eV, shown in Fig. A.8(b), is qualitatively analogous to the corresponding one obtained for $U' = U^{\mathrm{cRPA}} = 3.9$ eV (see Fig. 4.8), and confirm the polaron-driven character of the transition.

Eventually, an analysis including also the lattice distortions induced by the different U' values could change slightly this description, since the $S0$ and $S1$ polarons are affected to a different extent (as shown above in Fig. A.5). Specifically, a reduction of the U' parameter used in calculations could lead to an improved agreement with the experiment: A smaller U' disfavors the formation of $S0$ polarons, which takes place predominantly at $c_{V_{\mathrm{O}}} = 22.2\%$; therefore, the critical V_{O} concentration would be pushed towards the experimental measurement ($c_{V_{\mathrm{O}}} = 16\%$) upon decrease of the U' parameter.

A.4 Van der Waals interactions: Comparison among different methods

In general, the density functional theory does not provide a satisfying description of the long-range van-der-Waals interactions between the adsorbate and the substrate, due to the approximations used for the electronic correlation. Therefore, different computational setups were tested in order to simulate the CO adsorption on the rutile TiO_2(110) surface:

(i) no van der Waals correction (no-vdW);

(ii) the D3 correction method of Grimme *et al.* [220] with the Becke-Jonson damping [221] (PBE-D3);

(iii) the D3 correction, also including the revised version of the PBE functional [138] (revPBE-D3);

(iv) the optimized PBE functional [137], also including the correction proposed by Dion *et al.* [138] (optPBE-DF). This setup was used for the data presented in Ch. 5 (see method section, Sec. 2.1.9).

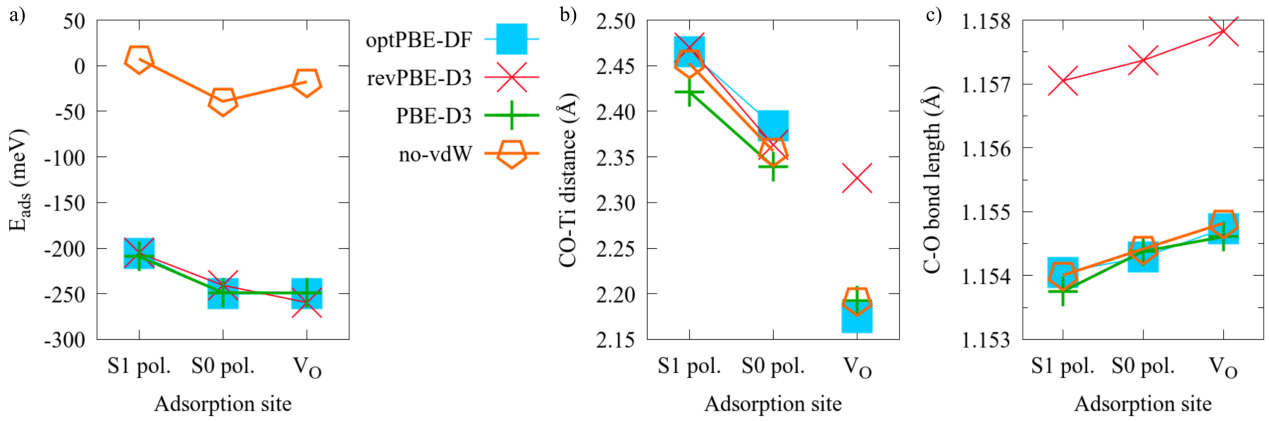

Figure A.9: Comparison among different computational methods. The adsorption energy (a), the CO distance from the rutile surface (b) and the C-O bond length (c) are shown for a weakly reduced slab (c_{V_O}= 5.6%). Various adsorption conditions are considered: CO adsorbed on NNN-Ti^{A}_{S0} in the presence of an $S1$ or $S0$ polaron, as well as CO adsorbed on the V_O. The distance from the surface is given in terms of the nearest Ti atom to the CO molecule. *Figure adapted from Phys. Rev. L, Supplemental Material ©2018 American Physical Society* [2].

Figure A.9 summarizes the most relevant quantities for the CO adsorption, as obtained by using the various setups (i-iv) described above. As shown in Fig. A.9(a), adsorptions are predicted to occur with E_{ads} in a range of -0.2, -0.3 eV, if a van der Waals correction of any type is included in the simulations. There is a satisfying agreement among all adopted schemes, at any considered adsorption site and polaronic configuration. As expected, neglecting the van der Waals correction leads to extremely small values for E_{ads}.

On the other hand, the distance of the CO molecule from the rutile surface is not sensitive to the inclusion of the van der Waals correction [Fig. A.9(b)]. However, a slight disagreement for the revPBE-D3 case for a CO molecule adsorbing on the oxygen vacancy site has to be reported. The revPBE-D3 method also slightly overestimates the C-O bond length by 0.3 pm, as compared to the other setups [Fig. A.9(c)]. The C-O bond length appears to be site dependent, with similar trends among the various computational setups. In particular, when the CO molecule is adsorbed on the NNN-Ti^{A}_{S0} site, the formation of a CO-$S0$-polaron complex increases the C-O bond length, due to the charge transfer towards the $2\pi^*$ antibonding CO orbitals, which does not occur in presence of $S1$ polarons (as described in Ch. 5).

Figure A.10 shows the effects of the computational setups (i-iv) on the vibrational frequency of the CO bond. At variance with the quantities analyzed above (*i.e.*, E_{ads} CO-TiO_2 distance and C-O bond length), the quantitative

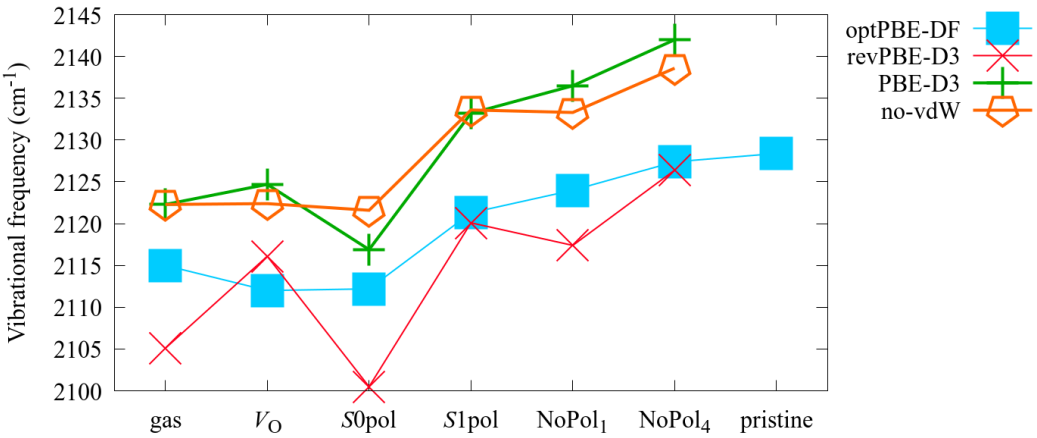

Figure A.10: CO vibrational frequency obtained by different computational methods. The data are shown from left to right for the CO in the gas phase (gas), or adsorbed (on a 9×2 slab with one V_O) on the V_O site (V_O), on the NNN-Ti^A_{S0} site combination with an $S0$ polaron ($S0$pol), or with an $S1$ polaron ($S1$pol), or in the absence of polarons in the proximity ($NoPol_1$), on a Ti_{5c} site far from the V_O and the polarons ($NoPol_4$), and, finally, on a Ti_{5c} on a pristine slab. This figure is analogous to Fig. 5.9, but here a stretched (0.5%) lattice vector along [001] was used to model the slab. *[Unpublished Figure]*

agreement among the different methods is poor. However, all the inspected setups agree on a qualitative level, except the revPBE-D3 method. In fact, for any of the other three methods considered, the vibrational frequency seems to be lowered by the CO molecule adsorbing on the V_O site or forming CO-$S0$-polaron complexes, as compared to the CO molecules at large distance. The frequency reaches larger values as far as the CO adsorption occurs further away from the V_O and the polarons, and tends to the value obtained for the pristine slab (calculated only in the optPBE-DF setup). This result is in qualitative agreement with the experimental infrared spectroscopy data available in literature [211] (see Sec. 5.2).

The computational description of the CO adsorption appears to be solid and robust, even upon change of the computational setup. However, a strong disagreement stands out by considering the vibrations of the CO molecule in the gas phase. In fact, the experiments reveal a blue shift of 45 cm^{-1} for the vibrational frequency of CO adsorbed on a pristine sample [211]. Conversely, the simulations result into a smaller shift (approximatively 20 cm^{-1}) and the value of the vibrational frequency of the gas phase is similar as for CO adsorbing on V_O or forming a CO-$S0$-polaron complex (in any investigate setup, with larger deviations for the revPBE-D3 setup).

Appendix B

Polarity-driven surface reconstructions in $KTaO_3$

Bulk terminated surfaces are typically unstable, and both electronic and atomic relaxations occur, including lattice reconstructions of the surface layers, as described in Chapter 4 for the polaron-driven surface reconstruction on TiO_2(110). In polar materials, the instability is mainly due to an uncompensated polarity. The $KTaO_3$ perovskite offers the possibility to study a wide range of polarity driven relaxations and reconstructions taking place on its (001) surface.

Within this doctorate project, the experiments have driven the study on this compound [5]. This Appendix reports the main findings, with a particular interest on the computational aspects.

Contents

B.1 Introduction

Typically for any material, the atomic structure at the surface differs from the lattice in the bulk. The broken bonds at a bulk terminated surface can induce minor atomic relaxations in order to minimize the surface energy. Alternatively, major structural reconstructions can occur. This is the case of the transition from a (1×1) surface to a (1×2) phase on rutile TiO_2(110), described in Chapter 4, due to the electronic charge trapping and formation of polarons. Another example is given by a well studied class of surface reconstructions due to the polarity of the materials [169].

All ionic materials have unstable, polar surfaces [16]. Ionic crystals can be considered as stacks of alternately charged lattice planes along certain crystallographic directions. When a crystal is terminated perpendicular to such a polar direction, the electrostatic energy diverges. The resulting instability can be compensated in various ways, *e.g.*, by charge transfer, structural reconstructions, changes in the surface morphology, or by chemical doping [222–224]. Such compensation mechanisms often create unusual physical and chemical materials properties [225, 226]. Surface polarity has been discussed controversially, particularly for perovskite oxides. These materials have a chemical formula ABO_3, where the larger A cation is 12-fold coordinated and the smaller B cation is 6-fold coordinated. Along the [001] direction, they contain AO and BO_2 planes that in many cases carry formal positive and negative charges. Tantalates and niobates (B=Ta or Nb) are prototypical examples of polar perovskites. Many compounds exhibit (incipient) ferroelectricity [227], providing attractive options for electronics and sensors. The built-in field can also enhance electron-hole separation in light-harvesting schemes [228]; indeed, these materials are highly efficient photocatalysts [229] with a record quantum efficiency for photochemical water splitting greater than 50% [230]. Because surfaces play a major role in all these applications, it is important to understand which response the system selects to relieve the electrostatic instability.

This Appendix shows how one system reacts in many different ways to alleviate the resulting energetic instability. The polar (001) surface of $KTaO_3$ is described as a representative case using atomically-resolved microscopy and spectroscopy, integral surface analysis techniques, and density functional theory. $KTaO_3$(001) undergoes an entire series of routes to polarity compensation.

This brief introduction is followed by some considerations on the bulk $KTaO_3$ and its description via several computational techniques (Sec. B.2). The description of the $KTaO_3$(001) surface includes a discussion on the two types of bulk termination, formed by KO or TaO_2 planes (Sec. B.3), the analysis of the energy minimization process upon annealing in vacuum (Sec. B.4)

and in a water environment (Sec. B.5). Details on the computational and experimental methods are described in Sec. B.6. This Appendix is concluded by Sec. B.7, which provides the reader with an overview of the whole study and points out the most interesting outcomes.

B.2 Bulk $KTaO_3$

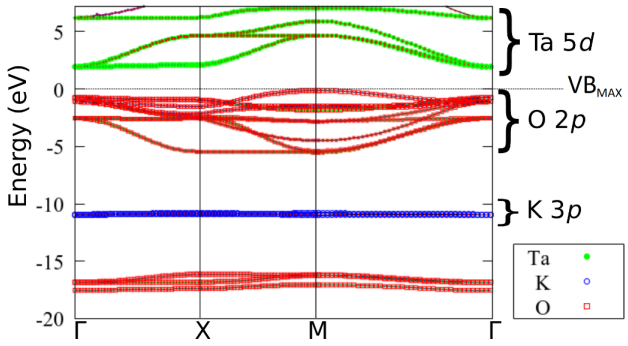

Figure B.1: Band structure of bulk $KTaO_3$. Different colors indicate the projection on the Ta (green), K (blue) and O (red) orbitals. *Figure adapted from Science ©2018, Supplemental Material* [5].

This study analyzes via computational and experimental techniques the electronic and structural properties of the $KTaO_3(001)$ surface. Calculations are performed in DFT framework, adopting the PBE functional (details of the computational setup in Sec. B.6).

Figure B.1 shows the calculated band structure of bulk $KTaO_3$, projected onto the various atomic orbitals. The conduction band is formed mainly by Ta $5d$ states partially mixed with O p states, while the valence band originates mainly from oxygen p states. K p states appear at deeper energies. The calculated band gap at the PBE level is approximatively 2 eV, significantly smaller than the experimental value of 3.6 eV [231], which is due to the well-known limitations of standard DFT. Beyond-DFT methods could certainly improve the description of the electronic structure of the bulk [232], however they would be too hardware-demanding when applied to slabs containing many atoms (this study involves large surface supercells with more than one thousand atoms).

Fig. B.2 shows a comparison for the energy band gap obtained by different methods. As mentioned already, the PBE functional is not able to reproduce the experimental band gap, unless a large correction to the on-site interaction is applied to the Ta atoms ($U_{\mathrm{Ta}} = 8.4$ eV), which is physically not justified.

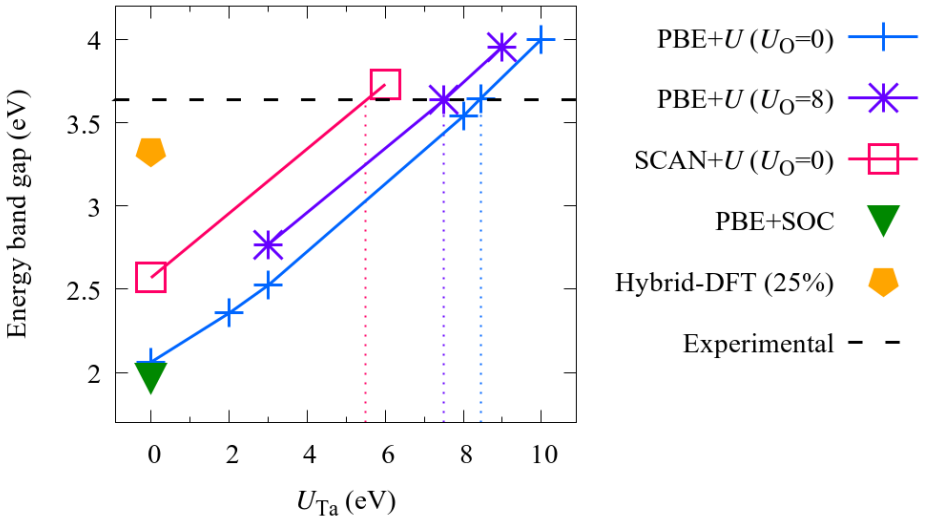

Figure B.2: Computational energy band gap of bulk $KTaO_3$. Different methods are compared to the experimental value (dashed line), shown as a function of the on-site interaction parameter used on the Ta atoms (U_{Ta}): PBE functional with no further correction [PBE+U ($U_O = 0$)]; PBE functional with further correction of the on-site interaction (U_O = 8 eV) on the O atoms [PBE+U ($U_O = 8$)]; SCAN functional [SCAN+U ($U_O = 0$)]; PBE functional, including spin orbit coupling (PBE+SOC); hybrid functional (Hybrid-DFT (25%)]. The dotted lines outline the intersection with the experimental value. *[Unpublished Figure]*

Adding a correction also on the O atoms (U_O = 8 eV) does not change the result substantially. Localized states are indeed expected to play a minor role in bulk $KTaO_3$, thus the DFT+U does not significantly improve the description of the system. The inclusion of the spin-orbit coupling term in the calculation is also irrelevant. While the SCAN [233] functional improves only slightly the band gap description, the real breakthrough is obtained only by adopting hybrid functionals. In this study, part of the PBE results for the $KTaO_3$(001) surface were compared to the hybrid functional calculations (on structures kept fixed at the atomic position relaxed by PBE). However, a full study of the $KTaO_3$(001) surface and its various surface reconstructions, including atomic relaxations performed at the hybrid functional level appears too demanding.

As shown in the following, the small band gap obtained in the PBE framework leads to some discrepancies with the experiments. Nevertheless, the overall picture is satisfyingly reproduced.

B.3 The $KTaO_3(001)$ terraces

A scanning tunneling microscopy (STM) image [Fig. B.3(A)] of the surface of a $KTaO_3(001)$ single crystal after cleaved in ultrahigh vacuum (UHV) shows three steps running horizontally along the [100] direction. These steps have a height of about 4 Å, *i.e.*, the $KTaO_3$ lattice constant. The entire area is covered by alternating KO and TaO_2 terraces separated by half-unit-cell steps. Interestingly, these terraces run uninterrupted across the full-height steps. The KO planes are always on top, while TaO_2 is in the ridge region; apparently the KO plane fractured more easily during cleavage. The KO and TaO_2 terminations have a formal charge of -1e and +1e per unit cell, respectively. The characteristic terrace size is 30 to 80 Å, and their ratio is 1:1. Thus, the top layer is polarity-compensated on a long-range scale [169]. Although the electronic structure appears delocalized with no measurable atomic corrugation in STM, noncontact atomic force microscopy (nc-AFM) readily shows at atomic resolution a perfect (1×1) bulk-terminated structure with a low defect concentration [Fig. B.3(B)]. In a constant-height AFM image, the darker regions with atomic resolution correspond to the higher-lying KO terraces, and bright, uniform regions are lower-lying TaO_2 terraces. All of the AFM images were taken in constant-height mode, and on TaO_2 terraces the attractive forces were smaller because of the larger tip-surface distance. The AFM imaging mechanism on the KO terraces appears analogous to the prototypical NaCl(001) surface, which has an identical arrangement of surface ions [234], while imaging the TaO_2 on the lower terraces proved more difficult.

Scanning tunneling spectroscopy (STS) showed that the two terminations have distinctly different electronic structures [Fig. B.3(C)]. The KO terraces have a wide band gap spanning from -3.5 to $+1$ V, whereas TaO_2 terraces appears metallic with a shallow state at -0.2 eV, and several deeper-lying states. These in-gap states does not appear on the smaller TaO_2 terraces (below approximatively 8 unit cells size), and were also absent in the border area (about 2 unit cell wide) around the KO islands. Figure B.3(E) shows a representative spatial distribution of the in-gap states. These states exhibited a characteristic wave-like pattern with approximatively 16 Å periodicity, indicative of their delocalized (band-like) character [48, 235]. The electric charge in the in-gap states counteract the electrostatic potential arising from the TaO_2^+ polarity. However, these states form only when the terrace width (and the related electrostatic potential) exceeds a certain critical limit. The situation bears similarities to the formation of the 2D electron gas at polar interfaces, where acritical film thickness is necessary [225, 236]. These in-gap states already form on as-cleaved surfaces, which do not show any defects, and DFT calculations indicate

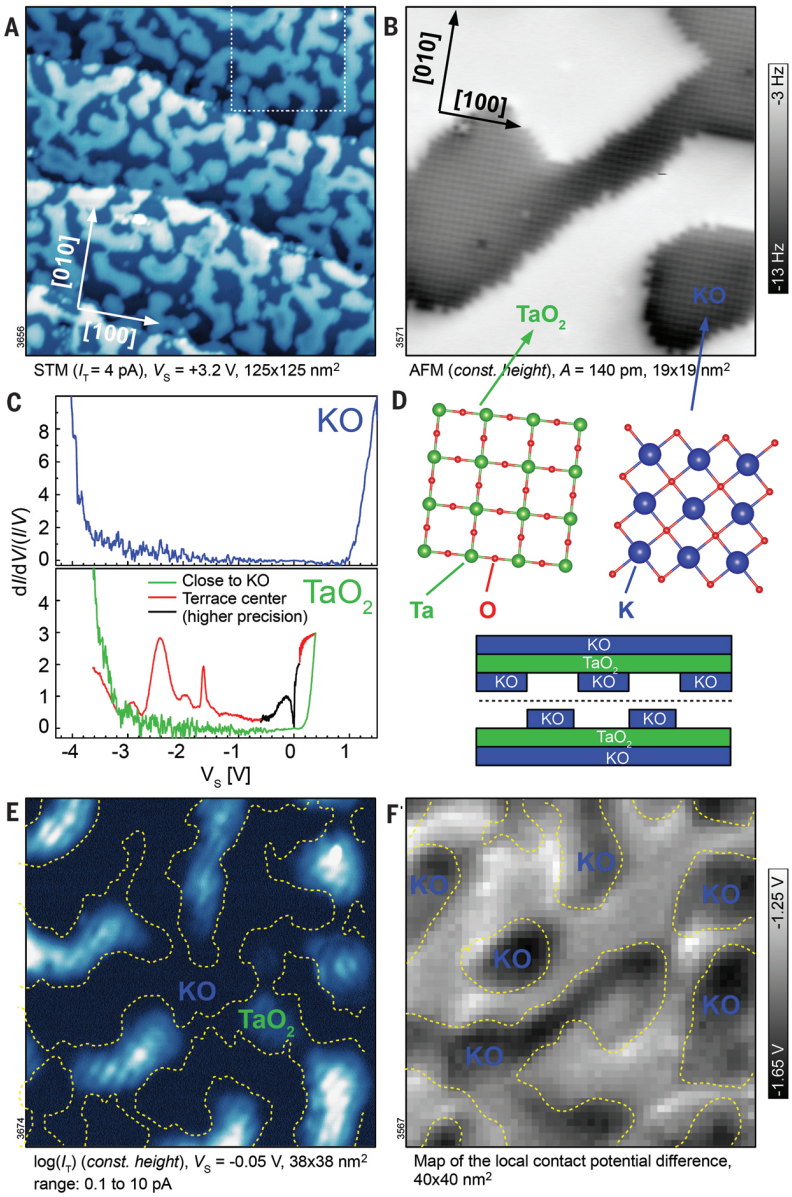

Figure B.3: Cleaved $KtaO_3(001)$ Large-area STM (A) and atomically-resolved AFM (B) images of a $KTaO_3(001)$ surface, obtained by cleaving at 261 K. STS spectra measured above the KO and TaO_2 terraces (C). Atomic structure of the TaO_2 and KO terraces, and schematic drawing of the cleaving (D). Spatial distribution of the in-gap states (E), measured in the region marked by a dashed square in panel A; dashed lines mark steps. KPFM image (F) showing the local electrostatic surface potential (measured on a different region). *Figure adapted from Science ©2018* [5].

a metalization of the surface. The uncompensated electrostatic potential is a driving force for further polarity-compensation mechanisms, and we estimated its magnitude using Kelvin probe force microscopy (KPFM). On as-cleaved surfaces, the local contact potential varied by 0.3 V. Defect-free surfaces were only achieved for samples cleaved below room temperature.

B.4 Annealing in vacuum and the labyrinth structure

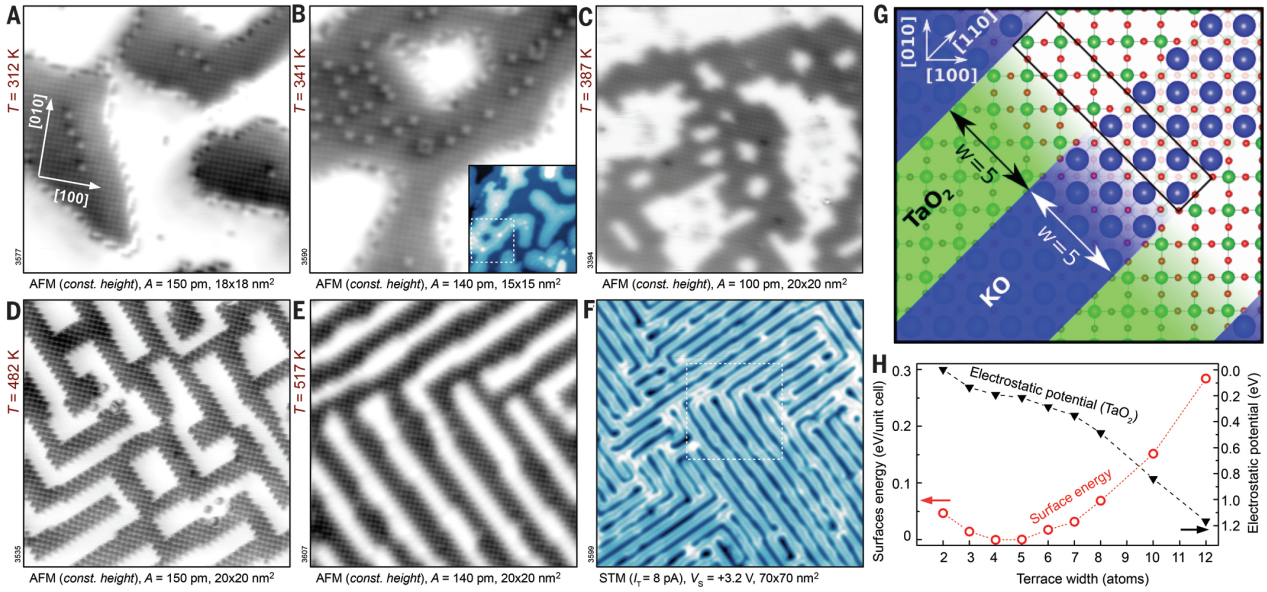

Figure B.4: $KTaO_3$ surface upon annealing. AFM images (measured at 4.8 K) of the surface after annealing in vacuum to 312 (A), 341 (B), 387 (C), 482 (D) and 517 K (E). The inset in B shows a larger-area STM image of the region. STM image (F); the corresponding area in E is marked by a dashed square. Top view of the model used for the DFT calculations (G); the 2D unit cell is marked by a rectangle. Calculated surface energy (circles) and electrostatic potential in the center of the TaO_2 terrace (triangles) as functions of the terrace width (H) *Figure adapted from Science ©2018* [5].

Annealing the surface in vacuum results in the development of more efficient polarity-compensation mechanisms. After raising the sample temperature to 312 K, defects forms on the KO terraces [Fig. B.4(A)]. AFM images of these defects agrees well with Cl vacancies observed on the prototypical NaCl(001) surface [234]. Accordingly, the defects are attributed to O vacancies, with

the corresponding formal charge of $+2e$ being suitable for compensating the negative charge of the KO regions. The vacancies appear in central regions of the large terraces, *i.e.*, at the locations with the highest electrostatic potential. The O vacancies are likely created by the migration of O atoms from the KO terraces toward the interface with TaO_2. Annealing at higher temperature ($T = 387$ K) results in small holes in the central regions of the KO terraces [Fig. B.4(C)]. The steps tend to align along $\langle 110 \rangle$, the nonpolar step direction of KO. Upon further annealing to 482 and 517 K, the holes interconnect and form a labyrinth-like structure [Fig. B.4(D,E,F)]. At the atomic scale, the surface still shows the original bulk (1×1) termination, with the KO and TaO_2 terraces alternating in a quasiperiodic pattern separated by half-unit steps. The ratio of KO:TaO_2 remains 1:1, indicating that the process is only caused by KO rearrangement without desorption or diffusion from or to the bulk. KPFM measurements show that the O-vacancy formation reduces the original electrostatic potential by half, and after the surface rearranges into the labyrinth structure, the measured potential variations are negligible. The labyrinth structures has a characteristic terrace width of about 15 Å (4 to 5 atoms). Interestingly, the terrace width does not change upon further annealing: The pattern is remarkably stable up to 700 K. At even higher temperatures, the ordering is lost, likely because of K segregation from the bulk [237]. The magic size of the stripes likely originates from a competition between two driving forces: Minimizing the terrace size suppresses the electrostatic potential arising from the polarity, while surface steps cost energy. This hypothesis was tested by calculating the surface energy and electrostatic potential as a function of terrace width. The structural model consists of alternating KO and TaO_2 terraces of equal widths w (where w equals the number of K atoms in the 2D unit cell) separated by steps running along [110] [Fig. B.4(G)]. The energy minimum is achieved for a w of 4 to 5 atoms, in agreement with the experiment [circles in Fig. B.4(H)]. The electrostatic potential changes smoothly in the range $1 < w < 8$ and then startes to deviate rapidly for higher w, indicating increasing polar instability [triangles in Fig. B.4(H)].

Figure B.5 shows the calculated density of states as a function of the terrace width. A gradual metalization of the surface occurs.For the terrace width below 4 atoms, there are essentially no changes in the electronic structure and in the band gap. For wider terraces, the filled O p states of the KO terrace as well as the empty Ta d states lying on the TaO_2 terrace gradually approach the Fermi energy and start to overlap at $w = 12$. The mechanism shown in these calculations is consistent with the STS spectra shown in Fig. B.3(C): The shallow delocalized in-gap state centered at -0.2 eV can be attributed to the downwards shift of the conduction band and its partial electronic filling.

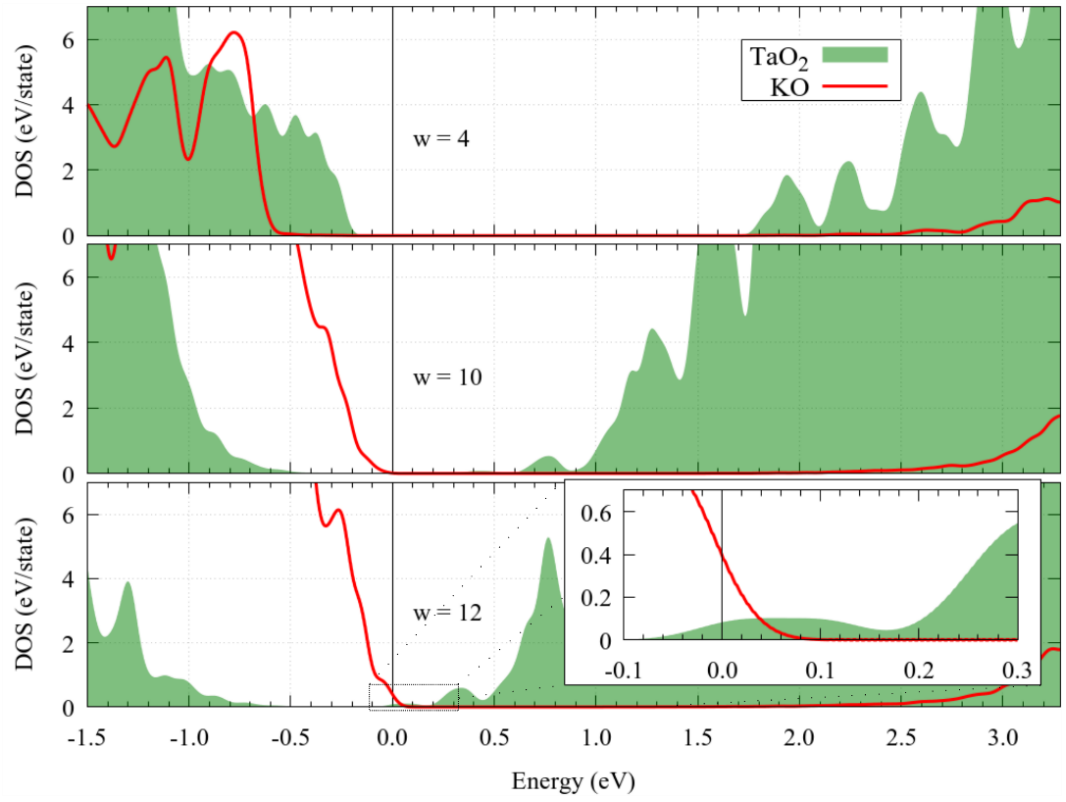

Figure B.5: $KTaO_3(001)$ density of states. Calculated DOS of the labyrinth phase for different terrace width ($w = 4$, $w = 10$ and $w = 12$ from top to bottom). The contributions from the TaO_2 and KO terraces are marked by green areas and red lines, respectively. The inset shows a detail of the metallic behavior at the large terraces ($w = 12$). *Figure adapted from Science ©2018, Supplemental Material* [5].

The experiment has been performed on a material with n-type doping, thus the conduction band is likely first filled by electrons from bulk dopants. The calculations were performed with stoichiometric slabs, thus the charge transfer to the TaO_2 terraces can only occur from the KO-termination. However, the computational setup used here can outline the fundamental mechanisms taking place in the polarity compensation, but it is not accurate enough for a full description of the problem. Most notably, standard DFT strongly underestimates the insulating gap (as discussed in Sec. B.2) and does not properly describe the electron localization effects, including polaron formation [141] (which could possibly be the character of the deeper in-gap states) and the energy gain associated with this phenomenon. In fact, the electron removal from KO could likely be associated with the formation of a hole-polaron. This probably occurs at the step edges, where the lattice flexibility is enhanced.

The electrons extracted from KO can subsequently form electron-polarons at the TaO2 terraces. The description of the polaronic effects is, however, beyond the scope of the present study, but will be addressed in the future.

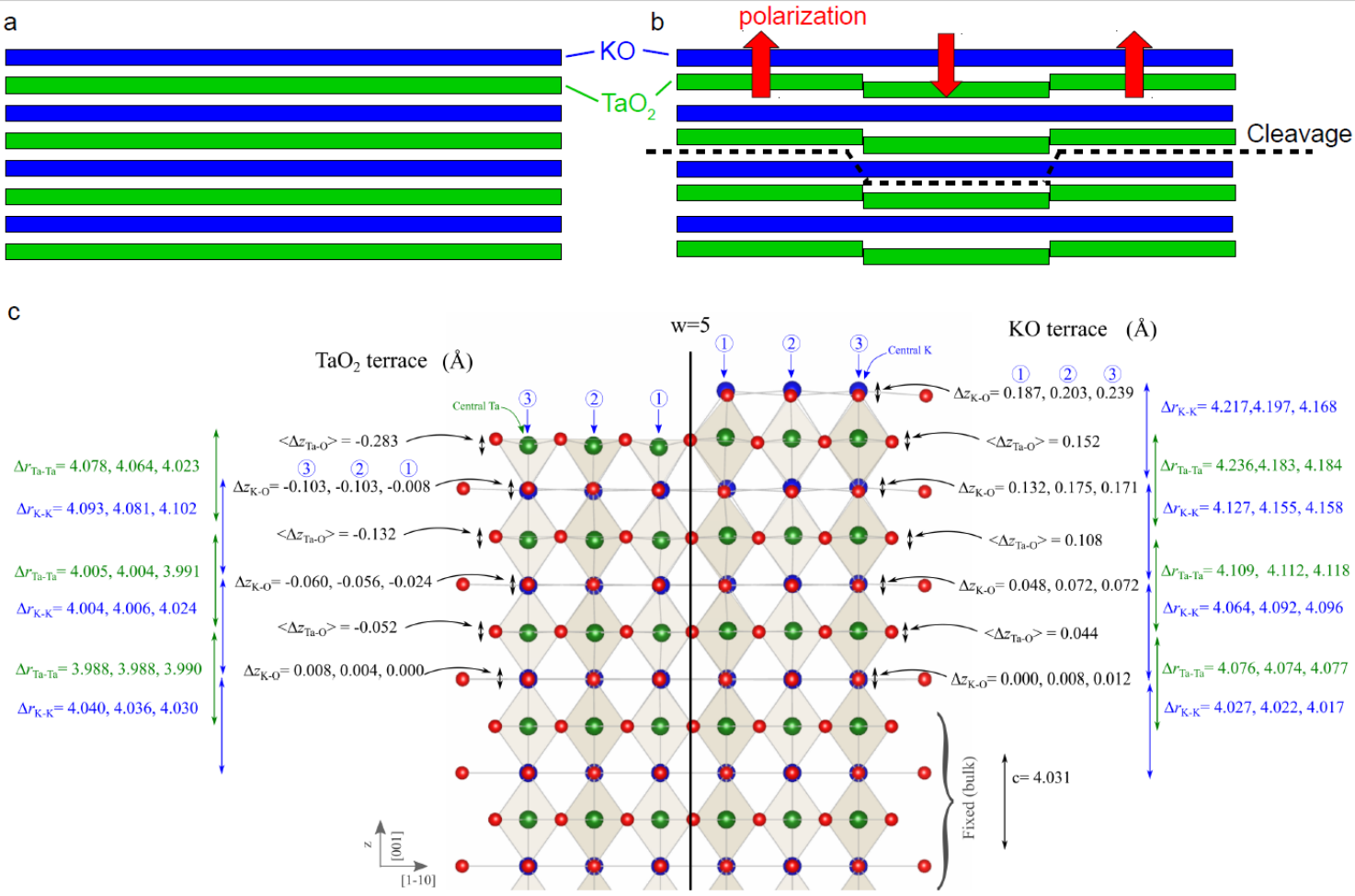

Figure B.6: Ferroelectricity. Sketch of the layered structure of the bulk $KTaO_3$ (a). Sketch of the strain-induced ferroelectric domains, associated with relaxation of the Ta octahedra (b). The crystal cleavage occurs at the point where the bonding towards the neighboring KO layer is weakened. Side view of the calculated slab with $w = 5$ (c). The lattice distortions are marked: The labels 1, 2, and 3 indicate the position with respect to the edge for both KO and TaO_2 terraces. Similar surface ferroelectric distortions can be obtained adopting different type of setups (a mirror symmetry with relaxed central layers, and a glide symmetry with relaxed central layers). *Figure adapted from Science ©2018, Supplemental Material* [5].

Considering these calculations, the exact polarity-compensation mechanism

of the as-cleaved KO terraces remains an open question. The low defect density and the absence of an electronic reconstruction should result in a relatively high electrostatic potential (> 1 V), yet the experimental KPFM data showed considerably smaller potential corrugations. The incipient-ferroelectric character of the material could contribute to the polarity compensation, allowing for generation of electric fields inside the material at no energy cost. The calculations show indeed ferroelectric-like lattice distortions (see Fig. B.6). Further, the sample cleaving always results in a very characteristic layout of the KO/TaO_2 terraces that cross full steps without interruption. Formation of strain-induced ferroelectric domains [238] could occur during the cleavage, and the resulting terrace layout would be a printout of these domains. Strain results in ferroelectricity, small domains of opposite orientations form to avoid a huge energy of the electrostatic field. The ferroelectric distortion is typically associated with relaxation of the B-type cation lattice (Ta in this case). As a result, bonding towards the neighboring KO plane is weakened, and the crystal cleavage proceeds through this plane. The KO terraces formed during the cleaving typically cross full-unit-steps without being interrupted, which supports their relation to the bulk domain structure. A similar effect was reported for the layout of SrO/TiO_2 on cleaved $SrTiO_3(001)$ surfaces [239]. Figure B.6(c) shows a front view of the calculated $w = 5$ slab, symmetric along $[1\bar{1}0]$ (*i.e.*, with respect to the central atoms indicated in the figure) and [001]. The calculations confirm the existence of ferroelectric relaxations (Δz) involving both Ta and K atoms, with a larger relative displacements of the Ta layers (Δr), according to the schematic drawing in Fig. B.6(b). This indicates that the ferroelectric lattice distortions remain in the material even after the cleavage, stabilized by the surface polarity.

B.5 The water induced reconstruction

The most efficient polarity-compensation mechanism develops after exposing the surface to H_2O vapor. Water induces a complete restructuring of the surface layer, even in UHV and at room temperature. After dosing 300 Langmuir (L) of water vapor at 325 K the surface becomes flat, with only full-unit-cell steps [Fig. B.7(A)]. More detailed AFM shows a homogeneous phase with a (2×1) symmetry; low-energy electron diffraction confirms that the entire surface has been transformed [Fig. B.7(B)]. This transition requires high doses of water; Fig. B.7(C) shows a surface exposed to 100 L of H_2O. Here the occasional small island of the original bulk-terminated KO is found, interfaced with the (2×1) overlayer. The (2×1) termination can be switched back to the (1×1). Annealing above 488 K in UHV results in water desorption,

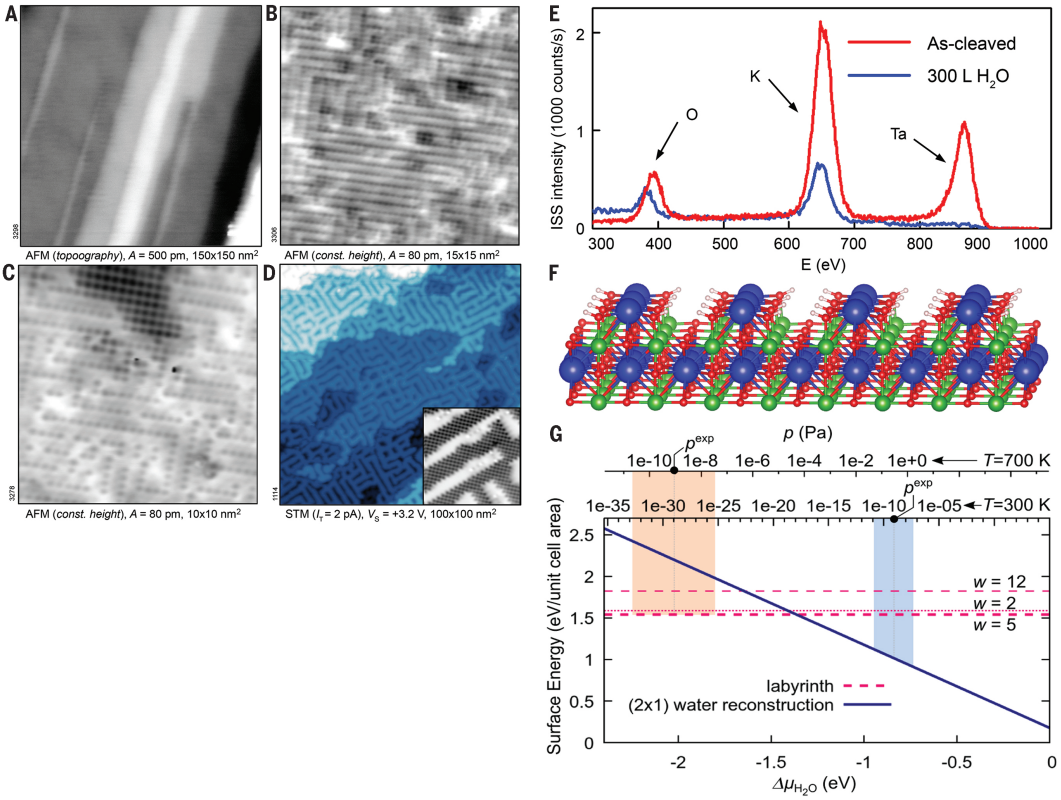

Figure B.7: The hydroxylated (2×1) surface. AFM image of the $KTaO_3$(001) surface after exposure to 300 L H_2O at 325 K (A). Atomically resolved detail (B), showing a homogeneous superstructure with (2×1) ordering. AFM image of the surface exposed to 100 L H_2O at 298 K (C), showing the interface between an original (1×1) KO terrace and the (2×1) phase. STM image (D) of the (2×1) surface after annealing to 488 K; the inset shows an atomically resolved AFM image. Low-energy He^+ ion scattering spectra of the as-cleaved, bulk-terminated surface and the (2×1) overlayer (E). Atomic model of the (2×1) overlayer (F). Phase diagram for the transition between the (1×1) bulk termination and the (2×1) structure (G). *Figure adapted from Science ©2018* [5].

and formation of the labyrinth-like structure of alternating KO/TaO_2 terraces, confirming reversibility between these two surface phases [Fig. B.7(D)]. To determine the chemical composition of the (2×1) superstructure, low-energy He^+ ion scattering is an ideal method because it is only sensitive to the very top layer of the surface. The red curve in Fig. B.7(E) was measured on an as-cleaved surface. As expected, O, K, and Ta are present. After dosing with water, the Ta signal completely disappears. X-ray photoelectron spectroscopy reveals the hydroxylated character of the (2×1) termination, and also excludes

any possible contamination from the water exposure. It appears that water dissolves the KO islands and redistributes them across the TaO_2 planes. A proposed structural model is shown in Fig. B.7(F). Each KO unit reacts with one H_2O molecule, resulting in one $K(OH)_2$ unit per (2×1) unit cell. This termination is also polarity-compensated, with a net charge of $-0.5e$ per (1×1) unit cell. A (2×1) termination of $KTaO_3$(001) has already been reported [240] and investigated theoretically [241], but the presence of water had not been considered.

B.6 Computational and experimental methods

[B.6.1] **Simulations**

Simulations were performed in the DFT framework using the Vienna ab initio package (VASP) [118, 119] and adopting the generalized gradient approximation (GGA) within the Perdew, Burke, and Ernzerhof parametrization [120]. An accurate description for the bulk $KTaO_3$ structure was achieved by using a plane-wave energy cutoff of 500 eV and a $12 \times 12 \times 12$ k-point mesh for the integration in the reciprocal space.

The same energy cutoff and k-point 2D density were used to model the $KTaO_3$(001) surfaces. The labyrinth structure was modeled with a symmetric slab containing 10 layers of KO and 9 layers of TaO_2, with 15 Å of vacuum region. The 5 central layers were kept fixed at the bulk positions, while the others were relaxed with standard convergence criteria. Different terrace widths were considered ($w = 2, 3, 4, 5, 6, 7, 8, 10, 12$) by using large ($w\sqrt{2} \times \sqrt{2}$) 2D unit-cell (leading to supercells containing up to 1080 atoms). The structural relaxation for each width was performed in the ($w\sqrt{2} \times \sqrt{2}$) cell.

The comparison of the ground state energies of the various terraces was performed by using suitable supercells, which minimize the size differences among each others. Such supercells were constructed following the least common multiple strategy discussed below. A ($8\sqrt{2} \times \sqrt{2}$) cell was used for the $w = 2, 8$ structures, ($10\sqrt{2} \times \sqrt{2}$) for the $w = 2, 5, 10$ structures, ($12\sqrt{2} \times \sqrt{2}$) for the $w = 2, 3, 4, 6, 12$ structures, and ($14\sqrt{2} \times \sqrt{2}$) for $w = 2, 7$. The largest $w = 14$ cells contain 1260 atoms. All energies have been slightly shifted (*i.e.*, by about 10 meV) in order to keep the energy of the $w = 2$ phase equal in all four cases. The electrostatic potential energy was computed as the average potential centered around the Ta ions in the middle of the TaO_2 terraces.

The (2×1) water-induced reconstruction was initially relaxed using a 2×1 unit-cell, while the final surface energy was computed with a ($12\sqrt{2} \times \sqrt{2}$) set-up in order to compare the stability of this phase with the labyrinth structure.

The surface free energy γ was calculated using standard ab initio atomistic thermodynamics [135], by neglecting the configuration entropy and phonon contributions, using the formula:

$$\gamma = \frac{1}{2A}\left[E^{\text{slab}} - N_{\text{K}}E^{\text{bulk}}_{\text{KTaO}_3} - \frac{N_{\text{H}}}{2}\left(E_{\text{H}_2\text{O}} + \Delta\mu_{\text{H}_2\text{O}}(T,p)\right)\right] \tag{B.1}$$

where the factor $2A$ scales the energy to the surface unit-cell area, N_{K} and N_{H} are the numbers of K and H atoms respectively, E^{slab} is the total energy calculated for the various structures [w-labyrinth and the (2×1) reconstruction], $E^{\text{bulk}}_{\text{KTaO}_3}$ is the energy of the $KTaO_3$ bulk system, $E_{\text{H}_2\text{O}}$ is the ground state energy of water, and $\Delta\mu_{\text{H}_2\text{O}}(T,p) = \mu_{\text{H}_2\text{O}} - E_{\text{H}_2\text{O}}$ represents the relative chemical potential of water as a function of temperature (T) and pressure (p), subjected to the condition $\mu_{\text{H}_2\text{O}} < E_{\text{H}_2\text{O}}$ (i.e. $\Delta\mu_{\text{H}_2\text{O}} < 0$) [242].

[B.6.2] Experiments

Synthetic single-crystalline $KTaO_3$ samples were prepared by solidification from a nonstoichiometric melt. Trace impurities of Ba, Cu and Yb were used to ensure n-type electrical conductivity for stable STM operation. The samples were cleaved under UHV conditions at temperatures ranging from 250 to 350 K by using a tungsten-carbide blade.

Combined STM/AFM measurements were performed at 4.8 K in a UHV chamber with a base pressure of 10^{-9} Pa. Tuning-fork-based AFM sensors with W tips and a separate wire for the tunneling current were used. Typical STM imaging was performed at a sample bias of approximately +3 V. Controlled annealing of the samples was performed in a manipulator outside the STM/AFM head. The sample temperature was measured by a thermocouple with an absolute precision of ±5 K. The low-energy ion scattering experiments (ISS) were performed using an incident He^+ ion energy of 1 keV was used. ISS, XPS and LEED turned out to partially damage the surface, therefore the surface was newly prepared before each measurement. These techniques probably induce oxygen vacancies in the surface layer, which alters the polarity-compensation mechanisms. The KPFM measurements were performed with a distance of 13 Å from the surface (STM feedback was used for adjusting the tip-sample distance at each location). All data have been obtained on the same surface and no significant tip changes occurred during the entire session.

B.7 Final considerations

The $KTaO_3$(001) surface exhibits a rich spectrum of mechanisms for compensating the surface polarity, and a proper control of the environment can

be used to tailor which one is at work. The phenomena observed on the as-cleaved surfaces, *i.e.*, electronic reconstruction and ferroelectric lattice distortions, are well known from perovskite heterostructures. Two-dimensional electron gas (2DEG)-like states are spatially confined to the highly polar regions. The labyrinth-like pattern formed upon annealing represents an interesting template for charge-carrier separation in light-harvesting devices, but protection against environmental influences would need to be facilitated for practical use. Although such a structure minimizes the surface energy, the corresponding energy gain is almost an order of magnitude lower compared to chemically-induced polarity compensation by water. The phase diagram in Fig. B.7(G) shows that the mechanisms encountered in UHV decreases the surface energy by tenths of electron volts, whereas hydroxylation brought an order of magnitude higher. Perovskite surfaces in ambient conditions are typically hydroxylated and near the bulk-termination, but little is known about the exact surface structure. The (2×1) reconstruction observed here could therefore serve as a working model for future studies into the surface chemistry of perovskite oxides.

Appendix C

Additional figures

The figures collected in this Appendix aim to provide the reader with additional information. These figures show technical details, which would be too tedious to show in the main text. However, they are useful to deliver a more comprehensive picture of the polaron formation phenomenon on oxides surfaces.

List of additional figures:

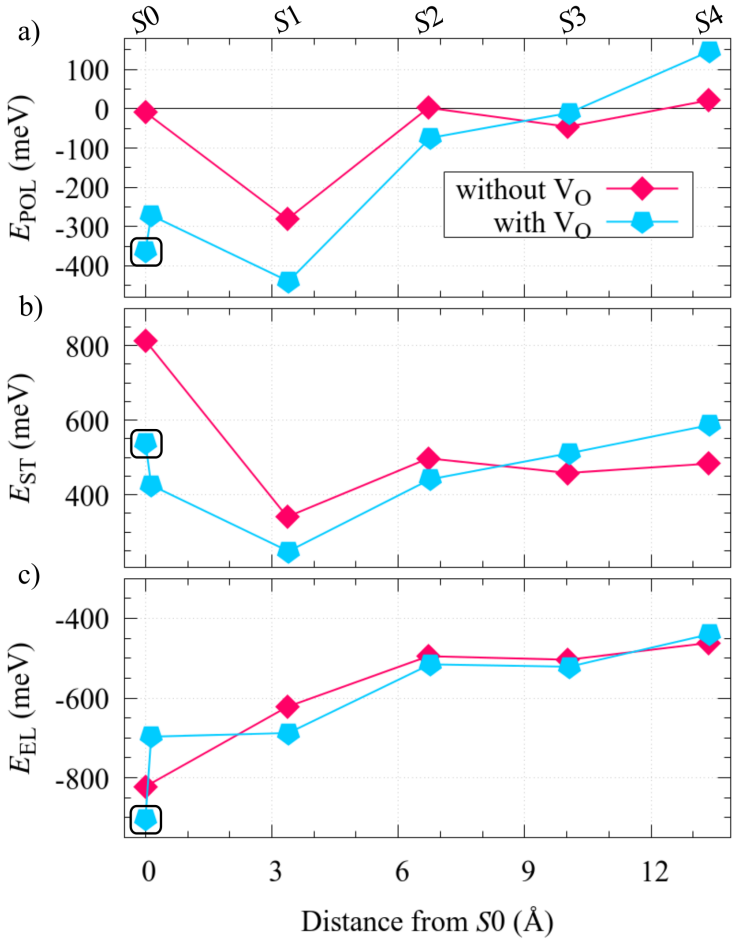

Figure C.1: Trend of the polaronic properties towards the bulk. Polaron formation energy E_{POL} (a), strain energy E_{ST} (b), and electronic energy E_{EL} (c) of polaron localized on Ti^A sites on various layers (from $S0$ to $S4$). Data obtained by using a 8-layer deep, 3×2-large slab with one polaron considering both the cases of one and no V_{O} on the surface. The Ti^A sites closest to the V_{O} were considered, while the circled point refers to the next nearest neighbor Ti^A_{S0} site from the vacancy. *Comment on the Figure: The trend of the polaronic energies (E_{POL}, E_{ST} and E_{EL}) for polarons on shallow layers (i.e., $S0$, $S1$ and $S2$) are discussed in Fig. 3.3: the energy values of $S2$ polarons seem to be converged to the bulk values defined by the deeper layers (i.e., $S3$ and $S4$). Figure adapted from Physical Review B ©2018 American Physical Society [3].*

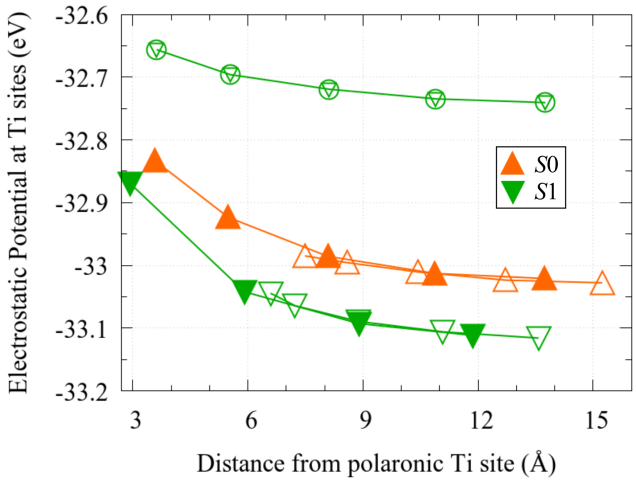

Figure C.2: Electrostatic potential energy around a Ti^{A}_{S1} polaron. An excess electron was introduced into a pristine slab ($-e$ charged system), forming a Ti^{A}_{S1} polaron. The averaged electrostatic potential E_{pot} is evaluated at Ti^{A} sites on the $S0$ (upper-pointing triangle) and $S1$ (down-pointing triangle) layers; circled points refer to Ti^{B}_{S1} sites. Filled and empty symbols refer to Ti sites with the same and different y component as for the polaron, respectively. *Comment on the Figure: The Ti^{A}_{S1} polaron affects the electrostatic potential on the surrounding Ti^{A}_{S1}, Ti^{B}_{S1} and Ti^{A}_{S0} atoms, and, consequently, the formation of additional polarons (analyzed in Fig. 3.4). The trend shown in the figure confirms the repulsive polaron-polaron interaction: Negative charges in the surroundings of the polaron experience an E_{pot} higher than at large distance. At large distance from the polaron, Ti^{B}_{S1} sites show the most unfavorable E_{pot} for charge localization, among the considered sites. [Unpublished Figure]*

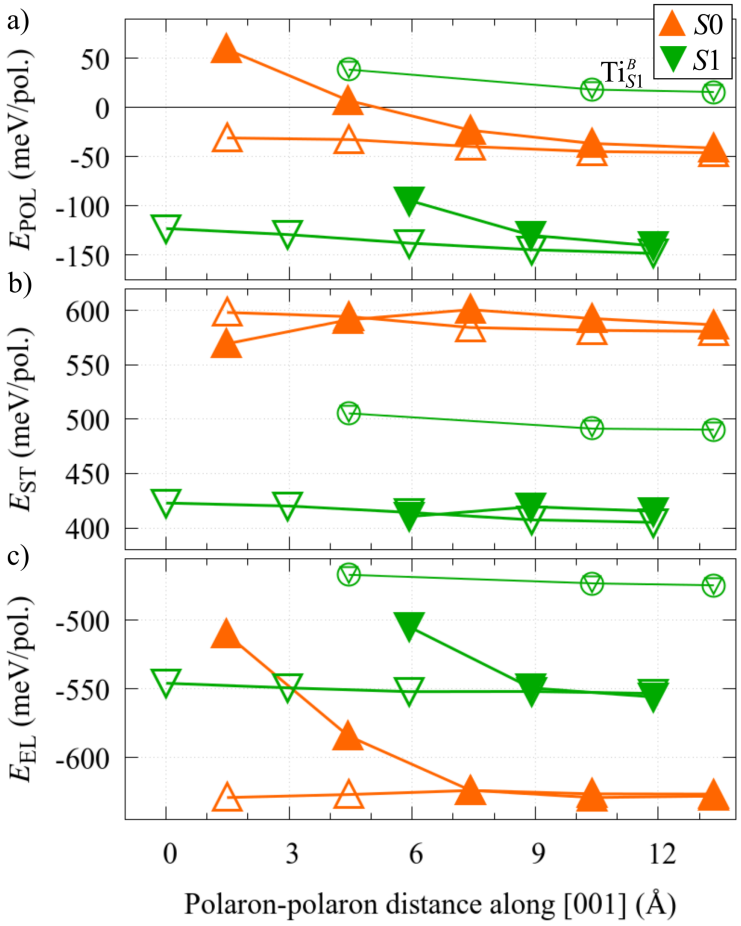

Figure C.3: Details of the polaron-polaron interaction. E_{POL} (a), E_{ST} (b) and E_{EL} (c) as a function of the polaron-polaron distance (expressed in terms of the [001] component) The system is modeled by using a 9×2-large pristine slab and manually introducing two excess electrons (*i.e.*, $-2e$ charged state). One polaron is fixed at a Ti^{A}_{S1} site, while the other one explores both the $S0$ (up-pointing triangles) and $S1$ (down-pointing triangles) layers. Filled (empty) symbols represent polarons on Ti rows with the same (different) y coordinate(s). Circled points refer to Ti^{B}_{S1} sites for the second polaron. These data complements the results collected in Fig. 3.4. *Figure adapted from Physical Review B ©2018 American Physical Society* [3].

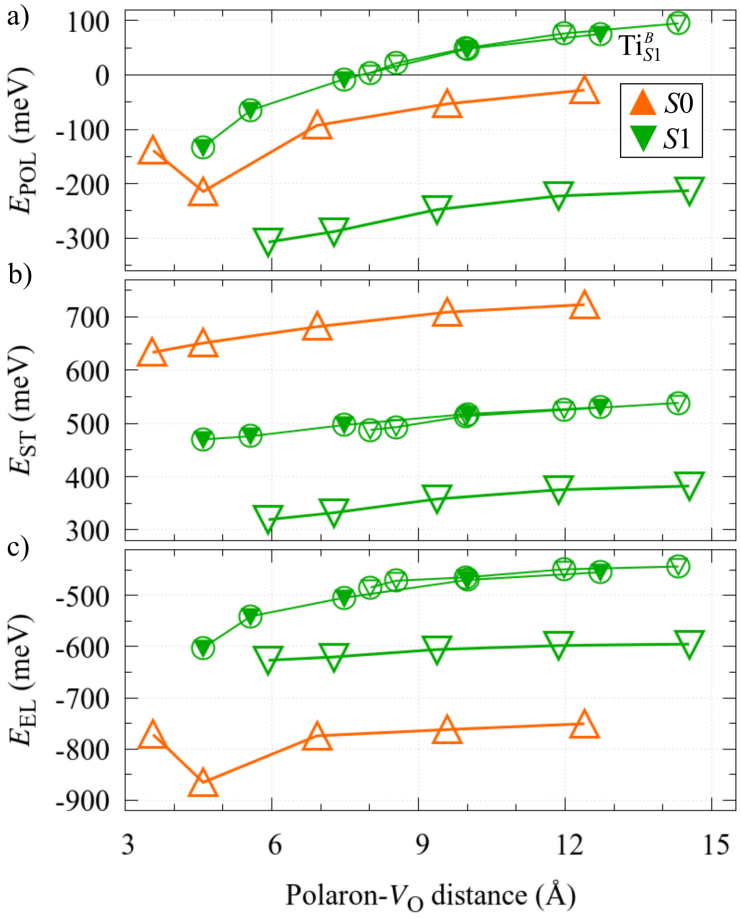

Figure C.4: Details of the polaron-V_O interaction. E_{POL} (a), E_{ST} (b) and E_{EL} (c) as a function of the polaron-V_O distance. A 9×2-large slab with one V_O is used: one electron is manually removed (the system is in a $+e$ charged state). The polaron explores Ti sites on both the $S0$ (up-pointing triangles) and $S1$ (down-pointing triangles) layers. Empty symbols represent polaron positions with different $[1\bar{1}0]$ coordinate with respect to V_O. Circled points refer to Ti^B_{S1} sites; Ti^B_{S0} polarons (not reported) were obtained only on sites adjacent to the V_O, showing a positive E_{POL} ($\simeq$ 300 meV). *Figure adapted from Physical Review B* ©*2018 American Physical Society* [3].

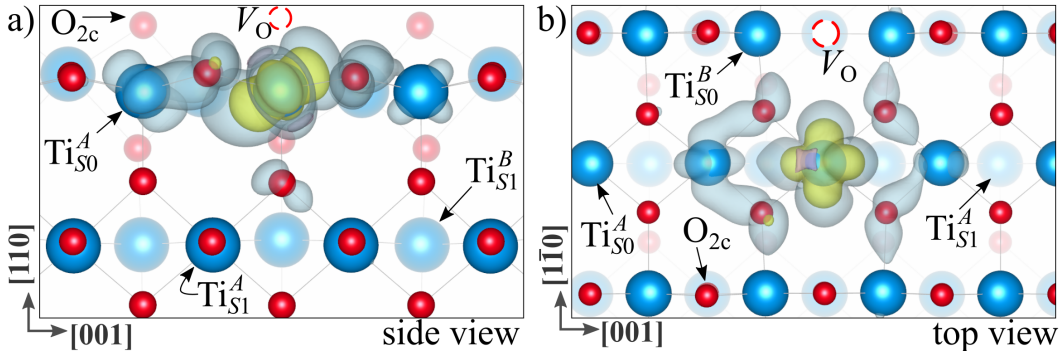

Figure C.5: Charge density for the NN-Ti^A_{S0} polaron. Side (a) and top view (b) are shown, with faded spheres representing background atoms. A $+e$-charged 9×2-large slab with one V_O was used. *[Unpublished Figure]*

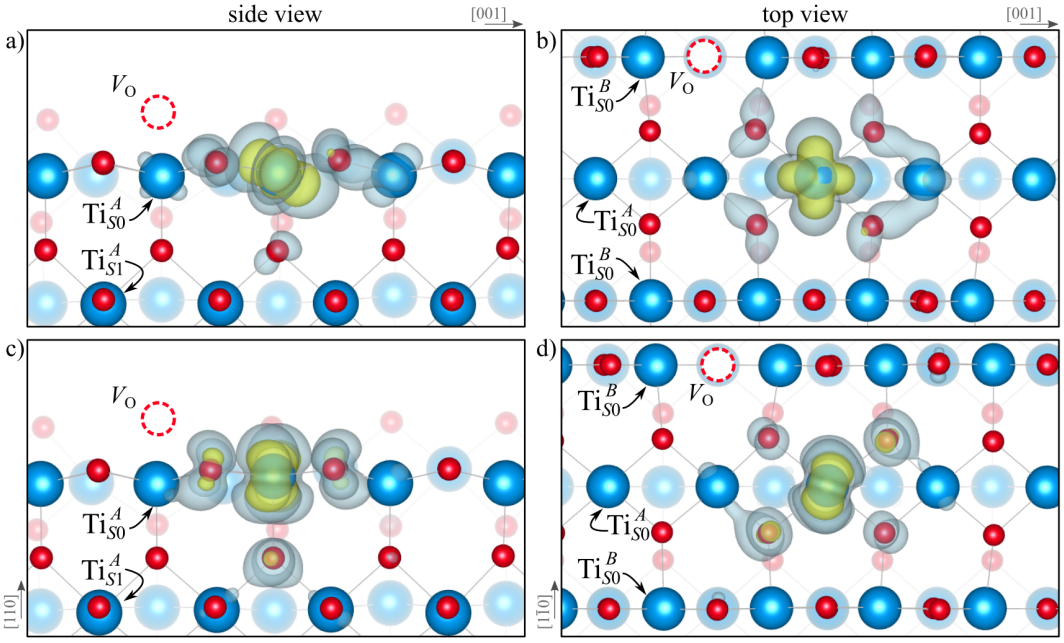

Figure C.6: Alternative orbital symmetries for the NNN-Ti^A_{S0} polaron. The $d_{x^2-y^2}$ (a,b) and the d_{yz} (c,d) flavors for the NNN-Ti^A_{S0} polaron are shown in the side (a,c) and top (b,d) view images. The most stable flavor, *i.e.*, d_{xz}-d_{yz}, is shown in Fig. 3.2(a,b) for an isolated $S0$ polaron. *[Unpublished Figure]*

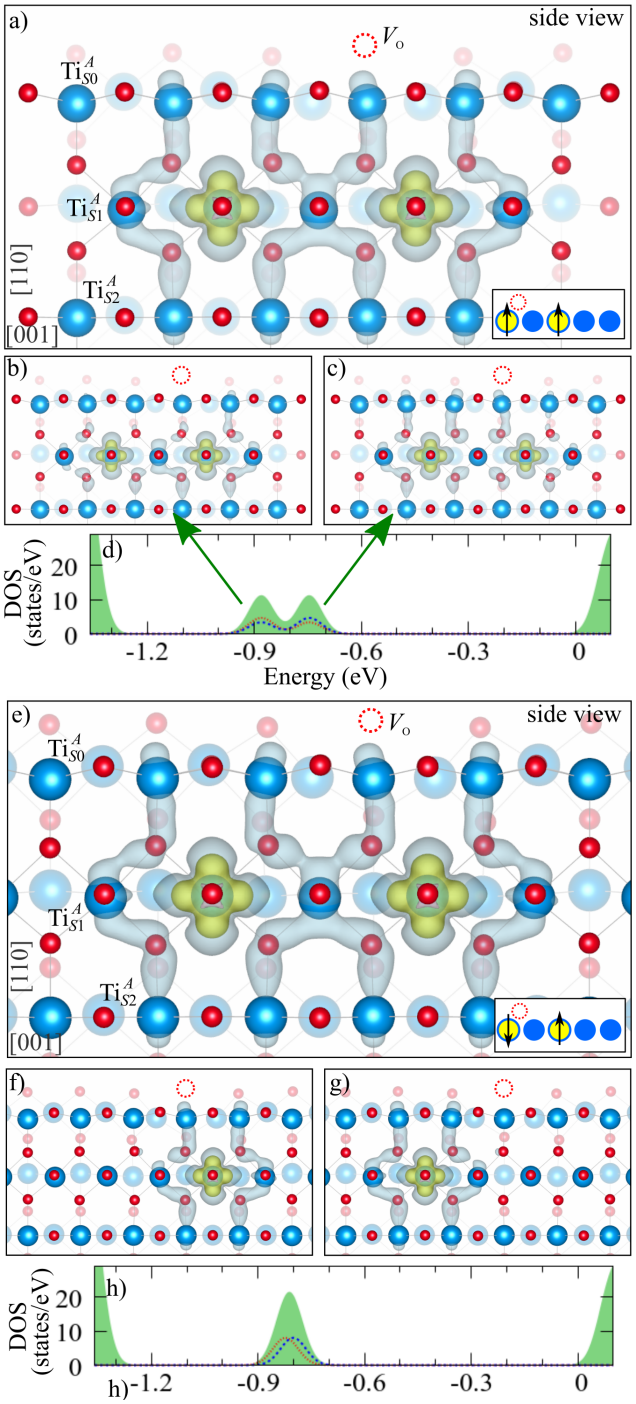

Figure C.7: Next nearest neighbor Ti^A_{S1} polarons. The polarons have either parallel (a-d) or opposite (e-h) spins. Side view of the total (a and e) and individual (b,c and f,g) charge densities of the two polarons (in a charge-neutral slab, with one V_O). The insets shows the geometry. The DOS is also shown (d and h). *[Unpublished Figure]*

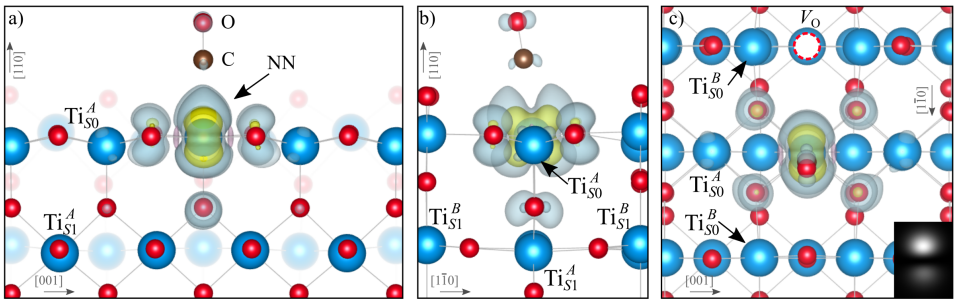

Figure C.8: The CO+$S0$-polaron complex at NN-Ti^A_{S0}. Side (a), front (b) and top (c) views of the charge density of a $S0$ polaron bounded to CO at the NN-Ti^A_{S0} site (simulated STM in the inset). *Comment on the Figure: The in-gap charge orbitals of the CO+S0-polaron complex show a similar STM signal with respect to CO+S0-polaron complexes at the NNN-Ti^A_{S0} site shown in Fig. 5.1(b), but with a different orientation. [Unpublished Figure]*

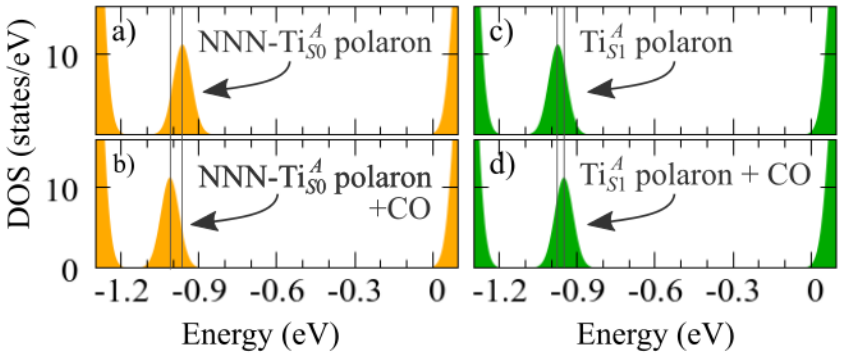

Figure C.9: CO effect on the $S0$ and $S1$ polaron in-gap state. A polaron is localized either on the NNN-Ti^A_{S0} site (a,b) or on the $S1$ layer in the proximity of V_O (c,d). The DOS are calculated either for the clean surface (a,c) or in the presence of a CO molecule adsorbed on NNN-Ti^A_{S0}. *Comment on the Figure: The CO molecule shift the S0-polaron state towards deeper energies, while the S1-polaron state is shifted towards shallower energies. [Unpublished Figure]*

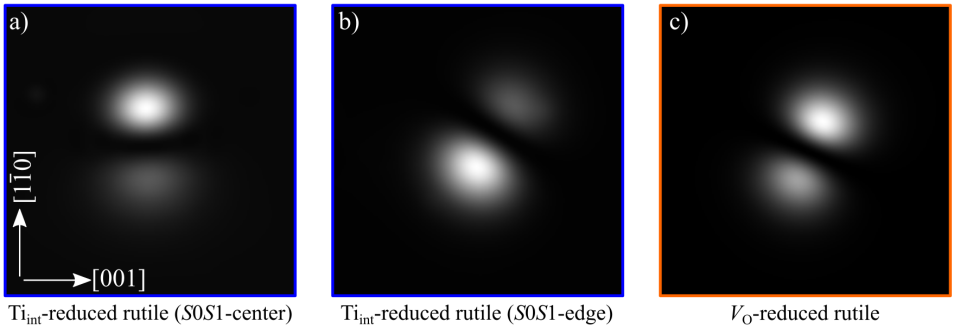

Figure C.10: STM double-lobed spots for the CO+*S*0-polaron complex. Simulated filled-state STM images for the CO+*S*0-polaron complex formed in the proximity of a Ti_{int} in the *S*0*S*1-center (a) and *S*0*S*1-edge (b) geometries. The STM simulations for the CO+*S*0-polaron complex on the NNN-Ti^{A}_{S0} site from V_O (on the Ti_{int}-free slab) is also shown for comparison (c). *Figure adapted from Phys. Rev. L, Supplemental Material* ©*2018 American Physical Society* [2].

Acknowledgements

Here, I warmly thank all people who contributed to the accomplishment of the doctorate project.

I am grateful to the reviewers for their kind and immediate availability. I hope you have appreciated reading this dissertation.

Thanks to the Austrian Science Fund (FWF, ViCoM), and the Doctorate Completion Fellowship awarded by the University of Vienna, which financed our research and, in particular, me playing physics.

Bibliography

[1] M. Reticcioli, U. Diebold, G. Kresse, and C. Franchini, "Small polarons in transition metal oxides," in *Handbook of Materials Modeling 2nd edition* (accepted by Springer, 2018).

[2] M. Reticcioli, I. Sokolović, M. Schmid, U. Diebold, M. Setvin, and C. Franchini, arXiv 1807.05859 (2018), accepted by Phys. Rev. Lett.

[3] M. Reticcioli, M. Setvin, M. Schmid, U. Diebold, and C. Franchini, Physical Review B **98**, 045306 (2018).

[4] M. Reticcioli, M. Setvin, X. Hao, P. Flauger, G. Kresse, M. Schmid, U. Diebold, and C. Franchini, Phys. Rev. X **7**, 031053 (2017).

[5] M. Setvin, M. Reticcioli, F. Poelzleitner, J. Hulva, M. Schmid, L. A. Boatner, C. Franchini, and U. Diebold, Science **359**, 572 (2018).

[6] G. Pacchioni, Nature Reviews Materials **2**, 17071 (2017).

[7] R. Pool, Wiley Microscopy & Analysis **2**, 7 (2018).

[8] U. Diebold, S.-C. Li, and M. Schmid, Annual Review of Physical Chemistry **61**, 129 (2010).

[9] C. N. R. Rao, Annual Review of Physical Chemistry **40**, 291 (1989).

[10] J. Jupille and G. Thornton, *Defects at Oxide Surfaces* (Springer, 2015).

[11] M. Todorova, W. X. Li, M. V. Ganduglia-Pirovano, C. Stampfl, K. Reuter, and M. Scheffler, Physical Review Letters **89**, 096103 (2002).

[12] U. Diebold, Surface Science Reports **48**, 53 (2003).

[13] F. A. Grant, Reviews of Modern Physics **31**, 646 (1959).

[14] M. Ramamoorthy, D. Vanderbilt, and R. D. King-Smith, Physical Review B **49**, 16721 (1994).

[15] M. V. Ganduglia-Pirovano, A. Hofmann, and J. Sauer, Surface Science Reports **62**, 219 (2007).

[16] P. W. Tasker, Journal of Physics C: Solid State Physics **12**, 4977 (1979).

[17] H. Onishi and Y. Iwasawa, Surface Science **313**, L783 (1994).

[18] H. Onishi, K.-i. Fukui, and Y. Iwasawa, Bulletin of the Chemical Society of Japan **68**, 2447 (1995).

[19] H. Onishi and Y. Iwasawa, Physical Review Letters **76**, 791 (1996).

[20] I. Mochizuki, H. Ariga, Y. Fukaya, K. Wada, M. Maekawa, A. Kawasuso, T. Shidara, K. Asakura, and T. Hyodo, Phys. Chem. Chem. Phys. **18**, 7085 (2016).

[21] Q. Wang, A. R. Oganov, Q. Zhu, and X.-F. Zhou, Physical Review Letters **113**, 266101 (2014).

[22] S. Livraghi, M. C. Paganini, E. Giamello, A. Selloni, C. Di Valentin, and G. Pacchioni, Journal of the American Chemical Society **128**, 15666 (2006).

[23] C. Di Valentin, G. Pacchioni, and A. Selloni, Chemistry of Materials **17**, 6656 (2005).

[24] C. Di Valentin, G. Pacchioni, and A. Selloni, Journal of Physical Chemistry C **113**, 20543 (2009).

[25] A. L. Shluger and A. M. Stoneham, Journal of Physics: Condensed Matter **5**, 3049 (1993).

[26] P. Deák, B. Aradi, and T. Frauenheim, Physical Review B **86**, 195206 (2012).

[27] S. Yang, A. T. Brant, N. C. Giles, and L. E. Halliburton, Physical Review B **87**, 125201 (2013).

[28] V. N. Bogomolov and D. N. Mirlin, Physica Status Solidi (b) **27**, 443 (1968).

[29] S. Moser, L. Moreschini, J. Jaćimović, O. S. Barišić, H. Berger, A. Magrez, Y. J. Chang, K. S. Kim, A. Bostwick, E. Rotenberg, L. Forró, and M. Grioni, Physical Review Letters **110**, 196403 (2013).

[30] C. Di Valentin, G. Pacchioni, A. Selloni, S. Livraghi, and E. Giamello, The Journal of Physical Chemistry B **109**, 11414 (2005).

[31] C. Di Valentin, E. Finazzi, G. Pacchioni, A. Selloni, S. Livraghi, M. C. Paganini, and E. Giamello, Chemical Physics **339**, 44 (2007).

[32] C. Di Valentin, E. Finazzi, G. Pacchioni, A. Selloni, S. Livraghi, A. M. Czoska, M. C. Paganini, and E. Giamello, Chemistry of Materials **20**, 3706 (2008).

[33] C. Franchini, G. Kresse, and R. Podloucky, Physical Review Letters **102**, 256402 (2009).

[34] P. Nagels, M. Denayer, and J. Devreese, Solid State Communications **1**, 35 (1963).

[35] C. Verdi, F. Caruso, and F. Giustino, Nature Communications **8**, 15769 (2017).

[36] H. Sezen, M. Buchholz, A. Nefedov, C. Natzeck, S. Heissler, C. Di Valentin, and C. Wöll, Scientific Reports **4**, 3808 (2014).

[37] F. Freytag, G. Corradi, and M. Imlau, Scientific Reports **6**, 36929 (2016).

[38] N. W. Ashcroft and N. D. Mermin, *Solid State Physics* (W. B. Saunders Co., 1976).

[39] L. M. S. James H. Crawford Jr., *Point Defects in Solids* (Springer, 1972).

[40] C. Freysoldt, B. Grabowski, T. Hickel, J. Neugebauer, G. Kresse, A. Janotti, and C. G. Van de Walle, Reviews of Modern Physics **86**, 253 (2014).

[41] G. Pacchioni, "Numerical Simulations of Defective Structures: The Nature of Oxygen Vacancy in Non-reducible (MgO, SiO_2, ZrO_2) and Reducible (TiO_2, NiO, WO_3) Oxides," in *Defects at Oxide Surfaces*, edited by J. Jupille and G. Thornton (Springer, 2015) Chap. 1, pp. 1–28.

[42] M. Chiesa, M. C. Paganini, E. Giamello, D. M. Murphy, C. Di Valentin, and G. Pacchioni, Accounts of Chemical Research **39**, 861 (2006).

[43] T. Holstein, Annals of Physics **8**, 325 (1959).

[44] H. Fröhlich, Advances in Physics **3**, 325 (1954).

[45] N. A. Deskins, R. Rousseau, and M. Dupuis, Journal of Physical Chemistry C **113**, 14583 (2009).

[46] P. M. Kowalski, M. F. Camellone, N. N. Nair, B. Meyer, and D. Marx, Physical Review Letters **105**, 146405 (2010).

[47] N. A. Deskins, R. Rousseau, and M. Dupuis, Journal of Physical Chemistry C **115**, 7562 (2011).

[48] M. Setvin, C. Franchini, X. Hao, M. Schmid, A. Janotti, M. Kaltak, C. G. Van De Walle, G. Kresse, and U. Diebold, Physical Review Letters **113**, 086402 (2014).

[49] M. Setvin, X. Hao, B. Daniel, J. Pavelec, Z. Novotny, G. S. Parkinson, M. Schmid, G. Kresse, C. Franchini, and U. Diebold, Angewandte Chemie International Edition **53**, 4714 (2014).

[50] C. Crevecoeur and H. De Wit, Journal of Physics and Chemistry of Solids **31**, 783 (1970).

[51] E. Salje, A. S. Alexandrov, and W. Y. Liang, *Polarons and Bipolarons in High-Tc Superconductors and Related Materials* (Cambridge University Press, Cambridge, England, 2005).

[52] J. M. D. Teresa, M. R. Ibarra, P. A. Algarabel, C. Ritter, C. Marquina, J. Blasco, J. García, A. del Moral, and Z. Arnold, Nature **386**, 256 (1997).

[53] H. M. Rønnow, C. Renner, G. Aeppli, T. Kimura, and Y. Tokura, Nature **440**, 1025 (2006).

[54] M. Wang, C. Bi, L. Li, S. Long, Q. Liu, H. Lv, N. Lu, P. Sun, and M. Liu, Nature Communications **5**, 4598 (2014).

[55] D. Cortecchia, J. Yin, A. Bruno, S.-Z. A. Lo, G. G. Gurzadyan, S. Mhaisalkar, J.-L. Brédas, and C. Soci, Journal of Materials Chemistry C **5**, 2771 (2017).

[56] A. L. Linsebigler, G. Lu, and J. T. Yates, Chemical Reviews **95**, 735 (1995).

[57] L. D. Landau, Phys. Z. Sowjet. **664** (1933).

[58] S. I. Pekar, Zh. Eksp. Teor. Fiz. **335** (1946).

[59] A. S. Alexandrov and J. T. Devreese, *Advances in Polaron Physics* (Springer, 2010).

[60] L. D. Landau and S. I. Pekar, "The effective mass of the polaron," in *Collected Papers of L.D. Landau*, Vol. 53 (Elsevier, 1965) pp. 478–483.

[61] H. Fröhlich, H. Pelzer, and S. Zienau, The London, Edinburgh, and Dublin Philosophical Magazine and Journal of Science **41**, 221 (1950).

[62] J. T. Devreese, "Polarons," in *Encyclopedia of Applied Physics*, Vol. 14 (Wiley-VCH Publishers, Inc., 1996) pp. 383–409, arXiv:cond-mat/0004497 .

[63] D. Emin, *Polarons* (Cambridge University Press, 2013).

[64] R. Ramakumar and A. N. Das, The European Physical Journal B **41**, 197 (2004).

[65] T. Holstein, Annals of Physics **281**, 725 (2000).

[66] E. I. Rashba, "Polarons," in *Encyclopedia of Condensed Matter Physics*, edited by F. Bassani, G. L. Liedl, and P. Wyder (Elsevier, 2005) Chap. 4, pp. 347–355.

[67] N. F. Mott and A. M. Stoneham, Journal of Physics C: Solid State Physics **10**, 3391 (1977).

[68] S. Lany, Journal of Physics: Condensed Matter **27**, 283203 (2015).

[69] R. P. Feynman, Physical Review **97**, 660 (1955).

[70] N. V. Prokof'ev and B. V. Svistunov, Physical Review Letters **81**, 2514 (1998).

[71] A. S. Mishchenko, N. V. Prokof'ev, A. Sakamoto, and B. V. Svistunov, Physical Review B **62**, 6317 (2000).

[72] R. Rosenfelder and A. Schreiber, Physics Letters A **284**, 63 (2001).

[73] B. Gerlach, F. Kalina, and M. Smondyrev, physica status solidi (b) **237**, 204 (2003).

[74] B. Gerlach and M. A. Smondyrev, Physical Review B **77**, 174303 (2008).

[75] T. Hahn, S. Klimin, J. Tempere, J. T. Devreese, and C. Franchini, Physical Review B **97**, 134305 (2018).

[76] K. Miyata, D. Meggiolaro, M. T. Trinh, P. P. Joshi, E. Mosconi, S. C. Jones, F. De Angelis, and X.-Y. Zhu, Science Advances **3**, e1701217 (2017).

[77] H. Tuller and A. Nowick, Journal of Physics and Chemistry of Solids **38**, 859 (1977).

[78] E. Possenriede, H. Kröse, T. Varnhorst, R. Scharfschwerdt, and O. F. Schirmer, Ferroelectrics **151**, 199 (1994).

[79] S. X. Zhang, D. C. Kundaliya, W. Yu, S. Dhar, S. Y. Young, L. G. Salamanca-Riba, S. B. Ogale, R. D. Vispute, and T. Venkatesan, Journal of Applied Physics **102**, 013701 (2007).

[80] P. Krüger, S. Bourgeois, B. Domenichini, H. Magnan, D. Chandesris, P. Le Fèvre, A. M. Flank, J. Jupille, L. Floreano, A. Cossaro, A. Verdini, and A. Morgante, Physical Review Letters **100**, 055501 (2008).

[81] Y. Cao, M. Yu, S. Qi, S. Huang, T. Wang, M. Xu, S. Hu, and S. Yan, Scientific Reports **7**, 6148 (2017).

[82] A. M. Stoneham, J. Gavartin, A. L. Shluger, A. V. Kimmel, D. M. Ramo, H. M. Rønnow, G. Aeppli, and C. Renner, Journal of Physics: Condensed Matter **19**, 255208 (2007).

[83] A. Bosman and H. van Daal, Advances in Physics **19**, 1 (1970).

[84] S. Aronson, J. E. Rulli, and B. E. Schaner, The Journal of Chemical Physics **35**, 1382 (1961).

[85] S. Lenjer, O. F. Schirmer, H. Hesse, and T. W. Kool, Physical Review B **66**, 165106 (2002).

[86] A. Klein, Journal of the American Ceramic Society **96**, 331 (2013).

[87] P. Krüger, J. Jupille, S. Bourgeois, B. Domenichini, A. Verdini, L. Floreano, and A. Morgante, Physical Review Letters **108**, 126803 (2012).

[88] S. Chambers, Surface Science Reports **16**, 261 (1992).

[89] E. Bertel, R. Stockbauer, and T. E. Madey, Physical Review B **27**, 1939 (1983).

[90] A. Locatelli, T. Pabisiak, A. Pavlovska, T. O. Mentes, L. Aballe, A. Kiejna, and E. Bauer, Journal of Physics: Condensed Matter **19**, 082202 (2007).

[91] F. Giustino, Reviews of Modern Physics **89**, 015003 (2017).

[92] M. Gerosa, C. E. Bottani, L. Caramella, G. Onida, C. Di Valentin, and G. Pacchioni, Journal of Chemical Physics **143**, 134702 (2015).

[93] S. Bourgeois, "Excess Electrons at Oxide Surfaces," in *Defects at Oxide Surfaces*, edited by B. Domenichini and J. Jupille (Springer, 2015) Chap. 4, pp. 123–148.

[94] J. Janak, Physical Review B **18**, 7165 (1978).

[95] J. P. Perdew, R. G. Parr, M. Levy, and J. L. Balduz, Physical Review Letters **49**, 1691 (1982).

[96] J. P. Perdew and M. Levy, Physical Review Letters **51**, 1884 (1983).

[97] J. To, A. A. Sokol, S. A. French, N. Kaltsoyannis, and C. R. A. Catlow, The Journal of Chemical Physics **122**, 144704 (2005).

[98] A. D. Becke, The Journal of Chemical Physics **98**, 1372 (1993).

[99] J. He and C. Franchini, Physical Review B **86**, 235117 (2012).

[100] L. Kronik, T. Stein, S. Refaely-Abramson, and R. Baer, Journal of Chemical Theory and Computation **8**, 1515 (2012).

[101] A. R. Elmaslmane, J. Wetherell, M. J. P. Hodgson, K. P. McKenna, and R. W. Godby, Physical Review Materials **2**, 040801 (2018).

[102] J. He and C. Franchini, Journal of Physics: Condensed Matter **29**, 454004 (2017).

[103] W. Chen, G. Miceli, G.-M. Rignanese, and A. Pasquarello, Physical Review Materials **2**, 073803 (2018).

[104] Z.-H. Cui, Y.-C. Wang, M.-Y. Zhang, X. Xu, and H. Jiang, The Journal of Physical Chemistry Letters **9**, 2338 (2018).

[105] T. Maxisch, F. Zhou, and G. Ceder, Physical Review B **73**, 104301 (2006).

[106] M. Nolan and G. W. Watson, Journal of Chemical Physics **125**, 144701 (2006).

[107] J. L. F. Da Silva, M. V. Ganduglia-Pirovano, J. Sauer, V. Bayer, and G. Kresse, Physical Review B **75**, 045121 (2007).

[108] V. I. Anisimov, J. Zaanen, and O. K. Andersen, Physical Review B **44**, 943 (1991).

[109] V. I. Anisimov, I. V. Solovyev, M. A. Korotin, M. T. Czyżyk, and G. A. Sawatzky, Physical Review B **48**, 16929 (1993).

[110] A. I. Liechtenstein, V. I. Anisimov, and J. Zaanen, Physical Review B **52**, 5467 (1995).

[111] S. L. Dudarev, G. A. Botton, S. Y. Savrasov, C. J. Humphreys, and a. P. Sutton, Physical Review B **57**, 1505 (1998).

[112] S. L. Dudarev, G. A. Botton, S. Y. Savrasov, Z. Szotek, W. M. Temmerman, and A. P. Sutton, Electronic Structure and Elastic Properties **166**, 429 (1998).

[113] O. Gunnarsson, Physical Review B **41**, 514 (1990).

[114] M. Cococcioni and S. de Gironcoli, Physical Review B **71**, 035105 (2005).

[115] F. Aryasetiawan, M. Imada, A. Georges, G. Kotliar, S. Biermann, and A. I. Lichtenstein, Physical Review B **70**, 195104 (2004).

[116] S. Lany and A. Zunger, Physical Review B **80**, 085202 (2009).

[117] S. Lany, Physica Status Solidi (B) Basic Research **248**, 1052 (2011).

[118] G. Kresse and J. Furthmüller, Physical Review B **54**, 11169 (1996).

[119] G. Kresse and J. Furthmüller, Computational Materials Science **6**, 15 (1996).

[120] J. P. Perdew, K. Burke, and M. Ernzerhof, Physical Review Letters **77**, 3865 (1996).

[121] G. Kresse, M. Marsman, and J. Furthmüller, *VASP the guide, On site Coulomb interaction: L(S)DA+U* (2016).

[122] H. Cheng and A. Selloni, Physical Review B **79**, 092101 (2009).

[123] H. Li, Y. Guo, and J. Robertson, Journal of Physical Chemistry C **119**, 18160 (2015).

[124] G. Kresse, M. Marsman, and J. Furthmüller, *VASP the guide, LVTOT tag, and core level shifts* (2016).

[125] T. Shibuya, K. Yasuoka, S. Mirbt, and B. Sanyal, The Journal of Physical Chemistry C **121**, 11325 (2017).

[126] X. Hao, Z. Wang, M. Schmid, U. Diebold, and C. Franchini, Physical Review B **91**, 085204 (2015).

[127] A. C. Papageorgiou, N. S. Beglitis, C. L. Pang, G. Teobaldi, G. Cabailh, Q. Chen, A. J. Fisher, W. A. Hofer, and G. Thornton, Proceedings of the National Academy of Sciences **107**, 2391 (2010).

[128] B. Meredig, A. Thompson, H. A. Hansen, C. Wolverton, and A. van de Walle, Physical Review B **82**, 195128 (2010).

[129] B. J. Morgan and G. W. Watson, Physical Review B **80**, 233102 (2009).

[130] A. Malashevich, M. Jain, and S. G. Louie, Physical Review B **89**, 075205 (2014).

[131] G. Kresse and J. Hafner, Physical Review B **47**, 558 (1993).

[132] S. Nosé, The Journal of Chemical Physics **81**, 511 (1984).

[133] A. Janotti, C. Franchini, J. B. Varley, G. Kresse, and C. G. Van de Walle, physica status solidi (RRL) - Rapid Research Letters **7**, 199 (2013).

[134] L. Sun, X. Huang, L. Wang, and A. Janotti, Physical Review B **95**, 245101 (2017).

[135] K. Reuter and M. Scheffler, Physical Review B **65**, 035406 (2001).

[136] J. Tersoff and D. R. Hamann, Physical Review B **31**, 805 (1985).

[137] J. J. Klimeš, D. R. Bowler, and A. Michaelides, Journal of Physics: Condensed Matter **22**, 022201 (2010).

[138] M. Dion, H. Rydberg, E. Schröder, D. C. Langreth, and B. I. Lundqvist, Physical Review Letters **92**, 246401 (2004).

[139] Z. Majzik, M. Setvín, A. Bettac, A. Feltz, V. Cháb, and P. Jelínek, Beilstein Journal of Nanotechnology **3**, 249 (2012).

[140] M. Setvín, J. Javorský, D. Turčinková, I. Matolínová, P. Sobotík, P. Kocán, and I. Ošt'ádal, Ultramicroscopy **113**, 152 (2012).

[141] I. G. Austin and N. F. Mott, Advances in Physics **50**, 757 (2001).

[142] S. Wendt, P. T. Sprunger, E. Lira, G. K. H. Madsen, Z. Li, J. O. b. Hansen, J. Matthiesen, A. Blekinge-Rasmussen, E. Laegsgaard, B. Hammer, and F. Besenbacher, Science **320**, 1755 (2008).

[143] T. Shibuya, K. Yasuoka, S. Mirbt, and B. Sanyal, Journal of Physics: Condensed Matter **24**, 435504 (2012).

[144] C. M. Yim, M. B. Watkins, M. J. Wolf, C. L. Pang, K. Hermansson, and G. Thornton, Physical Review Letters **117**, 116402 (2016).

[145] C. J. Calzado, N. C. Hernández, and J. F. Sanz, Physical Review B **77**, 045118 (2008).

[146] A. Janotti, J. B. Varley, P. Rinke, N. Umezawa, G. Kresse, and C. G. Van de Walle, Physical Review B **81**, 085212 (2010).

[147] P. G. Moses, A. Janotti, C. Franchini, G. Kresse, and C. G. Van de Walle, Journal of Applied Physics **119**, 181503 (2016).

[148] T. Shibuya, K. Yasuoka, S. Mirbt, and B. Sanyal, The Journal of Physical Chemistry C **118**, 9429 (2014).

[149] C. Di Valentin, G. Pacchioni, and A. Selloni, Physical Review Letters **97**, 166803 (2006).

[150] W. Mackrodt, E.-a. Simson, and N. Harrison, Surface Science **384**, 192 (1997).

[151] M. Chiesa, S. Livraghi, E. Giamello, E. Albanese, and G. Pacchioni, Angewandte Chemie International Edition **56**, 2604 (2017).

[152] S. Lakkis, C. Schlenker, B. K. Chakraverty, R. Buder, and M. Marezio, Physical Review B **14**, 1429 (1976).

[153] N. A. Deskins and M. Dupuis, Physical Review B **75**, 195212 (2007).

[154] Z. Dohnálek, I. Lyubinetsky, and R. Rousseau, Progress in Surface Science **85**, 161 (2010).

[155] L. Yan, J. E. Elenewski, W. Jiang, and H. Chen, Physical Chemistry Chemical Physics **17**, 29949 (2015).

[156] S. Selcuk and A. Selloni, Nature Materials **15**, 1107 (2016).

[157] A. Amore Bonapasta, F. Filippone, G. Mattioli, and P. Alippi, Catalysis Today **144**, 177 (2009).

[158] E. Finazzi, C. D. Valentin, G. Pacchioni, C. Di Valentin, and G. Pacchioni, The Journal of Physical Chemistry C **113**, 3382 (2009).

[159] Y.-Y. Yu and X.-Q. Gong, ACS Catalysis **5**, 2042 (2015).

[160] K. Morita, T. Shibuya, and K. Yasuoka, The Journal of Physical Chemistry C **121**, 1602 (2017).

[161] B. Wen, W.-J. Yin, A. Selloni, and L.-M. Liu, The Journal of Physical Chemistry Letters **9**, 5281 (2018).

[162] Y. Yoon, Y. Du, J. C. Garcia, Z. Zhu, Z.-T. Wang, N. G. Petrik, G. A. Kimmel, Z. Dohnalek, M. A. Henderson, R. Rousseau, N. A. Deskins, and I. Lyubinetsky, ChemPhysChem **16**, 313 (2015).

[163] M. Li, W. Hebenstreit, and U. Diebold, Surface Science **414**, L951 (1998).

[164] G. E. Murgida, V. Ferrari, M. V. Ganduglia-Pirovano, and A. M. Llois, Physical Review B **90**, 115120 (2014).

[165] M. V. Ganduglia-Pirovano, J. L. F. Da Silva, and J. Sauer, Physical Review Letters **102**, 026101 (2009).

[166] N. Bondarenko, O. Eriksson, and N. V. Skorodumova, Physical Review B **92**, 165119 (2015).

[167] M. V. Ganduglia-Pirovano, "Oxygen Defects at Reducible Oxide Surfaces: The Example of Ceria and Vanadia," in *Defects at Oxide Surfaces*, edited by J. Jupille and G. Thornton (Springer, 2015) Chap. 5, pp. 149–190.

[168] K. Oura, V. G. Lifshits, A. A. Saranin, A. V. Zotov, and M. Katayama, *Surface Science - An Introduction* (Springer, Berlin, Heidelberg, 2003).

[169] C. Noguera, Journal of Physics: Condensed Matter **12**, R367 (2000).

[170] X.-q. Wang, Physical Review Letters **67**, 3547 (1991).

[171] G. Binnig, H. Rohrer, C. Gerber, and E. Weibel, Physical Review Letters **50**, 120 (1983).

[172] K. D. Brommer, M. Needels, B. Larson, and J. D. Joannopoulos, Physical Review Letters **68**, 1355 (1992).

[173] J. A. Enterkin, A. K. Subramanian, B. C. Russell, M. R. Castell, K. R. Poeppelmeier, and L. D. Marks, Nature Materials **9**, 245 (2010).

[174] Z. Wang, A. Loon, A. Subramanian, S. Gerhold, E. McDermott, J. A. Enterkin, M. Hieckel, B. C. Russell, R. J. Green, A. Moewes, J. Guo, P. Blaha, M. R. Castell, U. Diebold, and L. D. Marks, Nano Letters **16**, 2407 (2016).

[175] H.-J. Freund and G. Pacchioni, Chemical Society Reviews **37**, 2224 (2008).

[176] G. Profeta and E. Tosatti, Physical Review Letters **98**, 086401 (2007).

[177] P. G. Lustemberg, Y. Pan, B.-J. Shaw, D. Grinter, C. Pang, G. Thornton, R. Pérez, M. V. Ganduglia-Pirovano, and N. Nilius, Physical Review Letters **116**, 236101 (2016).

[178] M. Li, W. Hebenstreit, L. Gross, U. Diebold, M. Henderson, D. Jennison, P. Schultz, and M. Sears, Surface Science **437**, 173 (1999).

[179] M. Li, W. Hebenstreit, and U. Diebold, Physical Review B **61**, 4926 (2000).

[180] K. McCarty and N. Bartelt, Surface Science **527**, L203 (2003).

[181] K. F. McCarty and N. C. Bartelt, Physical Review Letters **90**, 046104 (2003).

[182] C. Pang, S. Haycock, H. Raza, P. Murray, G. Thornton, O. Gulseren, R. James, and D. Bullett, Physical Review B **58**, 1586 (1998).

[183] K. T. Park, M. Pan, V. Meunier, and E. W. Plummer, Physical Review B **75**, 245415 (2007).

[184] N. Shibata, A. Goto, S.-Y. Choi, T. Mizoguchi, S. D. Findlay, T. Yamamoto, and Y. Ikuhara, Science **322**, 570 (2008).

[185] K.-o. Ng and D. Vanderbilt, Physical Review B **56**, 10544 (1997).

[186] M. Batzill, K. Katsiev, D. J. Gaspar, and U. Diebold, Physical Review B **66**, 235401 (2002).

[187] C. Sánchez-Sánchez, M. G. Garnier, P. Aebi, M. Blanco-Rey, P. L. De Andres, J. A. Martín-Gago, and M. F. López, Surface Science **608**, 92 (2013).

[188] C. M. Yim, C. L. Pang, and G. Thornton, Surface Science **650**, 71 (2016).

[189] Z. Zhang, Q. Ge, S.-c. Li, B. D. Kay, J. M. White, and Z. Dohnálek, Physical Review Letters **99**, 126105 (2007).

[190] S. Livraghi, S. Maurelli, M. C. Paganini, M. Chiesa, and E. Giamello, Angewandte Chemie International Edition **50**, 8038 (2011).

[191] V. E. Henrich, G. Dresselhaus, and H. J. Zeiger, Physical Review Letters **36**, 1335 (1976).

[192] P. Deák, B. Aradi, and T. Frauenheim, Physical Review B **92**, 045204 (2015).

[193] N. Erdman, K. R. Poeppelmeier, M. Asta, O. Warschkow, D. E. Ellis, and L. D. Marks, Nature **419**, 55 (2002).

[194] R. Olbrich, G. E. Murgida, V. Ferrari, C. Barth, A. M. Llois, M. Reichling, and M. V. Ganduglia-Pirovano, The Journal of Physical Chemistry C **121**, 6844 (2017).

[195] G. E. Murgida, V. Ferrari, A. M. Llois, and M. V. Ganduglia-Pirovano, Physical Review Materials **2**, 083609 (2018).

[196] Z.-K. Han, Y.-Z. Yang, B. Zhu, M. V. Ganduglia-Pirovano, and Y. Gao, Physical Review Materials **2**, 035802 (2018).

[197] C. Cancellieri, A. S. Mishchenko, U. Aschauer, A. Filippetti, C. Faber, O. S. Barišić, V. A. Rogalev, T. Schmitt, N. Nagaosa, and V. N. Strocov, Nature Communications **7**, 10386 (2016).

[198] R. Shimizu, K. Iwaya, T. Ohsawa, T. Hasegawa, T. Hashizume, and T. Hitosugi, Applied Surface Science **257**, 4867 (2011).

[199] A. Song, E. S. Skibinski, W. J. Debenedetti, A. G. Ortoll-Bloch, and M. A. Hines, Journal of Physical Chemistry C **120**, 9326 (2016).

[200] R. Bechstein, C. González, J. Schütte, P. Jelínek, R. Pérez, and A. Kühnle, Nanotechnology **20**, 505703 (2009).

[201] E. Gale, Semiconductor Science and Technology **29**, 104004 (2014).

[202] M. A. Henderson, Surface Science Reports **66**, 185 (2011).

[203] G. Pacchioni, The Chemical Record **14**, 910 (2014).

[204] D. Vogtenhuber, R. Podloucky, and J. Redinger, Surface Science **402-404**, 798 (1998).

[205] M. V. Ganduglia-Pirovano, Catalysis Today **253**, 20 (2015).

[206] J. Carrasco, L. Barrio, P. Liu, J. A. Rodriguez, and M. V. Ganduglia-Pirovano, Journal of Physical Chemistry C **117**, 8241 (2013).

[207] J. P. Prates Ramalho, F. Illas, and J. R. B. Gomes, Physical Chemistry Chemical Physics **19**, 2487 (2017).

[208] N. G. Petrik and G. A. Kimmel, The Journal of Physical Chemistry Letters **3**, 3425 (2012).

[209] R. Mu, A. Dahal, Z.-T. Wang, Z. Dohnálek, G. A. Kimmel, N. G. Petrik, and I. Lyubinetsky, The Journal of Physical Chemistry Letters **8**, 4565 (2017).

[210] Y. Zhao, Z. Wang, X. Cui, T. Huang, B. Wang, Y. Luo, J. Yang, and J. Hou, Journal of the American Chemical Society **131**, 7958 (2009).

[211] M. Xu, H. Noei, K. Fink, M. Muhler, Y. Wang, and C. Wöll, Angewandte Chemie International Edition **51**, 4731 (2012).

[212] P. S. Bagus, C. J. Nelin, and C. W. Bauschlicher, Physical Review B **28**, 5423 (1983).

[213] K. I. Hadjiivanov and G. N. Vayssilov, "Characterization of oxide surfaces and zeolites by carbon monoxide as an IR probe molecule," in *Advances in Catalysis*, Vol. 47 (Academic Press, 2002) pp. 307–511.

[214] M. Farnesi Camellone, P. M. Kowalski, and D. Marx, Physical Review B **84**, 035413 (2011).

[215] M. Setvin, M. Buchholz, W. Hou, C. Zhang, B. Stöger, J. Hulva, T. Simschitz, X. Shi, J. Pavelec, G. S. Parkinson, M. Xu, Y. Wang, M. Schmid, C. Wöll, A. Selloni, and U. Diebold, The Journal of Physical Chemistry C **119**, 21044 (2015).

[216] H. Perron, C. Domain, J. Roques, R. Drot, E. Simoni, and H. Catalette, Theoretical Chemistry Accounts **117**, 565 (2007).

[217] C. Sun, L.-M. Liu, A. Selloni, G. Q. M. Lu, and S. C. Smith, Journal of Materials Chemistry **20**, 10319 (2010).

[218] L. A. Harris and A. A. Quong, Physical Review Letters **93**, 086105 (2004).

[219] T. Bredow, L. Giordano, F. Cinquini, and G. Pacchioni, Physical Review B **70**, 035419 (2004).

[220] S. Grimme, J. Antony, S. Ehrlich, and H. Krieg, The Journal of Chemical Physics **132**, 154104 (2010).

[221] S. Grimme, S. Ehrlich, and L. Goerigk, Journal of Computational Chemistry **32**, 1456 (2011).

[222] A. F. Santander-Syro, O. Copie, T. Kondo, F. Fortuna, S. Pailhès, R. Weht, X. G. Qiu, F. Bertran, A. Nicolaou, A. Taleb-Ibrahimi, P. Le Fèvre, G. Herranz, M. Bibes, N. Reyren, Y. Apertet, P. Lecoeur, A. Barthélémy, and M. J. Rozenberg, Nature **469**, 189 (2011).

[223] B. Meyer, Physical Review B **69**, 045416 (2004).

[224] O. Dulub, U. Diebold, and G. Kresse, Physical Review Letters **90**, 016102 (2003).

[225] S. Thiel, Science **313**, 1942 (2006).

[226] A. Bruix, Y. Lykhach, I. Matolínová, A. Neitzel, T. Skála, N. Tsud, M. Vorokhta, V. Stetsovych, K. Ševčíková, J. Mysliveček, R. Fiala, M. Václav, K. C. Prince, S. Bruyère, V. Potin, F. Illas, V. Matolín, J. Libuda, and K. M. Neyman, Angewandte Chemie International Edition **53**, 10525 (2014).

[227] D. J. Singh, Physical Review B **53**, 176 (1996).

[228] I. Grinberg, D. V. West, M. Torres, G. Gou, D. M. Stein, L. Wu, G. Chen, E. M. Gallo, A. R. Akbashev, P. K. Davies, J. E. Spanier, and A. M. Rappe, Nature **503**, 509 (2013).

[229] E. Grabowska, Applied Catalysis B: Environmental **186**, 97 (2016).

[230] H. Kato, K. Asakura, and A. Kudo, Journal of the American Chemical Society **125**, 3082 (2003).

[231] P. Zhang, J. Zhang, and J. Gong, Chem. Soc. Rev. **43**, 4395 (2014).

[232] A. Benrekia, N. Benkhettou, A. Nassour, M. Driz, M. Sahnoun, and S. Lebègue, Physica B: Condensed Matter **407**, 2632 (2012).

[233] J. Sun, R. C. Remsing, Y. Zhang, Z. Sun, A. Ruzsinszky, H. Peng, Z. Yang, A. Paul, U. Waghmare, X. Wu, M. L. Klein, and J. P. Perdew, Nature chemistry **8**, 831 (2016).

[234] L. Gross, B. Schuler, F. Mohn, N. Moll, N. Pavliček, W. Steurer, I. Scivetti, K. Kotsis, M. Persson, and G. Meyer, Physical Review B **90**, 155455 (2014).

[235] P. D. C. King, R. H. He, T. Eknapakul, P. Buaphet, S.-K. Mo, Y. Kaneko, S. Harashima, Y. Hikita, M. S. Bahramy, C. Bell, Z. Hussain, Y. Tokura, Z.-X. Shen, H. Y. Hwang, F. Baumberger, and W. Meevasana, Physical Review Letters **108**, 117602 (2012).

[236] P. R. Willmott, S. A. Pauli, R. Herger, C. M. Schlepütz, D. Martoccia, B. D. Patterson, B. Delley, R. Clarke, D. Kumah, C. Cionca, and Y. Yacoby, Physical Review Letters **99**, 155502 (2007).

[237] K. Szot, W. Speier, M. Pawelczyk, J. Kwapuliński, J. Hulliger, H. Hesse, U. Breuer, and W. Quadakkers, Journal of Physics: Condensed Matter **12**, 4687 (2000).

[238] J. H. Haeni, P. Irvin, W. Chang, R. Uecker, P. Reiche, Y. L. Li, S. Choudhury, W. Tian, M. E. Hawley, B. Craigo, A. K. Tagantsev, X. Q. Pan, S. K. Streiffer, L. Q. Chen, S. W. Kirchoefer, J. Levy, and D. G. Schlom, Nature **430**, 758 (2004).

[239] T. Y. Chien, J. Chakhalian, J. W. Freeland, and N. P. Guisinger, Advanced Functional Materials **23**, 2565 (2013).

[240] T. W. Trelenberg, R. Fatema, J. A. Li, E. A. Akhadov, D. H. Van Winkle, J. G. Skofronick, S. A. Safron, F. A. Flaherty, and L. A. Boatner, Journal of Physics: Condensed Matter **22**, 304009 (2010).

[241] D. E. E. Deacon-Smith, D. O. Scanlon, C. R. A. Catlow, A. A. Sokol, and S. M. Woodley, Advanced Materials **26**, 7252 (2014).

[242] E. Heifets, E. A. Kotomin, Y. A. Mastrikov, S. Piskunov, J. Maier, E. A., Y. A., S. Piskunov, and J. Maier, "Thermodynamics of ABO_3-Type Perovskite Surfaces," in *Thermodynamics - Interaction Studies - Solids, Liquids and Gases* (InTech, 2011).

Complete list of publications

Complete list of personal publications

2018 M. Reticcioli, U. Diebold, G. Kresse and C. Franchini, *Small polarons in transition metal oxides*, **Springer Handbook of Materials Modeling 2nd edition** (accepted in 2018).

2018 M. Reticcioli, I. Sokolović, M. Schmid, U. Diebold, M. Setvin and C. Franchini, *Interplay between adsorbates and polarons: CO on rutile TiO_2(110)*, **Phys. Rev. Lett.** (accepted in 2018). [arXiv:1807.05859]

2018 M. Reticcioli, M. Setvin, M. Schmid, U. Diebold and C. Franchini, *Formation and dynamics of small polarons on the rutile TiO_2(110) surface*, **Phys. Rev. B** 98, 045306 (2018). [DOI:10.1103/PhysRevB.98.045306, arXiv:1805.01849]

2018 M. Setvin, M. Reticcioli, F. Poelzleitner, J. Hulva, M. Schmid, L. A. Boatner, C. Franchini and U. Diebold, *Polarity compensation mechanisms on the perovskite surface $KTaO_3$(001)*, **Science** 359, 6375, 572-575 (2018). [DOI:10.1126/science.aar2287]

2018 M. Ulreich, L. A. Boatner, I. Sokolović, M. Reticcioli, F. Poelzleitner, C. Franchini, M. Schmid, U. Diebold, M. Setvin, *Defect chemistry of Eu dopants in NaI scintillators studied by atomically resolved force microscopy*, **letter under review** (2018). [arXiv:1809.01347]

2017 M. Reticcioli, M. Setvin, X. Hao, P. Flauger, G. Kresse, M. Schmid, U. Diebold and C. Franchini, *Polaron-Driven Surface Reconstructions*, **Phys. Rev. X** 7, 031053 (2017). [DOI:10.1103/PhysRevX.7.031053]

2017 M. Reticcioli, G. Profeta, C. Franchini and A. Continenza, *Ru doping in iron-based pnictides: The "unfolded" dominant role of structural effects for superconductivity*, **Phys. Rev. B** 95, 214510 (2017). [DOI:10.1103/PhysRevB.95.214510, arXiv:1701.02498]

2016 P. Liu, M. Reticcioli, B. Kim, A. Continenza, G. Kresse, D. D. Sarma, X. Q. Chen and C. Franchini, *Electron and hole doping in the relativistic Mott insulator Sr_2IrO_4: A first-principles study using band unfolding technique*, **Phys. Rev. B** 94, 195145 (2016). [DOI:10.1103/PhysRevB.94.195145]

2016 M. Reticcioli, G. Profeta, C. Franchini and A. Continenza, *Effective band structure of Ru-doped $BaFe_2As_2$*, **Journal of Physics: Conference Series** 689, 1 (2016). [DOI:10.1088/1742-6596/689/1/012027]